THE UNIVERSITY of EDINBURGH

This thesis has been submitted in fulfilment of the requirements for a postgraduate degree (e.g. PhD, MPhil, DClinPsychol) at the University of Edinburgh. Please note the following terms and conditions of use:

This work is protected by copyright and other intellectual property rights, which are retained by the thesis author, unless otherwise stated.
A copy can be downloaded for personal non-commercial research or study, without prior permission or charge.
This thesis cannot be reproduced or quoted extensively from without first obtaining permission in writing from the author.
The content must not be changed in any way or sold commercially in any format or medium without the formal permission of the author.
When referring to this work, full bibliographic details including the author, title, awarding institution and date of the thesis must be given.

Quantification of cardiac magnetic resonance imaging perfusion in the clinical setting at 3T

Giorgos Papanastasiou

A thesis submitted for the degree of Doctorate of Philosophy

School of Clinical Sciences

College of Medicine and Veterinary Medicine

The University of Edinburgh

2016

Declaration

This thesis has been composed by the student.

The student has been a member of a research group and has made substantial contribution to the work submitted. Led development of part of the image acquisition protocol, developed the image analysis software, performed and interpreted analysis of the magnetic resonance imaging data.

No portion of this work has been submitted for any other degree or professional qualification.

Abstract

Dynamic contrast enhanced (DCE) cardiac magnetic resonance imaging (MRI) is well-established as a non-invasive method for qualitatively detecting obstructive coronary artery disease (CAD) which can impair myocardial blood flow and may result in myocardial infarction. Mathematical modelling of cardiac DCE-MRI data can provide quantitative assessment of myocardial blood flow. Quantitative assessment of myocardial blood flow may have merit in further stratification of patients with obstructive CAD and to improve the diagnosis and prognostication of the disease in the clinical setting. This thesis investigates the development of a quantitative analysis protocol for cardiac DCE-MRI data.

In the first study presented in this thesis, Fermi and distributed parameter (DP) modelling are compared in single bolus versus dual bolus analysis. For model-based myocardial blood flow quantification, the convolution of a model with the arterial input function (i.e. contrast agent concentration-time curve extracted from the left ventricular cavity) is fitted to the tissue contrast agent concentration-time curve. In contrast to dual bolus DCE-MRI protocols, single bolus protocols reduce patient discomfort and acquisition protocol duration/complexity but, are prone to arterial input function saturation caused in the left ventricular cavity by the high concentration of contrast agent during bolus passage. Saturation effects can degrade the accuracy of quantification using Fermi modelling. The analysis presented in this study showed that DP modelling is less dependent on arterial input function saturation than Fermi modelling in eight healthy volunteers. In a pilot cohort of five

patients, DP modelling detected for the first time reduced myocardial blood flow in all stenotic vessels versus standard clinical assessments.

In the second study, it was investigated whether first-pass DP modelling can give accurate myocardial blood flow, against ideal values generated by numerical simulations. Unlike Fermi modelling which is convolved with only the first-pass range of the arterial input function, DP modelling is convolved with the entire contrast agent concentration-time course. In noisy and/or dual bolus data, it can be particularly challenging to identify the end point of the first-pass in the arterial input function. This study demonstrated that contrary to Fermi modelling, myocardial blood flow analysis using DP modelling does not depend on the number of time points used for fitting. Furthermore, this data suggests that DP modelling can reduce the quantitative variability caused by subjectivity in selection of the first-pass range in cardiac MR data. This in turn may help to facilitate the development of more automated software algorithms for myocardial blood flow quantification.

In the third study, Fermi and DP modelling were compared against invasive clinical assessments and visual MR estimates, to assess their diagnostic ability in detecting obstructive CAD. A single bolus DCE-MRI protocol was implemented in twenty-four patients. In per vessel analysis, DP modelling reached superior sensitivity and negative predictive value in detecting obstructive CAD compared to Fermi modelling and visual estimates. In per patient analysis, DP modelling reached the highest sensitivity and negative predictive value in detecting obstructive CAD.

These studies show that DP modelling analysis of cardiac single bolus DCE-MRI data can provide important functional information and can establish haemodynamic biomarkers to non-invasively improve the diagnosis and prognostication of obstructive CAD.

Lay summary

The heart, the blood and the blood vessels are the main components of the cardiovascular system. The cardiovascular system allows blood to circulate and transport oxygen, vital nutrients, carbon dioxide, hormones and blood cells around the body. The blood flows across the cardiovascular system and modulates body temperature, helps to fight diseases, provides nourishment to all organs and tissues and maintains life.

The heart is a hollow muscular organ that pumps blood throughout the cardiovascular system by rhythmic contraction and dilation. The myocardium is the heart muscle which contains cardiomyocytes, the cells that cause the heart to contract and pump blood into the circulation. The myocardium is supplied with blood flow through a very dense network of small blood vessels called the coronary circulation to allow it to function. In patients with coronary artery disease, stenotic lesions may develop in these coronary vessels. If they grow further, these stenotic lesions may narrow the inside of coronary vessels and can restrict blood flow to the heart, limiting the ability of the heart to function correctly. This is called obstructive coronary artery disease which may cause irreversible damage to the myocardium and can lead to death.

This work used magnetic resonance imaging to generate cardiac data from healthy volunteers and patients with coronary artery disease. Magnetic resonance imaging is a medical imaging technique that uses magnetic fields and electromagnetic (radio) waves to acquire images from the body, without the need of radiation exposure. It is possible to acquire magnetic resonance images for investigating both cardiac anatomy (structure) as well as function.

During the magnetic resonance image acquisition, a contrast agent was injected in the cardiovascular system of all subjects. The contrast agent focally brightens myocardial tissue areas in magnetic resonance images when it passes through the heart. Successive images were acquired rapidly to track the passage of the contrast agent across different myocardial areas. At the final stage of our method development, two mathematical models (called 1) Fermi and 2) distributed parameter modelling) and computer programming were used to analyse the magnetic resonance images in order to quantify myocardial blood flow. Mathematical models can potentially describe the passage of the contrast agent through the heart and can be used for myocardial blood flow quantification.

In the first study, cardiac magnetic resonance images were acquired from eight healthy volunteers using a technique called dual bolus imaging. Unlike the more commonly used single bolus imaging technique, dual bolus imaging eliminates technical problems that can degrade the accuracy of Fermi modelling for calculation of myocardial blood flow, but increase patient discomfort and complexity in image acquisition and analysis. It was investigated whether either of the mathematical models applied can give accurate measurements of myocardial blood flow from the single bolus components of the dual bolus protocol. The author confirmed what other groups have shown, that Fermi modelling values were prone to technical problems in single bolus data. Also, the author demonstrated that distributed parameter modelling was less dependent to technical problems in single bolus data. Single bolus values were compared against values obtained for dual bolus analysis (which was used as a reference standard for performing comparisons).

In the second study, computer simulations were used which gave access to “ideal” (simulated) data with known myocardial blood flow values to investigate further the distributed parameter model analysis. It was shown that distributed parameter modelling can reliably give measurements of myocardial blood flow when only part of the data will be used for analysis (this is called the first-pass of the data).

In the third study, both mathematical models were implemented in a cohort of twenty four patients with coronary artery disease. Visual assessment from experienced clinicians is currently the standard clinical method for assessing obstructive coronary artery disease from cardiac magnetic resonance images in clinical environments. Our model analysis and visual assessments were compared against invasive methods (which currently are the reference standards for detecting obstructive coronary artery disease) acquired in these subjects. Invasive methods involve the introduction of tiny instruments inside the coronary vessels to detect stenotic lesions. It was showed that mathematical model analysis of magnetic resonance imaging data can potentially improve the detection and diagnosis of obstructive coronary artery disease compared to visual assessments. It was also demonstrated that distributed parameter modelling may be able to more accurately detect more vessels with obstructive coronary artery disease against invasive methods, compared to Fermi modelling.

Contents

1. Introduction……………………………………………………………………..17

2. Background theory ……………………………………………………………..21

2.1 Coronary artery disease. ………………………………………………………21

2.2 Magnetic resonance imaging ……………………..………………………23

2.2.1 Basic principles of MRI acquisition ……………………………………23

2.2.2 MR signal detection ………………………………………………………29

2.2.3 T_1 and T_2 mechanisms of relaxation ……………………………………38

2.2.4 Basic MR pulse sequences ………………………………………………... 41

2.2.5 Contrast agents ... ………………………………………………………… 46

2.2.6 T_1 mapping ... ………………………………………………………….. 47

2.2.7 Myocardial perfusion imaging……………………………..……..........….50

2.3 Computed tomography ………………………………………………….... 53

2.3.1 Basic principles of CT acquisition ……………………………………53

2.3.2 CT signal detection ……………………………………………………55

2.3.3 CT angiography and perfusion …………………………………….... 58

3. Literature review…………………………………………………………….. 63

3.1 MRI cardiac perfusion ……………………………………………….. 63

3.1.1 Contrast agent concentration…………………………… …………... 63

3.1.2 Quantitative analysis in MRI ……………………………………….... 66

3.1.3 Model independent analysis …………………………………………66

3.1.4 Model based analysis……………………………………………….….. 69

3.1.5 Arterial input function ……………………………………………………74

3.2 Previous work in CT ………………………………………………………... 77

3.2.1 Computed tomography angiography …………………………………... 77

3.2.2 Computed tomography perfusion ………………………………………… 78
3.3 Invasive methods ……………………………………………………………… 81
4. Description and validation of methods used in subsequent chapters …….. 83
4.1 Validation of MOLLI technique …………………………………………… 83
4.2 MR image acquisition. ……………………………………………………… 90
4.3 Cardiac contouring and segmentation ………………………………………… 99
4.4 Development and validation of Matlab software ………………………….104
4.5 Validation of saturation recovery FLASH equation ……………………….106
4.6 Arterial input function extraction ……………………………………………111
4.7 Validation of conversion algorithm ………………………………………….113
4.8 Optimization of dual bolus protocol …………………………………………119
4.9 CT image acquisition …………………………………………………………121
5. Measurement of myocardial blood flow by magnetic resonance perfusion imaging. Comparison of distributed parameter and Fermi models with single and dual bolus ……………………………………………………………………123
5.1 Background ………………………………………………………………..123
5.2 Methods ……………………………………………………………………124
5.2.1 Study population ……………………………………………………125
5.2.2 Image acquisition ……………………………………………………125
5.2.3 Contrast agent bolus administration …………………………………..126
5.2.4 Invasive coronary angiography and fractional flow reserve …………127
5.2.5 Cardiac contouring ……………………………………………………127
5.2.6 Image processing ……………………………………………………..128
5.2.7 Model equations ………………………………………………………129

5.2.8 Statistical analysis ……………………………………………………132
5.3 Results ………………………………………………………………133
5.3.1 Comparison of Fermi and distributed parameter models in healthy volunteers ………………………………………………………. ………. 133
5.3.2 Distributed parameter and Fermi analysis in patients with coronary artery disease ……………………………………………………………..142
5.4 Discussion ……………………………………………………………146
5.4.1 Model comparison in healthy volunteers ……………………………146
5.4.2 The impact of contrast agent dose ……………………………………147
5.4.3 Distributed parameter and Fermi analysis in patients ………………..147
5.4.4 Study limitations ………………………………………………………148
5.5. Conclusions ……………………………………………………………150
6. Assessing the accuracy and reproducibility of distributed parameter and first-pass distributed parameter modelling using numerical simulations …153
6.1 Background ……………………………………………………………153
6.2 Methods ……………………………………………………………..157
6.2.1 Simulations …………………………………………………………..157
6.2.2 Statistical analysis ……………………………………………………160
6.3 Results …..……………………………………………………………162
6.4 Discussion ……………………………………………………………168
6.4.1 Assessment of DP and first-pass DP modelling ……………………168
6.4.2 Study limitations ……………………………………………………..173
6.5 Conclusions …………………………………………………………175

7. Quantitative assessment of myocardial blood flow in coronary artery disease by magnetic resonance: a comparison with invasive methods and visual assessment from MR and CT ……………………………………………177

7.1 Background ………………………………………………………………177

7.2 Methods ……………………………………………………………………..180

7.2.1 Study population and design ………………………………………180

7.2.2 Cardiac magnetic resonance imaging ………………………………..180

7.2.3 Cardiac multi-detector computed tomography imaging ………………181

7.2.4 Invasive coronary angiography and fractional flow reserve …………183

7.2.5 Visual analysis ……………………………………………………183

7.2.6 Quantitative MR analysis ……………………………………………184

7.2.7 Statistical analysis ……………………………………………………184

7.3 Results ……………………………………………………………………186

7.3.1 Study population ……………………………………………………186

7.3.2 Visual MR analysis versus invasive methods ………………………..186

7.3.3 Quantitative MR analysis versus invasive methods …………………..190

7.3.4 Visual CT analysis versus invasive methods ..…………………….…208

7.4 Discussion ………………………………………………………………209

7.4.1 Visual versus quantitative MR analysis ……………………………..209

7.4.2 Haemodynamics in quantitative MR analysis ………………………..212

7.4.3 Per vessel based quantitative MR analysis ……………………………217

7.4.4 Physiological considerations in per vessel analysis …………………..217

7.4.5 Methodological considerations in per vessel analysis ………………..219

7.4.6 Per patient based quantitative MR analysis …………………………...219

7.4.7 Physiological interpretations in per patient analysis ……………………220

7.4.8 Visual CT versus quantitative MR analysis …………………………...221

7.4.9 Study limitations ………………………………………………………222

7.5 Conclusions ……………………………………………………………..224

8. Conclusions and future work ………………………………………………227

8.1 Summary of conclusions ………………………………………………..227

8.2 Further discussion ……………………………………………………231

8.3 Future work …………………………………………………………….234

9. References ………………………………………………………………...237

10. Appendix ………………………………………………………………...261

10.1 Appendix 1 ……………………………………………………………261

10.2 Appendix 2 ……………………………………………………………268

10.3 Appendix 3 ……………………………………………………………269

10.4 Appendix 4 ……………………………………………………………272

List of figures ………………………………………………………………...283

List of tables ………………………………………………………………...299

Acknowledgments …………………………………………………………...303

Publication ………………………………………………………………...305

1. Introduction

This thesis describes development of a cardiac perfusion analysis protocol, through the application of mathematical modelling of dynamic contrast enhanced magnetic resonance imaging (DCE-MRI) data. Visual assessment by radiologist or trained observer is currently the noninvasive reference standard for the detection of perfusion abnormalities in obstructive coronary artery disease (CAD) from cardiac DCE-MRI data. Quantitative assessments of myocardial perfusion have the potential to objectively improve the diagnosis and enhance the stratification of patients with obstructive CAD, as well as streamline and speed up analysis of myocardial perfusion MRI data.

This work focused on developing and interpreting myocardial perfusion analysis from cardiac DCE-MRI data using two mathematical modelling approaches: a Fermi and a distributed parameter model. At the time of writing this thesis, Fermi modelling was the most popular and well-published approach used to estimate myocardial blood flow during the first-pass of gadolinium-based contrast agents. Distributed parameter modelling had recently been introduced as a new approach for cardiac data (see reference 66, chapters 3, 5 and 6) and in addition to myocardial blood flow, it can be used to calculate other potentially physiologically relevant microvascular characteristics. To structure the steps followed for development of this cardiac perfusion analysis protocol, three main aims have been addressed in chapters 5, 6 and 7 in which model application was assessed using data from healthy volunteers (and a pilot cohort of five patients), and simulated data and clinical data from patients with known or suspected CAD, respectively. The structure of the thesis is presented in the next paragraphs.

Chapter 2 describes theory of the basic topics of this thesis. It details CAD and provides fundamental theory of MR and computed tomography (CT) imaging, implemented to generate healthy volunteer and patient data used for analysis in this work.

Chapter 3 details a review of previously published methods and provides context for the information contained in the result chapters 5, 6 and 7. Chapter 3 focuses on the use of quantitative myocardial blood flow analysis methods in cardiac DCE-MRI. It also reviews work utilising CT angiography and examining qualitative and quantitative analysis of cardiac CT perfusion imaging. Additionally, it introduces previous work with reference to invasive methods, the current clinical standards for assessing CAD.

Chapter 4 details methods developed, validated and used in the studies presented in chapters 5, 6 and 7. These studies combine material which has been or will be published in international scientific journals and conference proceedings.

Chapter 5 is in the form of peer-reviewed journal publication and addresses the first aim of this work, to investigate the application of Fermi and distributed parameter modelling in single and dual bolus DCE-MRI protocols using data from healthy volunteers. The sensitivity of Fermi and distributed parameter modelling in detecting reduced myocardial blood flow in stenotic vessel territories was also examined, using data from a pilot cohort of five patients.

Chapter 6 addresses the second aim of this thesis, to investigate further the distributed parameter model using simulated data. In particular, it was examined whether first-pass distributed parameter modelling can give accurate estimates of blood flow and of microvascular characteristics, compared to ideal values from numerical simulations.

Chapter 7 investigates the third aim of this thesis, to assess the diagnostic accuracy of Fermi and distributed parameter modelling at the setting of detection of obstructive CAD, against invasive clinical assessments acquired in twenty four patients. Quantitative assessments using both models were also compared against visual assessments from MR and CT data, acquired at the same patient cohort.

This work gave access to quantitative assessment of cardiac perfusion using healthy volunteer and simulated data, whilst provided the opportunity to assess the clinical value of coronary haemodynamic analysis in data of patients with CAD. Finally, chapter 8 summarises the results and conclusions and provides suggestions for further work.

2. Background theory

Summary

This chapter introduces fundamental theory of the basic subjects of this thesis. It presents a description of coronary artery disease [4]. It also provides relevant background theory of magnetic resonance [7-9] and computed tomography imaging [17-20] which were implemented to generate healthy volunteers' and patients' data, used for analysis in this thesis. For additional information with respect to the above concepts, the reader can consult references [1-22]. Images derived from handbooks or papers are accordingly referenced. Images with no references have been designed by the author.

2.1 Coronary artery disease

Cardiovascular diseases are the main cause of mortality worldwide. In Europe, cardiovascular diseases account for over 4.35 million deaths each year. According to European cardiovascular disease statistics, coronary artery disease is the most prevalent cause of death in Europe, being responsible for approximately 1.92 million deaths each year, nearly half of all deaths from cardiovascular diseases [1].

Atherosclerosis is the main cause of coronary artery disease. Atherosclerotic lesions are asymmetric focal plaques which develop at the innermost layer of the artery, the intima. The term "atherosclerosis" derives from the Ancient Greek word "atheroma" which means encysted tumor and "sclerosis" which means hardening, and describes the reduction of the elasticity of the arteries due to the presence of atheromatous plaque. One of the currently prevailing theories was first introduced by Russell Ross and John Glomset in 1973, suggesting that atherosclerosis develops as an inflammatory-proliferative response to repetitive injury of the arterial endothelium [2, 3]. The endothelium is the essence of vasa vasorum in the adventitia. Hence, the response to injury theory considers pathogenesis in the entire vascular wall [4].

Although physical forces can be responsible for injury, one other main mode of injury is biochemical in nature. Hypertension, hypercholesterolemia, diabetes mellitus, smoking, and age lead to increased vascular oxidative stress and are all important risk factors for the development of coronary artery disease. Oxidative stress activates molecular processes which lead to the development of atherosclerotic plaques in the coronary walls. Following initiation, coronary artery disease progresses to a complicated disease [4].

Recent studies have shown that non-invasive techniques for the detection and monitoring of myocardial ischaemia can potentially improve the diagnosis and the assessment of prognosis of coronary artery disease [5, 6]. Magnetic resonance and computed tomography imaging have been widely used in the clinical setting to detect and assess coronary artery disease, providing different but also similar advantages and perspectives. The background theory of these techniques will be discussed in the next paragraphs.

2.2 Magnetic resonance imaging

2.2.1 Basic principles of MRI acquisition

MRI recruits three different types of magnetic fields: a) the main magnetic field of the scanner B_o, b) the radiofrequency pulses and c) the gradients. In respect of radiofrequency pulses, three of their basic functions will be described in this chapter: exciting, inverting and refocusing magnetisation. With reference to MR gradients, their applications for spatial localisation of the receiving signal will be thoroughly discussed in this chapter.

To probe the human body using MRI, the magnetic behaviour of the hydrogen nucleus is monitored. The main reason is that human body consists of millions of hydrogen atoms found in tissues, organs and fat. Each hydrogen atom is a single positively charged proton. The nuclear spin or nuclear spin angular momentum is an intrinsic property of an atom according to which the nucleus can be considered to rotate about an axis at a constant rate or velocity.

A basic principle of Maxwell's electromagnetism theory states that a moving charge (i.e. the rotational motion of the positively charged nucleus) creates an associated magnetic field. Thus, each nucleus has a local magnetic field called the magnetic moment which is orientated parallel to the axis of rotation (Figure 2-1).

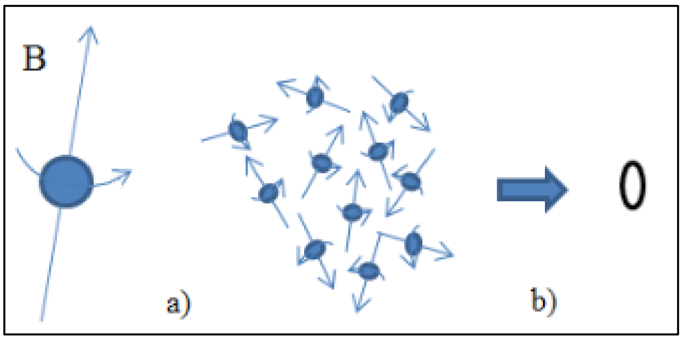

Figure 2-1) (a) The rotation of a positively charged nucleus producing a local magnetic field (magnetic moment) is shown. (b) Randomly orientated magnetic moments of individual protons in the absence of an external magnetic field. Their net magnetisation vector sum is 0.

In the absence of an external magnetic field, the spin vectors of the protons are randomly oriented in all directions such that their magnetisation vector sum is zero. When a tissue of interest is placed inside a magnetic field B_o, all the individual protons start to precess about the magnetic field. By convention, the axis of the main magnetic field in Cartesian coordinates is the z-axis. The rate of precession is proportional to the strength of B_0 and can be expressed by equation 2-1 which can be derived by using both classical and quantum mechanics theory (Larmor equation) [7, 8]:

$$\omega_o = \gamma \cdot B_o \tag{2-1}$$

where ω_o is the Larmor frequency measured in MHz, γ is the gyromagnetic ratio which is constant for each nucleus measured in $\sec^{-1}$Tesla $(T)^{-1}$ and B_0 is the magnetic field strength in T.

In the presence of $B_{0,}$ the alignment of protons with the magnetic field can be described using two eigenstates. In one energy eigenstate, the protons are aligned in the parallel direction to the main magnetic field (z direction) whilst in the second eigenstate, the protons are aligned in the anti-parallel direction (-z direction). The anti-parallel eigenstate requires slightly more energy than the parallel one. A proton selects one of the two eigenstates depending on its integral energy. For a large sample of protons within a tissue, this is described by the Boltzmann distribution:

$$\frac{N_{up}}{N_{down}} = e^{\frac{-\Delta\varepsilon}{K_B \cdot T}} \qquad (2\text{-}2)$$

where $\Delta\varepsilon$ is the energy difference between the two states (equal to $\Delta\varepsilon = \gamma \cdot h / 2\pi \cdot B_O$), h is the Planck's constant (equal to 6.63 x 10^{-34} m^2 kg / s), K_B is the Boltzmann constant (equal to 1.39 x 10^{-23} J / K) and T is the temperature (K).

In the presence of B_0, the parallel orientation is of lower energy and its configuration contains more protons than the anti-parallel orientation. This unequal number of protons in each energy level means that the vector sum of spins will be nonzero, pointing parallel to B_0. The tissue will therefore become magnetised with a value M_0, known as the net magnetisation, which is aligned with B_0.

It is important to note that the possible states of proton alignment are in fact weighted sums of the eigenstates, which indicates that there are many more states available to the protons than only parallel, or anti-parallel. In other words, the above eigenstates have elements of magnetisation perpendicular to the magnetic field, in addition to longitudinal components. Thus, the energy eigenstates form a so-called basis for all possible states.

MRI is essentially based on the manipulation of the net magnetisation M_0 using radiofrequency pulses which are electromagnetic fields oscillating at radiofrequencies. In other words, radiofrequency pulses are in the form of electromagnetic energy containing a variety of frequencies spread over a narrow bandwidth. The orientation of the radiofrequency pulses is perpendicular to $B_{0,}$ creating an effective magnetic field indicated as $B_{1.}$ Following radiofrequency pulse emission, protons absorb part of the energy corresponding to Larmor frequency. This causes the net magnetisation M_0 to rotate about B_1 (Figure 2-2). All radiofrequency pulses used to tip the M_0 in the transverse plane are called excitation pulses.

Absorption of this radiofrequency energy leads to transitions between the two energy eigenstates with protons from the low energy state being excited to the high energy state whilst protons from the high energy state are stimulated to the low energy state. There is an equal probability for each type of transition. When the radiofrequency pulse has enough amplitude and duration, the absorbed energy tilts the M_0 to rotate completely into the transverse plane, known as a 90° pulse.

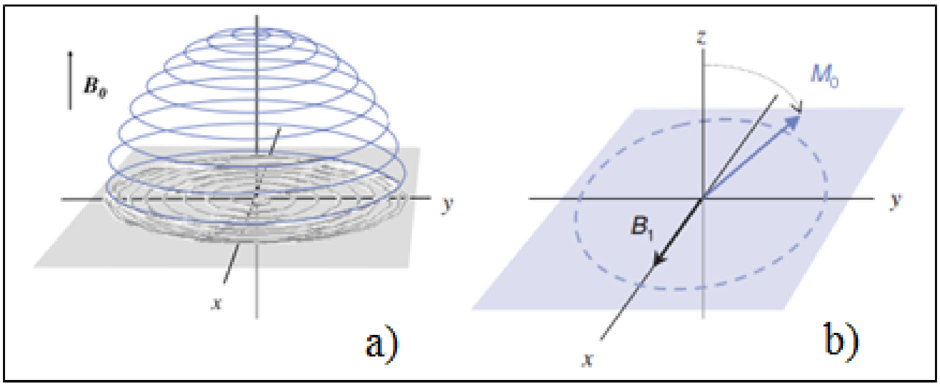

Figure 2-2) (a) At equilibrium, M_0 is parallel to B_0. As the 90° excitation radiofrequency pulse is applied, M_0 is tilted to rotate in a spiral path to end up perpendicular with B_0. (b) M_0 start to precess about B_1 (MRI: From picture to proton, 2006).

Similarly, if the amplitude of the radiofrequency pulse is further increased, M_0 can be tilted to the –z axis direction in which all the protons in the low energy state invert to the high energy state and vice versa. At this stage, the system is considered to be inverted and the radiofrequency pulse is known as an inversion pulse or 180^o pulse. The amount of the resulting rotation through application of a radiofrequency pulse of M_0 is called the flip angle. Modifying the strength and duration of B_1, it is possible to create different flip angles.

The application of a radiofrequency pulse brings all spins into phase coherence meaning that at each energy eigenstate, spins simultaneously point to the same direction during their precession. After the radiofrequency pulse is switched off, local inhomogeneities in B_0 and small differences in the precessional frequencies of different protons cause protons to start dephasing with respect to each other. The net magnetisation gradually returns back to equilibrium through mechanisms known as T_1 and T_2 relaxation which will be discussed in subsection 2.2.3. These protons can be made to induce a voltage in a receiver coil, this signal being known as the free induction decay [7, 8].

Receiver coils are used for better signal reception. Surface receiver coils are often used, which are placed on and around the surface of a patient. Array coil systems are collections of small surface coils whose signal can both be combined as well as can be fed into independent receiver circuitries (outputs). Phased array coils are groups of usually overlapping coils linked into a common receiver circuitry [7, 8]. More details about phased array coils and their application in cardiac MR imaging will be given in section 4.2 (chapter 4).

The actual MRI signal derives from echoes created when radiofrequency pulses are used to rephase the protons (Figure 2-3). There are two major types of echoes, spin and gradient echoes (subsection 2.2.4). The echoes are received by the MR signal detector (i.e. receiver coil) and are mathematically processed to form the image.

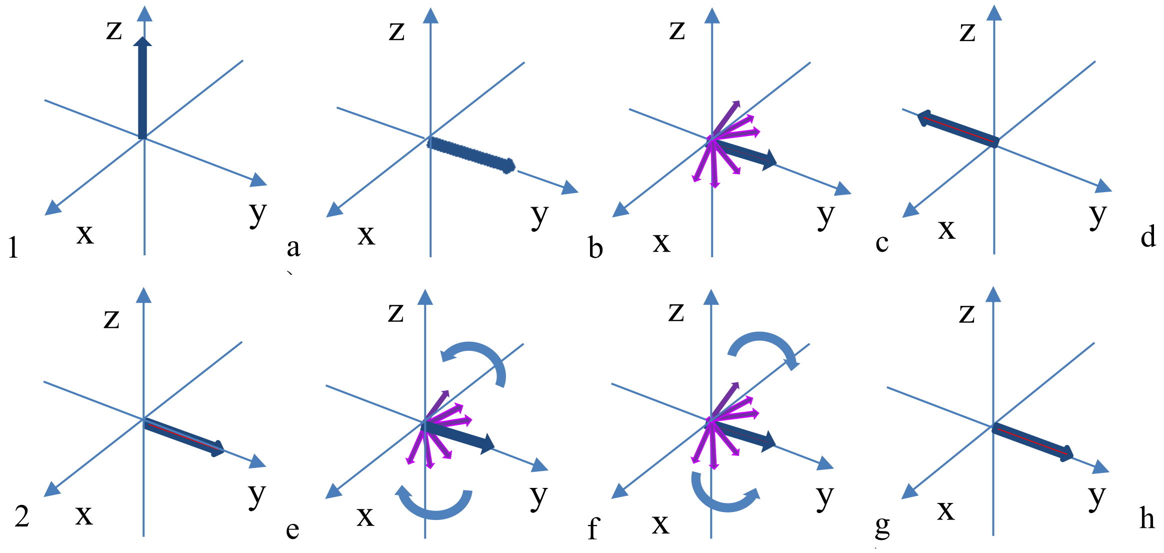

Figure 2-3) The following can be viewed if the observer is placed in the rotating frame of reference (the frame rotation matches the Larmor frequency). 1. Spin-echo (a) Protons dephasing and rephasing. Net magnetization M_0 (shown as the thick blue arrow) before the application of radiofrequency pulse, aligned along the longitudinal z-direction parallel to B_0. (b) M_0 is tilted along the transverse x-y orientation after the application of a 90^o excitation radiofrequency pulse. (c) Protons lose phase coherence and start to dephase. (d) After the application of a 180^o refocusing pulse and subsequent time, protons rephase and create a spin-echo. 2. Gradient echo (e) Immediately after a 90^o pulse, all spins are in phase. (f) Application of a gradient will increase the precession frequency of some spins whilst reduce it in others. (g) Application of a gradient of different polarity at time T causes the spins to refocus. (h) Spins eventually return back into their initial state and at subsequent time, create a gradient-echo.

2.2.2. MR signal detection

The echoes (MR signals) are spatially localized using gradients. These gradients are small magnetic fields superimposed on the main magnetic field B_0, causing linear magnetic field variations which can be mathematically described:

$$B_i = B_0 + G_T \otimes r_i \tag{2-3}$$

where B_i is the magnetic field at location r_i and G_T is the total gradient amplitude mathematically represented as a tensor. The gradients produce linear magnetic field perturbations primarily along one main direction hence, G_T can also be reduced to a vector representation [8, 9].

The exact frequency that a proton experiences in the presence of a magnetic field gradient can be given by adapting the Larmor equation:

$$\omega_i = \gamma \cdot \left(B_0 + G \cdot r_i\right) \tag{2-4}$$

where ω_i and G are the proton frequency and a vector representing the gradient amplitude at position r_i respectively. Three magnetic field gradients are used to localise the MR signal. Each gradient is commonly assigned to perform one of the three main functionalities with respect to MR signal localisation: slice selection, frequency encoding or readout and phase encoding [8, 9].

A slice selective gradient G_{SS} is a magnetic field gradient which limits a narrow range of radiofrequencies centred about the Larmor frequency during excitation (Figure 2-4) and determines the slice orientation, thickness and position. The resonance (Larmor) frequency ω_o used to generate the MR signal varies with position along the gradient direction. As shown, the transmitted gradient causes proton excitation only at and to a close proximity to the region which satisfies the resonant condition.

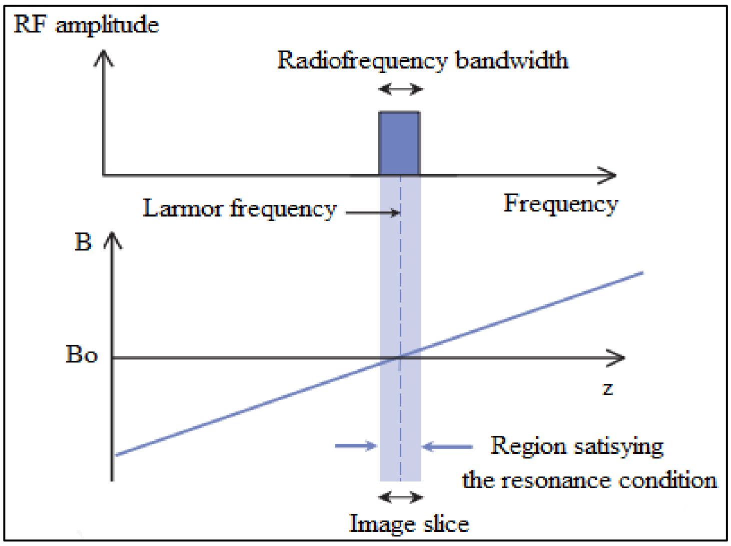

Figure 2-4) The slice selective gradient is presented. The radiofrequency bandwidth is centred about the Larmor frequency. Only protons inside the radiofrequency bandwidth are excited. The thickness of the slice relates to the gradient strength and the radiofrequency bandwidth range (MRI: From Picture to Proton, 2006).

To change the position of the slice, it is possible to move electronically the region satisfying the resonance condition. To manipulate the slice thickness, changes in the amplitude and the strength of the gradient can be applied. In particular, a thinner slice can be either derived by narrowing the frequency bandwidth (the frequency zone satisfying the resonance condition) or by increasing the strength of the gradient. To modify the slice orientation, a different slice selective gradient direction can be selected. For example, assuming the same Cartesian coordinates for the magnetisation, the gradients and the scanner, if the slice selective gradient is implemented along the z-axis direction, the excited protons will form a slice along the transverse plane, creating a transverse slice. Similarly, a sagittal slice can be formed using a slice selective gradient along the x-axis, whilst a coronal slice can be created using a gradient along the y-axis.

The two visual dimensions of the image are created using the frequency encoding (or readout) and phase encoding gradients, G_{RO} and G_{PE} respectively. During the production of an echo, a readout gradient is applied perpendicular to the slice direction causing the protons to precess at different frequencies depending on their position according to equation 2-4. The spatial resolution in the frequency encoding (or readout) direction expressed as the voxel size (VOX) depends on two user defined parameters, the field of view (FOV) and the number of sample points (N) in the readout direction:

$$VOX_{RO}=FOV_{RO}/N_{RO} \tag{2-5}$$

with units mm/voxel (where $_{RO}$ represents the readout direction). For a given bandwidth of frequencies, it is possible to reduce the field of view increasing the amplitude of the readout gradient and vice versa [8].

The phase encoding gradient is used to form the third dimension of an MR image and is applied perpendicular to the previous two gradients. Before the application of a phase encoding gradient, the protons within the slice precess about the Larmor frequency. In the presence of the phase encoding gradient, the precessional frequency increases or decreases depending on a proton’s position. When the gradient is switched off, the protons return back to the original precession frequency however, keeping their phase difference compared to their previous state. This means that protons precede or follow their previous precession. As in the case of the readout gradient, the phase difference depends on the magnitude and duration of the gradient as well as the proton position (described by equation 2-4) [8].

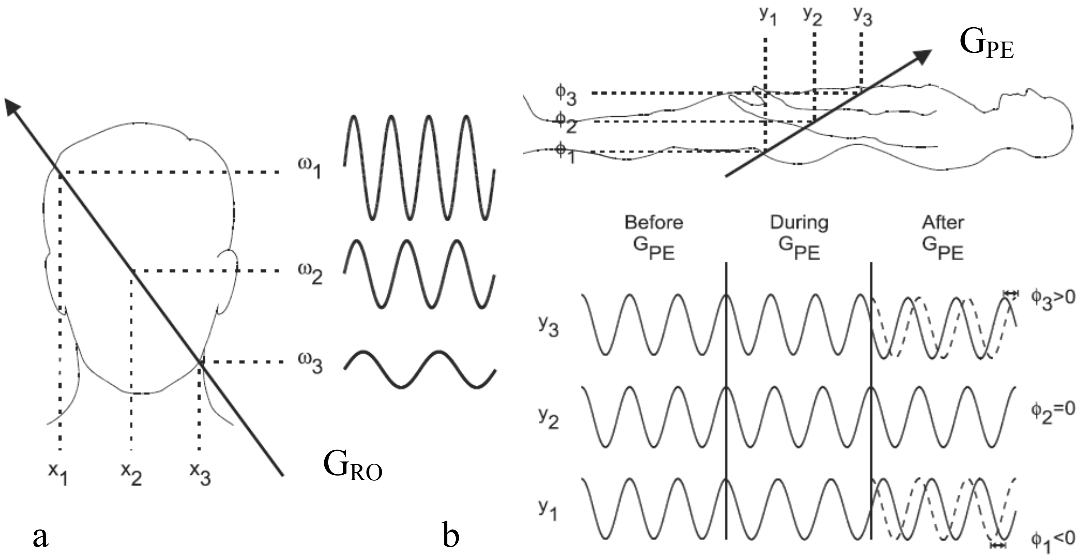

Figure 2-5) (a) Frequency encoding gradient. After excitation, all protons within the excited (slice) volume precess at the same frequency. When G_{RO} is applied, it causes a variation in the frequencies of the protons. The frequency of precession for each proton depends upon its position (according to equation 2-4). (b) Phase encoding gradient. Similarly to the concept of the frequency encoding gradient, before the application of G_{PE}, all protons precess at the same frequency. Following application of G_{PE}, a proton increases or decreases its precessional frequency depending upon its position (equation 2-4). As shown, a proton located in $y_2=0$ experiences no effect from G_{PE}. However, a proton located at y_3 precesses faster during the application of G_{PE}. When G_{PE} is switched off, the proton precesses at its original frequency but is now ahead (phase shift φ_3) of the reference frequency (shown here with the dashed line). A phase shift has been induced in the proton by G_{PE}. In the same way, a proton located at y_1, decreases its frequency during the application of G_{PE}. Thus, after G_{PE} is turned off, it precesses at its original frequency but is now behind (phase shift φ_1) the reference frequency (MRI: Basic pulse principles and applications, 2010).

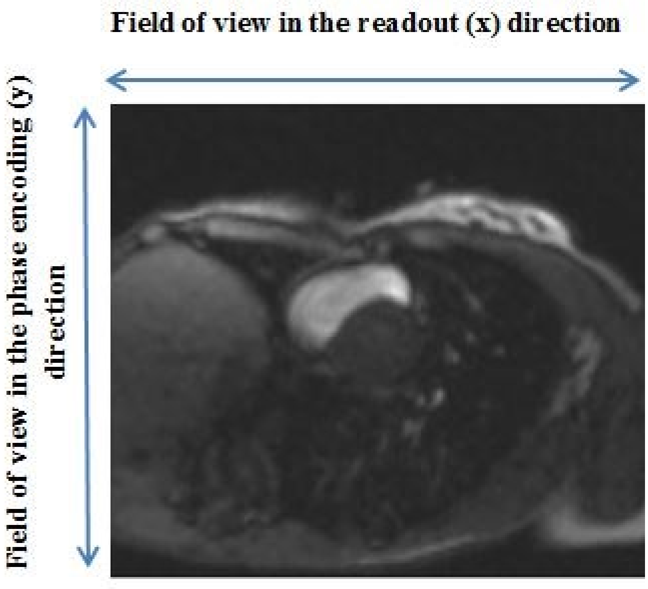
Field of view in the readout (x) direction
Field of view in the phase encoding (y) direction

Figure 2-6) One of the visualised directions in all MR images is the readout direction. The other is the phase encoding direction as shown.

The MR information is completed once the slice excitation and signal detection is repeated multiple times, each one using different amplitude of the phase encoding gradient. Each value of phase encoding can be considered as a template corresponding to a specific 'spatial frequency'. One phase encoding gradient is required for every line of data (i.e. 256 phase encoding gradients for a 256 voxel image in the phase encoding direction). The spatial resolution is again expressed as the voxel size:

$$VOX_{PE}=FOV_{PE}/N_{PE} \tag{2-6}$$

The gradient-induced changes from both G_{RO} and G_{PE} are applied to the echo and are received by the receiver coils. The echoes are then saved in a raw data matrix commonly referred to as k-space so that each phase encoding step is a line of k-space (Figure 2-7).

The most common and dominant method to fill k-space is the row-by-row Cartesian method, although other types such as spiral and radially oriented k-space trajectory techniques are rapidly developing [7, 8]. The row-by-row Cartesian method provides a better basis to describe k-space filling whilst has also been implemented to acquire data for this thesis. This method will be discussed in the following paragraphs.

According to the row-by-row Cartesian method, the cells of k-space (shown in Figure 2-7.a) are commonly displayed on rectangular grid with axes k_x and k_y. These k-axes represent spatial frequencies in the x- and y- directions and therefore, individual (k_x, k_y) points do not directly correspond to individual (x, y) pixels in the image. However, there is a direct one-to-one relationship between points in k-space and gradient strength [7, 8].

Thanks to the application of frequency and phase encoding gradients (Figure 2-5) the phase of the signal of a given spin, depends upon its location. If the signal is sampled at time t after turning the frequency encoding (x direction in Figure 2-6) gradient, the phase induced at the spins at location x by the readout gradient alone will be:

$$\Delta\varphi(t) = \omega_o t + \gamma G_x x t \qquad (2\text{-}7)$$

The phase induced on spins by the phase encoding (y direction in Figure 2-6) gradient alone, at location y, will be:

$$\Delta\varphi(t) = \omega_o t + \gamma G_y y \tau \qquad (2\text{-}8)$$

Hence the total phase shift for a voxel at location (x, y) will be:

$$\Delta\varphi(t) = \omega_o t + \gamma G_x x t + \gamma G_y y \tau \qquad (2\text{-}9)$$

Because the signal emitted by a small voxel at location (x, y) is proportional to the number of spins at that location and will have phase given by equation 2-9, the signal S (x, y, t) from a voxel at (x, y) is proportional to:

$$S(x,y,t) = \rho(x,y) \cdot \exp(i\omega_o t + i\gamma G_x xt + i\gamma G_y y\tau) \qquad \text{(2-10)}$$

where ρ(x, y) is the spin density function which will be displayed as a gray scale MR image at end of the MR signal detection and processing procedure. The receiver coil equally sums contributions from all locations, so that the signal detected is the sum of these contributions:

$$S(t) = \iint \rho(x,y) \cdot e^{i\omega_o t + i\gamma G_x xt + i\gamma G_y y\tau} dxdy \qquad \text{(2-11)}$$

The Larmor frequency can be (and in fact is) neglected by the detection hardware and thus, can be moved out of the integral:

$$S(t) = \iint \rho(x,y) \cdot e^{i\gamma G_x xt + i\gamma G_y y\tau} dxdy \qquad \text{(2-12)}$$

This integral is over the spatial frequencies and it is useful to define $k_x = (-\gamma G_x t)$ and $k_y = (-\gamma G_y t)$ where k represents the spatial frequency measured in cycles/m. k relates to the wavelength by the formula $k = 1/\lambda$.

$$S(t) = \iint \rho(x,y) \cdot e^{-ik_x x - ik_y y} dxdy \qquad \text{(2-13)}$$

Assuming that x and k_x (as well as y and k_y) are conjugate variables, equation 2-13 represents a 2D Fourier integral. To solve for ρ (x, y), the inverse Fourier transform of the detected signal is needed:

$$\rho(x,y) = FT^{-1}[S(k_x,k_y)] = \iint S(k_x,k_y)\cdot e^{ik_x x + ik_y y} dk_x dk_y \qquad (2\text{-}14)$$

To summarise, the value of k_{xy} determines the spatial periodicity of each frequency sample that contributes to that time point of the signal. The signal is therefore sampled not as a function of time, but as a function of k (the difference between k and t is the scale factor γG). Each point in k-space matrix is represented by a complex number which is the magnitude of the amplitude and phase of the signal for that sample point. The image (gray value for each voxel) is finally calculated by measuring ρ(x, y) through the implementation of inverse Fourier transform [9].

By convention, rows near the centre of k-space correspond to low order phase encoding steps, whilst rows near the top and bottom are defined to correspond to higher order phase encoding steps. Image data acquired with the maximum phase encoding gradient $+G_{PE}$, will be saved along the rightmost margin in k-space. Image data acquired with the phase encoding gradient equal to zero, will be saved along the central vertical axis in k-space. k-space values near the edges of the k-space matrix define spatial resolution in the image whilst those near the centre determine shape and contrast in the image. Because echo amplitudes are higher at the low order phase encoding steps due to the fact that there is less gradient induced dephasing, the values of k-space will be greater near the centre of the matrix [7-9].

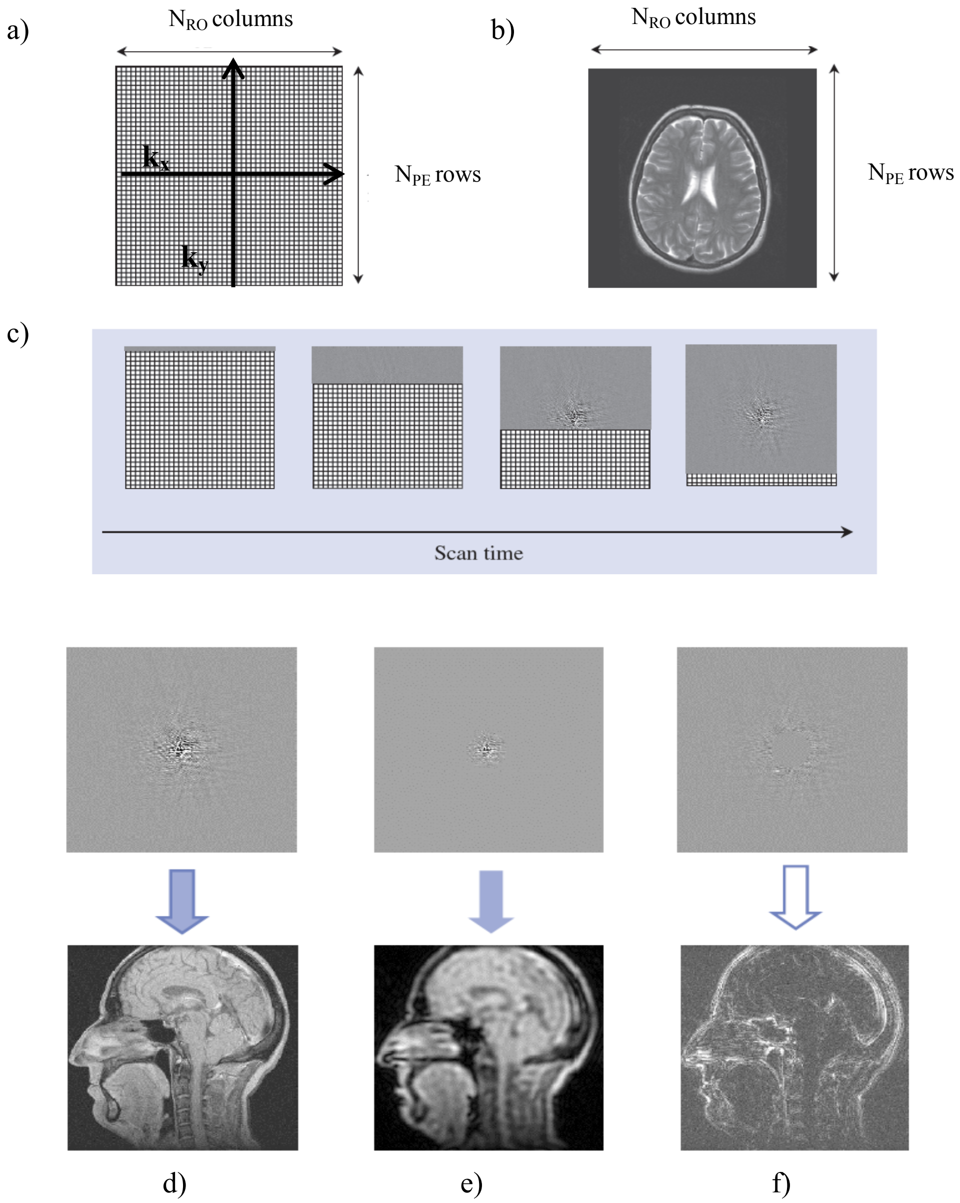
a)
N_RO columns
k_x
k_y
N_PE rows
b)
N_RO columns
N_PE rows
c)
Scan time
d)
e)
f)

Figure 2-7) k-space representation. (a) k-space matrix is a raw data matrix having the same number of rows (number of readout or frequency encoding steps defined as N_{RO}) and columns (number of phase encoding steps defined as N_{PE}) as (b) the final image. (c) k-space filling for different (reverse linear) phase encoding steps. k-space and corresponding images showing: (d) image reconstruction using all spatial frequencies, (e) using only low spatial frequencies from the centre of k-space and (f) using only high spatial frequencies from the edges of k-space.

The row-by-row Cartesian method involves different profile orders which determine the way of k-space filling. One of the standard ways of k-space filling is to acquire one k-space line after the other, from the bottom of k-space to the top (linear phase encoding). The reverse order is to perform the same process but from the top to bottom (reverse-linear phase encoding). Centric k-space filling is also often involved in the row-by-row Cartesian method, in which the middle line of k-space (k_o) is acquired first and then the k-space filling continues towards the top and the bottom [7-9]. Centric phase encoding k-space filling was used in order to acquire myocardial perfusion MR imaging data for this thesis (see 2.2.7 and 4.5 for further discussion in centric phase encoding).

2.2.3 T_1 and T_2 mechanisms of relaxation

After each excitation pulse is applied and switched off, the protons re-emit the absorbed energy and start to relax back to equilibrium through T_1 and T_2 relaxation.

T_1 relaxation is also known as longitudinal relaxation time or spin-lattice relaxation time. Following an excitation pulse, it is the time required for the z component of the net magnetisation M_o to return back to 63% of its original value. During T_1 relaxation, protons interact with their surrounding tissues. The absorbed energy is transferred from the excited protons (spin) to their surroundings (lattice). Although both mechanisms occur simultaneously, T_1 relaxation is much slower process than T_2 relaxation.

After the excitation pulse is applied, more protons precess in the high energy state which is thermodynamically stable and thus, it requires energy to stimulate the transition back to the low energy state. The required energy is found in the presence of molecular motion (such as rotation or vibration) within the surrounding tissues, experiencing a relatively broad range of intrinsic frequencies. The closer these intrinsic frequencies to Larmor frequency ω_o, the more efficiently this energy transfer occurs and the shorter T_1 relaxation becomes. In different tissues, the nature and concentration of proteins and metal ions vary. Hence, T_1 relaxation is characteristic for each tissue. Unlike T_2, T_1 relaxation is field-dependent. This means that at higher B_0, fewer molecules within tissues can reach ω_o leading to longer T_1 relaxation [7, 8].

T_2 relaxation is also known as transverse or spin-spin relaxation time and is the time required for the transverse component of M_0 to decay to 37% of its initial value. After an excitation pulse, protons start to dephase due to small differences in their precessional frequencies in the magnetic field. Protons precess and move in random directions inside the tissue volume. When two protons approach each other, each one of them experiences a slightly higher or lower magnetic field depending on whether the magnetic moment of the other proton adds or subtracts from the main magnetic field. The protons modify their precessional frequencies to match this slightly different local field and start to dephase. After protons recede, they return back to Larmor frequency but the phase difference in precession is maintained. Each proton interacts with thousands of other protons resulting in gradually bigger differences between the phase angles and this occurs until the vector sum of the magnetic moments decays down to zero. T_2 relaxation is a quick mechanism occurring in hundreds of milliseconds.

T_2^* relaxation is also often defined as the process by which the transverse magnetisation is gradually lost due to magnetic field inhomogeneities. As mentioned, perfectly homogeneous main magnetic fields are practically never possible. Inhomogeneities in the main magnetic field may be the result of intrinsic defects of the magnet or of susceptibility induced field distortions produced by the tissue or other materials placed in (and interacting with) the field. These inhomogeneities cause transverse magnetisation decays known as T_2^* relaxation mechanisms which are equal or (more commonly) faster, than would be predicted by T_2 mechanisms [7, 8]. T_2^* relaxation can be mathematically described as:

$$\frac{1}{T_2 *} = \frac{1}{T_2} + \frac{1}{T_2 in} \qquad (2\text{-}15)$$

Where $1/T_{2in}$ is the relaxation rate due to field inhomogeneities (ΔB_i) across a voxel and is equal to $\gamma \Delta B_i$.

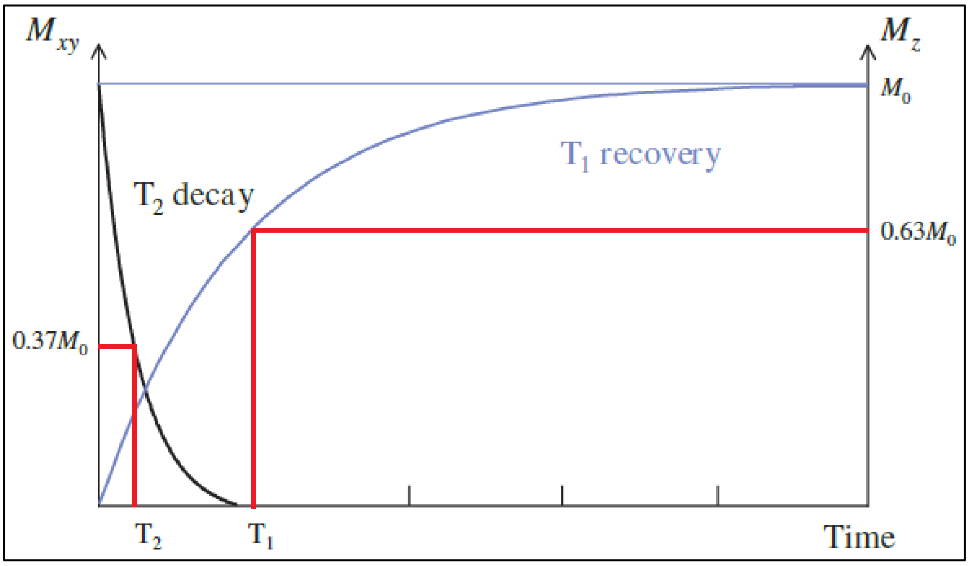

Figure 2-8) Longitudinal (T_1) and transverse (T_2) relaxation time illustrated. Although they occur simultaneously, T_1 is much slower than T_2 (MRI: Basic pulse principles and applications, 2010).

An important versatility of MRI is that the MR signal can be made sensitive to different relaxation mechanisms. For example, the MR signal can be made sensitive to T_1 or T_2 relaxation times, creating images known as T_1- or T_2-weighted respectively. In these images, the image contrast between a region of interest and its surroundings depends on the relative relaxation times (T_1, T_2 or T_2*) which have been selected to either emphasize differences in tissue structures or in tissue functions. Similarly, the MR signal can be made sensitive to the relative number of protons in each tissue leading to the formation of data known as proton density (PD)-weighted images [7, 8].

2.2.4 Basic MR pulse sequences

The combination of radiofrequency pulses, gradients, data sampling periods and the timing selected between each one of these parameters used to create the image is called the pulse sequence. The spin and gradient echo techniques are the major methods used to create echoes (MR signals) and their pulse sequence characteristics are described here.

In the spin echo case, the pulse sequence starts with a 90^o excitation pulse and spins are left to dephase for a selected time interval. During dephasing, spins experiencing lower magnetic fields precess slower and those experiencing higher magnetic fields precess faster, compared to their precessional frequency before dephasing started. Then a 180^o pulse is applied, exciting the low energy spins to the high energy state (now start to rotate clockwise) and stimulating the high energy spins to the low energy state (start to rotate anti-clockwise). After a time equal to the time interval between the intial 90^o and 180^o pulse, all spins are brought back into phase coherence and a spin echo is formed. Gradient pulses of opposite polarity in the readout and slice selection directions are also combined to refocus the protons (see Figure 2-9).

In a spin echo sequence, the repetition time (TR) is the time elapsed between consecutive excitation pulses for the same slice. The echo time (TE) is the time from the excitation pulse to the maximum peak of the spin echo. A representation of a timing diagram with respect to a standard spin echo pulse sequence is illustrated in Figure 2-9.

Both spin and gradient echo sequences can potentially be used to generate T_1, T_2 and proton density weighted images by modifying the TR, TE and flip angle. Standard spin echo sequences are basically used to form T_1-weighted images when combined with relatively short TR and TE. In clinical practice, additional MR information is required and spin echo sequences often use subsequent 180^o refocusing pulses to acquire multiple echoes. For example, standard multi-echo sequences apply successive 180^o refocusing pulses to produce spin echoes using a single phase encoding gradient for each excitation pulse. Multi-echo sequences are applied to generate proton density weighted images using short TE as well as T_2-weighted images using long TE in combination with a long TR to allow relatively full T_1 relaxation. Another type of spin-echo sequences, are the echo-train spin echo sequences. The echo-train length represents the number of 180^o refocusing pulses applied after an excitation pulse. Although this is very similar to the standard multi-echo sequences, it uses multiple 180^o refocusing pulses in combination with a different phase encoding gradient (for each refocusing pulse) to acquire multiple lines of k-space and accelerate imaging. The echo-train spin echo pulse sequences are generally used to produce T_2-weighted images which can be efficiently achieved by using a long TR and a modest echo train length [7, 8].

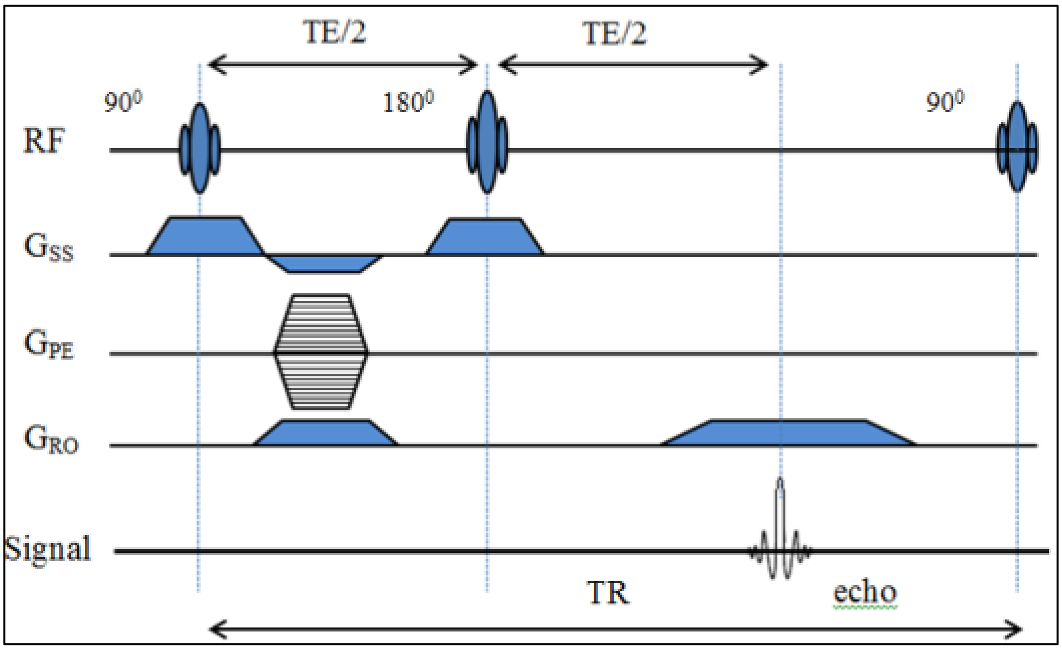

Figure 2-9) A standard spin echo sequence is shown. A single echo is produced at time TE after the excitation pulse and localised by a slice selective gradient (G_{SS}), a readout gradient (G_{RO}) and a single phase encoding gradient (G_{PE}).

In gradient echo sequences, the echo signal is generated through gradient reversal. As mentioned in subsection 2.2.1, the implementation of a negative gradient causes proton dephasing. The application of a subsequent gradient of equal amplitude and duration but of different polarity (positive) induces proton rephasing and creates an echo. The mechanism is analogous to the one described in spin echo rephasing process. The main difference is that in gradient echo sequences, the protons rephase due to their interaction with gradients rather than with refocusing pulses. All gradient echo pulse sequences use excitation pulses less than 90^o, which by convention are described as radiofrequency pulses with flip angle denoted by alpha (α) and implement reversal gradients in at least two directions to produce the echo signal: the slice selective and the readout directions.

Here, the repetition time TR, is the time between successive α pulses and the echo time TE, is the time between the α pulse and the echo produced (Figure 2-10). There are two main categories of gradient echo sequences: a) spoiled gradient echo and b) refocused or steady state gradient echo techniques. Spoiled gradient echo techniques were used for the production of T_1 weighted images for this thesis and these will be discussed in the following paragraphs.

In spoiled gradient echo sequences, the radiofrequency pulse applied at the start of each TR creates a transverse component of net magnetisation which decays due to T_2* relaxation caused by local field inhomogeneities. Because TR is generally short in gradient-echo imaging, there will always be some residual transverse magnetisation before the application of the next α pulse. Spoiling gradients and/or radiofrequency pulses applied with randomised phase, can fully dephase the transverse magnetisation (through T_2 relaxation) and feed the longitudinal magnetisation recovery (T_1 relaxation). As a result, each one of the applied flip angles acts only on the longitudinal magnetisation. This allows the longitudinal magnetisation to settle into a steady state after a number of successive α pulses, the magnitude of which increases as the flip angle decreases. An increased magnitude for the longitudinal magnetisation steady state is important for T_1 weighted imaging.

To acquire T_1-weighted images in spoiled gradient echo, short TR and TE combined with large excitation α pulses are used. However, for a given ratio of TR/T_1 there is an optimal flip angle (known as Ernst angle) which leads to the highest signal. This optimal flip angle is small for a short TR which is generally used in gradient echo sequences. Ultrafast spoiled gradient echo techniques overcome this limitation using a preparation pulse (typically 90° or 180° although much more complicated schemes are available) and small flip angles to produce T_1-weighted images.

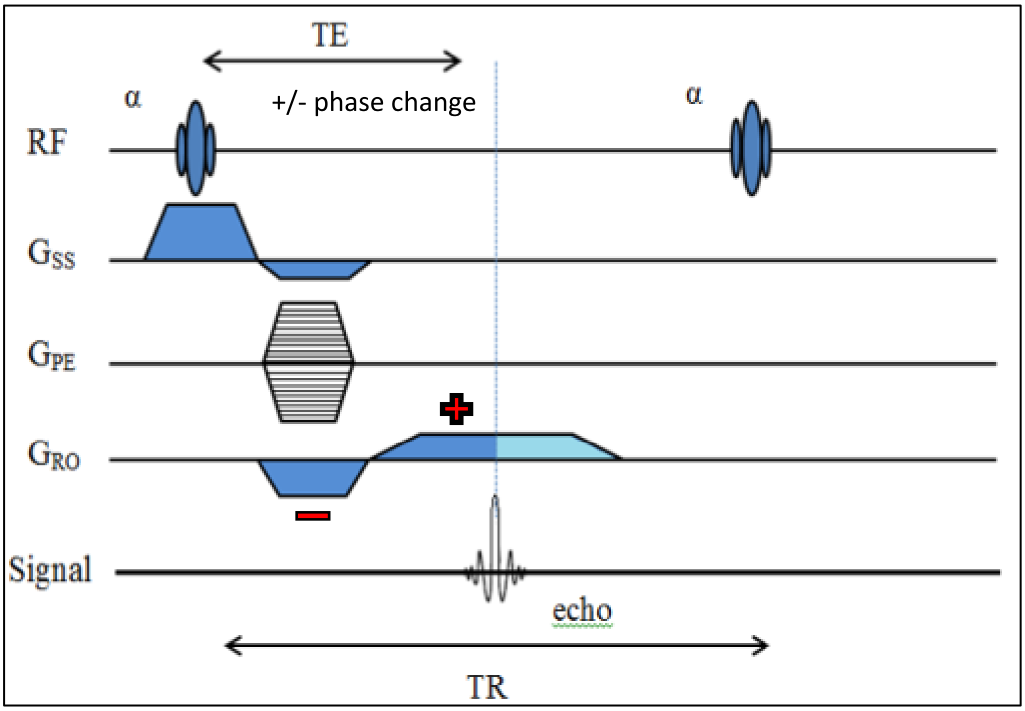

Figure 2-10) Following an α pulse, an echo is formed after the application of a phase offset to each successive flip angle (i.e. same flip angle but in a different direction) and/ or a negative (-) and a positive (+) gradient in the readout direction (G_{RO}). The two gradients are of the same magnitude but of different polarity.

Gradient echo sequences can achieve rapid acquisitions and can enable more slices to be acquired within the same TR than spin echo sequences. This is the reason why gradient echo sequences are more commonly used in cardiac MR imaging which needs to be rapid in order to overcome the cardiac movement, whilst also needs to be acquired within a breath-hold duration. Characteristic example applications are in perfusion imaging and in angiography in which T_1-weighted images can be acquired in less than a second. This allows accurate detection of a contrast agent bolus arrival and passage through a tissue of interest as will be discussed in the following subsections [7, 8].

2.2.5 Contrast agents

T_1 relaxation time is characteristic for each tissue. Shortening of the T_1 relaxation time in a region of interest can increase the signal intensity in T_1-weighted images. T_1 relaxation time can be shortened by using exogenous contrast agents.

The most common application of exogenous contrast agents in cardiovascular imaging are gadolinium-based contrast agents. These are administered as salt complexes of gadolinium either with chelating agents such as diethylene-triamine-penta-acetic acid or with dihydroxy-hydroxymethylpropyltetraazacyclododecane-triacetic acid. The gadolinium ion is strongly paramagnetic as it contains 7 unpaired electrons and it is surrounded by the chelating agent which is important to reduce the toxicity of the contrast agent. After intravenous injection, the gadolinium agent interacts with water molecules found close to the contrast agent complex and shortens their T_1 relaxation time. In T_1 weighted images, this can be mathematically described as:

$$\frac{1}{T_1(t)} = \frac{1}{T_1(0)} + r_1 \cdot [Gd] \qquad (2\text{-}16)$$

where $T_1(t)$ is the relaxation time during contrast enhancement and $T_1(0)$ is the native relaxation time of the tissue in the absence of gadolinium, r_1 is the relaxivity measured in L mmol $^{-1}$ s^{-1} and [Gd] is the gadolinium concentration. This relationship describes T_1 relaxation time shortening as gadolinium concentration increases. The linearity of this relationship has been validated in phantoms [10] and in rat myocardium [11].

2.2.6 T_1 mapping

MRI can assess cardiac function and directly detect structural changes within the tissues. Healthy tissues have different T_1 relaxation rates compared to pathological tissues. T_1 mapping is the measurement of T_1 relaxation time of tissues in order to achieve tissue characterisation and quantification. T_1 mapping has been used in a variety of clinical applications. In clinical practice, T_1 mapping needs to be accurate, robust and rapid. There are several methods which have been used to measure T_1 relaxation rate in tissues. Here, the a) most conventional and b) one of the most innovative methods for T_1 mapping will be described.

The most conventional method for measuring T_1 is the spin echo inversion recovery technique. In a spin echo inversion recovery experiment, the net magnetization vector M_0 is tipped through the application of a 180^0 inversion pulse, so that the longitudinal (net) magnetization vector has an initial value of $-M_0$. The net magnetization vector starts to recover towards its equilibrium value M_0. Then at the inversion time TI, a second radiofrequency pulse of 90^0 is sent which tips the magnetization vector into the transverse plane and the magnetization signal can be sampled through the application of field gradients. The value of the transverse magnetization gives the signal intensity of the image (which is analogous to the longitudinal component of the net magnetization) [7, 8].

This magnetisation equation which mathematically describes a standard spin echo sequence is:

$$M(t) = M_O\left[1 - 2\lambda \exp\left(-\frac{TI}{T_1}\right) + (2\lambda - 1)\exp\left(-\frac{TR}{T_1}\right)\right]\exp\left(-\frac{TE}{T_2}\right) \qquad (2\text{-}17)$$

where M (t) is the magnetisation detected in the transverse plane at each inversion time (TI), M_0 is the net magnetisation at equilibrium, TR is the repetition time, TE is the echo time and λ is the inversion efficiency (λ=1 if the inversion pulse is perfect). During a spin echo, it is assumed that $TE \ll T_2$ and $TR \gg T_1$ and the second and third exponential parameters are equal to 0 and 1 respectively and can be neglected [7, 8].

To derive accurate T_1 measurements, at least 6 to 10 90^o saturation pulses have to be applied after an inversion pulse. Before the application of each saturation pulse, it is necessary to allow for full magnetisation recovery. Full magnetisation recovery might require a relaxation period of up to 4 to 5 times the duration of the T_1 relaxation in question. Thus, although spin echo inversion recovery technique is considered the gold standard for measuring T_1, it is time-consuming and not practical to be included in clinical protocols [7].

One of the most innovative and now widely used rapid clinical T_1 mapping techniques is the modified Look-Locker inversion recovery (MOLLI) method [12]. The standard technique was first described by Look and Locker [13] and is a multipoint approach which samples the relaxation curve multiple times after an initial preparation pulse [12]. The MOLLI approach introduces two major developments to the standard Look and Locker technique: a) uses electrocardiogram (ECG)-gated image acquisition at end-diastole and b) merges images from three consecutive inversion recovery experiments into one data set. The accuracy of MOLLI technique has been validated in gel phantoms using a wide range of heart rates derived from simulated ECG signals [12]. The MOLLI pulse sequence scheme is illustrated in Figure 2-11.

The signal intensity equation for the MOLLI technique is:

$$M(t) = A - B \cdot \exp(-\frac{t}{T_1^*}) \tag{2-18}$$

where $A = M_o^* = M_o \cdot T_1^* / T_1$ and $B = M_o + M_o^* = M_o \cdot (1 + T_1^* / T_1)$. The derivation of equation 2-18 is mathematically described in the Appendix (Appendix 1). A, B and T_1^* may be obtained by a three parameter fit. T_1 can be calculated from the resulting parameters by applying the equation 2-19 [14]:

$$T_1 = T_1^* \cdot ((B / A - 1) \tag{2-19}$$

With the application of MOLLI technique, native T_1 mapping of the myocardium in the absence of contrast enhancement was made possible. The estimation of contrast agent concentration-time curves is an essential step prior to the implementation of mathematical modelling for myocardial blood flow quantification. Native T_1 relaxation times of the blood pool and myocardial tissue are needed in order to estimate contrast agent concentration curves (using equation 2-16, see further description in subsection 3.1.1).

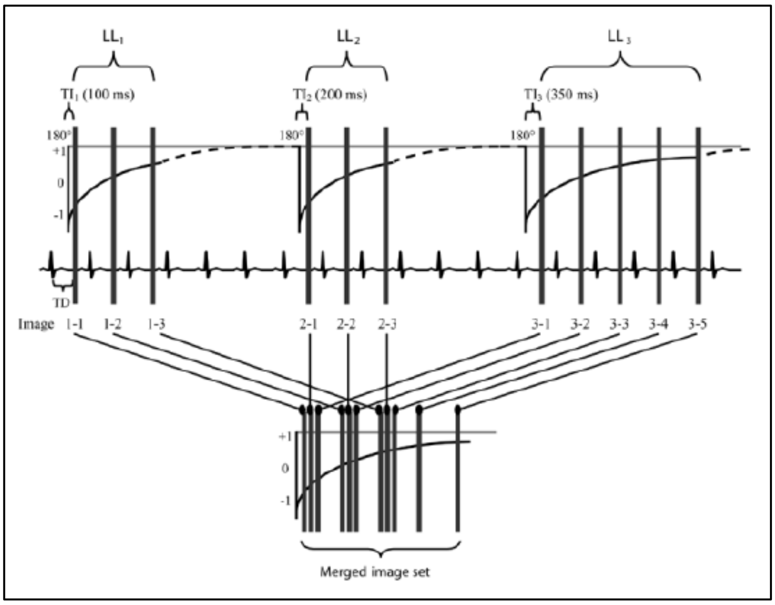

Figure 2-11) MOLLI pulse sequence scheme is shown. Each vertical bar represents one image acquisition. Three sets of Look-Locker (LL) experiments are performed successively (LL1 = three images, LL2 = three images, LL3 = five images) with increasing inversion time within one breath-hold's time. To select end-diastole, images were acquired using a specific trigger delay (TD). For T_1 calculation, images are regrouped for post-processing according to their effective inversion time (Messroghli et al, Magn Reson Med, 2004).

2.2.7 Myocardial perfusion imaging

Myocardial perfusion imaging is often used as a method to estimate myocardial blood flow [15]. It is based on measuring the delivery of contrast agent to the myocardium (following a bolus injection). Dynamic contrast enhanced-MRI (DCE-MRI) has been widely used for myocardial perfusion imaging and commonly involves the injection of a gadolinium-based contrast agent. Following a bolus injection, the acquisition of dynamic images is performed either at diastole or systole using ECG-gating. The signal intensity is enhanced by the contrast agent which shortens the T_1 relaxation time and results in a brighter signal using a T_1-weighted imaging pulse sequence (see Figure 4-9 in chapter 4). This allows for qualitative assessment of myocardial perfusion: myocardial regions with lower regional blood flow appear hypointense. Mathematical modelling of myocardial perfusion imaging data allows quantitative assessment of blood flow in ml/min/ml of tissue. This is possible through the mathematical analysis of the dynamics of the myocardial signal intensity measurement as a function of time (see subsections 3.1.3 and 3.1.4). Myocardial perfusion reserve can also be estimated from the ratio of myocardial blood flow at hyperaemia (stress) to myocardial blood flow at rest. Hyperaemia is induced using vasodilation agents such as adenosine or dipyridamole. Vasodilators increase the blood flow in normal vessels whilst the haemodynamic response to vasodilators is reduced in stenotic vessels [15].

For myocardial perfusion imaging there are some imaging requirements which need to be met. For quantitative perfusion, the left ventricle and myocardial tissue signal need to be sampled in every heartbeat. The spatial resolution must be adequate (<3 mm in plane) to allow detection of subendocardial ischaemia and to assess transmural extent of perfusion defects. A full coverage of the heart is required to cover at least 16 segments of the myocardium which can be achieved by using a minimum of 3 slices (see Figure 4-8 in chapter 4) [16]. Furthermore, a quantifiable relationship between signal intensity and contrast agent concentration is needed to quantify perfusion (see subsection 4.5). The image quality must be sufficient and free of artifacts to provide contrast between normal and ischaemic regions for qualitative perfusion assessments (see Figure 4-9) [15].

A saturation recovery preparation (Figure 2-12) is the most commonly implemented method for T_1-weighted perfusion imaging and can be used with various methods for image readout. In saturation recovery preparation schemes, there is a trigger delay (TD) between the radiofrequency preparation pulse and the initiation of image acquisition. The signal intensity is determined by the delay to the centre of k-space. This is often referred to as the inversion time (TI) and is commonly in the beginning of the readout in centric phase encode ordering (note: TD and TI is the same for centric phase encode ordering but different for linear phase encode ordering, see subsection 4.5 for further discussion in centric phase encode ordering) [15]. The fast low angle shot (FLASH) MRI is a spoiled gradient echo technique which combines a low-flip angle radiofrequency excitation with a rapid repetition of the basic sequence. This allows for rapid dynamic image acquisition.

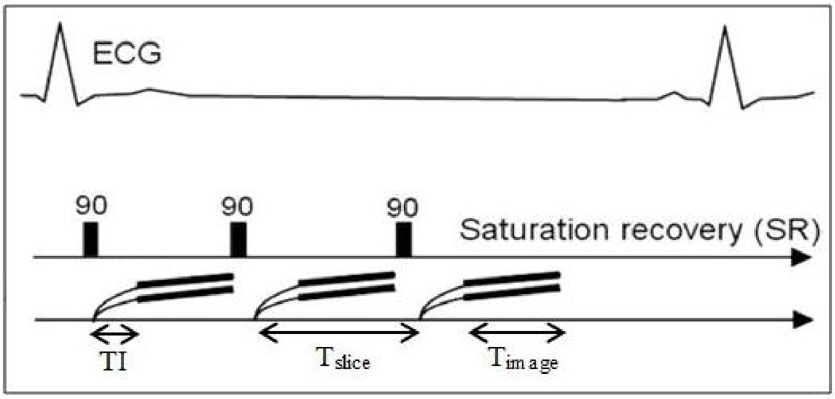

Figure 2-12) A multislice saturation recovery FLASH scheme. TI is the inversion time which is the time between the saturation pulse and the centre of the readout (centre of k-space), T_{slice} is the time per slice and T_{image} is the time for image readout (adapted by Kellman et al, J Cardiovasc Magn Reson, 2007).

2.3 Computed tomography

2.3.1 Basic principles of CT acquisition

The basic principle of CT acquisition is based on X-ray radiation. X-ray radiation is generated by the deceleration of fast electrons entering a solid metal anode. The electrons are emitted from a filament (cathode) which is heated to overcome the binding energy of the electrons to the metal of the filament. The deceleration of the electrons results from the interaction with the atomic nucleus and the orbital electrons in the anode. As explained in classical electrodynamics, acceleration and deceleration of charged particles induces an electric dipole and electromagnetic waves (photons) are radiated. Several photons can emerge throughout the complete deceleration process of a single electron. These electromagnetic waves have a range of wavelengths (between 10^{-8} and 10^{-13} m). The radiation energy depends on the electron velocity v, which in turn, depends on the acceleration voltage V_a, between cathode and anode. The electron velocity can be determined by the law of conservation of energy:

$$e \cdot V_a = \frac{1}{2} \cdot m_e v^2 \tag{2-20}$$

where m_e is the mass of the electron ($9.1 * 10^{-31}$ kg) and e is the electron charge ($1.6 * 10^{-19}$ C) [17].

X-ray radiation is capable of matter penetration during which the radiation intensity (which is proportional to the number of photons) decreases exponentially while passing through an object along the incident direction. The reason for this exponential reduction in photon numbers (attenuation) is that each photon is individually removed from the incident beam due to scattering and absorption mechanisms. CT imaging is based on photon-tissue interactions which lead to attenuation of x-ray radiation. The attenuation can be measured by advanced detectors incorporated in the CT scanner [17, 18].

After passing a distance Δη through an object, the radiation intensity can be determined by:

$$I \cdot (\eta + \Delta\eta) = I(\eta) - \mu(\eta) \cdot I(\eta) \cdot \Delta\eta \qquad (2\text{-}21)$$

where μ is the attenuation coefficient. Reordering equation (2-21) and taking the limit for Δη tending to 0, leads to the differential equation:

$$\frac{dI}{d\eta} = -\mu(\eta) \cdot I(\eta) \qquad (2\text{-}22)$$

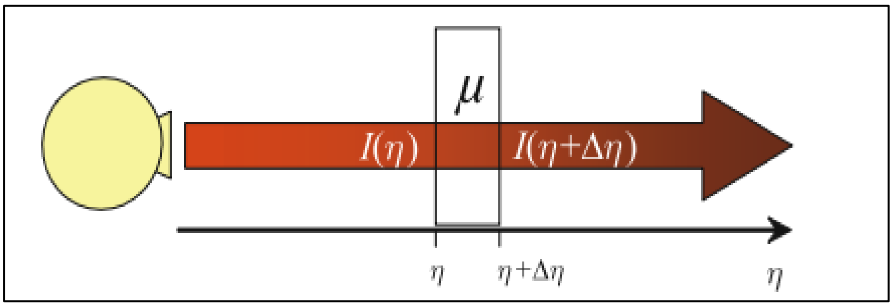

Figure 2-13) A mathematical approximation of monochromatic x-ray attenuation. An object of thickness Δη with a constant attenuation coefficient μ is assumed. Equal parts of the same absorbing medium attenuate equal fractions of the x-ray radiation (Computed Tomography: From photon statistics to modern cone-beam, 2008).

Reordering and integrating both sides of equation 2-22 leads to:

$$\ln I = -\mu \cdot \eta + C \qquad (2\text{-}23)$$

With exponentiation and under the initial condition that I(0)=I$_0$:

$$I(\eta) = I_0 \cdot e^{-\mu\eta} \tag{2-24}$$

However, the attenuation coefficient depends on the properties of the penetrated material (tissue). Thus, there is a spatially varying attenuation that needs to be considered and the intensity after a running length s, can be given by:

$$I(s) = I_0 \cdot e^{-\int_0^s \mu(\eta)\delta\eta} \tag{2-25}$$

The attenuation of x-rays is well understood and can be modelled by using equation 2-25. The benefit of CT imaging is that high values of the attenuation coefficient μ are due to a high density or high atomic number of the medium. This means that the grey values of the CT images are a direct physical representation of the tissue properties [17].

2.3.2 CT signal detection

To calculate the spatial distribution of the attenuation coefficient μ(x, y), the projection modelled by (2-25) has to be reversed. For each projection angle, the x-rays are attenuated at different extents depending on the local properties and morphologies of the tissues under examination. These local attenuations are measured using detector arrays. However, to acquire distinct tissue structures from a three-dimensional object, the implementation of advanced mathematical techniques is required. In Figure 2-14, the history of the three generations of CT scanners and the corresponding advances in CT technology is illustrated [17].

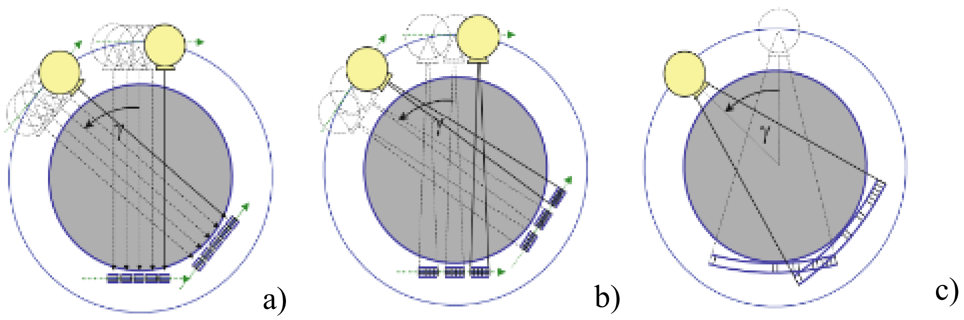

Figure 2-14) a) The first generation of CT scanners used a pencil beam geometry and a single detector. The above configuration is rotated through different projection angles γ (through 180^0). Each point inside the field of view needs to be irradiated from all different positions. b) The second generation CT scanners used x-ray sources with fan-beam geometry, combined with a short detector array. The configuration in b needs also to be rotated since the fan angle is about 10^0. c) The third generation of CT scanners uses fan angle of about 40^0-60^0 whilst the detection array consists of up to 1000 detector elements. The entire field of view can be measured simultaneously and the acquisition time has been considerably reduced (Computed Tomography: From photon statistics to modern cone-beam, 2008).

To determine the distribution of attenuation coefficients, it is important to irradiate the object from all directions (through a projection angle interval of at least 180^0). For simplification, a coordinate system (ξ, η) is defined which rotates together with the source of x-rays and the detector. In Figure 2-15, p_γ (ξ) represents the attenuation profile of the x-ray beam versus the coordinate ξ of the detector array, for a particular projection angle γ. When the attenuation profiles are plotted over all projection angles γ, a sinusoidal arrangement of the attenuation is obtained. The representation of these attenuation profiles in two dimension defines the set of raw data, known as Radon space. The spatial distribution of the attenuation coefficients within a sampling unit must then be estimated and reconstructed from the sequence of all measured attenuation profiles ($p_{\gamma 1}$ (ξ), $p_{\gamma 2}$ (ξ), $p_{\gamma 3}$ (ξ),..,$p_{\gamma n}$ (ξ)) [17, 18].

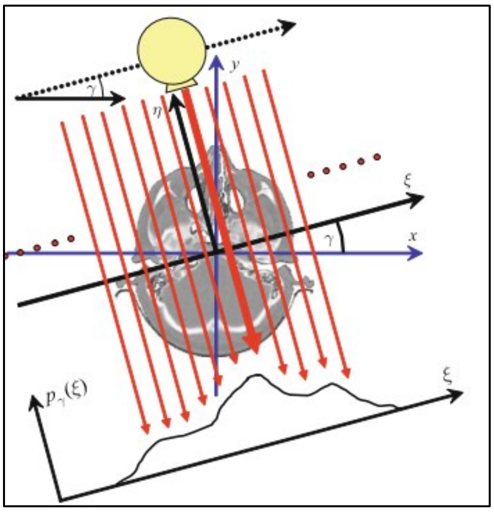

Figure 2-15) Rotating frame (ξ, η) compared to the fixed frame (x, y) is shown. p_γ (ξ) represents the attenuation profile of the x-ray beam versus the coordinate ξ of the detector array, for the particular projection angle γ (Computed Tomography: From photon statistics to modern cone-beam, 2008).

The spatial distribution of the attenuation coefficients within a selected slice of the patient has to be reconstructed from the set of the parallel attenuation profiles p(ξ). One of the most time-efficient mathematical methods to solve the so called inverse problem and efficiently achieve image reconstruction is the Fourier slice theorem. The Fourier slice theorem can be accomplished in three basic steps. The first step is the calculation of the Fourier transform $p_\gamma(q)$ of the Radon space data $p_\gamma(\xi)$:

$$p_\gamma(q) = \int_{-\infty}^{\infty} p_\gamma(\xi) \cdot e^{-2\pi i q \xi} d\xi \tag{2-26}$$

However, Radon space data and their Fourier transforms are given in polar coordinates, (ξ, γ) and (q, γ) respectively. The second step is to induce a change in the coordinates of the Fourier transformed data, from polar to Cartesian coordinates.

To calculate the Cartesian coordinates (u, v) from the polar coordinates (q, γ), the following set of equations is used:

$$u = q \cdot \cos(\gamma), \quad v = q \cdot \sin(\gamma). \tag{2-27}$$

Using the set of equations 2-27, it is possible to calculate F(u, v) which is the two dimensional Fourier spectrum. Finally, the third step is to calculate the inverse Fourier transform of F(u, v) leading to the calculation of f(x, y), which is the spatial distribution of the attenuation coefficients within a given slice of the patient [17, 18]. The implementation of the third step provides the CT image in which the spatial distribution of attenuation coefficients is provided in the (x, y) plane within a slice of the patient.

2.3.3 CT angiography and perfusion

The new generation of multidetector computed tomography (MDCT) scanners have enabled the implementation of coronary CT angiography and perfusion within one cardiac imaging protocol (for example images see chapter 7, Figure 7-1). In clinical practice, the main advantage of MDCT scanners is the reduction in scan time and radiation dose, whilst allowing the detection of highly defined anatomical details of coronary arteries reducing respiratory motion and arrhythmias artifacts [19, 20]. Furthermore, the application of MDCT scanners introduced a different approach to image analysis in which the operator can reconstruct and navigate planar images through the use of dedicated software tools [20].

CT angiography is a rapidly evolving technique in the field of cardiac imaging. It has the potential to detect anatomically significant coronary artery disease with high sensitivity and negative predictive value when compared with invasive coronary angiography (which is considered the current gold standard for assessing luminal stenosis). Compared to invasive coronary angiography, the diagnostic procedure using CT angiography benefits from multiple views of the coronary artery tree. When iodine-based contrast agents are introduced intravenously into the circulatory system, they are capable of increasing the x-ray attenuation of the blood making it possible to visualise the blood pool within vessels and cardiac chambers. Using MDCT imaging and after the injection of an iodine-based contrast agent bolus, the whole cardiac volume can be obtained within one cardiac cycle, provided the heart rate is low enough (see use of beta blockers in CT imaging for reducing heart rate in section 4.9). Sections of the coronary arteries can be retrospectively reconstructed using dedicated software tools. For example, unlike in invasive coronary angiography, cross-sectional views of the vessels can be obtained from data acquired using MDCT. Thus, an important step for angiographic analysis using MDCT data is to analyse reconstructed images from different phases of the cardiac cycle in order to assess where the contrast enhancement is optimum for visualising (even subtle areas of) the coronary artery tree, and where motion artifacts are eliminated or reduced [20].

A systematic analysis of CT angiographic data involves a) examination of the anatomical distribution of coronary arteries aiming to identify normal variants or congenital abnormalities, b) detection and localisation of coronary artery lesions, c) careful exclusion of sections or interposed structures creating image artifacts, d) evaluate the morphology and composition of the lesion and e) perform qualitative and quantitative assessment of the luminal stenosis. Moreover, calcified coronary plaques can be detected and assessed using CT angiography [20].

CT angiography alone has a limited ability to determine the physiologic functional significance of coronary stenoses compared to other non-invasive methods involving myocardial perfusion imaging. After contrast agent injection (the same bolus injection used for CT angiography), MDCT images may provide qualitative or semi-quantitative information about myocardial perfusion. Short axis views of the left ventricle and myocardium can be reconstructed from the MDCT data (see description and images of short axis view in sections 4.2 and 4.9) and the presence of a myocardial perfusion defect can be detected from a ‘snapshot’ (or static) image during the arterial phase of contrast enhancement. Both animal [21] and clinical studies [22] have shown that in CT images, the signal intensity of myocardial areas corresponding to infarcted myocardium can be significantly reduced compared to areas with non-infarcted myocardium.

Unlike in MR perfusion imaging, dynamic acquisition of CT perfusion images using ECG-gating is restricted due to radiation exposure limitations. Most clinical CT perfusion protocols are limited to acquire a snapshot image at the peak of contrast enhancement both during vasodilator-induced stress and at rest. Absolute myocardial blood flow quantification from snapshot perfusion data is therefore not possible. Analysis of these static CT perfusion images using dedicated software can provide semi-quantitative information of myocardial perfusion. Some early dynamic CT perfusion acquisition protocols have been introduced (with limited cardiac coverage) and absolute myocardial blood flow quantification has been made possible. The concepts of snapshot and dynamic CT perfusion acquisition and analysis in literature will be further discussed in chapter 3.

3. Literature review

Summary

This chapter presents a review of previously published methods for quantitative myocardial blood flow analysis in cardiac MR perfusion imaging. It also introduces previous work utilising CT angiography and recent publications for qualitative analysis of cardiac CT perfusion images as well as for semi- and absolute quantification of myocardial blood flow in CT perfusion imaging. Moreover, it presents previous work in the literature with reference to invasive methods which are the current clinical standards for assessing coronary artery disease. These topics are important to provide context for the information contained in the result chapters 5-7.

3.1 MRI cardiac perfusion

3.1.1 Contrast agent concentration

The quantitative assessment of myocardial blood flow can provide important functional information for the detection and assessment of coronary artery disease. Assessment of blood flow with MRI using this methodology (see dynamic contrast enhanced-MRI, subsection 2.2.7) is based on measuring the rate at which the contrast agent arrives in the tissue of interest, in this case the myocardium. As described in subsection 2.2.5, the most commonly used contrast agents in DCE-MRI are gadolinium-based contrast agents. The concentration of gadolinium in the myocardium can be indirectly detected by the change in signal intensity in a T_1 weighted image (as described in chapter 2, equation 2-16). The signal intensity extracted from the myocardium and blood pool is converted to tissue gadolinium concentration curves using equation 2-16 [23]. This equation states that change in R_1 ($=1/T_1$) in a homogeneous voxel, is directly proportional to the gadolinium concentration. In this equation, the proportionality constant is the T_1 relaxivity of gadolinium (r_1). This conversion to gadolinium concentration aims to minimise the influence of signal saturation effects that can be present in the myocardial tissue and blood pool signal and which can significantly affect blood flow quantification [24]. For low gadolinium concentrations and/ or low T_1 sensitivity (or low T_1 weighting, see subsection 3.1.5) sequences, the signal enhancement is approximately proportional to gadolinium concentration [15]. However, in clinical practice, to reach sufficient contrast-to-noise ratio in the myocardium, imaging protocols use combinations of high gadolinium concentrations and high T_1 sensitivity sequences (strong T_1 weighting) [15, 24]. This often leads to a non-linear dependence of signal enhancement on gadolinium concentration in both the myocardium and the blood pool, known as signal saturation [24]. Signal saturation can become pronounced at higher gadolinium concentrations (commonly found in blood pool from which the arterial input function is extracted) and can lead to concentration underestimation. Methods to correct for this phenomenon will be discussed thoroughly later in this chapter.

As mentioned (chapter 2, subsection 2.2.6), T_1 mapping is important to calculate native T_1 relaxation time of the tissue of interest, in the absence of contrast enhancement. Depending on the selected pulse sequence used for perfusion imaging, a signal intensity equation is needed to derive the T_1 relaxation time from the observed changes in signal intensity during contrast enhancement of the myocardial tissue and blood pool. For the saturation recovery prepared single-shot gradient echo pulse sequence which is used on the Siemens Verio MRI system in Edinburgh for the work presented in this thesis, the signal intensity and R_1 are related by the following equation [25]:

$$SI = \Psi\left[\left(1-e^{-PD\cdot R_1}\right)\cdot a^{n-1} + b\frac{1-a^{n-1}}{1-a}\right] \tag{3-1}$$

where SI is the equilibrium signal intensity, Ψ is a calibration constant dependent on instrument conditions such as the receiver gain, proton density and the flip angle α. PD is the pre-pulse delay which is the time between saturation pulse and the central line of k-space, n is the number of applied pulses of flip angle α, $a = \cos(\alpha)\cdot e^{-TR\cdot R_1}$ and $b = 1 - e^{-TR\cdot R_1}$. TR is the time interval per phase encoding step (between repetitions of the α-radiofrequency pulses) and R_1 is the relaxation rate. Ψ is assumed to be constant throughout the dynamic perfusion image acquisition and can initially be calculated from equation 3-1 using native T_1 and signal intensities derived from regions of interest (i.e. arterial input function, myocardial segments) in the absence of contrast enhancement. $R_1(t)$ at time t of contrast enhancement can then be calculated from equation 3-1, using Ψ and signal intensity values extracted from the same region of interest in each of the dynamic perfusion images. Contrast agent concentration-time curves can be calculated using equation 2-16. The mathematical process leading to equation 3-1 is presented in the Appendix (Appendix 2).

The above method for converting signal intensity time curves into contrast agent concentration time curves was first described by Larsson et al [25], was further validated by Fritz-Hansen et al [26, 27] and has been used in a variety of myocardial perfusion studies [24-31].

3.1.2 Quantitative analysis in MRI

There are two main approaches which can be used for myocardial blood flow quantification from the DCE-MRI (perfusion) data. These approaches can be classified into two main categories, the first is the model independent and the second is model based [24].

3.1.3 Model independent analysis

Model-independent approaches are fundamentally based on the central volume principle which was first described by Zierler et al [32, 33]. This is based on the principle introduced by Eugen Fick which states that the rate at which a substance aggregates in a tissue of interest can be given by the concentration difference of the contrast agent entering and leaving the region multiplied by the flow rate (F). This can be mathematically described as [24, 32, 33]:

$$F \cdot (c_{out} - c_{in}) = dq(t)/dt \tag{3-2}$$

where c_{in}, c_{out} are the contrast agent concentrations at the inlet and outlet of the region respectively, q(t) is the mass of the contrast agent and dq(t)/dt is its rate of change in time (t). This is a statement of mass balance which describes that the amount of contrast agent which has entered the tissue of interest and has not yet exited, has remained in the region of interest.

Based on the above mass balance principle, equation 3-2 (in its integral form) can be rewritten in the form of a convolution integral which relates the amount of the contrast agent in the region q(t) with its arterial input:

$$q(t) = \int_0^t [F \cdot (c_{out}(\tau) - c_{in}(\tau))] d\tau = \int_0^t c_{in}(t-\tau) \cdot R(\tau) d\tau \qquad (3\text{-}3)$$

R represents the tissue impulse response if an impulse input of contrast agent is applied at the region input, such as a Dirac-delta input function (δ(t)). The theory of convolution and tissue impulse response is further described in the Appendix (Appendix 3). With such an impulse input $c_{in}(t)=\delta(t)$ at time t=0, there can be no contrast agent leaving the tissue. Thus, it can be shown that for t=0, R(t)=F which means that the initial amplitude of the tissue impulse response is equal to the blood flow entering the region of interest [24]. This essentially summarizes the central volume principle described by Zierler [32, 33].

Based on the central volume principle, it is possible to quantify the blood flow from the initial amplitude of the tissue impulse response given that q(t) and $c_{in}(t)$ are measured quantities (they correspond to the measured contrast agent concentration time curves derived from the tissue and the blood pool respectively). The process of extracting the tissue impulse response R(t) from the contrast agent concentration time curves derived from the tissue q(t) and the blood pool $c_{in}(t)$, is called deconvolution analysis as it reverses the convolution operation (equation 3-3) [24, Appendix 3].

However, this is a mathematically unstable approach for calculating the tissue impulse response from q(t) and $c_{in}(t)$. These instabilities in the calculation of the tissue impulse response are inherent to the nature of the deconvolution problem [24]. Jerosch-Herold developed a model independent deconvolution approach which improved the numerical stability and imposed some smoothness constraints on the solution [34]. This method is based on the idea that the tissue impulse response R(t) can be represented as a sum of piece-wise smooth B-spline functions:

$$R(t) = \sum_{j=1}^{p} B_j^{(k)}(t) \cdot a_j \tag{3-4}$$

Parameterising the tissue impulse function R(t) with B-spline functions and using least square minimization and Tikhonov regularization [35], it is possible to arrive at a solution for R(t):

$$\min\left\{ \|q(t) - R(t) \otimes c_{in}(t)\|^2 + \lambda^2 \|\nabla R(t)\|^2 \right\} \tag{3-5}$$

where λ is the regularization parameter, $\otimes$ represents the convolution process, ∇ denotes the temporal difference operator and $\|\ \|$ represents the Euclidean norm. The above method has been used in a variety of studies for myocardial blood flow quantification [34, 36-38]. Similar approaches using B-spline polynomial functions in order to stabilize the solution of the tissue impulse response can also be found in pharmacokinetic analysis for several applications [39]. Other mathematical approaches for accurately and robustly resolving the instability of the tissue impulse response have also been suggested as potential solutions. Characteristic examples are a) the exponential basis deconvolution [40] and b) the autoregressive moving average (ARMA) models [41-43]. Nevertheless, these models have not been fully explored and validated by other groups in the field.

All of these methods essentially focus on measurement of the initial amplitude of the tissue impulse response from which the blood flow can be quantified. A number of smoothness constraints and assumptions need to be imposed for accurately measuring the specifics of the tissue impulse response. The main limitation of these model-independent approaches is that they focus only on the calculation of myocardial blood flow, whilst they lack any interpretation of other microvascular characteristics such as the intravascular space or the permeability surface area product which may be very physiologically (or at least functionally) relevant. To calculate additional microvascular characteristics which can help to obtain a more complete interpretation of the coronary haemodynamics, a model (-based analysis) needs to be specified [24].

3.1.4 Model based analysis

In model-based approaches, a physiologically-specific model is used to describe the passage of the contrast agent through the tissue of interest. The first studies which implemented model-based approaches for quantitative analysis of DCE-MRI data aimed to assess the blood-brain barrier permeability [44-46]. A comparison between some of these specific model approaches [47] provided a consensus standardising measured quantities and symbols [48], and set the basis for quantitative analysis of DCE-MRI data that were used in numerous (mainly) oncological studies to assess response to treatment [49,50].

For quantitative analysis of cardiac perfusion data, Larsson et al introduced a tracer kinetics analysis to assess myocardial perfusion from DCE-MRI data [25]. This method focused on the quantification of K^{trans}, a parameter which reflects a combination of myocardial blood flow and permeability surface area product [25, 48, 50]. This is based on the idea that the transport of the contrast agent across the membrane of the capillary walls can be described by a first order differential equation [51]:

$$\frac{q(t)}{dt} = K^{trans} \cdot c_{in}(t) - k_{ep} \cdot q(t) \tag{3-6}$$

$$q(t) = c_{in}(t) \otimes K^{trans} \cdot e^{-k_{ep} \cdot t} \tag{3-7}$$

where K^{trans} represents the kinetic rate constant of contrast agent flow from the intravascular into the extravascular-extracellular space, k_{ep} denotes the kinetic rate constant of contrast agent flow from the extravascular-extracellular space into the intravascular space and q(t) and $c_{in}(t)$ are the measured contrast agent concentration time curves derived from the tissue and the blood pool respectively. Equation 3-7 is the analytical solution of equation 3-6 in which the tissue contrast agent concentration q(t) is represented by the convolution of the contrast agent concentration derived from the blood pool $c_{in}(t)$ with the system impulse response function R(t) ($= K^{trans} \cdot e^{-k_{ep} \cdot t}$). This model approach has been implemented by others [37, 48]. Although the calculation of K^{trans} can reflect the haemodynamic state of coronary arteries and its physiological interpretation reflects a combination of myocardial blood flow and permeability surface area product [48, 50], this early stage analysis did not provide absolute quantification of myocardial blood flow.

In the concept of tracer kinetics analysis, Axel described for the first time a parametric representation of the tissue impulse response for the analysis of brain perfusion studies by CT, known as the Fermi function [24, 52]. The Fermi function was chosen based on the idea that its shape resembles the expected shape of a tissue impulse response for an intravascular contrast agent. Its mathematical equation is given here:

$$R(t) = \frac{1}{\exp[(t - \tau_o) \cdot k] + 1} \tag{3-8}$$

where the parameter t represents time, and τ_o defines the width of the initial plateau of the tissue impulse response before it decays mono-exponentially at a rate given by the parameter k. The central volume principle is also applied in model-based deconvolution approaches such as Fermi modelling, according to which the initial amplitude (for t=0) of the tissue impulse response R(t) corresponds to the blood flow [24, 50, 52]. Fermi models have been applied in a variety of myocardial perfusion studies in healthy subjects [24, 28, 29, 31, 37, 43, 53-57], in patients [58, 59], in canines [30, 56] and in hardware phantoms [43, 60].

In 1953, Sangren and Sheppard developed a mathematical analysis to describe the exchange of a labelled substance between the intravascular and the extravascular-extracellular space [61], known as distributed parameter model. The distributed parameter model was applied by Goresky et al [62] and was further validated in outflow data from the isolated liver [50, 63] and in canine coronary circulation [64], by the same group. To derive the model equation, the distributed parameter model can be considered as a sequence of infinitesimal two-compartmental exchange models [50].

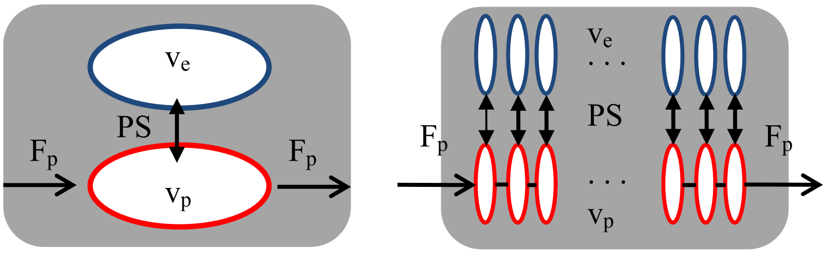

Two-compartment exchange model Distributed-parameter model

Figure 3-1) Left panel: Two compartment exchange model which assumes that the extravascular-extracellular space (v_e) and the intravascular plasma space (v_p) are both compartments. In each of these compartments, the contrast agent concentration is assumed to be homogeneous. Right panel: The distributed parameter model can be considered as a sequence of infinitesimal two compartment exchange models. The contrast agent concentrations in each of these compartments depend on the position x along the capillary direction.

The tissue contrast agent concentration within each compartment of the intravascular space is $c_p(x,t) \cdot v_p \cdot dx / L$, whilst the outflux from the intravascular into the extravascular-extracellular space through the wall is $c_p(x,t) \cdot PS \cdot dx / L$ and the local flux from the extravascular-extracellular space back into the intravascular space is $c_e(x,t) \cdot PS \cdot dx / L$. The parameters c_p, v_p, c_e, PS, dx and L represent the intravascular plasma concentration, the intravascular plasma space, the extravascular-extracellular concentration, the permeability surface area product, the width of the infinitesimal compartment and the full length of the vessel tube respectively [50]. When all the expressions of fluxes and concentrations are inserted and for $dx \to 0$, the following partial differential equation can be produced [50, 64]:

$$\frac{v_p}{L}\frac{\partial c_p}{\partial t}(x,t) = -F_p \frac{\partial c_p}{\partial x}(x,t) - \frac{PS}{L}c_p(x,t) + \frac{PS}{L}c_e(x,t) \tag{3-9}$$

where F_p denotes the intravascular plasma flow. Equation 3-9 does not allow axial transport of the contrast agent within the extravascular-extracellular space whilst all the contrast agent concentrations depend on the position x. The distributed parameter model has an analytical solution both in the time and in the Laplace domain. By fitting the Laplace domain model equation, it is possible to avoid the discontinuities of the time step-function that can be present when fitting the distributed parameter model in the time domain [65, 66]. The Laplace domain model equation has been used for myocardial blood flow analysis in this thesis and it is provided here [50, 66]:

$$R(s) = \frac{1-\exp\left[-s\cdot\left(T + s\cdot T_c\cdot T_e\right)/\left(1+s\cdot T_e\right)\right]}{s} \tag{3-10}$$

where $s = i\cdot 2\cdot \pi \cdot f$ and f is the frequency variable in the Fourier transformed data [65, 66]. Using the distributed parameter model, it is possible to also calculate other parameters apart from blood flow such as the intravascular space, extravascular-extracellular space, volume of distribution (the fraction of tissue that is accessible to the contrast agent, equals the sum of the intravascular space and extravascular-extracellular space), permeability surface area product (measures the rate at which contrast agent particles leak out of the plasma) and extraction fraction (defined as the fraction of the contrast agent particles that is extracted into the interstitium) [50]. Broadbent et al have recently applied distributed parameter modelling in cardiac MR perfusion data for absolute myocardial blood flow quantification. In addition to blood flow estimation, their data analysis also demonstrated that the coronary wall offers a barrier to contrast agent transport from the intravascular into the extravascular space [66].

3.1.5 Arterial input function

As mentioned in subsections 3.1.3 and 3.1.4, methods for quantifying myocardial blood flow use the arterial input function as reference, which is the contrast agent concentration derived from the blood pool [24, 50]. It has been shown that any underestimation of the arterial input function leads to systematic overestimation of myocardial blood flow [24].

The high concentration of (gadolinium-based) contrast agents during bolus passage, leads to significant signal saturation which causes concentration underestimation in the left ventricular cavity that cannot be corrected with the mathematical conversion of signal intensity curves into gadolinium concentration curves (equations 2-16 and 3-1). As gadolinium concentration increases, this concentration underestimation becomes even more pronounced [24].

To overcome this limitation, some possible solutions that have been used in previous studies are summarized here. First is the use of lower gadolinium dosages (0.025-0.050 mmol/kg at 1.5 T, 0.025-0.040 mmol/kg at 3T) [24, 67, 68]. This results in a lower peak of contrast enhancement in the blood pool which is less susceptible to signal saturation effects. Although this approach can almost always be implemented in healthy volunteers, it may not be feasible in patients with impaired cardiac function. In these patients, the gadolinium bolus passage might undergo slow dispersion which would lead to reduced signal to noise ratio in the MR perfusion images. A sufficient signal-to-noise ratio is required for clinicians to discriminate normal from hypoperfused myocardium. When myocardial blood flow quantification is involved, the contrast agent dose needs to be reduced to minimize signal saturation effects which may compromise image quality [24, 67, 68]. It is important to consider that when even higher doses (such as 0.10 mmol/kg at 1.5 and 3T) are used to improve image quality, signal saturation effects can be substantial and it is possible to underestimate myocardial contrast agent concentration [67, 68].

Another approach is to implement dual contrast sequences [69-71]. For each cardiac cycle, this involves the acquisition of a low resolution and weakly T1-weighted short axis view image with a short saturation-recovery time to measure the arterial input function and eliminate signal saturation; followed by a standard high resolution (and more strongly T1-weighted) short axis view with a long saturation recovery time to increase the signal to noise ratio in the myocardium. For the low resolution image, fewer phase-encoding steps are implemented between the magnetization preparation and the readout of central phase-encodings. This allows for a shorter delay after magnetization preparation (i.e. saturation or inversion pulse). At higher concentrations, the short delay can improve the linearity of the signal intensity versus R_1 (=1/T_1) relationship described in equation 2-16 [24].

Furthermore, another approach to correct the signal saturation in the blood pool is through post-processing using calibration curves [72-74]. Calibration curves can be generated with numerical simulations, pre-contrast T_1 measurements and for specific sequence parameters [24]. To date, both dual contrast and the calculation of calibration curve techniques has not been extensively implemented and validated in cardiac perfusion imaging in the clinical setting.

The most well established method for correcting signal saturation in the blood pool is the implementation of dual bolus imaging [24, 30, 31, 54, 55, 58, 59, 67, 75]. Dual bolus imaging involves the injection of a low dose contrast agent bolus (pre-bolus) to extract the contrast agent concentration-time curve from the blood pool, followed by a higher dose bolus to extract the myocardial contrast agent concentration time curves. With the pre-bolus injection, signal saturation leading to gadolinium underestimation can be avoided, whilst the higher (main) bolus follow-up injection provides adequate signal-to-noise ratio in the myocardial tissue. These two boluses are injected in a pre-determined ratio of gadolinium-based contrast agent dose (e.g. 1:5, 1:10), which is used to scale up the arterial input function from the low dose data to the equivalent concentration in the main bolus data [24, 30]. It has been shown that compared to single bolus imaging in which Fermi modelling derived myocardial blood flow is systematically overestimated, dual bolus imaging eliminates signal saturation and improves myocardial blood flow measurements [31, 75]. Dual bolus imaging protocols eliminate arterial input function saturation but are more complicated both in terms of practical implementation at the point of image acquisition, as well as in post-processing, compared to single bolus protocols [24, 76].

3.2 Previous work in CT

3.2.1 Computed tomography angiography

Recent studies using MDCT scanners have demonstrated that non-invasive CT coronary angiography has the potential to exclude significant coronary artery disease [77-79] and to provide prognostic information in patients with suspected coronary artery disease [80-83]. Using modern imaging technology, CT coronary angiography (CTCA) can reach excellent sensitivity in detecting significant coronary artery disease [84, 85].

However, the specificity of these modern techniques is relatively reduced due to their tendency to overestimate heavily calcified lesions [84, 86]. Moreover, some studies have shown that CT coronary angiography is a poor predictor of reversible myocardial ischaemia [87-89] and that functional information is needed, particularly in patients with moderate to severe coronary artery disease [90].

To overcome these limitations of CTCA alone, additional information on the physiological significance of coronary artery stenosis is needed from CT scanning. Cardiac CT perfusion imaging may provide additional physiological information and has the potential to improve the diagnostic accuracy of CT angiography for the detection of coronary stenoses, albeit at the cost of additional ionizing radiation exposures [90].

The high radiation doses involved in cardiac CT angiography imaging have raised serious concerns in literature, as the risks of radiation-induced malignancy are not negligible [91, 92]. Methods to minimize the radiation dose in cardiac CT angiography protocols have been proposed, such as using prospective ECG-triggering with which it is possible to image only specific parts of the cardiac cycle [91, 93].

3.2.2 Computed tomography perfusion

CT angiography and perfusion may be performed in one examination to acquire both anatomical and functional information on modern, advanced wide detector CT systems. Despite the introduction of some early dynamic CT perfusion protocols in animal and human studies, the vast majority of CT perfusion imaging applications in the clinical setting is still limited to a ‘snapshot’ acquisition at the peak of contrast enhancement, in order to limit the overall radiation dose exposure which would be unacceptable in a truly “dynamic” CT perfusion examination.

Several studies have been published which have focused in evaluating myocardial perfusion using modern techniques in MDCT scanners. In general, ‘spiral’ CT image acquisition involves transport of a patient at a constant speed through the gantry, whilst spiral (also known as ‘helical’) CT data are simultaneously and continuously acquired over multiple gantry rotations [94]. With the standard spiral acquisition mode of conventional (i.e. with narrower detector arrays) MDCT scanners, it is feasible to image only an early phase of first pass contrast enhancement [95]. This has allowed semi-quantification measurements of myocardial perfusion such as regional signal density ratio (i.e. myocardial signal density/ left ventricular signal density) [95] and the generation of qualitative perfusion maps [96], in canines. Kido et al have reported the use of conventional 16-slice MDCT scanners for non-ECG gated dynamic perfusion image acquisition in human subjects [97]. Nevertheless, this protocol was unable to cover the entire left ventricle at each dynamic image acquisition.

Recent studies in human subjects using new generation wide detector MDCT scanners (such as 64-, 256- and 320- slice systems), have shown that the diagnostic accuracy of CT angiography for the detection of significant coronary artery disease can be improved, when combined with snapshot CT perfusion imaging [90, 98]. Snapshot perfusion images can be acquired both under vasodilator-induced stress and at rest. These studies showed that CT perfusion imaging can detect transmural differences in myocardial perfusion, which can be quantified as the transmural perfusion ratio (i.e. subendocardial/subepicardial attenuation density) [90]. In a case study using a 320-slice MDCT scanner, perfusion defects have been accurately detected, as compared with invasive coronary angiography, with the application of a low radiation dose (snapshot) perfusion acquisition protocol [99].

Wide detector MDCT scanners can potentially provide improved temporal resolution together with high spatial resolution whilst can allow full cardiac coverage using lower radiation doses [100]. With the use of modern acquisition techniques in these new generation scanners, it is possible to dynamically visualize different phases of first pass myocardial contrast agent kinetics, which are needed for absolute myocardial blood flow measurements [100]. Using a 64-slice MDCT scanner, dynamic CT perfusion images have been acquired in canines, which allowed absolute myocardial blood flow quantification using two-compartmental modelling [101].

Dual energy MDCT imaging has also been used to generate perfusion-maps from snapshot images at the peak of contrast enhancement using relatively low radiation doses in patients with suspected coronary artery disease [102, 103]. The operation of dual energy MDCT scanners is based on the application of two simultaneous x-ray sources with different photon energy which can acquire two data sets with different attenuation levels. Images acquired at two different attenuation levels can then be processed with specific software applications and differences in tissue composition can be emphasized [104].

With the application of dual energy MDCT scanners, the acquisition of dynamic ECG-triggered myocardial perfusion images in patients with known or suspected coronary artery disease was made possible [105, 106]. However, these dynamic perfusion protocols were still unable to cover the entire left ventricle [84, 105, 106]. Model-independent deconvolution analysis of these dynamic CT perfusion data provided absolute myocardial blood flow values in the myocardial areas which were imaged [105, 106]. For the specific model-independent analysis, a mathematical procedure was applied to limit the deleterious effects of noise which would otherwise cause serious problems for the calculation of myocardial blood flow [107,108]. The above method has provided accurate myocardial blood flow measurements when compared with invasive coronary angiography outcomes from patients with suspected coronary artery disease [105].

3.3 Invasive methods

Invasive coronary angiography involves injection of a radiocontrast agent through coronary catheterization whilst an x-ray camera dynamically images the contrast enhancement of the coronary tree from multiple angles [109].

Studies have previously shown that the extent and severity of myocardial ischemia are determinant risk factors for patients with coronary artery disease and thus, ischaemia reduction is currently considered as an important therapeutic goal [109-112]. It has been demonstrated that revascularization of stenotic coronary arteries can improve patient outcome and functional status, whilst it can reduce the long-term risk of major cardiovascular events [112-114]. On the other hand, the benefits of revascularization in stenotic lesions not associated with ischaemia, is less clear [112-116]. It has been shown that compared to drug therapy, revascularization does not reduce major cardiovascular events in non-ischaemic coronary lesions [115,116]. In patients with multivessel disease, it is often not feasible to accurately determine which lesions are associated with reversible myocardial ischaemia [117]. Clinically, coronary lesions with a diameter stenosis of ≥50% on invasive coronary angiography are often considered for revascularization [115]. Although invasive coronary angiography is often inaccurate in predicting which lesions are causing myocardial ischaemia and may result in underestimation or overestimation of lesion severity [109], is still the standard technique for decision making about revascularization in patients with coronary artery disease [118, 119].

Fractional flow reserve is an index of the physiological significance of a coronary stenosis [109]. It is defined at the ratio between distal coronary pressure and aortic pressure (which is the reference standard), both measured during vasodilator-induced hyperaemia [109]. Fractional flow reserve can be measured during invasive coronary angiography, by calculating the ratio of distal coronary pressure using a coronary pressure guide-wire, to aortic pressure using simultaneously a guide catheter [109, 117]. Fractional flow reserve in a normal coronary artery equals 1.0, whilst a value of 0.80 or less detects physiologically significant lesions (i.e. coronary stenoses causing ischaemia) with an accuracy of more than 90% [109, 120-121].

It has been shown that when patients with multivessel coronary artery disease undergo revascularization after fractional flow reserve and invasive coronary angiography guidance, there is a significant reduction in major cardiovascular events at 1 year, compared to revascularization guided by angiography alone [109]. Furthermore, invasive coronary angiography is not accurate in detecting physiological significance of coronary stenoses in 50-70 % and in 70-90 % diameter stenoses in patients with multivessel disease, as compared to fractional flow reserve [117]. In patients with stable coronary artery disease and at least one vessel with a fractional flow reserve of 0.80 or less, fractional flow reserve-guided revascularization plus the best available drug therapy as compared with medical therapy alone, decreased the rate of urgent revascularization [122]. In addition, among patients with non-significant stenoses identified using fractional flow reserve, the best available drug treatment alone led to excellent clinical outcomes, indicating that drug therapy can be the best treatment for non-ischaemic coronary arteries [122].

4. Description and validation of methods used in subsequent chapters

Summary

This chapter details image acquisition methods that were used to generate healthy volunteer and patient data. It describes post-processing and image analysis methods that were developed to analyse myocardial blood flow from MR data. Moreover, it presents experiments and measurements performed by the author to validate image analysis methods that are presented throughout the next chapters. The MR methods and validation measurements are presented in chronological sequence of application.

This chapter presents the validation experiment to assess the MOLLI technique, the MR image acquisition protocol and cardiac contouring. It describes development and validation of the Matlab software developed for extracting signal intensities and validation of a saturation recovery FLASH equation. It also details arterial input function extraction, validation of algorithm for converting signal intensity curves into gadolinium concentration curves and optimization procedure of the dual bolus imaging protocol. In the last subsection, it also provides information about the CT image acquisition protocol.

4.1 Validation of MOLLI technique

In chapter 2, the MOLLI technique was introduced which at the time of writing this thesis is the most widely used clinical T_1 mapping technique [12]. In addition, it was discussed that although the conventional spin echo inversion recovery technique is time-consuming and impractical to be included in clinical protocols, it is the gold standard technique for measuring T_1 relaxation times [7, 8]. It was also described that prior to myocardial MR perfusion data acquisition (from which myocardial blood flow quantification may be possible), T_1 mapping can confirm measurements of native (intrinsic) T_1 relaxation times of myocardial tissues and blood pools [12] and may therefore improve gadolinium concentration measurements (through equation 2-16) for myocardial blood flow quantification.

Before applying MOLLI in a healthy volunteer and patient cohort, it was important to validate its accuracy versus the conventional spin echo inversion recovery technique. For this purpose, an experiment was designed and performed using 9 pre-existing phantoms with different gadolinium concentrations. The gadolinium concentration of individual phantoms increases, starting from the lowest concentration in phantom 1 up to the highest concentration in phantom 9 (see Table 4-1).

All phantoms were imaged using spin echo inversion recovery and MOLLI techniques. For spin echo inversion recovery and MOLLI imaging techniques and for all 9 phantoms, 6 and 11 images (Figure 4-1) were generated respectively, each of which corresponded to a different inversion time, as described in chapter 2. The inversion times for the spin echo inversion recovery experiment were (TI=50, 200, 800, 1200, 2000, 3500 ms) and for the MOLLI experiment were (TI=105, 185, 265, 1121, 1185, 1265, 2121, 2201, 2265, 3281 and 4281 ms).

The overall acquisition time was approximately 51 minutes and 16 seconds for the spin echo inversion recovery and MOLLI experiments, respectively. For spin echo inversion recovery the acquisition parameters were repetition time/ echo time 4000 ms/30 ms, flip angle 90^o, slice thickness 5 mm, matrix size 256 x 256 and FoV 200 mm x 200 mm, number of phase encoding steps 128. For MOLLI, the acquisition parameters were repetition time (between successive α pulses)/ echo time 2.50 ms/1.09 ms, flip angle 35^o, slice thickness 5 mm, matrix size 102 x 128 and FoV 159 mm x 200 mm, number of phase encoding steps 102. The MOLLI experiment was performed using non-ECG gated acquisition (ECG gating was disconnected) therefore, MOLLI dependence on heart rate differences was not investigated.

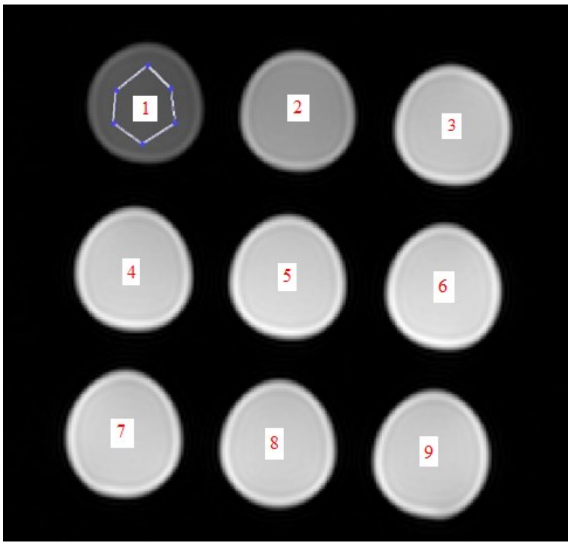

Figure 4-1) Example image of all 9 phantoms acquired using MOLLI and TI=2121 ms, visualised using MATLAB. From phantoms 1 to 9, the gadolinium concentration was gradually increased (see Table 4-1). A region of interested is shown in phantom 1, from which the signal intensity was extracted.

Matlab codes were created to draw regions of interest and extract signal intensity values for each phantom. Signal intensity values were extracted from each phantom across all images (each image generated using a different inversion time) for both experiments. Signal intensity is proportional to longitudinal magnetization recovery (see Figure 2-8), for a given inversion time. By extracting signal intensities from each phantom across all images, it was possible to generate signal intensity versus inversion time curves (for each phantom).

Matlab codes were developed to perform optimal fitting and quantification of T_1 relaxation times. To calculate the T_1 relaxation time of each phantom, model equations (2-17) and (2-18) were fitted to spin echo inversion recovery- and MOLLI-derived signal intensity versus inversion time curves, respectively. Two-parameter ((M_0, T_1), see equation 2-17) and three-parameter ((A, B, T_1^*), see equation 2-18) nonlinear curve fitting was used to calculate T_1 relaxation times from spin echo inversion recovery- and MOLLI-derived signal intensity versus inversion time curves, respectively. In the MOLLI experiment, T_1 can be calculated from A, B and T_1^* using equation (2-19). Unlike in the spin echo inversion recovery case, in the MOLLI sequence the inversion pulses are imperfect and therefore, λ is not considered to be equal to 1 (the mathematical derivation is analytically explained in the Appendix 1).

There was an excellent agreement between spin echo inversion recovery- and MOLLI-derived T_1 relaxation times. Linear regression analysis (Figure 4-2) indicated significantly strong correlation between T_1 relaxation times derived using the two different experimental processes (R^2~1). Values are summarised in Table 4-1. Example images of model fitting in signal intensity versus inversion time curves generated using spin echo inversion recovery (Figure 4-3) and MOLLI (Figure 4-4) techniques are presented. All modelling curves reached an optimum fit (r^2>0.99).

Table 4-1) Table with T_1 relaxation times for all 9 phantoms, calculated using spin echo inversion recovery (SEIR) and MOLLI experiments. Gd: Gadolinium.

Gd concentrations and T1 relaxation times (ms) of phantoms			
Phantoms	Gd concentrations (mM)	SEIR experiment	MOLLI experiment
1	0.07	1669	1699
2	0.09	1481	1511
3	0.10	1298	1320
4	0.13	1114	1154
5	0.16	950	990
6	0.21	775	803
7	0.35	499	520
8	0.67	278	293
9	1.35	143	139

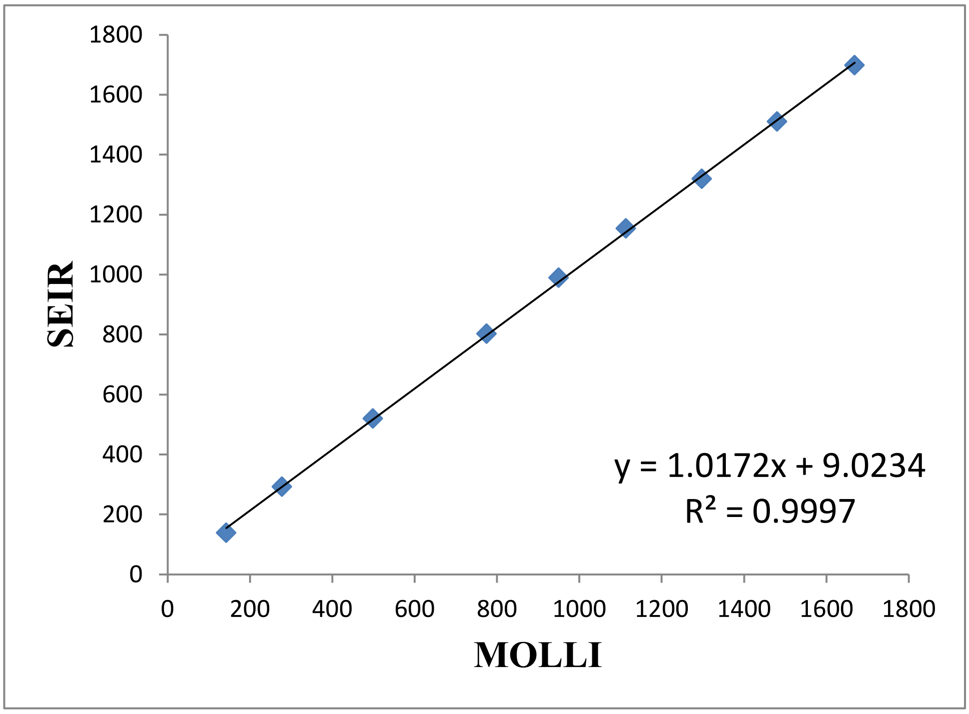

Figure 4-2) Linear regression analysis of T_1 relaxation times calculated using spin echo inversion recovery (SEIR) and MOLLI techniques.

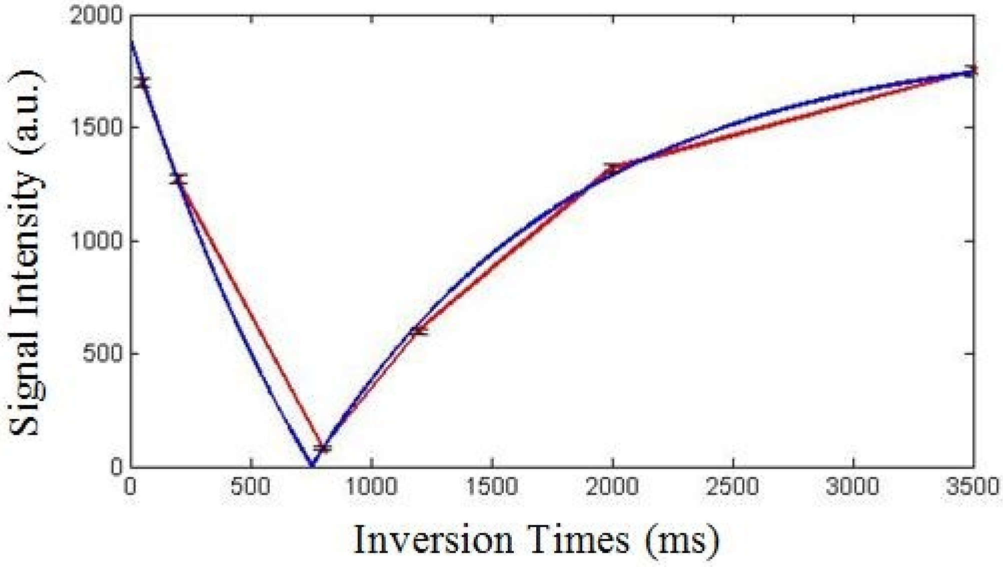

Figure 4-3) Spin echo inversion recovery experiment. Red curve: experimental curve for phantom 5 showing signal intensities (with standard deviations) versus inversion times. Blue curve: Model (equation 2-17) fit from which M_0 and T_1 relaxation time were calculated.

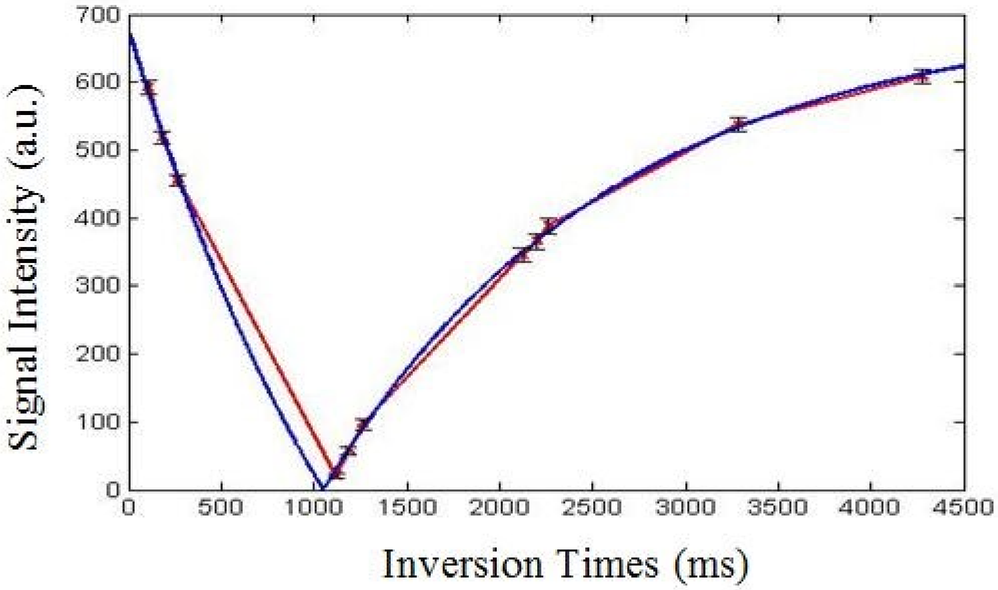

Figure 4-4) MOLLI experiment. Red curve: experimental curve for phantom 5 showing signal intensities (with standard deviations) versus inversion times. Blue curve: Model (equation 2-18) fit from which A, B, T_1^* and T_1 relaxation time were calculated.

The accuracy of the MOLLI technique has been validated versus conventional spin echo inversion recovery experiments in phantoms [123]. MOLLI application was used in all subjects in subsequent volunteer and patient data presented in this thesis before the implementation of perfusion imaging, to measure native T_1 relaxation time in the absence of contrast enhancement. Native T_1 relaxation time of the myocardium and blood pool is needed to mathematically convert signal intensity curves into gadolinium concentration curves, which is a necessary step towards absolute myocardial blood flow quantification and will be further discussed later in this chapter.

4.2 MR Image acquisition

Two of the major challenges in cardiac MR imaging are the elimination of a) cardiac and b) respiratory motion artifacts, which are created due to cardiac (cardiac cycle) and lung (respiratory cycle) motion, respectively. Cardiac motion artifacts are controlled by synchronizing imaging to the subject's electrocardiogram (ECG). Using ECG-gating, image acquisition can be performed at the same point in the cardiac cycle, commonly during the diastolic phase because cardiac motion is reducing compared to the systolic phase.

The ECG QRS complex is the central and most obvious part of ECG tracing and corresponds to the depolarization of the left and right ventricles of the human heart. The components of the QRS signal are identified in each of the three standard limb leads (i.e. electrodes) shown in Figure 4-5. To efficiently perform ECG-gated MR imaging, the ECG electrodes are placed relatively close together to minimize the differential voltage being induced in the ECG leads from the magnetohydrodynamic effect, gradients and RF pulses, which can contaminate the ECG signal. For the implementation of ECG-gating MRI, the R wave of the ECG signal is used as a reference point and data acquisition is initiated following a given delay after the R wave [7, 8].

Breath-held acquisitions help to reduce respiratory motion artifacts. Most commonly, respiratory motion may create structured image artefacts (commonly referred to as ghosts) in the phase encoding direction [43]. Breath-held acquisition is a standard approach for dynamic MR perfusion imaging in which, patients are asked to hold their breaths during image acquisition (provided that the length of breath-hold is compatible with the patient's clinical state) [29, 53, 67].

All subjects provided written informed consent before MR imaging. Further details about the study population, exclusion criteria and ethical approval for MR imaging will be presented in chapter 5 and 7. Before patients entered the MR scanner room for imaging, 12-lead ECG electrodes were placed on subjects to confirm suitability for cardiac stressing. These electrodes were then removed and the patient moved to the scanner room. MRI-compatible ECG electrodes were then applied which were used for MRI-gating. Subjects were prepared and cannulated in the right and left arm by radiographers for intravenous injections of contrast agent (gadolinium-based, Gadovist, Bayer Healthcare) and vasodilator agent (adenosine, Adenoscan, Sanofi Aventis), respectively. For reliable and reproducible intravenous injection of contrast, an automated infusion pump was used (Medrad Spectris Solaris, Medrad, Indianola, USA) and contrast agent was injected followed by 20 ml of saline flush, both at a rate of 4ml/s (see more details about the contrast agent dosages and adenosine infusion protocol in chapter 5).

A 3T Verio system (Siemens AG, Healthcare Sector, Erlangen, Germany) was used. Subjects were positioned supine with a 32-channel (phased array) cardiac coil placed over the chest (with a 16-element anterior section and a 16-element posterior element section, Siemens AG, Healthcare Sector, Erlangen, Germany). A schematic configuration of the MR system is shown in Figure 4-6.

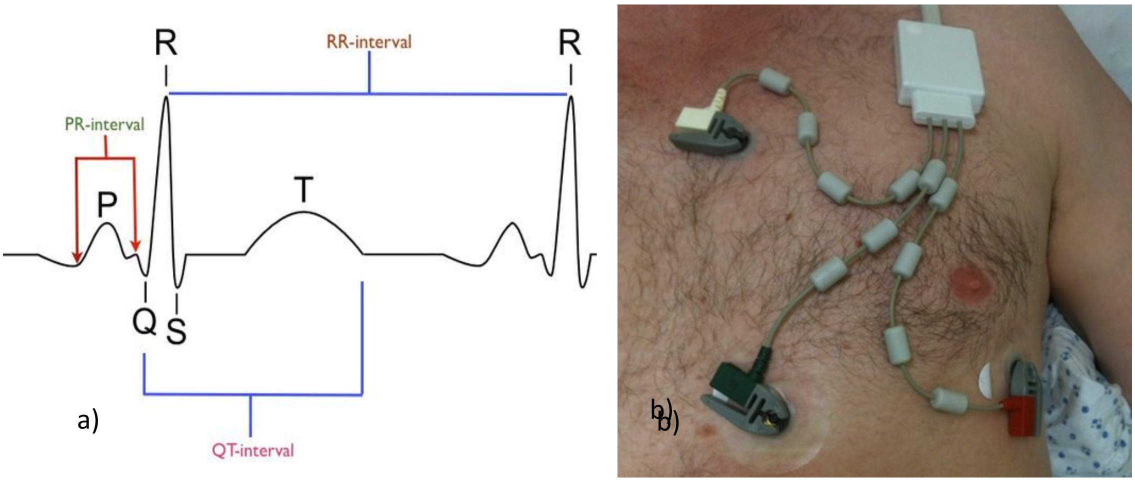

Figure 4-5) a) A typical ECG signal showing a P wave, a QRS complex and a T wave. b) MRI-compatible ECG electrodes used for MRI-gating.

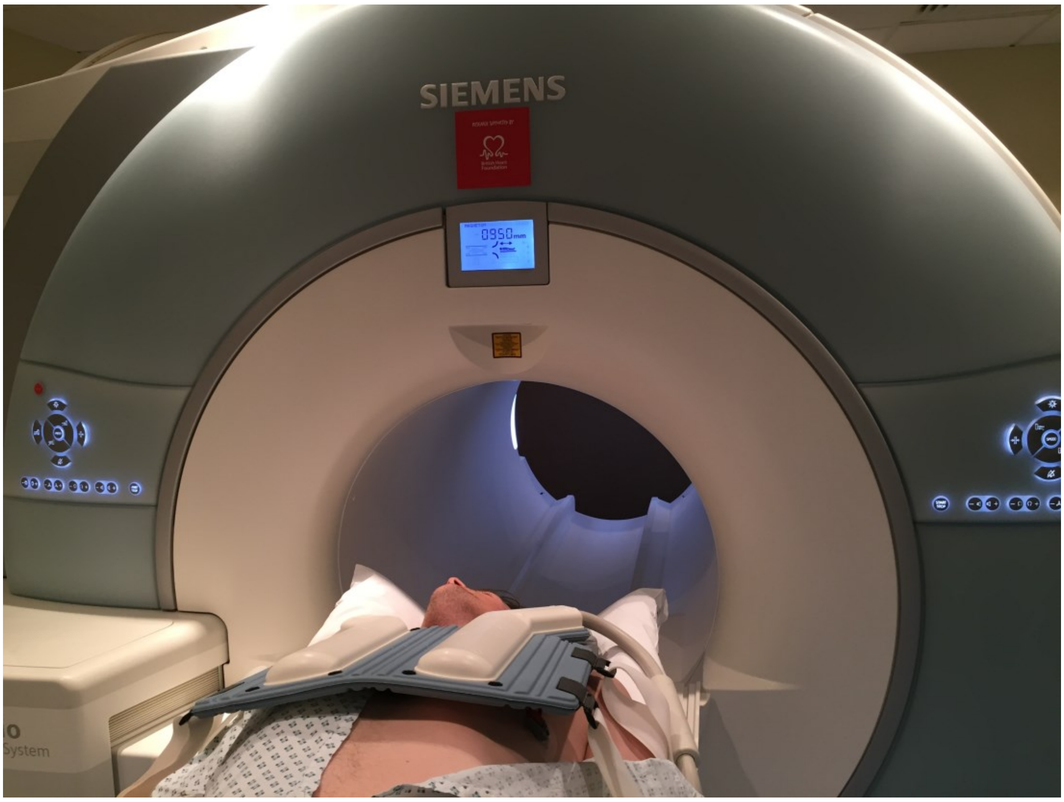
SIEMENS
095.0mm

Figure 4-6) Configuration of the 3T MR system and the 32-channel (phased array) cardiac coil placed over the chest.

Before the application of perfusion imaging, standard pilot images and cardiac views were achieved using breath-held acquisitions. Pilot images were obtained in sagittal, coronal and axial views by turboflash sequences (0.14 seconds / image). Sixteen slices on the axial plane were obtained by using Half Fourier Acquisition Single shot Turbo spin Echo (HASTE) sequences. True Fast Imaging with Steady State Precession (TrueFISP) sequence was then performed, using a mixture of T1 and T2 weighted imaging. TrueFISP technique provided two-, four-chamber and short axis cardiac view images (see Figure 4-7) with optimum contrast to noise ratio (repetition time (between successive α pulses): 3.00 ms, echo time: 1.51 ms, voxel size or in plane resolution: 1.8 mm x 1.3 mm x 6 mm and slice thickness: 6 mm). TrueFISP sequences can give high spatial resolution images with optimum contrast between soft tissues [124, 125]. During TrueFisp acquisition, ECG gating was used to acquire 25 short axis view images (known as cine-images) per heartbeat, across 7 heartbeats. On average, 175 cardiac views were acquired with high temporal resolution (of about 30 ms) across different slices of the heart.

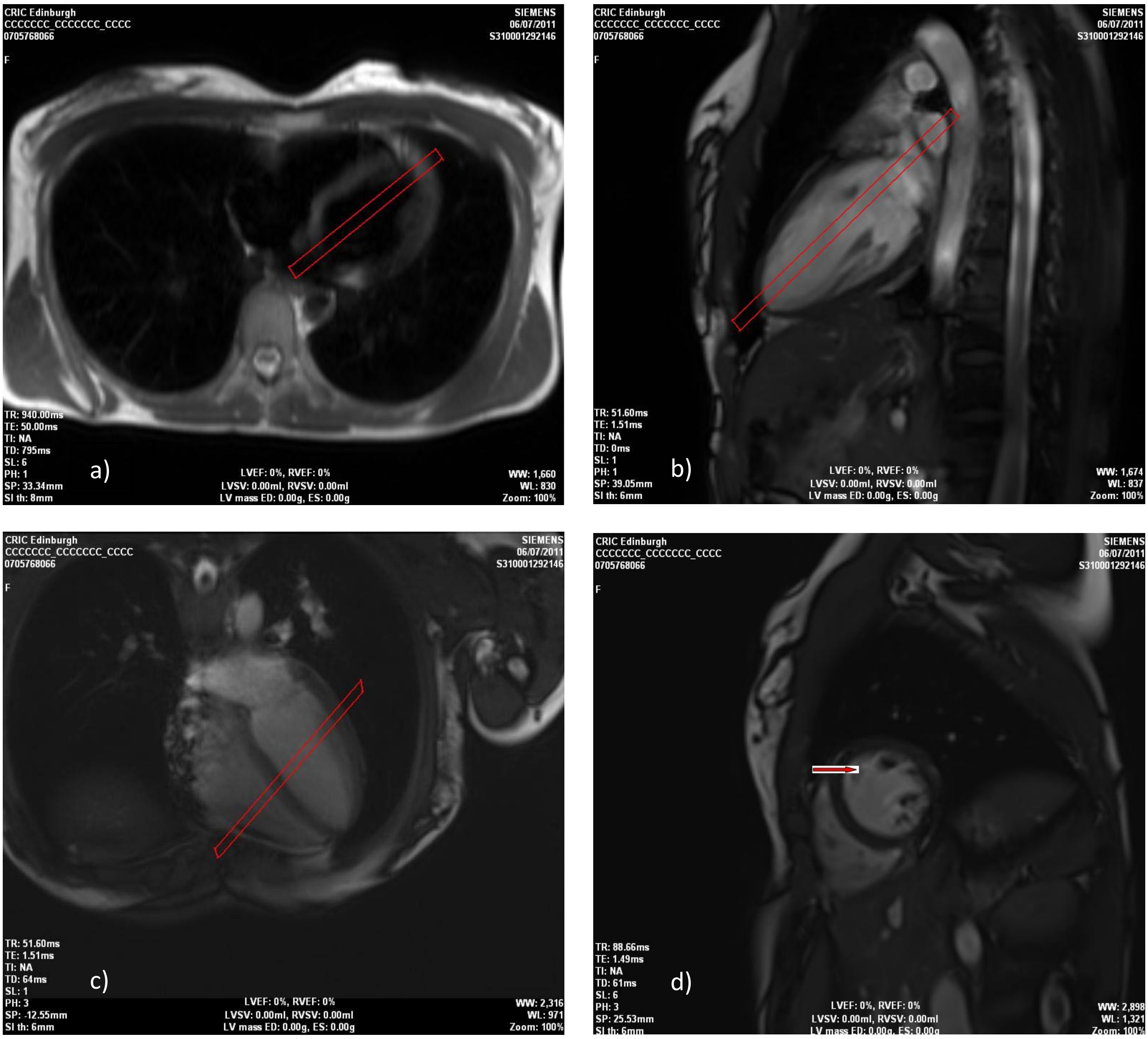
CRIC Edinburgh
CCCCCCC_CCCCCCC_CCCC
0705768066
SIEMENS
06/07/2011
S310001292146
F
TR: 940.00ms
TE: 50.00ms
TI: NA
TD: 795ms
SL: 6
PH: 1
SP: 33.34mm
Sl th: 8mm
a)
LVEF: 0%, RVEF: 0%
LVSV: 0.00ml, RVSV: 0.00ml
LV mass ED: 0.00g, ES: 0.00g
WW: 1,660
WL: 830
Zoom: 100%
TR: 51.60ms
TE: 1.51ms
TI: NA
TD: 0ms
SL: 1
PH: 1
SP: 39.05mm
Sl th: 6mm
b)
WW: 1,674
WL: 837
Zoom: 100%
TR: 51.60ms
TE: 1.51ms
TI: NA
TD: 64ms
SL: 1
PH: 3
SP: -12.55mm
Sl th: 6mm
c)
WW: 2,316
WL: 971
Zoom: 100%
TR: 88.66ms
TE: 1.49ms
TI: NA
TD: 61ms
SL: 6
PH: 3
SP: 25.53mm
Sl th: 6mm
d)
WW: 2,898
WL: 1,321
Zoom: 100%

Figure 4-7) a) HASTE images (on the axial plane). Along the long axis of the heart, it was possible to select the exact position for two-chamber view imaging, with the use of the MR system software. b) Two-chamber cardiac views were acquired (TrueFISP technique). The exact position for the acquisition of four-chamber views could be again selected through the MR system software. c) Four-chamber views were acquired (TrueFISP). It was then possible to choose the exact height at which the short axis views would be acquired. d) Short axis view scan, the images had optimum spatial resolution and the anatomy of the heart could be clearly visualised (e.g. papillary muscles inside the left ventricle which is located at the right part of the image-red arrow).

Native (intrinsic) T_1 relaxation time of myocardial tissues and blood pools were measured in the absence of contrast agent enhancement, using a MOLLI protocol (Siemens AG, Healthcare Sector, Erlangen, Germany). MOLLI was performed before myocardial perfusion imaging.

Prior to perfusion imaging, administration of adenosine was started. Subjects were checked for symptoms and changes in blood pressure by a qualified cardiology registrar. At the 3rd minute of adenosine injection, subjects were considered to have reached maximal vasodilation. Contrast agent was then administered and stress perfusion imaging was initiated using a FLASH technique in combination with parallel imaging (GRAPPA with accelerator factor of $R = 3$) [126, 127]. Parallel imaging is a robust method for accelerating MR data acquisition. The basic concept of parallel imaging is that it works by acquiring a reduced amount of k-space data and requires the use of multi-channel (phased array) receiver coils. Parallel imaging works by combining spatial information from each element of the (phased array) receiver coil. This can possibly result in image aliasing which can be avoided by using post-processing techniques and by considering the contribution of local sensitivities of each element in the phased array coil [128]. The same procedure but without adenosine injection was repeated for rest perfusion imaging. Rest imaging was performed 15 min after the adenosine-stress scan, to allow clearance of residual contrast agent. Pulse sequence details for the FLASH sequence will be described in chapter 5.

During the application of the perfusion sequence, four ECG-gated images were acquired at each RR interval: three short axis views across three mid-ventricular slices of the heart (from basis to the apex) and one long axis view. All cardiac views were selected based on the 16-segment American Heart Association (AHA) model [16]. Figure 4-8 shows the position of all four perfusion imaging views. According to the AHA model, the myocardium in the left ventricle can be divided into 16 segments. Each of these myocardial segments is assigned to one of the three main epicardial artery territories.

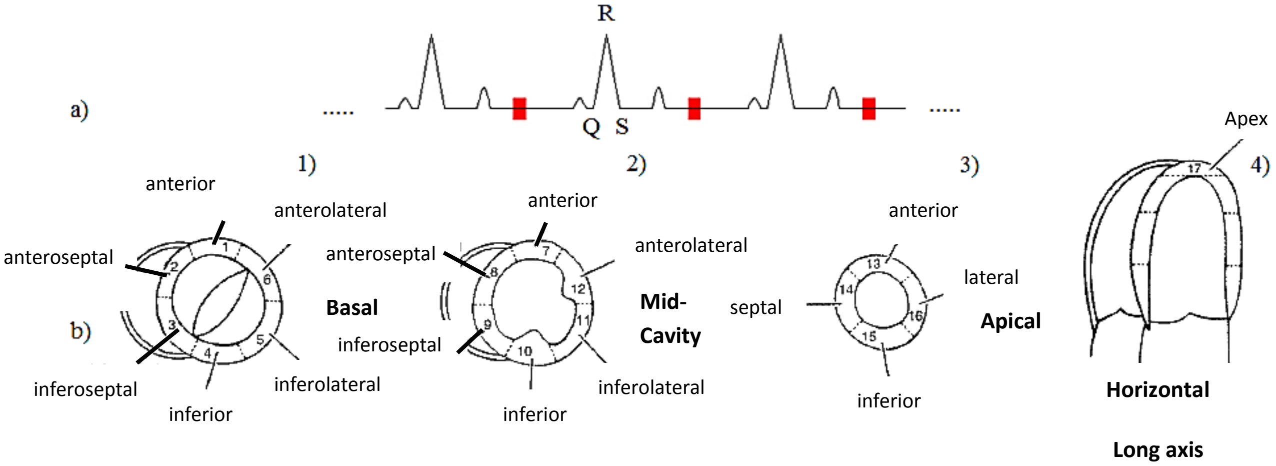
R
a)
.....
Q S
.....
Apex
1)
2)
3)
4)
anterior
anterolateral
anteroseptal
b)
inferoseptal
inferior
inferolateral
1
2
3
4
5
6
anterior
anteroseptal
Basal
inferoseptal
7
8
9
10
11
12
anterolateral
Mid-
Cavity
inferolateral
inferior
anterior
septal
lateral
Apical
inferior
13
14
15
16
17
Horizontal
Long axis

Figure 4-8) ECG-gating for dynamic perfusion acquisition. a) Using a specific time delay after the R peak (illustrated with the red box), b) three short axis views (from base to the apex of the left ventricle) and one long axis view could be acquired at diastole. Dynamic acquisition was possible during a breath-hold (to minimize respiratory motion artifacts) for 50 time points (i.e. sequential RR intervals), to track the delivery of the contrast agent through the cardiac chambers (adapted from Cerqueira et al, 2002).

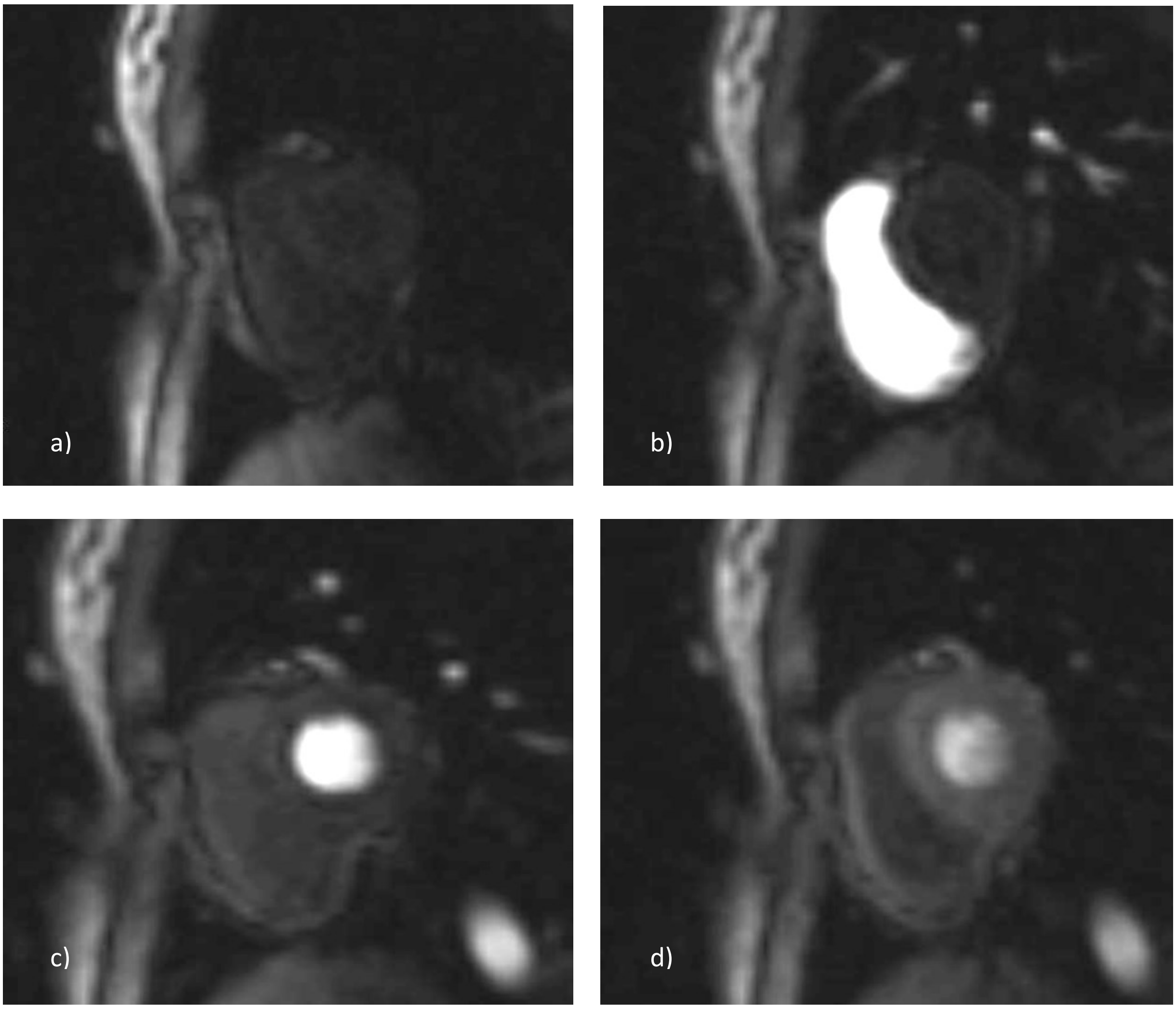

Figure 4-9) Four short axis view perfusion images are shown in different phases of contrast enhancement. a) Baseline (also known as pre-contrast) images before contrast arrive into the right atrium and ventricle. b) Contrast bolus arrival in the right ventricle. c) Contrast bolus passes into the lungs (through the pulmonary circulation) and then contrast enhancement in the left ventricle can be observed. d) Contrast bolus is passing from the left ventricle into the myocardium through the coronary arteries. Contrast enhancement in the myocardium is shown.

In the framework of developing a robust protocol for myocardial blood flow quantification in Clinical Research Imaging Centre of the University of Edinburgh, the author led development of a dual bolus perfusion imaging protocol. The above described MR sequences have been implemented using both conventional single and dual bolus imaging. Single bolus imaging involves two contrast agent injections (one at stress and one at rest), whilst dual bolus involves four. In dual bolus imaging, an additional pre-bolus infusion was administered both at stress and rest, to allow dual bolus blood flow quantification to be applied without the risk of signal saturation in the arterial input function. Further details about dual bolus imaging and whether it can determine the accuracy of blood flow quantifications are described in chapter 5.

4.3 Cardiac contouring and segmentation

ECG-gating and breath-held acquisitions (in TrueFisp images-Figure 4-7, perfusion imaging-Figure 4-9, MOLLI-Figure 4-10) aim to eliminate motion artifacts in MR images. However, MR images often need to be corrected for remaining artifacts due to cardiac and/ or respiratory motion. This can typically be the case in longer breath-hold acquisitions such as in MR perfusion imaging that can take commonly up to 45-60 seconds, and can therefore be subject to motion artifacts due to changes in ECG (causing blurring artefacts) and/or respiratory motion (causing more structured ghosting artefacts). These artifacts can commonly lead to contamination of myocardial tissue areas (see Figure 4-11) [129] which in turn may affect myocardial blood flow quantification [29].

In some perfusion images, a dark rim artifact can be observed during gadolinium enhancement (Figure 4-11). This dark rim artifact it is believed to be either due to susceptibility effects (derived from rapid changes in the magnetic field during gadolinium enhancement), or motion, or limited spatial resolution, or a combination of these [130].

In a previous study, it has been demonstrated that the application of post-processing algorithms for automatic image registration, can facilitate myocardial contouring and segmentation (by reducing motion artifacts) and can improve the accuracy of myocardial blood flow quantification [131]. Image registration involves transformation of images or sets of images into one coordinate system. A reference image is chosen and the other images are spatially registered to align with the reference image, using different post-processing techniques. The benefit of image registration in myocardial perfusion imaging data is that it may further allow application of automatic or semi-automatic approaches for myocardial contouring and segmentation. Although few software applications have been designed and provided with free access, cardiac perfusion protocols currently lack a validated post-processing tool for automatic image registration. For this reason, the author performed manual contouring to correct motion artifacts created due to cardiac displacements between sequential perfusion images.

For this thesis, the first post-processing step was to manually draw myocardial regions of interest (which will be used for myocardial blood flow analysis later). For this purpose, a dedicated commercial software package has been used (QMass, Medis, The Netherlands). With this software tool, it is possible to visualize MR images and manually draw endocardial and epicardial contours in T_1 maps (i.e. image providing tissue T_1 relaxation time values calculated using MOLLI, Figure 4-

10) and perfusion images. This software tool provides the opportunity to segment the myocardium of the left ventricle according to the 16-segment AHA model [16].

The main disadvantage of manual segmentation is that it can be time-consuming. The duration for manual contouring and segmentation of a full perfusion data set can be between 45 min-1.5 hours, depending on the quality of the data (i.e. whether they have been contaminated by cardiac, respiratory motion and dark rim artifacts) and the experience of the user. The alternative to manual contouring can be automatic contouring. However, at the time of analyzing cardiac MR results and writing this thesis, there was no software available to the author that could provide reliable automatic contouring.

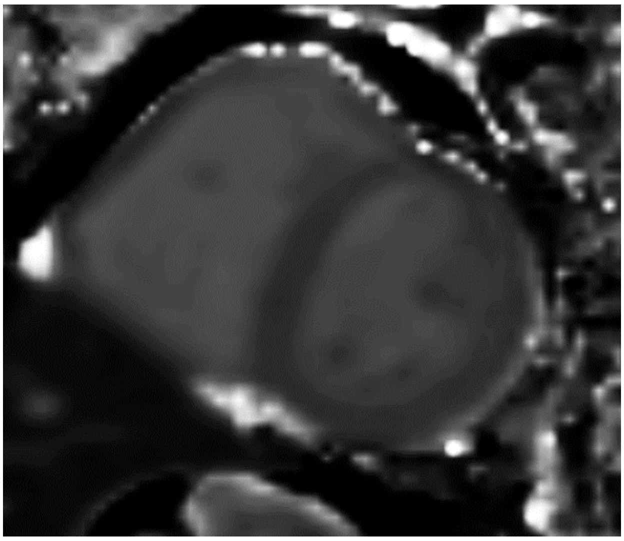

Figure 4-10) Short axis view T1 map generated using MOLLI. Signal intensity in each pixel corresponds to a tissue T_1 relaxation time.

Biglands et al, have demonstrated that conservative contour drawing (both endocardial and epicardial contours remaining in the myocardium), can result in more accurate myocardial blood flow values using Fermi modelling, than when generous contouring was used [29]. Conservative contouring was applied to exclude cardiac, respiratory motion and dark rim artifacts (Figure 4-11). Following this criterion, manual contouring and segmentation in QMass can be summarized in the following three steps: a) initially, endocardial and epicardial conservative contouring in T_1 maps and in all dynamic images across all three short axis view slices of perfusion data sets were drawn. b) An image was chosen to set the starting point in the conjunction of left and right ventricles and myocardial segmentation (16 segments across three slices [16]) can then be automatically adjusted by the software across all images of the same slice and c) save myocardial contours and segments (in a txt file).

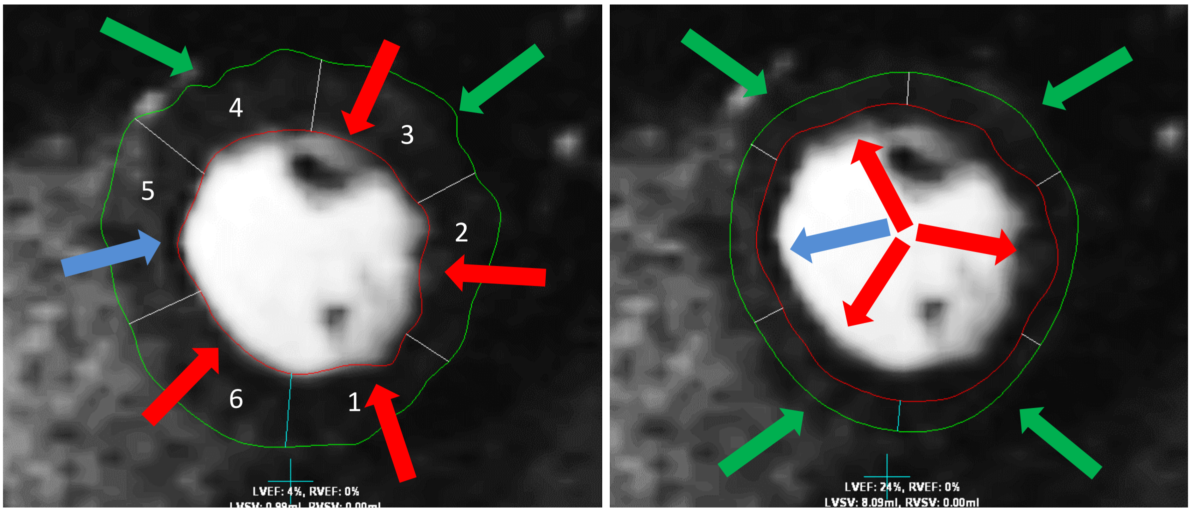

Figure 4-11) Endocardial (red) and epicardial (green) contours are presented in a perfusion image of a healthy volunteer during peak contrast enhancement. The blue cross indicates the starting point from which myocardial segmentation can be adjusted. Basal and mid-ventricular slices of the myocardium were automatically divided into 6 equal segments (apical slice was divided in 4 equal segments). a) Generous contouring: myocardial areas are exposed to contamination from blood pool signal (red arrows), dark rim artifacts (blue arrow) and contamination from the surrounding tissues (green arrows). b) Conservative contouring was performed to avoid contamination of myocardial areas from the left ventricle blood pool signal (red arrows), dark rim artifacts (blue arrow) and contamination from the surrounding tissues (green arrows). Contrast in the images has been adjusted to highlight artifacts which are not always distinctive but can affect quantification [131].

4.4 Development and validation of Matlab software

The second post-processing step was to extract the average signal intensity per myocardial segment. Although it is possible to extract signal intensity values for each myocardial segment across all perfusion images and T_1 maps using QMass software, it was necessary to develop a method for extracting accurate signal intensity values in Matlab whose operation could be controlled and validated. This involved replicating the QMass-selected cardiac contours and segmentation in Matlab. Through this programming process the author had the opportunity a) to be trained in Matlab environment, which is a necessary tool for post-processing biomedical data and b) to develop customised in-house software with which all the operations and calculations could be validated and checked. This process is based on the method described first by von Land et al [132], detailed in the thesis of van der Geest [133] and it is summarized in basic steps (see Appendix 4).

The accuracy of the aforementioned Matlab method for replicating myocardial contouring and segmentation was validated using perfusion data at stress from 4 healthy volunteers that have been previously scanned at the Clinical Research Imaging Center of the University of Edinburgh. The gadolinium dose used for perfusion imaging in these 4 healthy subjects was 0.025 mmol/kg.

Signal intensities per myocardial segment across two short axis view slices were extracted using both QMass and Matlab. A paired t-test showed no difference between dynamic signal intensity curves extracted using Matlab against dynamic signal intensity curves extracted using QMass, in a per myocardial segment comparison (for all myocardial segments P<0.00001). A characteristic example image is shown in Figure 4-12.

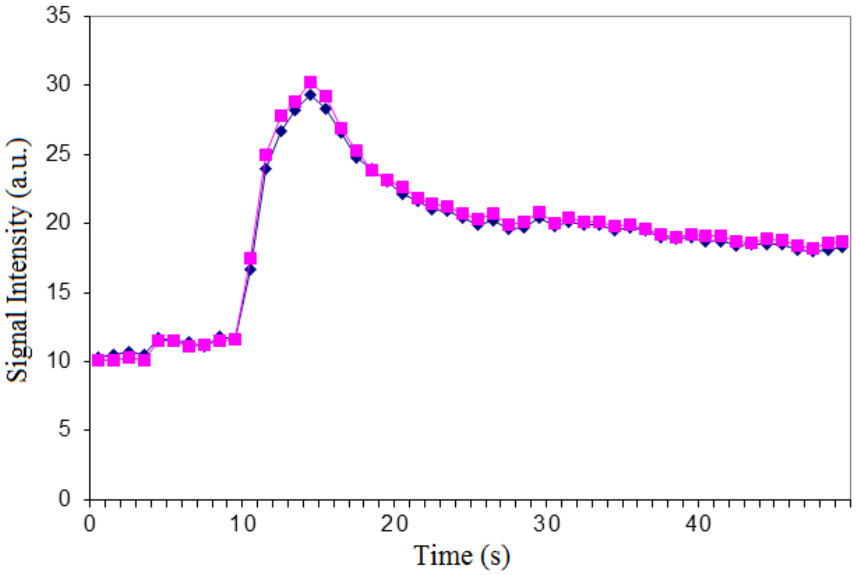

Figure 4-12) Dynamic signal intensity curves across all 50 time points for the same myocardial segment. Signal intensity values extracted using Matlab (magenta line) and signal intensity values extracted using QMass (blue line) are illustrated. A paired t-test showed no difference between myocardial segments for all 4 healthy volunteers.

4.5 Validation of saturation recovery FLASH equation

Using Qmass and Matlab post-processing, one signal intensity curve was extracted per myocardial segment across all dynamic perfusion images. For each subject, 50 dynamic perfusion images were acquired across three mid-ventricular short axis view slices both at stress and at rest and were used for myocardial blood flow analysis. As described in chapter 3, a necessary step prior to myocardial blood flow quantification is to convert signal intensity curves (i.e. one curve corresponds to a specific myocardial segment) into contrast agent concentration curves (equations 2-16 and 3-1).

Having calculated native (tissue) T_1 relaxation time with the MOLLI technique and using a literature value for gadolinium relaxivity at 3T (r_1=4.5 L · mmol^{-1} · s^{-1}) [10], the only unknown term in equation 2-16 is the tissue T_1 relaxation time during contrast enhancement. As described, for the saturation recovery prepared single-shot gradient echo pulse sequence, the signal intensity and R_1 are related using equation 3-1 [25]:

$$SI = \Psi \cdot \left[\left(1 - e^{-PD \cdot R_1}\right) \cdot a^{n-1} + b \cdot \frac{1 - a^{n-1}}{1 - a} \right]$$

All terms in equation 3-1 have been previously explained in chapter 3. The pre-pulse delay (PD in equation 3-1) used for perfusion imaging was 100 ms. PD is the time between the saturation pulse and the central line of k-space. Figure 4-13 shows magnetisation recovery (following the application of a saturation pulse) interrupted by consecutive flip angles represented here as α_1, α_2, $\alpha_3 ... \alpha_n$. Using a FLASH perfusion sequence, each α (flip angle) pulse fills a line in k-space in the phase encoding direction.

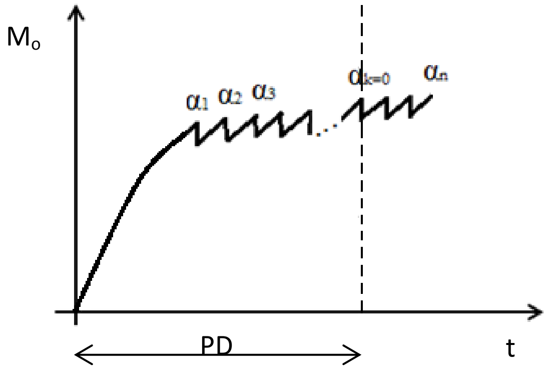

Figure 4-13) FLASH saturation recovery prepared single-shot gradient echo pulse sequence. Consecutive α pulses, PD and $\alpha_{k=0}$ are shown (note: for centric phase encoding $\alpha_{k=0}=\alpha_1$). This scheme is repeated within each RR interval at each dynamic perfusion image acquisition. During an RR interval, all lines of k-space are acquired for each (dynamic) perfusion image.

Hence, $\alpha_{k=0}$ fills the center of k-space in which the low spatial frequency information is saved. The low spatial frequency information saved around the center of k-space approximates to the majority of the contrast information in the MR image. This means that for a given PD and for centric k-space ordering applied for perfusion imaging in this thesis, n=1 and equation 3-1 is simplified to:

$$SI = \Psi \cdot (1 - e^{-PD \cdot R_1}) \qquad (4\text{-}1)$$

From which Ψ can be calculated in the absence of contrast enhancement as it is the only unknown parameter.

After acquiring a MR signal, this is saved in k-space and is then mathematically processed to derive the MR image. A standard way of k-space filling is one horizontal line after the other, starting from the middle line of k-space (k_0) first and then going towards the top and the bottom of k-space. This is called centric k-space ordering. Centric profile orders are formed in such a way, so that the central line of k-space (k_0) is the first line acquired (also known as centric low-high: 0, +1,-1,+2,-2…n number of phase encoding steps).

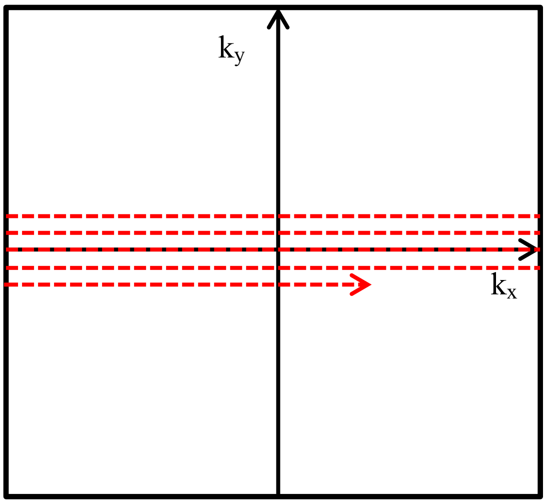

Figure 4-14) Centric k-space ordering.

To validate the accuracy of equation 4-1, an experiment was performed using the 9 phantoms that were previously presented in subsection 4.2. Perfusion imaging was implemented in all 9 phantoms. T_1 relaxation time values of individual phantoms have been calculated in subsection 4.2. Signal intensities (SI) were extracted from each phantom using Matlab (Figure 4-15, experimental value). Ψ was calculated by applying equation 4-1 and by using experimental signal intensity value and MOLLI-derived T_1 relaxation time value for phantom 1 (see Table 4-1). Subsequently, T_1

relaxation time values for each phantom (Table 4-1) were used in equation 4-1 to measure signal intensity values (Figure 4-15).

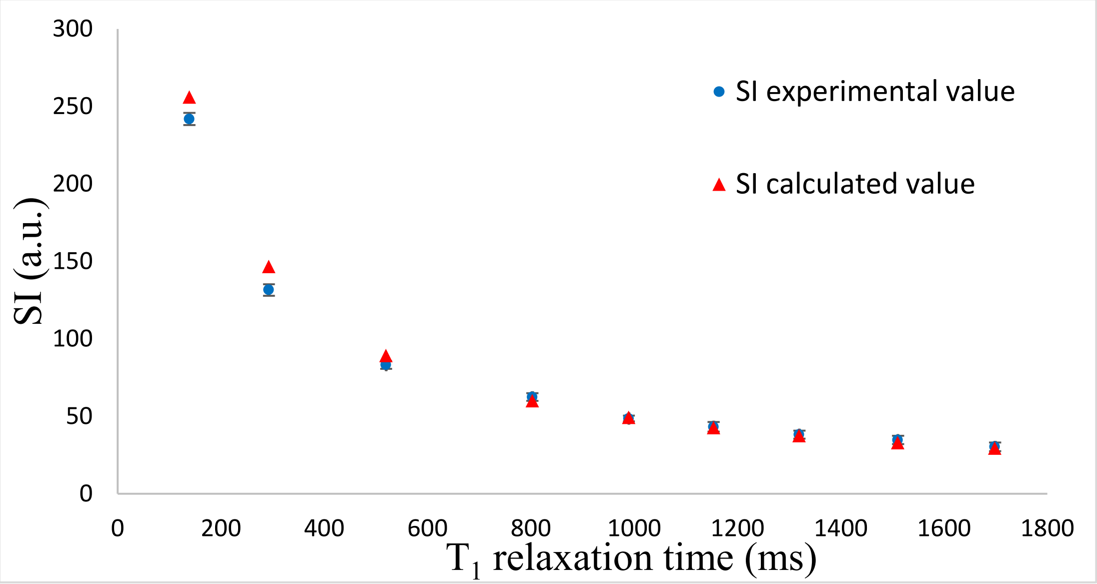

Figure 4-15) Signal intensities (SI) derived using Matlab (experimental mean values with standard deviations, blue curve) and calculated values estimated using equation 4-1 (red).

There was an excellent agreement between experimental and calculated values with linear regression analysis (Figure 4-16) showing strong correlation (R^2~1). Following the above validation, equation 4-1 was used in all subjects to calculate Ψ per myocardial segment before contrast enhancement (using known signal intensity and T_1 values). Equation 4-1 was then used to calculate T_1 relaxation times per myocardial segment during contrast enhancement. Ψ is assumed to be constant throughout myocardial perfusion image acquisition. Finally, equation 2-16 was used to measure gadolinium concentration per myocardial segment, during contrast enhancement.

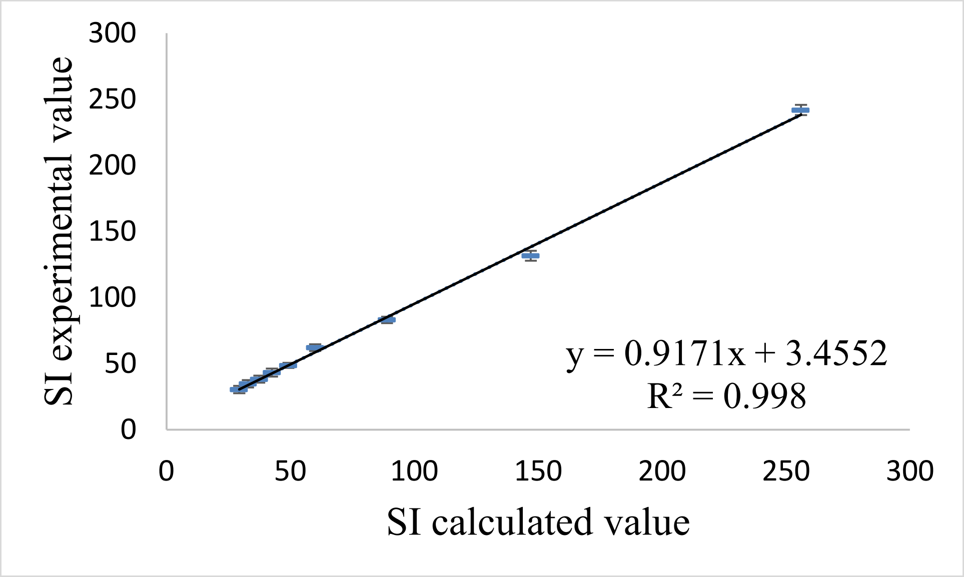

Figure 4-16) Linear regression analysis of signal intensity (SI) values are shown. Experimental SI (with standard deviations) on the y axis and calculated SI on the x axis measured using equation 4-1.

4.6 Arterial input function extraction

The signal intensity of the arterial input function was extracted by using a Matlab program from which it was possible to create a 9x9 pixel grid of a selected area within the left ventricle cavity. 81 signal intensity curves could be generated in total (1 signal intensity curve for each pixel). The pixel grid is illustrated in Figure 4-17.

In that way, it was possible to exclude areas of the left ventricle in which the signal intensity of the AIF was decreased by the presence of papillary muscles and/or endocardial walls. Furthermore, it was possible to exclude pixels with noisy baseline signal which commonly led to overestimation or underestimation of the peak of the arterial input function. An overestimated or underestimated peak could be compared against groups of pixels with similar peaks that were finally selected and averaged to a single arterial input function curve. All AIF curves were extracted from the basal slice [24, 29].

Signal intensity curves were extracted from a selected area (which is part of the 9x9 pixel grid) and are converted into gadolinium concentration curves using equations 2-16 and 4-1. A gadolinium concentration curve/per pixel was measured and an average gadolinium concentration curve was then calculated and used for myocardial blood flow analysis.

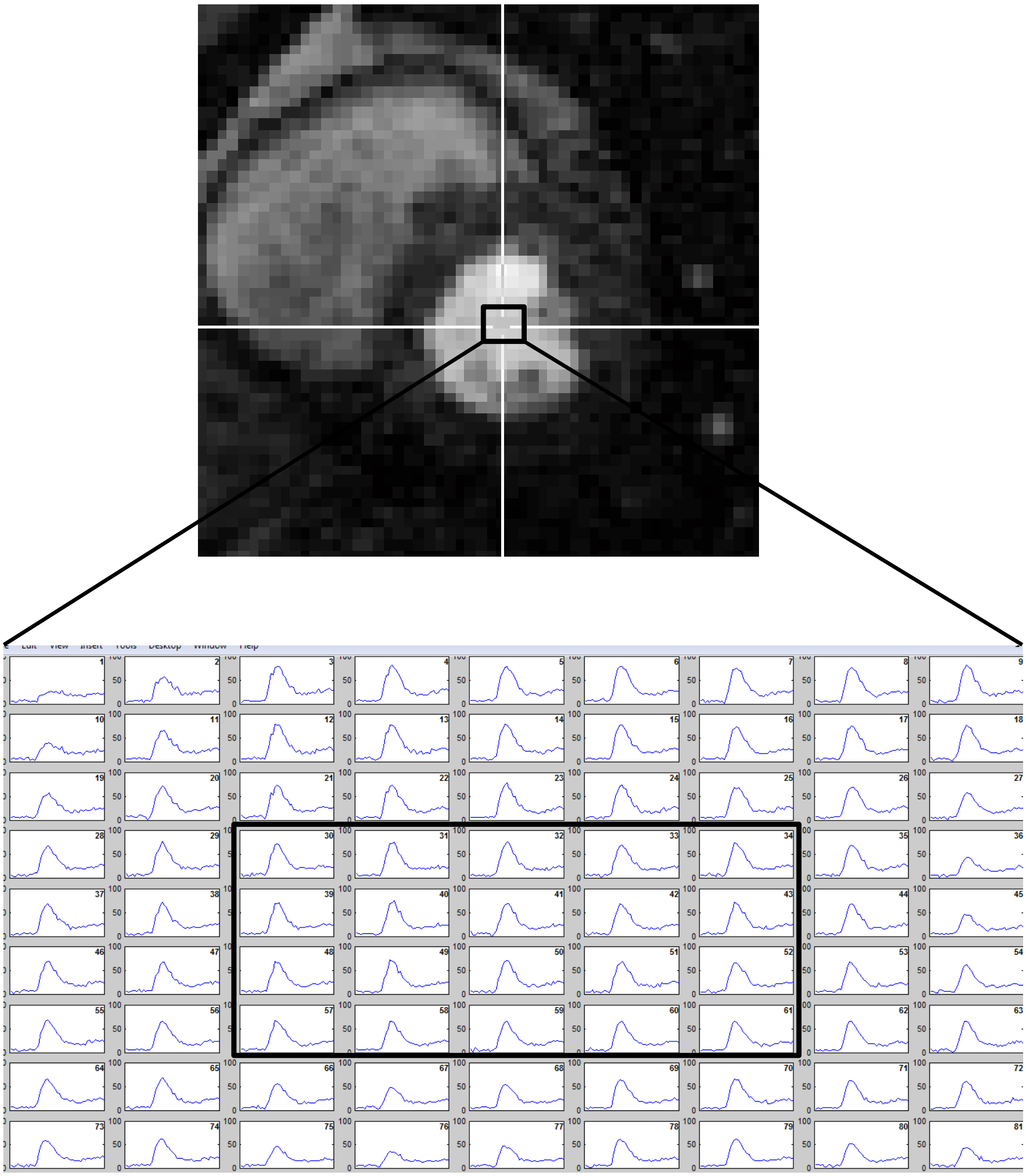
100
50
0
1
2
3
4
5
6
7
8
9
10
11
12
13
14
15
16
17
18
19
20
21
22
23
24
25
26
27
28
29
30
31
32
33
34
35
36
37
38
39
40
41
42
43
44
45
46
47
48
49
50
51
52
53
54
55
56
57
58
59
60
61
62
63
64
65
66
67
68
69
70
71
72
73
74
75
76
77
78
79
80
81

Figure 4-17) a) Left ventricle with selected area is shown from which b) a 9x9 pixel grid is extracted. Black frame surrounds all pixels from which signal intensity curves are extracted and converted into gadolinium concentration curves which are averaged and used for myocardial blood flow analysis.

4.7 Validation of conversion algorithm

In this subsection, the accuracy of equations 2-16 and 4-1 in converting signal intensity curves into gadolinium concentration curves has been validated. This validation was performed using actual peak arterial input function gadolinium concentrations as a reference standard to simulate a range of peak arterial input function gadolinium concentrations in phantoms. The basic steps for this validation process are described here.

1) Implementing the method described in subsection 4.6, arterial input function concentrations were measured from single bolus perfusion data at stress in 4 healthy volunteers (previously used for comparing QMass versus Matlab signal intensity curves). The peak gadolinium concentration value of each arterial input function was extracted. Peak values are presented in Table 4-2.

Table 4-2) Peak arterial input function concentrations for 4 healthy volunteers. AIF: Arterial input function. 1 mM=10^{-6} mol/ml.

Healthy volunteers	***Concentration at the peak of AIF (mM)***
1	2.2
2	2.0
3	5.0
4	4.0

As mentioned in the subsection 4.4, the gadolinium dose used in these 4 healthy volunteers was lower (0.025mmol/kg) compared to chapters 5 and 7, in which the gadolinium dose in healthy volunteers (0.03 mmol/kg) and patients (0.05 mmol/kg) respectively, was increased for allowing both visual and quantitative assessments. Note that the gadolinium doses were carefully adapted to be as low as possible for minimising arterial input function saturation effects at 3T, this will be further described in chapters 5 and 7.

2) 11 phantoms were prepared with known gadolinium concentrations. For phantom preparation, a commercial gadolinium solution (Gadovist, Bayer Healthcare) was used which contains 1.0 mmol/ml of gadolinium, 11 tubes of 50 ml each filled with distilled water. Each phantom simulated a different peak arterial input function concentration. For this experiment, phantoms included lower and higher gadolinium concentration values than expected actual arterial input function concentration values (Table 4-2), to examine the accuracy of the conversion algorithm in a range of gadolinium concentrations. The volumes of Gadovist solution that were used to simulate different peak arterial input function gadolinium concentrations were calculated by cross-multiplying for ml/ 50 ml tube volumes and are presented in Table 4-3.

3) T1 mapping was performed in all phantoms using spin echo inversion recovery technique.

4) Perfusion imaging was performed in all phantoms (see pulse sequence details in chapter 5).

5) Signal intensities were extracted using Matlab and T_1 quantification was performed (equation 2-17).

6) Ψ parameter was calculated using signal intensity and T_1 relaxation time values of phantom 1 in equation 4-1. T_1 relaxation times were then calculated for all phantoms using again equation 4-1. Equation 2-16 was finally used to calculate gadolinium concentration values.

Table 4-3) Range of peak arterial input function concentration simulations and corresponding volumes of Gadovist solution in ml/ 50 ml is presented.

Phantom	***Concentration at the peak (mM).***	***Volume of gadolinium (ml/50ml)***
1	0.5	$25 \cdot 10^{-3}$
2	1.0	$50 \cdot 10^{-3}$
3	1.5	$75 \cdot 10^{-3}$
4	2.0	$100 \cdot 10^{-3}$
5	2.5	$125 \cdot 10^{-3}$
6	3.0	$150 \cdot 10^{-3}$
7	4.0	$200 \cdot 10^{-3}$
8	5.0	$250 \cdot 10^{-3}$
9	6.5	$325 \cdot 10^{-3}$
10	7.5	$375 \cdot 10^{-3}$
11	10.0	$500 \cdot 10^{-3}$

Signal intensity values versus actual gadolinium concentrations in all phantoms are shown in Figure 4-18. Non-linearity is induced after phantom 4 (corresponds to a simulated peak concentration of 2 mM).

The conversion of signal intensities into gadolinium concentrations using equations 2-16 and 4-1 showed very good agreement with actual gadolinium concentration values (Figure 4-20) [26]. This conversion algorithm was accurate for phantoms 1-8 but as gadolinium concentration increases in phantoms 9-11, signal saturation becomes more pronounced and gadolinium concentration is underestimated.

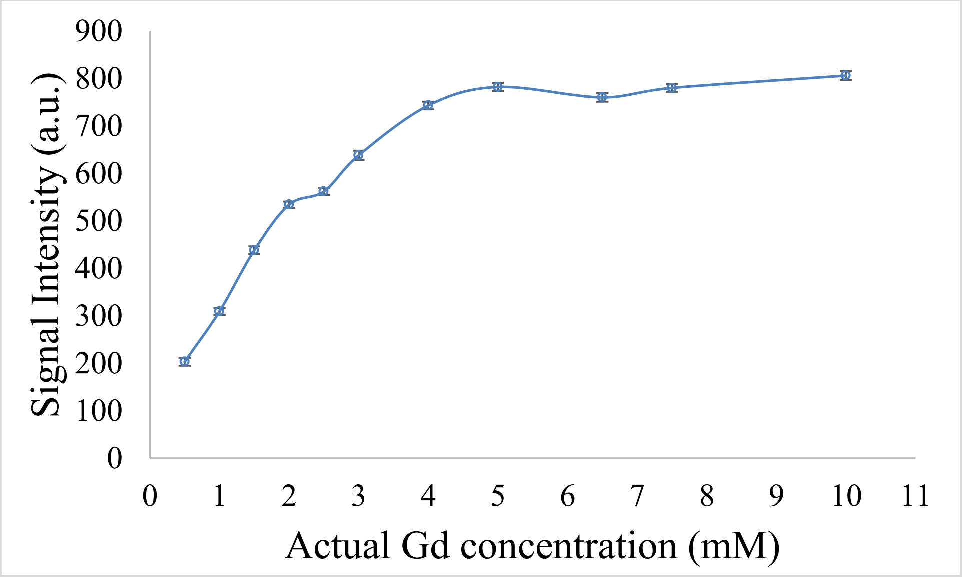

Figure 4-18) Signal intensity values (a.u.) (with standard deviations) versus actual Gd concentration (mM). Non-linearity is induced in phantoms 5-11, whilst a plateau is observed at higher concentrations (phantoms 7-11). Gd: gadolinium.

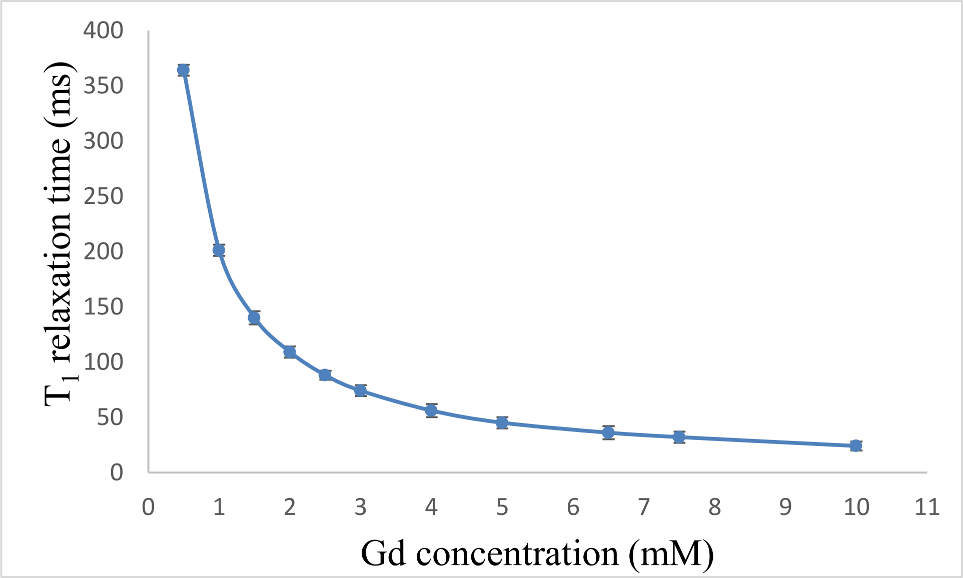

Figure 4-19) T1 relaxation times (ms) and standard deviations versus actual Gd concentrations (mM). Exponential decay of T1 relaxation time as gadolinium concentration is increasing is shown. Gd: gadolinium.

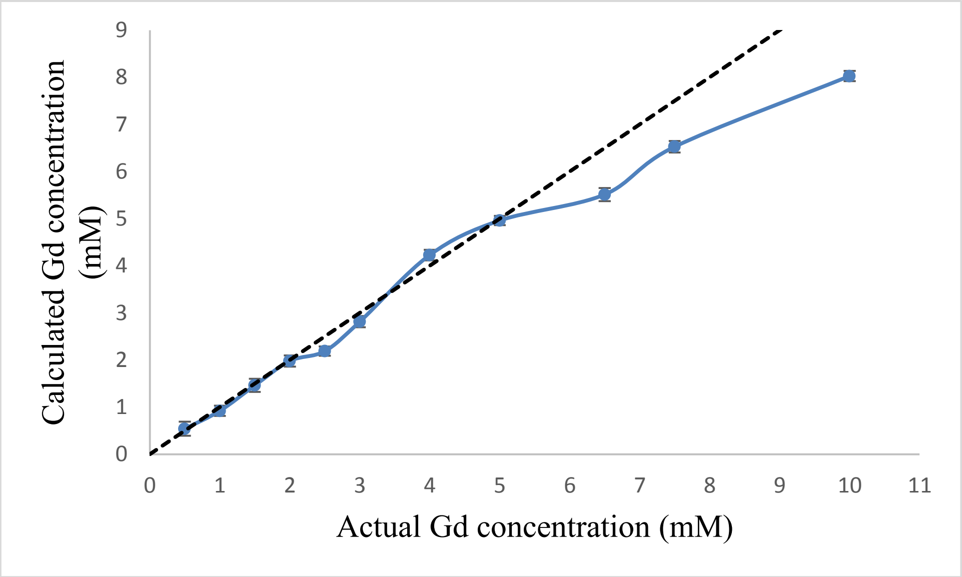

Figure 4-20) Calculated (standard deviations) versus actual Gd concentration (mM). Gd: gadolinium.

As shown in Table 4-2, for gadolinium doses equal to 0.025 mmol/kg at 3T, the peak of the arterial input function gadolinium concentration was commonly in the range of about 2.0-5.0 mM. Based on this validation experiment, the conversion algorithm can give accurate gadolinium concentration values in the range of 0.5-5.0 mM. Although the number of healthy volunteers is small, this can possibly indicate that with the use of the above gadolinium dose (in 3T), underestimation of the arterial input function gadolinium concentration can be avoided, perhaps allowing accurate myocardial blood flow measurements.

The conversion algorithm has not been validated in the range 5.0-6.5 mM and 6.5-7.5 mM. However, this validation experiment demonstrates that the conversion algorithm can underestimate gadolinium concentration for higher arterial input function peaks (e.g. phantoms 9-11), perhaps corresponding to higher gadolinium doses. In the clinical setting, higher gadolinium doses may need to be used in order to increase signal to noise ratio and visualize subtle myocardial areas and/ or myocardial infarction [24, 67]. When myocardial blood flow quantification is involved in higher gadolinium doses, a method to correct for arterial input function underestimation at the peak of contrast enhancement can be the use of dual bolus protocols.

4.8 Optimization of dual bolus protocol

As described, the dual bolus imaging technique involves the injection of an additional pre-bolus infusion. Pre-bolus is injected to allow dual bolus modelling to be applied without the risk of signal saturation in the arterial input function. This can be particularly useful when higher gadolinium-based contrast agent concentrations are involved.

For this thesis, a dual bolus protocol was optimized and implemented in healthy subjects. The two boluses were injected in a pre-determined concentration ratio (pre-bolus:main bolus, 1:5) with the pre-bolus diluted using 0.9% saline. A pair of syringes was used in the infusion pump (Medrad, Bayer, Germany), with syringe A injecting gadolinium boluses and syringe B containing 40-50 ml of 0.9% saline. After diluted pre-bolus is injected from syringe A, the tube is flushed with 20 ml of saline using syringe B. A small syringe which is connected with a three way stopcock is then used to refill the empty syringe A with the standard main gadolinium bolus. Main bolus is injected from syringe A and the tube is again flushed with 20 ml of saline using syringe B. Further details about specific contrast agent doses will be discussed in chapter 5.

After stress perfusion imaging, the pair of syringes used for pre- and main bolus injections at stress, were replaced by a new pair of syringes. The pair of syringes was replaced because otherwise, residual gadolinium from main bolus injections at stress was likely to contaminate pre-bolus injections at rest, if the same syringe would be used for both stress and rest imaging.

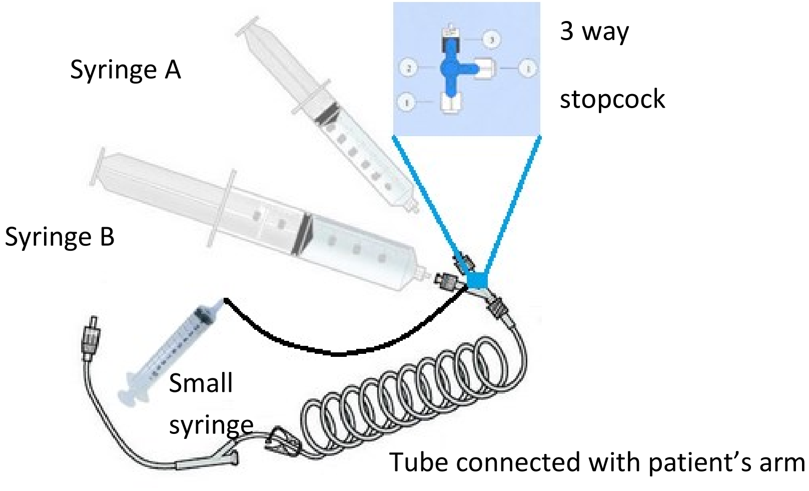
3 way
stopcock
Syringe A
Syringe B
Small
syringe
Tube connected with patient's arm

Figure 4-21) Dual bolus injection scheme.

4.9 CT image acquisition

As in MR image acquisition, written informed consent was given from all subjects before MDCT imaging. ECG was acquired and heart rate and blood pressure were checked. As mentioned, after the injection of iodine-based contrast agent bolus, the whole cardiac volume can be obtained within one cardiac cycle provided the heart rate is low enough. If the resting heart rate was > 65 beats per minute, beta blockers were administered to reduce heart rate [90]. Right and left antecubital veins were cannulated for the administration of iodinated contrast and adenosine respectively.

Patients were placed supine in a 320-slice MDCT scanner (Aquilion ONE, Toshiba Medical Systems). After acquisition of scout images, computed tomography coronary angiography and rest perfusion imaging were acquired simultaneously. Angiographic data were reconstructed at diastole (phase 60% to 70%).

20 minutes after rest imaging, adenosine infusion was initiated with continuous ECG monitoring. After 4 minutes of adenosine infusion, iodinated contrast (iomeprol, 400mg iodine/ml, Iomeron 400, Bracco, UK) was intravenously injected at a rate of 5 ml/s, followed by 30 ml of 0.9% saline. The iodinated contrast was administered based on body mass index (BMI) (i.e. <30 kg/m^2, 50 ml; >30 kg/m^2, 60 ml; >40 kg/m^2, 70 ml). The tube current and voltage were selected automatically based on the BMI and an ECG-gated snapshot image was acquired at end diastole. Real-time bolus tracking was implemented using a region of interest in the descending aorta and a fixed time delay (began 5 seconds after contrast administration was initiated). Stress MDCT perfusion imaging was acquired in the next one to two heart-beats after a threshold of 300 HU was achieved in the descending aorta [98]. Stress images were

reconstructed on the short axis at end diastole (phase 70% to 100%) according to the AHA model [16].

Figure 4-22) Patient being placed supine in Aquilion ONE CT scanner.

5. Measurement of myocardial blood flow by magnetic resonance perfusion imaging. Comparison of distributed parameter and Fermi models with single and dual bolus.

Introductory summary

This chapter describes a comparison between Fermi and distributed parameter modelling in single versus dual bolus analysis. Particularly, it assessed whether distributed parameter modelling might be less dependent on arterial input function saturation than Fermi modelling in healthy volunteers. The accuracy of each model in detecting reduced myocardial blood flow in stenotic vessels versus gold-standard invasive methods has also been examined in five patients with suspected coronary artery disease. This work has been previously published in the Journal of Cardiovascular Magnetic Resonance (Papanastasiou et al JCMR).

5.1 Background

Mathematical modelling of cardiac magnetic resonance perfusion imaging has the potential to allow quantitative assessment of myocardial blood flow [134, 135]. Establishing absolute quantification of blood flow could have clinical benefits since it may lead to an improvement in the diagnosis and prognostication of patients with coronary artery disease [24, 50, 136, 137].

Myocardial blood flow quantification using model-dependent analysis is based on fitting the convolution of a model with the arterial input function to the tissue contrast agent concentration-time curve. The model describes the passage of a contrast agent through the myocardium whilst the arterial input function is the observed contrast agent concentration-time curve derived from the blood pool. [24]. Fermi deconvolution modelling is a popular approach used to estimate myocardial blood flow during the first-pass of gadolinium-based extracellular contrast agents (CA) [24, 28, 29]. It is an empirical-mathematical model, which is convolved with the first-pass of the arterial input function [24]. The distributed parameter model assumes that the extravascular-extracellular space exchanges CA with nearby regions in the intravascular space, restricting axial transport of CA inside the extravascular-extracellular space [50]. In addition to myocardial blood flow, this model can also be used to calculate other microvascular characteristics including intravascular space, extravascular-extracellular space, permeability surface area product, extraction fraction and volume of distribution [66].

The high concentration of CA during bolus passage leads to signal saturation and causes concentration underestimation in the left ventricular cavity [69] (which is used to generate an arterial input function for model deconvolution analysis). This can degrade the accuracy and reproducibility of myocardial blood flow quantification using Fermi modelling, leading to systematic myocardial blood flow overestimation [24]. The dual bolus acquisition technique can eliminate signal saturation allowing more reliable quantification of myocardial blood flow in first-pass magnetic resonance perfusion imaging. In the dual bolus technique, an initial injection of dilute CA is used to acquire a non-saturated arterial input function before the main CA bolus. This is commonly referred to as the “pre-bolus” [30, 31]. However, compared to single bolus protocols [24, 28, 29, 66, 134, 135], dual bolus imaging protocols are characterized by increased complexity both in image acquisition and data analysis [24, 30, 31, 69].

In the present study, single and dual bolus estimates of myocardial blood flow in healthy volunteers using both distributed parameter and Fermi models were compared. It was also assessed whether these models can reliably detect areas with reduced myocardial blood flow compared to a clinical gold standard of invasive coronary angiography and fractional flow reserve in patients with coronary artery disease.

5.2 Methods

5.2.1 Study population

Eight healthy volunteers with no previous history of cardiovascular or renal disease, diabetes mellitus, asthma or any other clinically significant illness and five patients with suspected coronary artery disease were recruited into the study. Exclusion criteria included severely compromised renal function (estimated glomerular filtration rate <30 ml/min) and contraindications to magnetic resonance imaging. The study was performed with the approval of the local research ethics committee, in accordance with the Declaration of Helsinki and with the written informed consent of all subjects. Prior to magnetic resonance perfusion imaging, all subjects were asked to refrain from caffeine for 12 hours.

5.2.2 Image acquisition

All data were acquired using a 3T Verio system (Siemens AG, Healthcare Sector, Erlangen, Germany). Standard cardiac imaging planes and a short axis stack of left ventricular cine data were acquired using routine steady state free precession (TrueFISP) acquisitions. Native T_1 relaxation rates (i.e. in the absence of CA) were calculated using the modified Look-Locker inversion (MOLLI) recovery technique

[138]. Stress imaging was performed by intravenous infusion of 140 µg/kg/min of adenosine (Adenoscan, Sanofi Aventis). Fifty dynamic perfusion images were obtained at diastole across three short-axis view slices: basal, mid-ventricular and apical slices according to the standard 16-segment heart model [16]. Perfusion images were acquired using a turbo-fast low angle shot (FLASH) saturation recovery prepared single-shot gradient echo pulse sequence (repetition time/ echo time 2.20 ms/1.07 ms, flip angle 12^o, slice thickness 8 mm, preparation pulse delay (PD) to central line of k-space 100 ms, matrix size 192 x 108 and FoV 330 mm x 440 mm). With the application of GRAPPA (accelerator factor of 3) and partial Fourier acquisition of 0.75, each dynamic frame consisted of 48-phase encoded lines. All magnetic resonance imaging data were acquired using electrocardiogram gating.

5.2.3 Contrast agent bolus administration

In single bolus imaging, 0.05 mmol/kg of CA (Gadovist, Bayer Healthcare) was injected intravenously after 4 min of adenosine infusion, followed by 20 ml of 0.9% saline (Medrad Spectris Solaris, Medrad, USA) at 4 ml/s [24]. All patients with coronary artery disease were imaged using the single bolus protocol.

In the healthy volunteer cohort, an additional pre-bolus infusion was administered to allow dual bolus modelling to be applied without the risk of signal saturation in the arterial input function. In this dual bolus protocol, the two boluses were injected in a pre-determined concentration ratio (pre-bolus:main bolus, 1:5) with the pre-bolus diluted using 0.9% saline. After 3.5 min of adenosine infusion, the pre-bolus of 0.006 mmol/kg CA was injected and adenosine was continued until the main bolus of 0.03 mmol/kg had also been administered. The pre-bolus allows determination of the arterial input function whilst the main bolus allows measurement of myocardial CA concentration curves [76]. To allow clearance of residual CA, the rest perfusion imaging was performed 15 min after the adenosine-stress scan with the same acquisition protocol in all subjects [24, 28, 29, 76].

5.2.4 Invasive coronary angiography and fractional flow reserve

All five patients underwent invasive coronary angiography at the Royal Infirmary of Edinburgh. Fractional flow reserve was assessed for major epicardial vessels and defined as the ratio between distal coronary pressure and aortic pressure measured simultaneously at maximal adenosine-induced (intravenous 140µg/kg/min) hyperaemia [109, 117]. Haemodynamically significant coronary artery disease was defined as luminal stenosis ≥70% on invasive coronary angiography, or fractional flow reserve <0.80 and luminal stenosis ≥50 %. Outcomes from the three main coronary vessels were classified into 3 groups: Group 1, no or minor coronary artery disease with luminal stenosis <50%; Group 2, non-obstructive coronary artery disease with luminal stenosis ≥50% and fractional flow reserve >0.80; and Group 3, obstructive coronary artery disease with luminal stenosis of ≥70% alone, or luminal stenosis ≥50% and fractional flow reserve ≤0.80 [109, 117].

5.2.5 Cardiac contouring

Endocardial and epicardial contours were manually defined on the short axis magnetic resonance perfusion imaging data using dedicated cardiac image analysis software (QMass, Medis, The Netherlands) to generate a standardised 16-segment model of the heart [16]. Myocardial blood flow analysis was performed per myocardial segment. The signal intensity of the arterial input function was extracted from the left ventricular cavity excluding papillary muscles using customised in-house software created in Matlab (MathWorks Inc., Natick, MA) [139].

All arterial input function curves were extracted from the basal slice [24, 29]. In single bolus analysis, the arterial input function was extracted from the standard (main bolus) CA dose component. For the dual bolus analysis in healthy subjects, the pre-bolus arterial input function was scaled and used for deconvolution analysis [24, 30, 76].

5.2.6 Image processing

To correct for signal saturation, myocardial and arterial input function signal intensity-time curves were converted to CA concentration-time curves using the method of Larsson *et al* [25], as described previously [24, 26-31, 66] (see subsection 3.1.1). This method is based on the assumption that in a region of interest, the longitudinal relaxation rate R_1 ($1/T_1$) changes linearly as a function of contrast agent concentration influx c(t) at time t multiplied by its relaxivity r_1, according to equation 2-16:

$$\frac{1}{\mathrm{T_1(t)}} - \frac{1}{\mathrm{T_1(0)}} = r_1 \cdot c(t)$$

where $T_1(0)$ is the native longitudinal relaxation rate and $T_1(t)$ is the longitudinal relaxation rate at time t of contrast enhancement. By substituting $\Delta R_1 = \frac{1}{\mathrm{T_1(t)}} - \frac{1}{\mathrm{T_1(0)}}$, equation (2-16) can be re-written as:

$$c(t) = \frac{\Delta R_1}{r_1} \qquad (5\text{-}1)$$

In the above set of equations, $R_1(t)$ is unknown and can be calculated by adapting the MR signal equation for the saturation recovery prepared single-shot FLASH sequence (equation 3-1) [24, 25, 29]:

$$SI = \Psi \cdot \left[\left(1 - e^{-PD \cdot R_1}\right) \cdot a^{n-1} + b \cdot \frac{1 - a^{n-1}}{1 - a} \right]$$

where $R_1(t)$ at time t of contrast enhancement can be calculated as previously described (subsection 3.1.1). CA concentration-time curves were then calculated using equation (5-1).

5.2.7 Model equations

The model equations used for data fitting are summarized in Table 5-1. These equations represent the tissue impulse response R(t) the shape of which is determined by the fitted parameters [24]. To quantify myocardial blood flow and other parameters generated by the Fermi and distributed parameter models, model-constrained deconvolution was used [24, 29, 66]. The Fermi model was fitted in the time domain whilst the distributed parameter model was fitted in the Laplace domain in order to avoid discontinuities of the time step-function that can be present when fitting the distributed parameter model in the time domain [65, 66].

The convolution of the Fermi function with the first-pass of the arterial input function was fitted, setting the end-point at the CA concentration minimum before the recirculation component begins (this range varies from patient to patient but is commonly in the range between 20-35 dynamic frames). The convolution of the distributed parameter function with the entire CA concentration time course of the arterial input function (i.e. 50 dynamic frames per slice) was fitted.

Table 5-1) Model equations. Fitted parameters for distributed parameter: myocardial blood flow, T is mean overall transit time, T_c is mean capillary transit time, T_e is mean interstitial (i.e. extravascular-extracellular) transit time. Where $s = i \cdot 2 \cdot \pi \cdot f$ and f is the frequency variable in the Fourier transformed data. Fitted parameters for Fermi: myocardial blood flow, τ_0 characterized the width of the shoulder of the Fermi function and k determined the decay rate of R(t) due to contrast agent wash-out. t is the time variable. DP: distributed parameter model, MBF: myocardial blood flow.

Model	Fitted parameters	Fitting domain	Tissue impulse response *R*
DP	MBF, T, T_c, T_e	Laplace	$R(s) = \frac{1 - \exp[-s \cdot (T + s \cdot T_c \cdot T_e)/(1 + s \cdot T_e)]}{s}$
Fermi	MBF, τ_0, k	Time	$R(t) = \frac{1}{\exp[(t - \tau_o) \cdot k] + 1}$

To further investigate the behaviour of distributed parameter modelling in single and dual bolus analysis, the convolution of the distributed parameter model with the first-pass of the arterial input function (using the same number of time points as in Fermi modelling) was also fitted. All additional microvascular parameters were calculated using the relationships described in Table 5-2 [50, 66].

Table 5-2) Microvascular characteristics were calculated by incorporating the fitted parameters of the distributed parameter model into the following relationships (see reference [50]). Myocardial plasma flow (MPF) was used to calculate extravascular-extracellular space (v_e), distribution volume (v_d), permeability surface area product (PS) and extraction fraction (E) and myocardial blood flow (MBF) to calculate intravascular space (v_b). Hematocrit: hct.

Microvascular characteristics	Equation
v_b	$v_b = MBF \cdot T_c$
v_e	$v_e = MPF \cdot (T - T_c)$
v_d	$v_d = MPF \cdot T$
PS	$PS = \frac{MPF \cdot (T - T_c)}{T_e}$
E	$E = 1 - \exp(-\frac{PS}{MPF})$
MPF	$MPF = MBF \cdot (1 - hct)$

A haematocrit value of 0.45 was assumed in order to convert myocardial blood flow into plasma flow which was used to calculate permeability surface area product, extraction fraction, extravascular-extracellular space and volume of distribution. Both models were fitted using a constrained nonlinear optimization (fmincon) in Matlab [140]. Myocardial perfusion reserve (myocardial blood flow at stress/ myocardial blood flow at rest) was calculated for all healthy volunteer data.

Consistent with previous cardiac perfusion studies, vessel territories in patients with hyperaemic myocardial blood flow values less than 2.5 ml/min/ml of tissue were considered as regions with reduced myocardial blood flow [136, 137].

5.2.8 Statistical analysis

The R software was used for statistical analysis (R Foundation for statistical computing, Vienna, Austria). Identification of any systematic bias between dual bolus and single bolus modelling estimates was performed using Bland Altman plots for both models. Statistical differences were investigated between Fermi and distributed parameter modelling, between distributed parameter and first-pass distributed parameter modelling, between stress and rest modelling values as well as between dual and single bolus analysis by implementing a paired *t*-test. A Welch two sample *t*-test was used to investigate statistical differences in myocardial blood flow values between the different groups (Groups 1-3) classified at the time of invasive coronary angiography. Homogeneity of variances was verified using a Fisher's F-test. Comparison of mean myocardial blood flow and physiological parameters estimates in vessel territories of patients versus overall mean values in healthy volunteers was investigated using one sample *t*-test. Statistical significance was defined as two-sided P value<0.05.

5.3 Results

The distributed parameter model was fitted in eight healthy volunteers and five patients with coronary artery disease. Example images are shown in Figures 5-1 and 5-2. 416 CA concentration-time curves were generated from 13 subjects (16 myocardial segments per subject both at stress and rest). Distributed parameter model fits were successful in 398 CA concentration-time curves and non-convergent (when estimates of the capillary transit time were lower than the minimum sampling period of the data [66]) in 7 myocardial segments of one volunteer at stress, in 5 myocardial segments of one volunteer at rest and in 6 segments of one patient at stress. The Fermi model successfully fitted all CA concentration-time courses.

5.3.1 Comparison of Fermi and distributed parameter models in healthy volunteers

Initially, the Fermi and distributed parameter models were fitted to CA concentration-time curves for the healthy volunteer population using arterial input functions derived from the main bolus data. Examples of Fermi and distributed parameter model fits at rest and stress are presented in Figure 5-3. Examples of pre-bolus and main bolus arterial input functions are shown in Figure 5-4. Fermi-derived myocardial blood flow values were higher than distributed parameter-derived myocardial blood flow values for both stress and rest (P=0.0005 and P=0.007 respectively, Table 5-3).

Subsequently, the Fermi and distributed parameter models were fitted for the healthy volunteer population, using scaled arterial input functions from their pre-bolus data. Fermi-derived myocardial blood flow values were again higher than distributed parameter-derived myocardial blood flow values for both stress and rest (P=0.03 and P=0.003 respectively, Table 5-3).

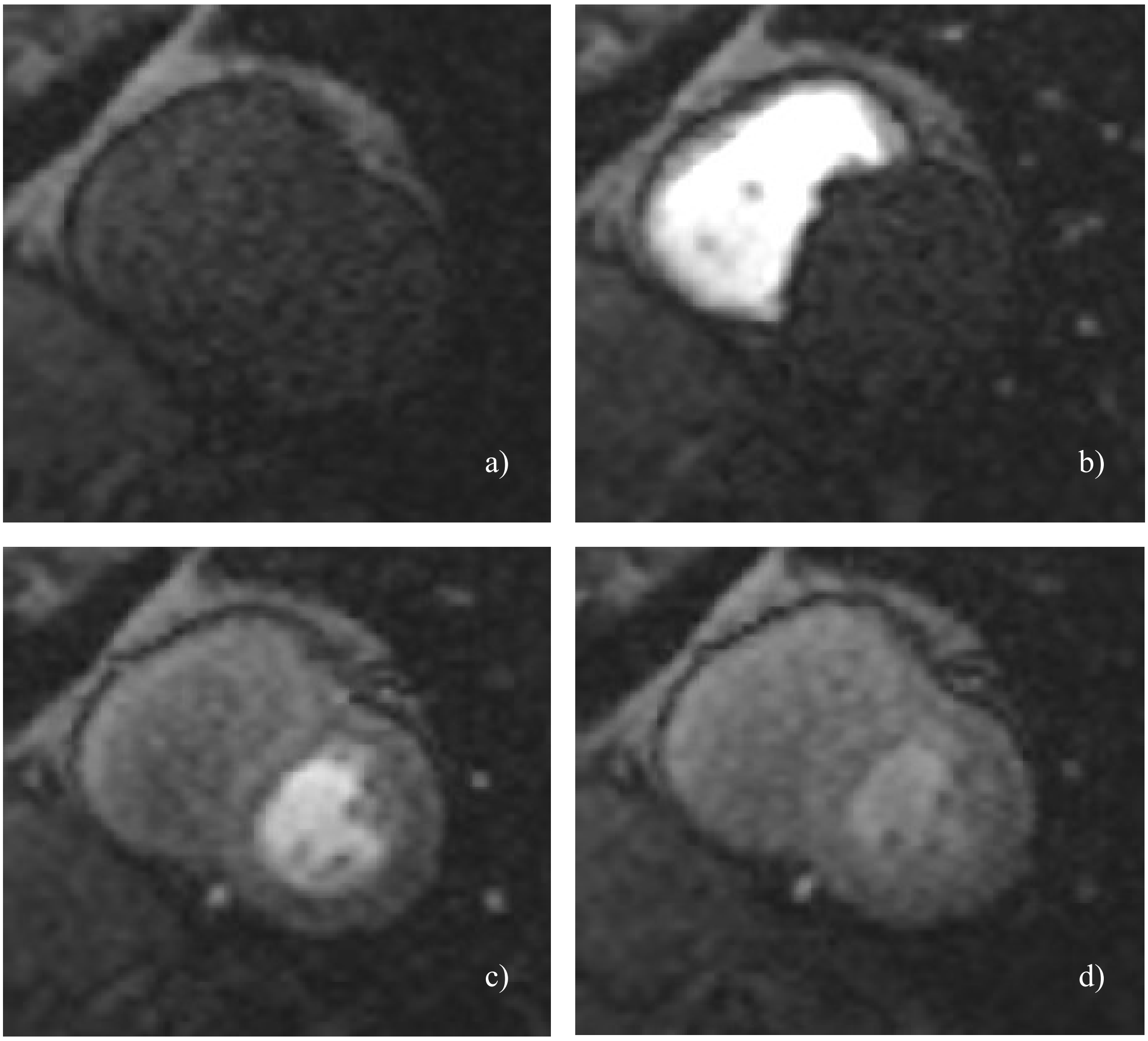

Figure 5-1) Mid-ventricular dynamic cardiac perfusion images are shown from a healthy volunteer. Dynamic perfusion image (a) before contrast enhancement, (b) contrast enhancement in the right ventricle, (c) peak contrast enhancement in myocardial tissue and (d) post (wash out) contrast enhancement in myocardial tissue.

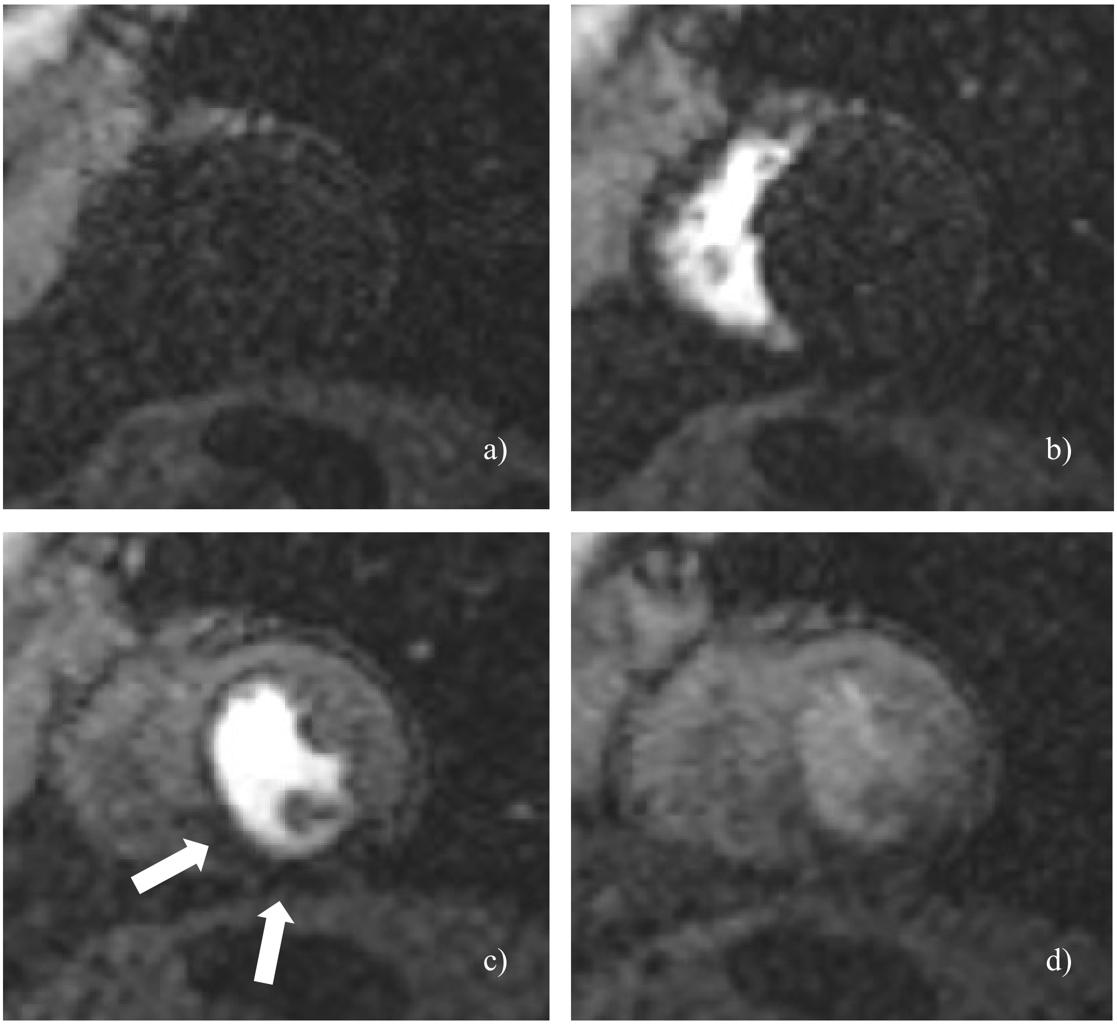

Figure 5-2) Mid-ventricular dynamic cardiac perfusion images are illustrated from a patient with a perfusion abnormality in the infero-septal and inferior myocardial regions (white arrows). Dynamic perfusion image (a) before contrast enhancement, (b) contrast enhancement in the right ventricle, (c) peak contrast enhancement in myocardial tissue and (d) post (wash out) contrast enhancement in myocardial tissue.

Mean distributed parameter model-derived myocardial blood flow at stress was not different in dual bolus compared to single bolus analysis (P=0.22) whilst mean Fermi model-derived myocardial blood flow at stress was higher in single bolus versus dual bolus analysis (P<0.0001, Table 5-3).

Systematic bias of the above comparisons was investigated using Bland Altman method (Figure 5-5). The average bias was computed as the blood flow values at stress determined in dual bolus minus the relative values determined in the single bolus analysis. For the Fermi model, the average bias was -1.00 ml/min/ml with 95% confidence intervals [-1.58, -0.42 ml/min/ml] and for the distributed parameter model, the average bias value was -0.38 ml/min/ml with 95% confidence intervals [-1.30, 0.53 ml/min/ml].

Mean Fermi and distributed parameter-derived myocardial blood flow at rest did not significantly change between single and dual bolus analysis (P=0.07 for both). The additional distributed parameter estimates were not significantly different in single bolus compared to dual bolus analysis (see values in Table 5-4).

Mean myocardial blood flow was higher during hyperaemia in all healthy volunteers for distributed parameter-dual bolus (P<0.0001), Fermi-dual bolus (P<0.0001), distributed parameter-single bolus (P<0.0001), and Fermi-single bolus analysis (P<0.0001). Mean myocardial perfusion reserve values were mean (SD): 2.59 (0.37) for distributed parameter-dual bolus, 2.42 (0.30) for distributed parameter-single bolus, 2.51 (0.48) for Fermi-dual bolus and 2.96 (0.34) for Fermi-single bolus analysis.

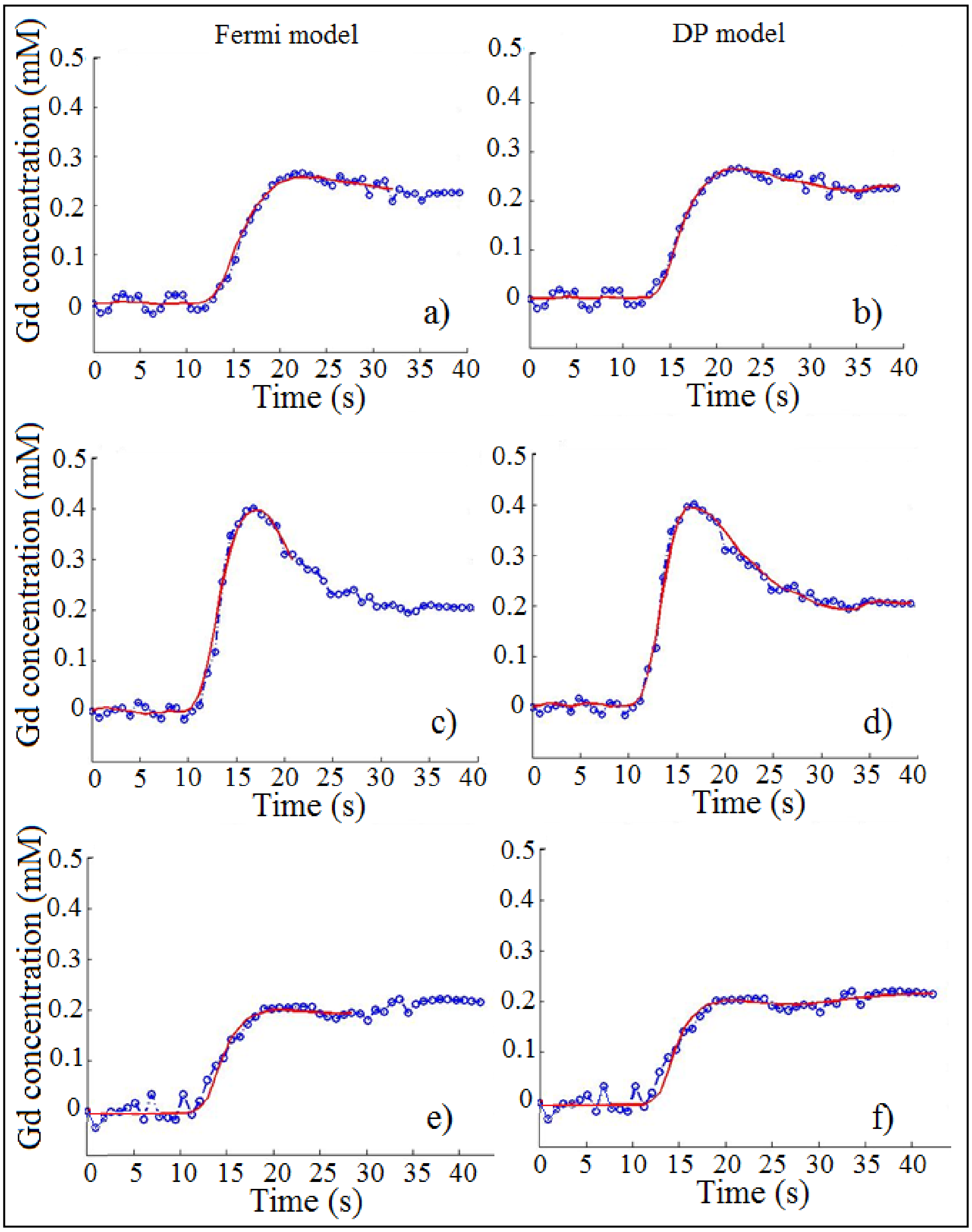

Figure 5-3) Examples of Fermi and distributed parameter model fits at rest (a, b) and at stress (c, d) from the same volunteer (dual bolus analysis). Fermi (e) and distributed parameter (f) model fits during hyperemia of a pathological myocardial segment (single bolus analysis). DP: distributed parameter model, Gd: gadolinium.

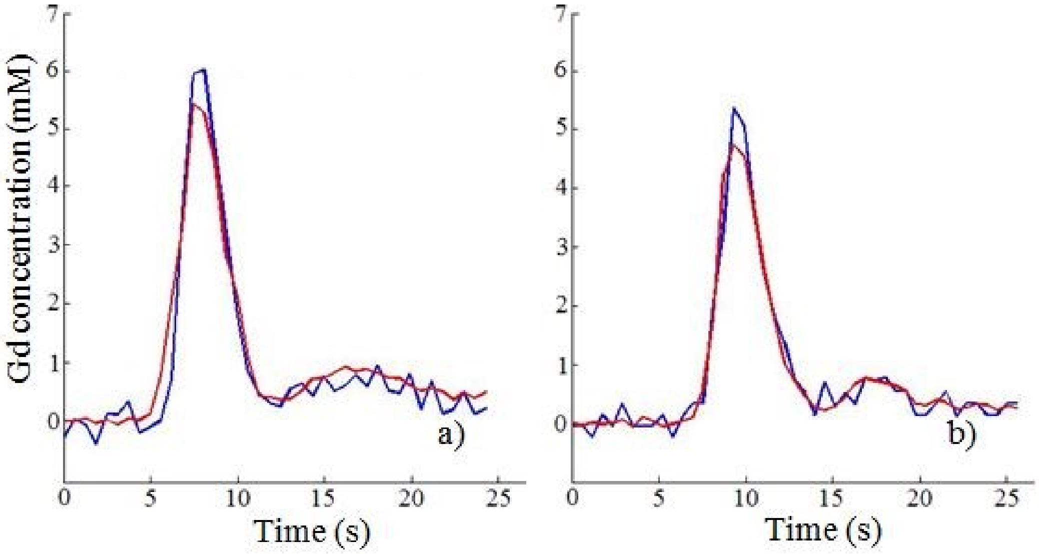

Figure 5-4) Scaled pre-bolus arterial input function versus standard arterial input function from the same examination. In volunteer 1 (a) and volunteer 2 (b) scaled pre-bolus (blue) arterial input function and main bolus arterial input function (red) are shown. Gd: gadolinium.

To investigate the lack of dependence of the distributed parameter model to arterial input function saturation observed in single bolus data, first-pass distributed parameter modelling was also performed. There was no difference between distributed parameter and first-pass distributed parameter myocardial blood flow values (P=0.17 in dual bolus, P=0.79 in single bolus analysis, Table 5-3). No difference was observed in first-pass distributed parameter-derived myocardial blood flow values between single and dual bolus analysis, for both stress (P=0.31) and rest (P=0.16) (Table 5-3).

Table 5-3) Healthy volunteer mean (SD) myocardial blood flow values calculated using dual and single bolus analysis. Statistical differences between single and dual bolus analysis are indicated with *. DP: distributed parameter model.

Modelling values/ Method	Fermi Dual bolus	Fermi Single bolus	DP Dual bolus	DP Single bolus	DP-First-pass Dual bolus	DP-First-pass Single bolus
Myocardial blood flow-Stress (ml/min/ml)	3.57 (0.59)*	4.57 (0.62)*	3.16 (0.71)	3.45 (0.48)	3.39 (0.56)	3.47 (0.50)
Myocardial blood flow-Rest (ml/min/ml)	1.48 (0.40)	1.57 (0.33)	1.23 (0.26)	1.46 (0.29)	1.18 (0.26)	1.34 (0.31)

Table 5-4) Mean microvascular characteristics (SD) estimates for healthy volunteers and for all 3 invasive coronary angiography/fractional flow reserve Groups. Notations as in Tables 5-1 and 5-2.

	DP Dual bolus	DP Single bolus	DP-First-pass Dual bolus	DP-First-pass Single bolus	Group 1	Group 2	Group 3
PS-Stress (ml/min/ml)	0.98 (0.32)	1.09 (0.21)	1.09 (0.33)	1.21 (0.24)	0.95 (0.18)	0.61 (0.20)	0.50 (0.20)
PS-Rest (ml/min/ml)	0.56 (0.15)	0.62 (0.14)	0.57 (0.12)	0.64 (0.13)	0.53 (0.10)	0.58 (0.10)	0.59 (0.14)
E-Stress (%)	0.45 (0.04)	0.45 (0.03)	0.46 (0.09)	0.48 (0.03)	0.47 (0.04)	0.50 (0.05)	0.52 (0.06)
E-Rest (%)	0.56 (0.04)	0.54 (0.03)	0.58 (0.01)	0.58 (0.02)	0.58 (0.02)	0.52 (0.04)	0.53 (0.05)
vb-Stress (%)	0.08 (0.02)	0.09 (0.02)	0.07 (0.02)	0.07 (0.02)	0.07 (0.01)	0.07 (0.03)	0.05 (0.03)
vb-Rest (%)	0.04 (0.01)	0.04 (0.01)	0.03 (0.01)	0.03 (0.01)	0.03 (0.01)	0.04 (0.02)	0.04 (0.02)
ve-Stress (%)	0.17 (0.05)	0.20 (0.04)	0.15 (0.06)	0.16 (0.03)	0.19 (0.03)	0.20 (0.07)	0.18 (0.06)
ve-Rest (%)	0.17 (0.06)	0.20 (0.05)	0.15 (0.04)	0.16 (0.04)	0.17 (0.04)	0.21 (0.04)	0.23 (0.05)
vd-Stress (%)	0.22 (0.03)	0.25 (0.03)	0.16 (0.04)	0.18 (0.04)	0.21 (0.04)	0.24 (0.05)	0.21 (0.05)
vd-Rest (%)	0.20 (0.04)	0.23 (0.02)	0.15 (0.04)	0.17 (0.04)	0.19 (0.04)	0.22 (0.05)	0.20 (0.05)

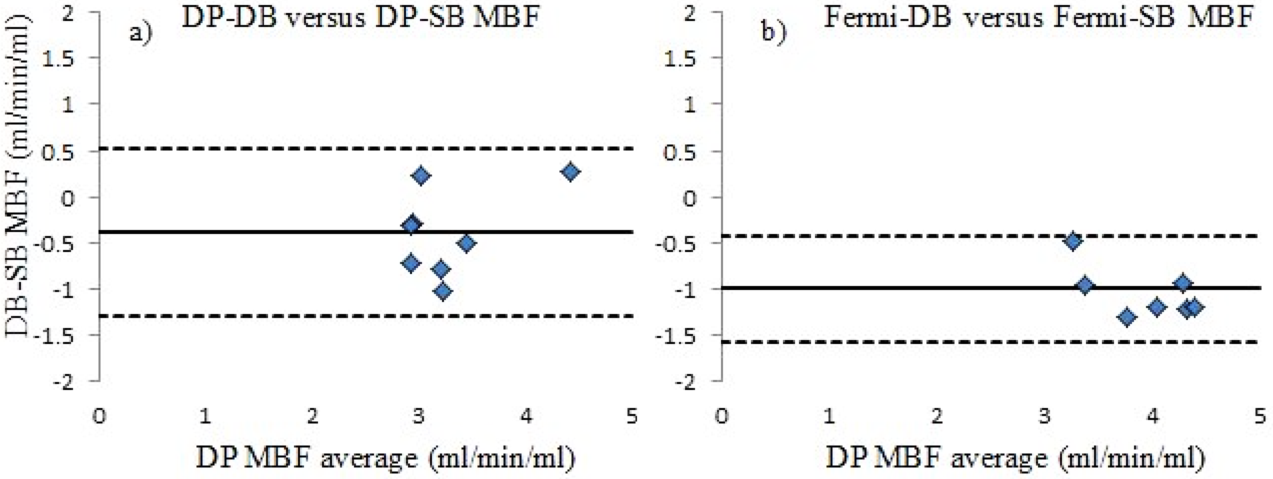

Figure 5-5) Bland Altman plots of a) dual bolus (DB)-distributed parameter (DP) versus single bolus (SB)-DP myocardial blood flow (MBF) values and b) DB-Fermi versus SB-Fermi MBF values in healthy volunteers.

5.3.2 Distributed parameter and Fermi analysis in patients with coronary artery disease

Invasive coronary angiography and fractional flow reserve identified 7 vessels with obstructive lesions (Group 3), 5 vessels with non-obstructive lesions (Group 2) and 3 vessels with no or minor coronary artery disease (Group 1).

Mean myocardial blood flow values were calculated in vessel territories of the three main coronary arteries for each patient using both models (Table 5-5, Figure 5-3e and 5-2f). The Fermi and distributed parameter models correctly identified reduced myocardial blood flow in 6 and 7 of the 7 vessels in Group 3 respectively. In addition, the Fermi and distributed parameter models correctly identified reduced myocardial blood flow in 3 and 5 of the 5 vessels in Group 2 respectively. Both models estimated myocardial blood flow within normal range in Group 1. A difference was observed in myocardial blood flow at stress and in myocardial perfusion reserve between Group 1 versus Groups 2 and 3 for both models (Figure 5-6, Table 5-5).

Mean physiological parameter values were also calculated using distributed parameter modelling in all vessel territories for all patients (see Table 5-4).

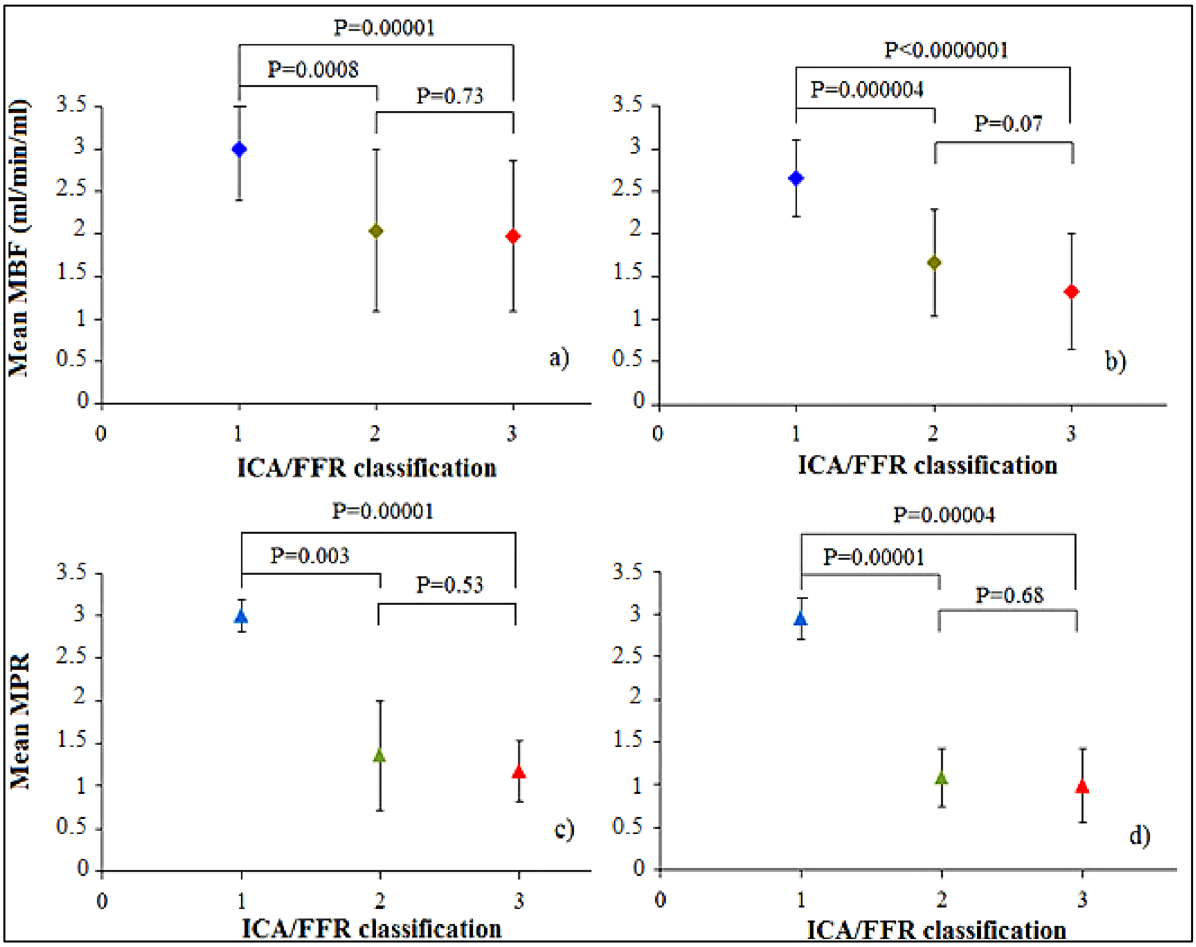

Figure 5-6) Mean Fermi-MBF (a), distributed parameter-MBF (b), Fermi-MPR (c), distributed parameter MPR (d) versus ICA/FFR classification. MBF: myocardial blood flow, MPR: myocardial perfusion reserve, ICA: invasive coronary angiography, FFR: fractional flow reserve.

Table 5-5) ICA/FFR classification and mean MBF (SD) at stress measured in ml/min/ml per vessel territories of the three main coronary arteries. LAD, LCX and RCA: left anterior descending, left circumflex and right coronary artery respectively. Vessels with reduced myocardial blood flow are indicated with *. Notations as in Table 5-1 and Figure 5-6.

		ICA/FFR	DP-MBF	Fermi-MBF	DP-MPR	Fermi-MPR
Patient 1	LAD	3	0.82 (0.28)*	1.68 (0.60)*	0.88 (0.29)	1.54 (0.47)
	LCX	3	0.94 (0.20)*	1.99 (0.41)*	0.91 (0.16)	1.73 (0.44)
	RCA	2	0.84 (0.17)*	1.77 (0.79)*	0.91 (0.24)	1.77 (0.44)
Patient 2	LAD	2	1.99 (0.30)*	3.37 (0.49)	1.68 (0.37)	2.15 (0.49)
	LCX	2	1.98 (0.27)*	2.61 (0.41)	1.26 (0.30)	1.87 (0.80)
	RCA	3	1.27 (0.27)*	1.80 (0.81)*	0.86 (0.30)	1.08 (0.33)
Patient 3	LAD	2	1.20 (0.10)*	1.19 (0.34)*	0.71 (0.11)	0.78 (0.44)
	LCX	3	1.34 (0.13)*	1.84 (1.11)*	0.65 (0.30)	0.96 (0.26)
	RCA	2	1.58 (0.31)*	1.18 (0.16)*	0.81 (0.20)	0.70 (0.12)
Patient 4	LAD	3	1.99 (0.31)*	3.02 (0.64)	1.21 (0.31)	1.22 (0.23)
	LCX	3	1.61 (0.73)*	1.98 (0.58)*	0.90 (0.35)	1.05 (0.34)
	RCA	3	0.75 (0.29)*	1.00 (0.44)*	0.58 (0.23)	0.65 (0.24)
Patient 5	LAD	1	2.86 (0.59)	3.26 (0.88)	3.26 (0.40)	3.37 (0.50)
	LCX	1	2.54 (0.24)	2.79 (0.30)	3.01 (0.60)	2.91 (0.34)
	RCA	1	2.60 (0.36)	2.88 (0.33)	2.68 (0.35)	3.04 (0.85)

5.4 Discussion

Single versus dual bolus estimates of myocardial blood flow in healthy volunteers using both Fermi and one-barrier, two-region distributed parameter models were compared. No difference was demonstrated in myocardial blood flow estimates using the distributed parameter model, between single and dual bolus analysis. In agreement with previous work, it was demonstrated an increase in stress myocardial blood flow estimates with application of Fermi modelling using single bolus data analysis, compared to dual bolus data analysis. For the first time, the distributed parameter model has been successfully fitted in patients with coronary artery disease.

5.4.1 Model comparison in healthy volunteers

Using the distributed parameter model, 96% of the data (398 in 416 CA concentration-time courses) were successfully fitted. Model comparison in eight healthy volunteers suggested that single bolus analysis of the distributed parameter model shows no statistically significant difference compared to dual bolus analysis, indicating that this model may be less dependent on arterial input function saturation than the Fermi model. Furthermore, distributed parameter modelling using the first-pass only, showed no statistically significant difference between single bolus and dual bolus analysis. This shows that the lack of dependence on single or dual bolus in the distributed parameter model using the full curve is not due to the increased number of time points used for fitting, compared to the first-pass Fermi model. Dual bolus [30, 31, 54, 76] and dual sequence [69, 72] (which includes a low resolution dynamic acquisition of the left ventricle to eliminate arterial input function saturation), are the most widely suggested techniques to solve the issue of arterial input function saturation. However, both of these techniques involve increased complexity in image acquisition and data analysis that have led to ongoing debate regarding whether either method might replace standard single bolus protocols for perfusion imaging and myocardial blood flow quantification. Whilst single bolus protocols are prone to arterial input function saturation, they are still widely used in clinical imaging and are suitable for qualitative assessment of myocardial perfusion. This work suggests that peak arterial input function saturation may not be such a dominant factor when quantifying myocardial blood flow in distributed parameter modelling compared with Fermi modelling.

It is important to consider that these non-statistically significant differences between single and dual bolus analysis for distributed parameter and first-pass distributed parameter modelling, can possibly be explained due to the mathematical architecture of its formula and number of fitted parameters (Table 5-1, four fitted parameters in the exponent for distributed parameter modelling, versus three for Fermi modelling). Further investigation is required to explore whether any influences due to arterial input function saturation effects in single bolus analysis can also affect/distribute across any of the other fitted parameters (apart from blood flow): i.e. either the mean capillary transit time, and/or the mean overall transit time, and/ or the mean interstitial transit time. Assessment of this interpretation may explain why distributed parameter modelling-derived myocardial blood flow measurements may be less dependent on saturation effects in single bolus, compared to dual bolus analysis.

Calculated values for myocardial blood flow and microvascular characteristic parameters generally agree with a previous study that was the first to introduce the one-barrier, two-region distributed parameter model in cardiac data [66]. Broadbent *et al* fitted a distributed parameter model in data acquired using a different protocol: short-axis view of the entire myocardial area across one mid-ventricular slice acquired in systole at 1.5 T. The distributed parameter model was here applied using a 16-segment heart model across three mid-ventricular slices acquired in diastole at 3T.

5.4.2 The impact of contrast agent dose

The dependence of Fermi and distributed parameter modelling in the presence of arterial input function saturation in single bolus data, was validated using a relatively low CA dose (0.03 mmol/kg) for this healthy volunteer cohort. The administration of the specific CA dose has possibly caused limited arterial input function saturation at the peak of contrast enhancement [24, 69] (as shown in Figure 5-4), compared to higher CA doses. This study demonstrates that Fermi modelling is still sensitive to any arterial input function saturation present in our single bolus data. In contrast, distributed parameter modelling is less dependent on any arterial input function saturation present in our data. Any increases in CA dose (at 3T), can increase the degree of arterial input function saturation in single bolus data of healthy volunteers, which would necessitate a de novo validation of distributed parameter modelling in single against dual bolus analysis.

5.4.3 Distributed parameter and Fermi analysis in patients

The distributed parameter model was capable of detecting reduced myocardial blood flow in patients with non-obstructive and obstructive coronary artery disease (Groups 2 and 3 respectively). Distributed parameter modelling correctly identified all 7 obstructive lesions and all 5 non-obstructive lesions. Fermi modelling correctly identified 6 out of 7 obstructive lesions and 3 out of 5 non-obstructive lesions. Both models showed decreased myocardial blood flow values as a function of luminal stenosis severity against invasive coronary angiography and fractional flow reserve classification (Figure 5-6).

5.4.4 Study limitations

The number of subjects included in this study is small. However, this is the first study demonstrating that a one-barrier, two-region distributed parameter model approach may be less dependent on arterial input function saturation than Fermi modelling. Distributed parameter modelling needs to be applied in larger patient cohorts to further validate its diagnostic accuracy. The behaviour of distributed parameter modelling in higher CA doses has not been validated. To reduce patient discomfort during administration of adenosine, dual bolus stress-rest protocol was not implemented in the patient cohort. As such, it was impossible to validate any systematic errors that may have contaminated myocardial blood flow quantifications in patients, due to arterial input function saturation. To overcome this limitation and to complement the above model comparison, the ability of both models in detecting reduced myocardial blood flow in stenotic vessels versus current invasive gold standard methods was further assessed. The CA dose used in patients was higher than in healthy volunteers to increase the signal-to-noise ratio due to an assumed reduction in blood flow in our patient cohort as compared to our healthy volunteer cohort. Although this higher dose in patients has possibly caused some myocardial blood flow overestimations in Fermi modelling (Table 5-5, in two epicardial vessels in patient 2, and one epicardial vessel in patient 4), the distributed parameter modelling showed excellent accuracy in detecting reduced haemodynamics at stress in all stenotic vessels compared to our invasive gold standard. The vessels with non-obstructive disease (Group 2) were all from patients who also had one or two other vessels with obstructive disease (Group 3). The coincidental effect of microvascular dysfunction could therefore explain the low myocardial blood flow measurements in Group 2. The vessels identified with no or minor coronary artery disease (Group 1) were all from the same patient, which may have affected the validity of the statistical comparisons in the above per vessel analysis. This may indicate that it can also be clinically important to investigate haemodynamic differences in both a per vessel and per patient basis for robust patient stratification, which is further described in chapter 7.

5.5 Conclusions

A one-barrier, two-region distributed parameter model was implemented in healthy volunteers and patients with coronary artery disease. Distributed parameter-derived myocardial blood flow did not significantly change when a single bolus arterial input function was used compared to the dual bolus case. Fermi modelling of the same data demonstrated significant overestimations in myocardial blood flow in single bolus compared to dual bolus analysis. This suggests that the distributed parameter model might be less dependent on arterial input function saturation than Fermi modelling. These findings suggest that following assessment of the impact of contrast agent dose, distributed parameter modelling may allow the application of single bolus imaging in the clinical setting.

The distributed parameter model detected reduced myocardial blood flow in all 7 vessels with obstructive lesions and in all 5 vessels with non-obstructive lesions as determined by invasive coronary angiography and fractional flow reserve classification in a pilot cohort of five patients with coronary artery disease.

Summary

This chapter described a comparison of single bolus versus dual bolus values which suggested that distributed parameter modelling is less dependent on arterial input function saturation than Fermi modelling. Distributed parameter modelling showed excellent accuracy in detecting reduced myocardial blood flow in all stenotic vessels versus invasive methods.

In this chapter, no difference was observed between distributed parameter and first-pass distributed parameter modelling, both in single and dual bolus analysis. The next chapter investigates a thorough comparison between distributed parameter and first-pass-distributed parameter modelling values against ideal values from synthetic data.

6. Assessing the accuracy and reproducibility of distributed parameter and first-pass distributed parameter modelling using numerical simulations.

Introductory summary

This chapter investigates the accuracy and reproducibility of distributed parameter and first-pass distributed parameter modelling using simulated data. Particularly, this chapter examines whether first-pass distributed parameter modelling can give accurate myocardial blood flow and microvascular characteristic values, against ideal values generated by numerical simulations.

6.1 Background

Fermi modelling has been used in numerous studies involving myocardial blood flow quantification from first-pass MR data [24-26, 30, 31, 37, 43, 53, 54, 56, 58-60, 66, 73, 75, 141]. Myocardial blood flow analysis in these studies was based on the assumption that the first-pass of an extravascular-extracellular contrast agent bolus is the phase of contrast enhancement most sensitive to changes in blood flow. Changes in blood flow can be induced either from pharmacological intervention, exercise or disease and can be made apparent in contrast agent concentration-time curves (see Figure 5-3) [24, 54]. According to this assumption, mathematical analysis of the first-pass phase of contrast agent concentration-time curves is able to detect changes in myocardial blood flow, induced from the aforementioned factors.

The Fermi model is convolved with the first-pass of the arterial input function and can be used to quantify myocardial blood flow as long as measurements do not exceed the first-pass of the blood pool [24]. Numerical simulations have shown that if the end point for myocardial blood flow analysis, is set at the contrast agent concentration minimum between the first-pass and recirculation peak (see Figure 6-1), first-pass perfusion modelling using the Fermi function can give accurate estimates of myocardial blood flow as compared with ideal values generated using simulated data [28]. These simulated data were generated using an axially distributed model of blood-tissue exchange with multiple parallel flow pathways [24, 28]. These pathways were composed of small vessels in series (each pathway composed of a small vessel) involving axially distributed capillary blood-tissue exchange [28]. Any extensions of this time range due to errors in the precise selection of the first-pass range can result in systematic underestimations [24], or overestimations [37] of Fermi-derived myocardial blood flow values.

In contrast to Fermi modelling, distributed parameter (DP) modelling is convolved with the entire contrast agent concentration-time course of the arterial input function (see chapter 5 and Figure 6-1) [50, 66]. In chapter 5, to further investigate the behaviour of DP modelling in single and dual bolus analysis, the convolution of the DP model with the first-pass of the arterial input function was fitted to tissue contrast agent concentration-time data, using the same number of time points as in Fermi modelling. This was referred to as first-pass DP modelling. Using MR perfusion data from eight healthy volunteers, it was demonstrated that there was no significant difference between DP- and first-pass DP-derived myocardial blood flow values.

In some cases, it can be particularly challenging to identify the end point of the first-pass in the arterial input function. Characteristic examples are a) when the concentration minimum is not clearly visible due to noise effects and b) in dual bolus imaging, in which the bolus dispersion of a scaled pre-bolus arterial input function can be different compared to a standard main bolus arterial input function (see Figure 6-2).

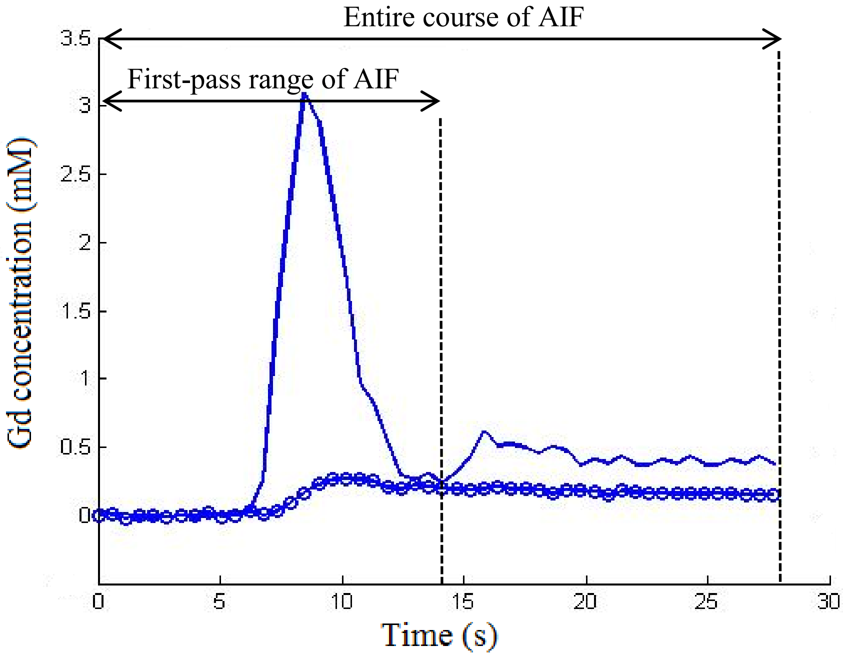

Figure 6-1) Arterial input function used to generate simulated data. First-pass and entire course of the contrast agent bolus in the blood pool is shown (AIF). Solid line: AIF (arterial input function), solid line with circles: simulated tissue curve.

Although it is known that any time extensions of the first-pass time range can influence Fermi modelling results, it is still unknown whether any differences in the time range selected for analysis can affect DP modelling results. In the present study, it was investigated whether DP modelling and first-pass DP modelling can give accurate estimates of blood flow and of microvascular characteristics, compared to ideal values from numerical simulations.

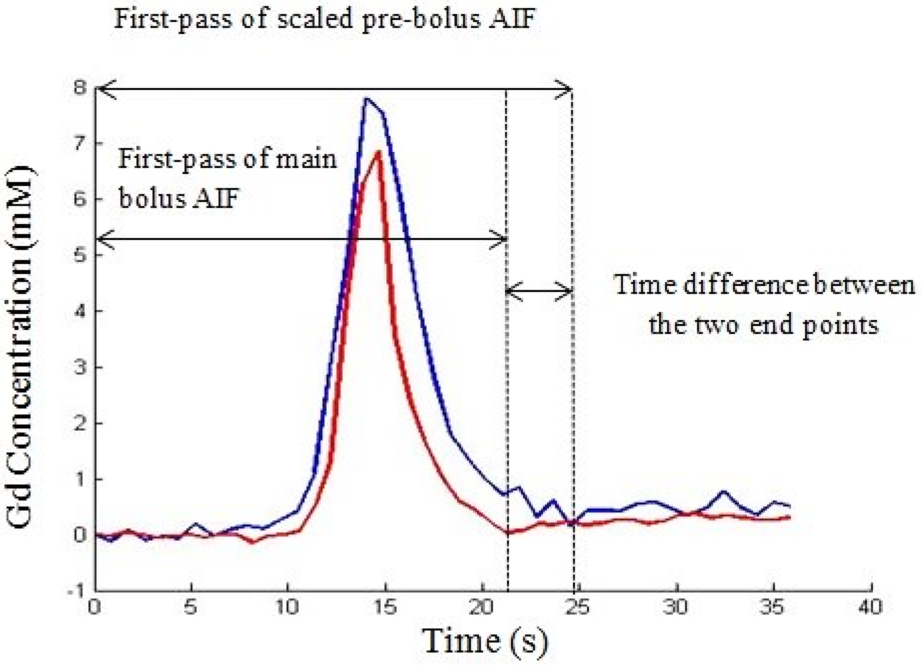

Figure 6-2) Scaled pre-bolus arterial input function (blue) and standard main bolus arterial input function (red). A difference in contrast agent bolus dispersion is apparent. This can influence the reproducibility of myocardial blood flow analysis as the selection of the end point of the first-pass range becomes subjective. Does the end point in the scaled pre-bolus or in the standard main bolus arterial input function define the first-pass range? Also, note that the end point of the first-pass is not obvious in the case of the scaled arterial input function due to substantial noise effects.

6.2 Methods

6.2.1 Simulations

Simulated data with known blood flow values were generated in Matlab (MathWorks Inc., Natick, MA). Simulated contrast agent concentration curves were produced using the DP model (see Table 5-1 for DP equation). The DP function was convolved with the entire contrast agent concentration-time course of the arterial input function in the Laplace domain [50, 66]. An optimum arterial input function was chosen from the main bolus data of a healthy volunteer (from healthy volunteer data, see Figure 6-1). The fitted parameters T_c, T_e and T (see Table 5.1) ranged from 0.8 to 2.5 sec, from 4.5 to 11.5 sec and from 5.5 to 15 sec respectively, to simulate a series of myocardial blood flow values between 1.0 and 5.0 ml/min/ml of tissue. These model parameters were chosen to mimic a physiologically realistic range according to previously published values [28]. In accordance with this physiologically realistic range, any increase in blood flow values implies decreases in T_c, T_e and T. Ideal blood flow and microvascular characteristic parameter values (see Table 6-1 and 6-2) were calculated based on the DP model parameters, according to the relationships presented in Table 5-2.

The above process was repeated for two types of tissue concentration-time curves: for a set of curves with a first-pass to recirculation peak ratio of a) 1.5 and of b) 1.4. The former type of curves feature lower recirculation peaks compared to the latter type of curves. Peak ratios were defined as the first-pass peak divided by the recirculation peak. Curves with a first-pass to recirculation peak ratios of approximately 1.5 were commonly found in the in-vivo MR perfusion data generated for this thesis. Curves with peak ratios of approximately 1.4 were less common in actual MR perfusion data but were occasionally observed for lower to average blood flow values range (i.e. between 1.5-3.0 ml/min/ml) (see Results section 6.3, for Figures illustrating these first-pass to recirculation peak ratios). Both sets of curves were generated by appropriately adjusting T_c, T_e and T. For example, decreasing T_c whilst maintaining T_e and T constant, leads to a reduction in the recirculation peak and thus, to a higher first-pass to recirculation peak ratio. In contrast, decreasing T_e whilst maintaining T_c and T constant, leads to an increase in the recirculation peak and to a lower first-pass to recirculation peak ratio.

Two Rician noise levels were added to the arterial input function and simulated curves (Figure 6-3). The range of noise level was chosen so that the contrast to noise ratio (CNR) was either 40 (noise level 1) or 10 (noise level 2), which correspond to the highest and lowest CNRs observed in actual MR perfusion data, respectively. CNR is defined as the ratio of the signal change from baseline to peak of contrast enhancement, divided by the standard deviation of the signal intensity curves in the absence of contrast [28, 43]. CNR levels were calculated for myocardial tissue simulated curves and the same noise levels were added in the arterial input function.

For DP and first-pass DP modelling, the convolution of the DP model with the entire (50 dynamic frames) and the first-pass (here 25 dynamic frames) of the arterial input function respectively, were fitted to the simulated curves. According to the aforementioned CNRs, noise levels 1 and 2 were added to the arterial input function and simulated curves. DP and first-pass DP modelling was repeated.

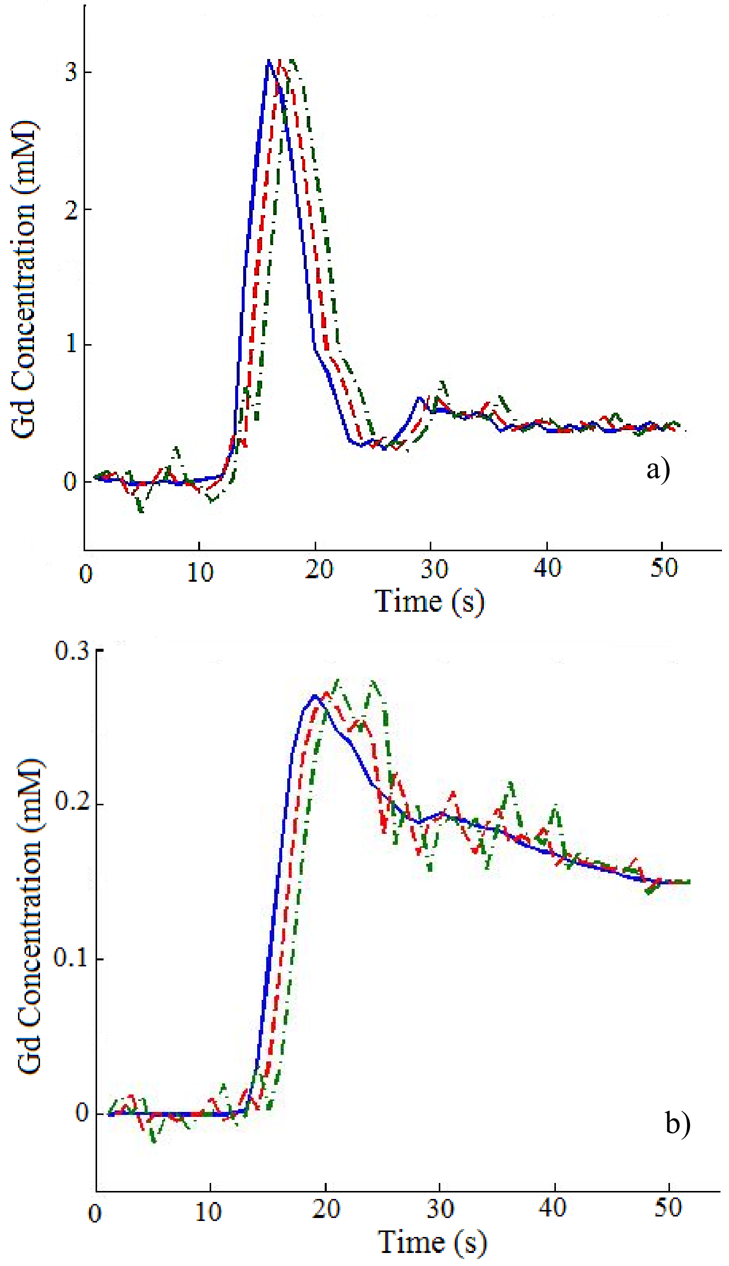

Figure 6-3) (a) Arterial input function without noise (blue line), with noise level 1 (red dashed line) and noise level 2 (green dashed-dot line). (b) Simulated curves without noise (blue line), with noise level 1 (red dashed line) and noise level 2 (green dashed-dot line). A time delay has been used between curves for clarity.

6.2.2 Statistical analysis

Statistical analysis was performed with a paired-test to investigate differences between DP and first-pass DP modelling values against ideal blood flow and microvascular characteristic parameter values across all simulated curves, with and without noise. Statistical significance was defined as two-sided P value<0.05.

Table 6-1) Ideal values for set of tissue concentration-time curves with first-pass to recirculation peak ratio of 1.5. F: blood flow, PS: permeability surface area product, E: extraction fraction, v_b=intravascular space, v_e=extravascular-extracellular space, v_d=volume distribution.

Ideal F (ml/min/ml)	Ideal PS (ml/min/ml)	Ideal E (%)	Ideal v_b (%)	Ideal v_e (%)	Ideal v_d (%)
1	0.62	0.44	0.03	0.07	0.09
1.5	0.63	0.45	0.04	0.08	0.10
2	0.65	0.45	0.04	0.08	0.10
2.5	0.81	0.45	0.05	0.10	0.13
3	0.97	0.45	0.06	0.12	0.15
3.5	1.14	0.45	0.07	0.14	0.18
4	1.30	0.45	0.08	0.16	0.20
4.5	1.46	0.45	0.09	0.18	0.23
5	1.62	0.45	0.10	0.20	0.25

Table 6-2) Ideal values for set of curves with first-pass to recirculation peak ratio of 1.4. Notations as in Table 6-1.

Ideal F (ml/min/ml)	Ideal PS (ml/min/ml)	Ideal E (%)	Ideal v_b (%)	Ideal v_e (%)	Ideal v_d (%)
1	0.65	0.44	0.07	0.15	0.20
1.5	0.67	0.45	0.07	0.14	0.19
2	0.70	0.47	0.08	0.15	0.20
2.5	0.83	0.45	0.09	0.18	0.23
3	1.00	0.45	0.07	0.17	0.21
3.5	1.12	0.44	0.08	0.19	0.23
4	1.22	0.43	0.09	0.20	0.25
4.5	1.38	0.43	0.09	0.17	0.22
5	1.91	0.50	0.10	0.23	0.28

6.3 Results

Initially, DP and first-pass DP modelling were implemented in the set of curves with a first-pass to recirculation peak ratio of 1.5. In the data that were free from noise, no significant differences were observed in DP- and first-pass DP-derived values versus ideal values for the following parameters: myocardial blood flow, permeability surface area product, extraction fraction and intravascular space (Table 6-3).

Similarly, no significant differences were detected in DP- and first-pass DP-derived values versus ideal values for the same parameters, when noise level 1 and noise level 2 were added in the arterial input function and simulated curves (Tables 6-3).

Significant reductions were observed between first-pass DP-derived values and ideal values only for extravascular-extracellular space and for distribution volume, which were consistent between subjects and were present in both data free of noise and data with added noise (Table 6-3, Figure 6-4).

Subsequently, DP and first-pass DP modelling were applied in the set of curves with first-pass to recirculation peak ratio of 1.4. No significant differences were identified in DP- and first-pass DP-derived values against ideal values for myocardial blood flow and for all microvascular characteristics (Tables 6-4).

There were again no significant differences in DP- and first-pass DP-derived values versus ideal values for all parameters, when noise level 1 and noise level 2 were added in the arterial input function and simulated curves (Tables 6-4). Example images of DP and first-pass DP fits in simulated curves are shown in Figures 6-5 and 6-6.

Table 6-3) P values from paired *t*-test comparisons between DP- and first pass DP-derived results versus actual values. Comparisons are shown in curves with first pass to recirculation peak ratio of 1.5. Mod: Modelling, F: flow (ml/min/ml), PS: permeability surface area product (ml/min/ml), E: extraction fraction (%), v_b: intravascular space (%), v_e: extravascular extracellular space (%), v_d: distribution volume (%), N_0: without noise, N_1: noise level 1, N_2: noise level 2, FPDP: first pass distributed parameter modelling. Statistically significant differences are indicated with *.

	Actual F	Mod F	Actual PS	Mod PS	Actual E	Mod E	Actual v_b	Mod v_b	Actual v_e	Mod v_e	Actual v_d	Mod v_d
DP N_0/1.5	0.747		0.83		0.08		0.36		0.90		0.90	
DP N_1/1.5	0.06		0.08		0.59		0.90		0.36		0.17	
DP N_2/1.5	0.08		0.60		0.90		0.90		0.36		0.08	
FPDP N_0/1.5	0.06		0.10		0.08		0.89		0.005*		0.005*	
FPDP N_1/1.5	0.11		0.95		0.11		0.90		0.000001*		0.000006*	
FPDP N_2/1.5	0.08		0.68		0.17		0.90		0.000001*		0.00002*	

Table 6-4) P values from paired *t*-test comparisons between DP- and first pass DP-derived results versus actual values. Comparisons are shown in curves with first pass to recirculation peak ratio of 1.4. Notations as in Table 6-3.

<table>
<tr><th></th><th>Actual F</th><th>Mod F</th><th>Actual PS</th><th>Mod PS</th><th>Actual E</th><th>Mod E</th><th>Actual v_b</th><th>Mod v_b</th><th>Actual v_e</th><th>Mod v_e</th><th>Actual v_d</th><th>Mod v_d</th></tr>
<tr><td>DP N_0/1.4</td><td colspan="2">0.29</td><td colspan="2">0.08</td><td colspan="2">0.07</td><td colspan="2">0.36</td><td colspan="2">0.17</td><td colspan="2">0.90</td></tr>
<tr><td>DP N_1/1.4</td><td colspan="2">0.26</td><td colspan="2">0.10</td><td colspan="2">0.06</td><td colspan="2">0.90</td><td colspan="2">0.60</td><td colspan="2">0.08</td></tr>
<tr><td>DP N_2/1.4</td><td colspan="2">0.08</td><td colspan="2">0.08</td><td colspan="2">0.08</td><td colspan="2">0.36</td><td colspan="2">0.60</td><td colspan="2">0.90</td></tr>
<tr><td>FPDP N_0/1.4</td><td colspan="2">0.06</td><td colspan="2">0.36</td><td colspan="2">0.28</td><td colspan="2">0.90</td><td colspan="2">0.10</td><td colspan="2">0.53</td></tr>
<tr><td>FPDP N_1/1.4</td><td colspan="2">0.48</td><td colspan="2">0.88</td><td colspan="2">0.55</td><td colspan="2">0.74</td><td colspan="2">0.39</td><td colspan="2">0.53</td></tr>
<tr><td>FPDP N_2/1.4</td><td colspan="2">0.08</td><td colspan="2">0.66</td><td colspan="2">0.90</td><td colspan="2">0.90</td><td colspan="2">0.25</td><td colspan="2">0.08</td></tr>
</table>

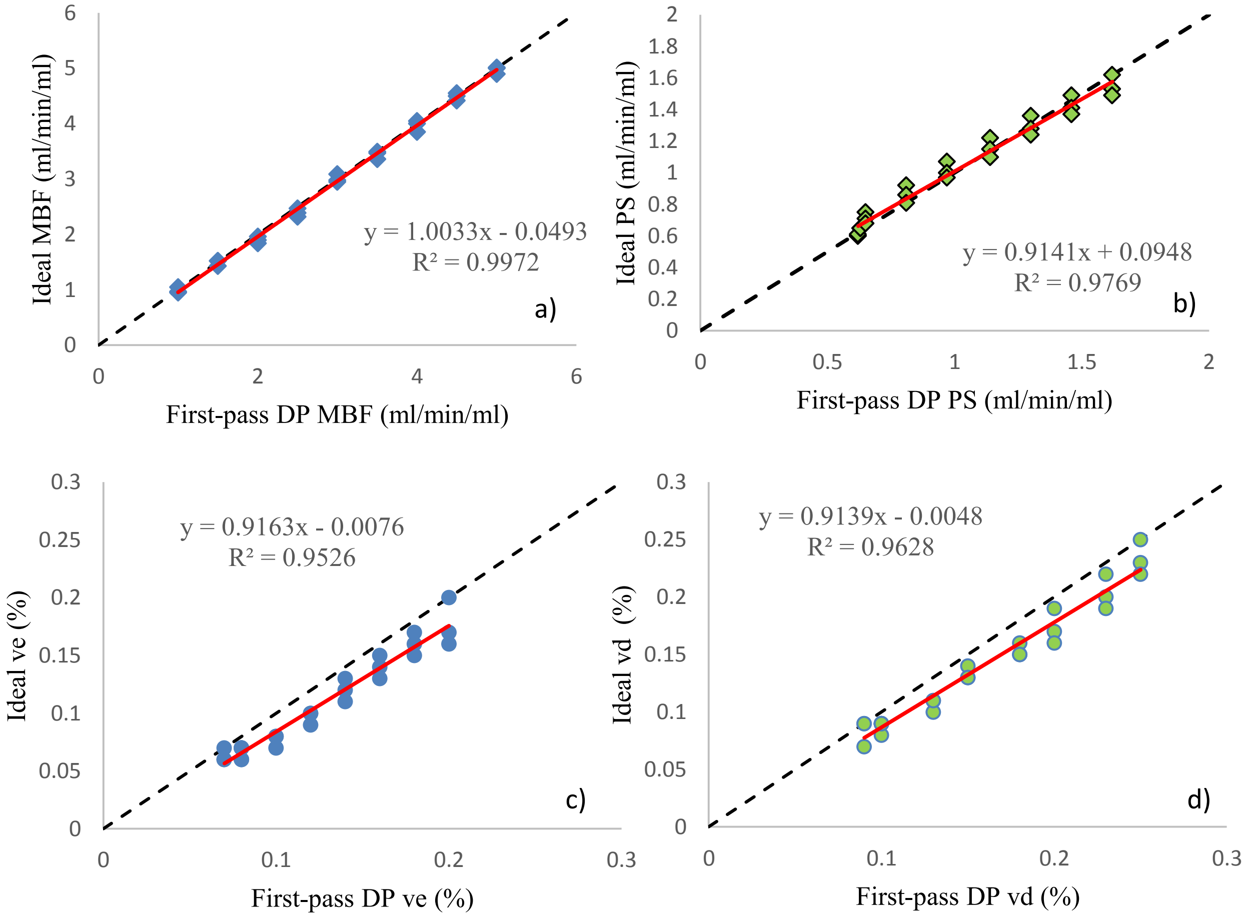

Figure 6-4) Visual representation of linear regression analysis showing ideal values versus first-pass distributed parameter modelling-derived values for myocardial blood flow (MBF, blue diamond), permeability surface area product (PS, green diamond), extravascular-extracellular space (v_e, blue circles) and volume of distribution (v_d, green circles). Black dashed line shows perfect relationship between y and x axis data (i.e. ideal values=measured values) for comparison. First-pass distributed parameter modelling-derived values for v_e and v_d were consistently underestimated as compared to ideal values.

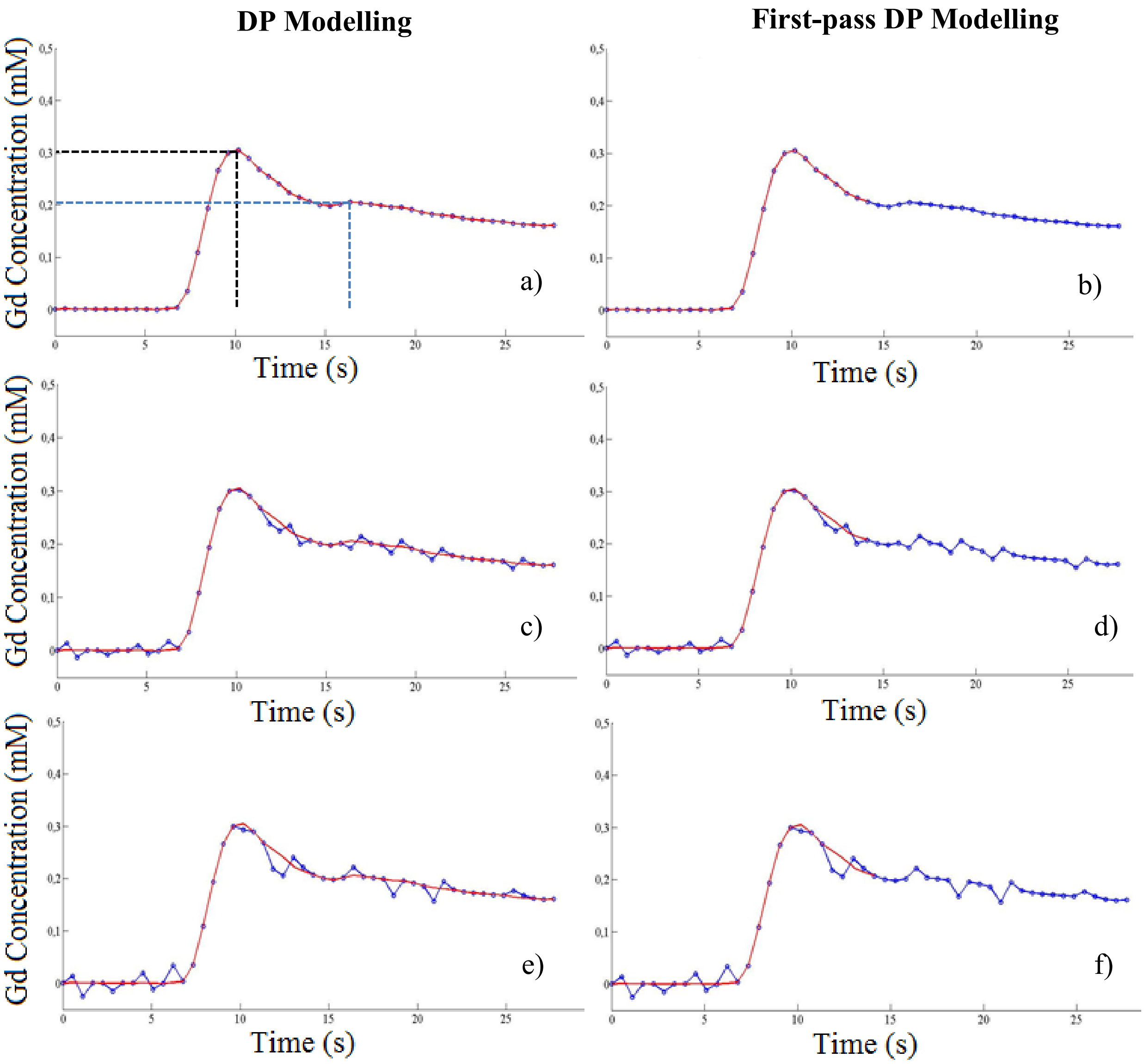

Figure 6-5) Example images of DP and first-pass DP modelling in simulated curves with first-pass to recirculation peak ratio of 1.5. Dashed black and blue lines indicate the height of the first-pass peak and of the recirculation peak, respectively. Simulated curves with no noise (a, b), with noise level 1 (c, d) and noise level 2 (e, f).

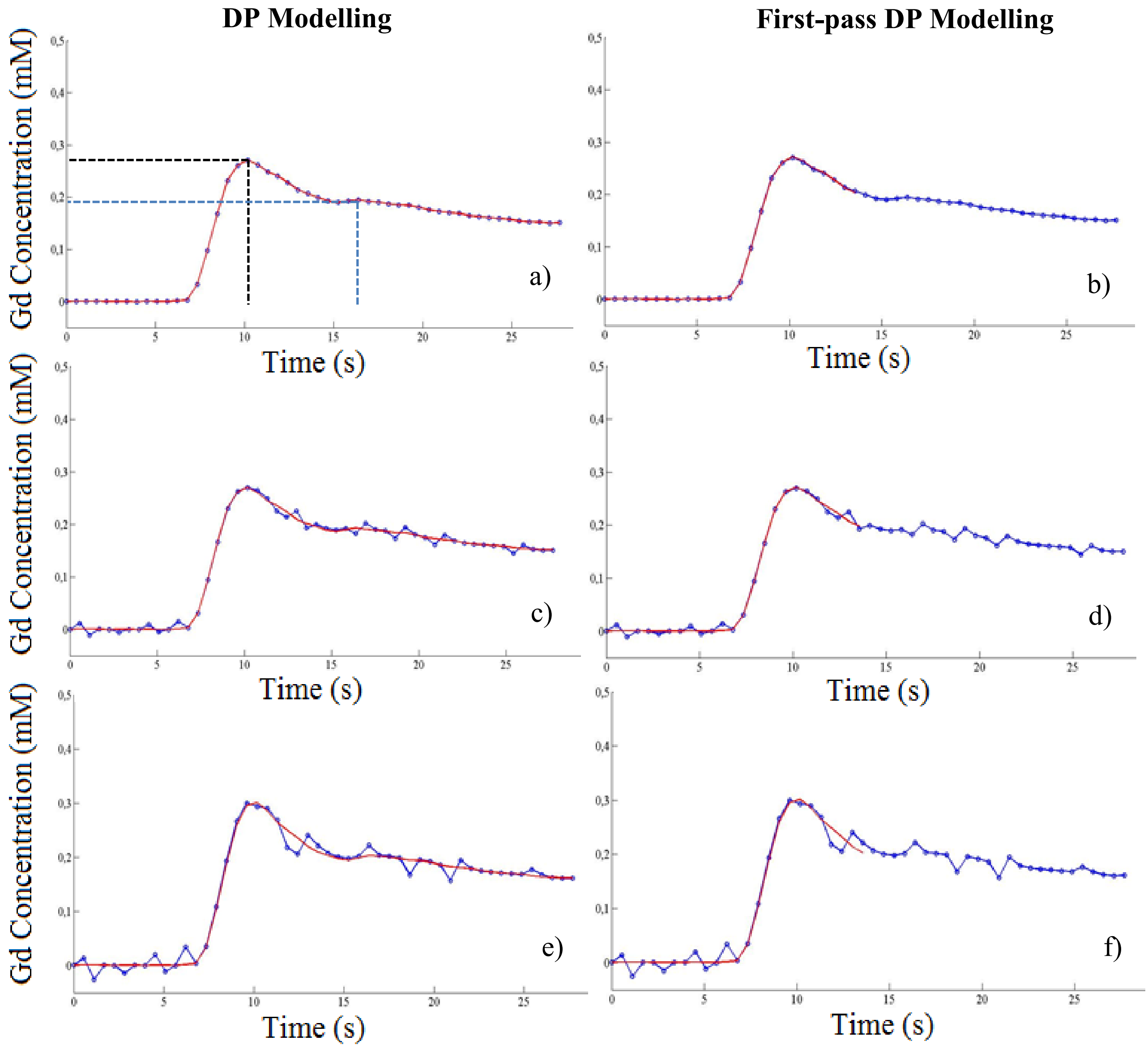

Figure 6-6) Example images of DP and first-pass DP modelling in simulated curves with first-pass to recirculation peak ratio of 1.4. Dashed black lines show the height of the first-pass peak whilst the dashed blue lines indicate the height of the recirculation peak. Simulated curves with no noise (a, b), with noise level 1 (c, d) and noise level 2 (e, f).

6.4 Discussion

6.4.1 Assessment of DP and first-pass DP modelling

Using numerical simulations, it was demonstrated that there is no significant difference in a) DP-derived and in b) first-pass DP-derived values versus ideal blood flow values from simulated data (Tables 6-3 and 6-4). It was also demonstrated that there were no significant differences in c) DP-derived and in d) first-pass DP-derived values against ideal microvascular characteristic values for myocardial blood flow, permeability surface area product, extraction fraction and intravascular space (Tables 6-3 and 6-4). Moreover, these results were independent of whether the recirculation peak is lower or higher (first-pass to recirculation peak of 1.5 and 1.4, respectively) compared to the first-pass peak.

With the use of numerical simulations, it has previously been shown that if the time frame selected for Fermi modelling analysis will be extended beyond the first-pass range, blood flow estimates can be significantly underestimated [24, 28]. Another study using 20 healthy subjects, demonstrated that Fermi modelling derived-blood flow estimates were significantly higher (approximately 25% on average) when all the acquired data were used for blood flow analysis versus when only the first-pass of contrast enhancement was analyzed. The perfusion acquisition time in this study was approximately one minute [37].

Performing numerical simulations, the current study demonstrated that DP modelling can be implemented for myocardial blood flow quantification independently of the number of time points used for fitting, provided that a time range that includes at least the first-pass in the blood pool is chosen for the analysis. As discussed in chapter 5, the first-pass range typically varies from subject to subject in in-vivo data but was commonly in the range between 20-35 dynamic frames in the perfusion data that were generated for this thesis. Determining the lack of dependence of DP modelling on the number of time points used for fitting, is important for assessment of the DP model's potential for myocardial blood flow analysis of clinical MR data, in which the length of the first-pass range can differ between single [28, 29, 34, 53, 66] and dual bolus [54-56] imaging protocols (described also in subsection 6.1 and illustrated in Figure 6-2). Both single and dual bolus protocols have been widely used for cardiac MR perfusion imaging [24]. Recently, dual bolus protocols were applied in patient cohorts in order to eliminate signal saturation at the peak of the arterial input function, for myocardial blood flow quantification [58, 59]. This raises again the question as to whether the first-pass range can be defined from the main bolus or the scaled pre-bolus arterial input function when one is analysing dual bolus data. Such a modelling approach, showing lack of dependence on the time range selected for analysis (provided that a time range that includes at least the first-pass in the blood pool is chosen for the analysis), can therefore reduce the subjectivity for the selection of the first-pass range in cardiac MR data. Furthermore, such a modelling approach could potentiallyu facilitate automatic software algorithms for myocardial blood flow quantification [56].

These results agree with the assumption that the first-pass range of MR data is likely to be the phase of contrast enhancement most sensitive to changes in blood flow [24, 54]. To date, only the Fermi model has been used to measure myocardial blood flow estimates from the first-pass of MR data, as described previously [24, 54]. Using numerical simulations it was shown here that although DP modelling is ideally implemented using the full curve in order to calculate both myocardial blood flow and microvascular characteristics, first-pass DP modelling can be as accurate as DP modelling, for myocardial blood flow quantification.

When the recirculation peak was higher (first-pass to recirculation peak of 1.4) compared to the first-pass peak, there were no significant differences in c) DP-derived and in d) first-pass DP-derived values against ideal microvascular characteristic values for all parameters. Significant differences between first-pass DP-derived and ideal values for extravascular-extracellular space and for distribution volume were observed, but only for the set of curves with first-pass to recirculation peak ratio of 1.5 (Table 6.3). As mentioned, tissue curves with first-pass to recirculation peak ratio of 1.5 were common in MR perfusion data of healthy volunteers generated for this thesis. Furthermore, both the extravascular-extracellular space and distribution volume were lower when first-pass DP modelling was implemented in MR data from eight healthy volunteers, compared to DP modelling analysis (chapter 5, Table 5-4). The fact that there are no significant differences between first-pass DP modelling and ideal values for blood flow and intravascular space in these curves, leads to the following concluding points (A and B, see next page) that can be derived from the microvascular characteristic relationships, presented in Table 5-2.

A. No significant differences between first-pass DP-derived and ideal values for intravascular space, means that the fitted parameters a) MBF (myocardial blood flow, see Table 5-1) and b) T_c (mean capillary transit time) remained unchanged:

$$v_b = MBF \cdot T_c$$

where v_b is intravascular space.

B. Considering unchanged values for blood flow and T_c, significant reductions observed in first-pass DP-derived extravascular-extracellular space and distribution volume versus ideal values, were caused by decreases in fitted parameter T (mean overall transit time, see Table 5-2) according to:

$$v_e = MPF \cdot \left(T - T_c\right)$$

$$v_d = MPF \cdot T$$

where v_e is extravascular-extracellular space, v_d is distribution volume and MPF is myocardial plasma flow. Plasma flow and blood flow are interrelated through:

$$MPF = MBF \cdot \left(1 - hct\right)$$

where hct is an assumed value for haematocrit (=0.45).

Consequently, the only parameter being influenced in first-pass DP modelling for the set of curves with first-pass to recirculation peak ratio of 1.5, was the fitted parameter T. Differences in the profile of the simulated curves between curves with first-pass to recirculation peak ratio of 1.5 and of 1.4, can possibly explain these reductions in T. Simulated curves with lower recirculation peak (peak ratio 1.5) have a steeper downslope during the wash out of the contrast agent (Figure 6-5), compared to simulated curves with higher recirculation peak (peak ratio of 1.4) which form a gradual downslope (Figure 6-6). In the former case, a rapid downslope may correspond to a faster wash out of contrast agent particles, which in turn may result in a lower value for T. The physiological definition of T is the mean time elapsed for contrast agent particles to enter and leave a myocardial segment [50].

In agreement with the above interpretation (point B), reductions in the fitted parameter T_e (note that the fitted parameter T_e is only used for the calculation of the permeability surface area product, PS) can possibly explain why the PS did not significantly change when the first-pass DP modelling was used.

These findings indicate that as the number of the time frame (used for model fitting) reduces, DP modelling may become over-parameterised because the contribution of v_e on the curve may decrease. Thus, v_e may not be possible to be estimated with precision. In that case, the application of the plug flow uptake model (50) may become appropriate. The tissue impulse response of the plug flow uptake model in the Laplace domain is:

$$R(s) = \frac{1 - e^{-s \cdot Tc}}{s} + E \cdot \frac{e^{-s \cdot Tc}}{s}$$

where $s = i \cdot 2 \cdot \pi \cdot f$ and f is the frequency variable in the Fourier transformed data. Fitted parameters for the plug flow uptake model: myocardial blood flow, mean capillary transit time T_c and extraction fraction E. It is important to note that the application of the plug flow uptake model would provide a practical mean to determine whether v_e is measurable as the time frame reduces, since it would not fit data where the no-efflux (back-diffusion from the extravascular-extracellular into the intravascular space) assumption is invalid (50).

This study assessed whether DP modelling and first-pass DP modelling can give accurate estimates of blood flow and of microvascular characteristics, compared to ideal values from numerical simulations. Thus, it was not in the objectives of this study to further assess which may be the minimum time frame required for DP analysis to accurately calculate extravascular-extracellular space and distribution volume in curves with first-pass to recirculation peak ratio of 1.5. This analysis can possibly suggest that for the precise calculation of microvascular characteristics, DP modelling may need to be extended beyond the first-pass range of the contrast agent bolus in the blood pool.

6.4.2 Study limitations

This study did not investigate independent pharmacokinetic model approaches for generating simulated data [28, 43], in order to compare against DP and Fermi modelling results. Despite the fact that such independent pharmacokinetic model approaches can be based upon theoretical assumptions of tracer kinetics analysis [28, 43], their accuracy in generating realistic simulated data has not been assessed versus simulated blood flow data from flow phantoms [43], or against results from microsphere techniques in animal models [28]. Independently of this, the above analysis aimed to assess whether first-pass DP modelling can give accurate estimates of blood flow and of microvascular characteristics, versus simulated data generated by convolving the DP model with the entire arterial input function curve.

Simulated data generated using the DP model were created using an optimum arterial input function from a healthy subject. This arterial input function curve was derived from dynamic perfusion data acquired using specific image acquisition parameters, presented in subsection 5.2.2. Thus, it has not been assessed whether first-pass DP modelling analysis can give accurate estimates of blood flow and of microvascular characteristics against simulated data generated using other combinations of scanners/image acquisition protocols which would possibly cause differences in temporal resolution and signal to noise ratio, compared to the data acquired for this thesis.

6.5 Conclusions

First-pass DP-derived myocardial blood flow was not significantly different compared to ideal values from numerical simulations. These results demonstrate that unlike Fermi modelling, myocardial blood flow analysis using DP modelling does not depend on the number of time points used for fitting.

DP modelling can be an appropriate approach for quantitatively analysing myocardial blood flow from the first-pass of MR data. For the precise calculation of the extravascular-extarcellular space and distribution volume parameters, DP modelling may need to be convolved with the entire arterial input function curve.

Summary

This chapter described a comparison of DP modelling and first-pass DP modelling-derived blood flow and microvascular characteristic values against ideal values from numerical simulations. First-pass DP modelling-derived blood flow values were not different compared to ideal values. This comparison may suggest that DP modelling can reduce the sensitivity in selection of the first-pass range used in other quantitative modelling of cardiac perfusion MR data. This may help to facilitate development of more reliable automated software algorithms for myocardial blood flow quantification in the clinical setting. Sensitivity to accurate selection of first-pass range currently limits many algorithms to require manual input for this process.

The next chapter investigates a model comparison between Fermi and DP modelling using a cohort of 24 patients with known or suspected coronary artery disease with a single bolus perfusion imaging protocol. The diagnostic ability of both modelling approaches is assessed in per vessel and per patient basis.

7. Quantitative assessment of myocardial blood flow in coronary artery disease by magnetic resonance: a comparison with invasive methods and visual assessment from MR and CT.

Introductory summary

The primary objective of this chapter describes an assessment of quantitative MR analysis against invasive clinical assessment. Fermi and distributed parameter modelling were compared against invasive coronary angiography and fractional flow reserve outcomes, to assess their diagnostic ability in detecting obstructive coronary artery disease. In addition, the diagnostic accuracy of visual estimates from MR and CT imaging in detecting obstructive coronary artery disease was also assessed against invasive methods. Visual assessment is the current noninvasive reference standard for the detection of coronary artery disease from clinical MR and CT data. Finally, the diagnostic accuracy between quantitative MR analysis (using both models) and visual estimates from MR and CT imaging were compared, for the detection of coronary artery disease.

7.1 Background

Magnetic resonance (MR) perfusion imaging is a promising technique for the non-invasive assessment of coronary artery disease [135, 142]. Clinically, the current standard method of assessment of MR perfusion imaged is based on visual estimates of the images, or in some studies a semi-quantitative assessment of perfusion index has been used [143, 144]. Visual assessments rely on the presence of myocardial areas with normal perfusion for direct comparison. Visual estimates are particularly difficult in multi-vessel disease where there may be minimal areas of normal perfusion to compare against, or in cases of severe left ventricular impairment [59] in which slow bolus dispersion may lead to homogenously low contrast enhancement in the myocardium . Mathematical modelling of perfusion imaging data allows absolute quantification of myocardial blood flow and may be particularly useful in multi-vessel disease. By quantifying perfusion, it also has the potential to minimize interobserver variability and to improve the diagnosis and prognostication of coronary artery disease [24, 59, 137].

As described in previous chapters (chapters 5 and 6), Fermi deconvolution modelling is an empirical-mathematical model used to estimate myocardial blood flow from MR perfusion imaging data during first-pass of gadolinium-based extracellular contrast agents [28, 29]. Distributed parameter deconvolution modelling is based upon physiological principles of tracer kinetics analysis and it can provide myocardial blood flow quantification and additional information about coronary vascularity and permeability [50, 66]. This includes estimates of intravascular space, extravascular-extracellular space, permeability surface area product, extraction fraction and volume of distribution.

Recent advances in multi-detector computed tomography (MDCT) have enhanced its role beyond the assessment of coronary artery stenosis [84, 90, 95, 98-101]. The major strength of CT coronary angiography has been shown to be the high sensitivity and negative predictive value in identifying and excluding obstructive coronary artery disease, respectively [16, 79, 84, 85, 90, 145]. However, in the context of obstructive coronary artery disease, the main disadvantage of CT angiography is its reduced specificity, due to its inclination to overestimate heavily calcified lesions [84, 86].

A further step towards accurate detection of functionally significant stenotic lesions using CT is the implementation of myocardial perfusion imaging. CT myocardial perfusion imaging is additive to CT angiography whilst it is useful in the evaluation of patients with coronary artery stents [146, 147]. The latest generation of 320-slice MDCT scanners, is capable of improved spatial resolution and image quality at lower radiation doses. Despite this, the main limitation to the dynamic investigation of cardiac perfusion with CT, is still the radiation exposure [84, 90, 95, 98-101, 148, 149]. Thus, the functional significance of coronary atherosclerosis may only currently be assessed using MDCT "snapshot" (or static) perfusion techniques [84, 90, 148-150]. The main challenge in snapshot MDCT imaging is that variability in heart rate under stress and rest conditions means that care must be taken to select the optimum timing for static image acquisition at the peak of contrast enhancement (in the myocardial tissue). If static images are obtained before or after the peak of contrast enhancement, assessment of relative hypo-enhancement in myocardial perfusion defect areas becomes challenging, either due to microvascular recirculation or due to venous drainage [150].

The objective of this chapter was two-fold. To investigate whether Fermi or distributed parameter modelling may be more accurate in detecting reduced myocardial blood flow in obstructive coronary artery disease versus the current invasive clinical standard assessment of invasive coronary angiography and fractional flow reserve. Also, the diagnostic accuracy of Fermi and distributed parameter modelling in detecting obstructive coronary artery disease was compared against the current clinical standard of visual estimate analysis of MR and CT perfusion imaging.

7.2 Methods

7.2.1 Study population and design

Twenty four patients with history of stable angina and with known or suspected coronary artery disease were recruited for MR perfusion imaging. All patients received MDCT 'snapshot' perfusion imaging within 30 days prior to MR perfusion imaging. Exclusion criteria for all subjects included history of severely compromised renal function (glomelural filtration rate ≤ 30 ml/min), pregnancy and contraindications to MR imaging or to iodinated contrast agent [151]. The study was performed with the approval of the institutional research ethics committee, in accordance with the Declaration of Helsinki and with the written informed consent of all subjects. All subjects were instructed to abstain from caffeine for 12 hours before MR and CT imaging. All patients underwent invasive coronary angiography and fractional flow reserve measurement.

7.2.2 Cardiac magnetic resonance imaging

As described in chapter 5, MR perfusion imaging data were acquired using a 3T Verio system (Siemens AG, Healthcare Sector, Erlangen, Germany) and a 32-channel coil. Standard cardiac imaging planes and a short axis stack of left ventricular cine data were acquired using routine steady state free precession (TrueFISP) acquisitions (subsection 4.2 and 5.2.2). The modified Look-Locker inversion (MOLLI) recovery technique was again used to calculate native T_1 relaxation rates (subsections 2.2.6, 4.1 and 5.2.2) [12, 138]. Stress imaging was performed by intravenously administering 140 µg/kg/min of adenosine for 4 minutes (Adenoscan, Sanofi Aventis). Fifty dynamic perfusion images were obtained at diastole across three short-axis view slices, covering 16 of the standard myocardial segments [16], using a turbo-fast low angle shot (FLASH) saturation recovery prepared single-shot gradient echo pulse sequence, as described in subsection 5.2.2.

A single bolus protocol was implemented in all subjects using 0.05 mmol/kg of a gadolinium-based contrast agent (Gadovist, Bayer Healthcare) injected at 4 ml/s. To allow clearance of residual contrast agent, rest perfusion imaging was performed 15 min after the adenosine-stress scan with the same acquisition protocol in all subjects [24, 28, 29, 76, 141].

7.2.3 Cardiac multi-detector computed tomography imaging

Prior to CT imaging, blood pressure and heart rate were monitored. Patients with resting heart rate above 60 beats/ min received heart rate-limiting medication either with intravenous infusion of metoprolol (2.5-50 mg) or with oral/ intravenous administration of verapamil (80 mg oral or 2.5-5 mg intravenous). Administration of rate-limiting medication occurred to improve image quality by reducing exposure to motion artifacts, which may affect image acquisition at higher heart rates [151].

Patients were placed supine in a 320-slice multidetector scanner (Aquilion One, Toshiba Medical Systems, Tustin, CA, USA). As in MR perfusion imaging, two intravenous lines (one for contrast delivery and one for adenosine infusion) were inserted in each patient.

Scout images were acquired to allow scan positioning corresponding to the minimum detector range [150]. Following the acquisition of scout images, patients underwent prospective electrocardiogram-gated (iodine-based) contrast enhanced CT angiography at rest (using iomeprol, 400 mg iodine/ml, Iomeron 400, Bracco, UK), with half-segment reconstruction and a 0.35 ms rotation time [99, 150, 151]. As mentioned in the subsection 4.9, the iodinated contrast was administered based on body mass index (BMI) (i.e. <30 kg/m^2, 50 ml; >30 kg/m^2, 60 ml; >40 kg/m^2, 70 ml). Tube voltage was selected based on body mass index whilst tube current was selected automatically based on scout image attenuation. Bolus tracking triggered the scan following a predetermined trigger delay, immediately after blood in the aorta reached 300 HU [150, 151]. A narrow window for acquisition was selected to reduce radiation exposure. A high tube current was applied for a narrow temporal window around end diastole in an attempt to optimally acquire detailed anatomical images with high spatial resolution. A low tube current was implemented for the rest of the cardiac cycle to obtain complementary functional (perfusion) information. A subsequent iodine-based contrast bolus injection was injected after 4 min of adenosine infusion (at a rate of 140 μg/kg/min, Adenoscan, Sanofi Aventis) and prospective ECG-gated images were again acquired at end diastole during stress, implementing the same image acquisition parameters.

For patients with a heart rate below 65 beats/ min, CT images were acquired using an acquisition window of 70-80% of the cardiac cycle (i.e. interval between two QRS complexes). For patients with a heart rate above 65 beats/ min, the acquisition window was widened (30-80%) to ensure image acquisition at end diastole.

Images were reconstructed using an iterative reconstruction algorithm (AIDR3D) and by processing the phase with the least cardiac motion for both CT angiograms and perfusion images [151]. CT angiograms were reconstructed with a slice thickness of

0.5 mm, whilst short axis view planes of (rest and stress) perfusion images were reconstructed with a slice thickness of 3 mm.

7.2.4 Invasive coronary angiography and fractional flow reserve

All patients underwent invasive coronary angiography and fractional flow reserve at the Royal Infirmary of Edinburgh. Fractional flow reserve was assessed for major epicardial vessels and defined as the ratio between distal coronary pressure and aortic pressure measured simultaneously at maximal adenosine-induced (intravenous 140μg/kg/min) hyperaemia [109, 117]. Epicardial vessels were classified as positive for obstructive coronary artery disease as previously described in subsection 5.2.4. Haemodynamically significant (obstructive) coronary artery disease was defined as luminal stenosis ≥70% on invasive coronary angiography, or fractional flow reserve <0.80 and luminal stenosis ≥50 %. Outcomes from the three main coronary vessels were classified into 2 groups: Group 1, (no, minor or non)-obstructive coronary artery disease with luminal stenosis <50% or with luminal stenosis ≥50% and fractional flow reserve>0.80; Group 2, obstructive coronary artery disease with luminal stenosis of ≥70% alone, or luminal stenosis ≥50% and fractional flow reserve ≤0.80 [109, 117].

7.2.5 Visual analysis

MR perfusion images were analyzed by 2 blinded experienced observers. CT angiograms and static CT perfusion images were visually assessed by 3 and 2 experienced blinded observers, respectively. The MR perfusion scans were classified as positive for obstructive coronary artery disease in the presence of a stress-induced perfusion defect which was transmural and/or involved ≥ 1 myocardial segment [58] and the CT perfusion scans classified as positive in the presence of a stress-induced perfusion defect involving ≥ 1 myocardial segment [98].

7.2.6 Quantitative MR analysis

Endocardial and epicardial MR contours were outlined using dedicated cardiac image analysis software (QMass, Medis, The Netherlands) to generate a standardized 16-segment model of the heart [16]. Quantification of myocardial blood flow was performed using customised in-house software developed in Matlab (MathWorks Inc., Natick, MA), as previously described in subsections 5.2.5-5.2.7. Myocardial and arterial input function signal intensity-time curves were converted to gadolinium concentration-time curves using the method of Larsson et al [24-29]. Model-dependent deconvolution analysis was implemented to measure myocardial blood flow using a) Fermi and b) 1-barrier 2-region distributed parameter functions. In distributed parameter modelling, additional microvascular characteristics were calculated using equations described in Table 5-2. Myocardial perfusion reserve was calculated by dividing the hyperemic myocardial blood flow by the resting flow. The mean myocardial perfusion reserve of the two lowest scoring myocardial segments for each perfusion territory was also calculated for each vessel territory and its accuracy in detecting obstructive coronary artery disease was examined [58, 59].

7.2.7 Statistical analysis

The R software was used for statistical analysis (R Foundation for statistical computing, Vienna, Austria). Receiver-operating characteristic (ROC) analysis was used to determine threshold values and positive likelihood ratios for absolute myocardial blood flow at stress, myocardial perfusion reserve and myocardial perfusion reserve of the two lowest scoring segments with the greatest sensitivity and specificity to detect obstructive coronary artery disease (Groups 2 versus Group 1). The maximal Youden Index was used to determine the optimal threshold values. The area under the curve was calculated using trapezoidal numerical integration.

An interobserver reliability analysis was performed for visual estimates using Cohen kappa statistic. Statistical differences in myocardial blood flow values and in myocardial perfusion ratios between patient Groups (Group 2 against Group 1), were investigated implementing a Welch two sample *t*-test. Statistical significance was defined as two-sided P value<0.05.

7.3 Results

7.3.1. Study population

Table 7-1 shows baseline characteristics of the study participants. Twenty four patients received MR perfusion imaging and CT perfusion imaging and angiography. MR perfusion images were not considered diagnostic in two patients due to low contrast to noise ratio. Thus, epicardial vessels from twenty two patients were visually assessed, corresponding to sixty six epicardial vessels available for visual MR analysis. Quantitative MR analysis and visual CT analysis were performed in all twenty four patients, corresponding to seventy two epicardial vessels.

All patients underwent invasive coronary angiography and fractional flow reserve assessment. Sixteen patients (67%) had at least 1 territory classified in Group 2. Ten had 1-vessel disease, two had 2-vessel disease and four had 3-vessel disease. Example images of MR perfusion imaging, CT perfusion imaging and angiography and invasive coronary angiography are shown in Figure 7-1.

7.3.2 Visual MR analysis versus invasive methods

The interobserver reliability was kappa=0.81 (95% CI: 0.69 to 0.89). In per vessel analysis, vessel classification occurred as described in subsection 7.2.4. In per patient analysis, patients with all vessel territories identified with (no, minor or non)-obstructive coronary artery disease were classified in Group 1, whilst patients with at least one vessel detected with obstructive coronary artery disease, were classified in Group 2. Based on these criteria (that were applied throughout this study), diagnostic accuracy (i.e. sensitivity, specificity, positive predictive value and negative predictive value) in per vessel and per patient visual MR analysis against invasive methods, are presented in Table 7-2.

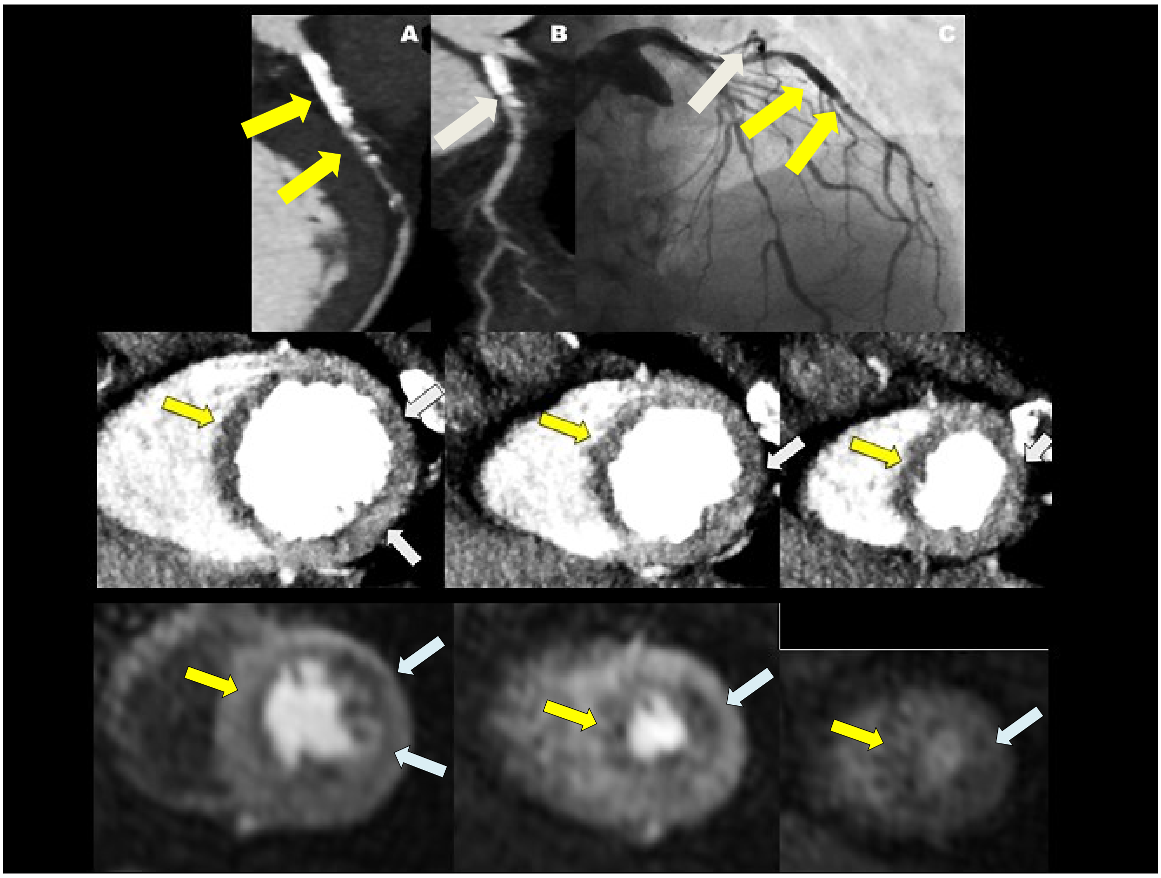

Figure 7-1) Images from the same patient. Upper panel: Computed tomography coronary angiography (**A** and **B**) and invasive coronary angiography (**C**) images showing stenoses in the left anterior descending, first diagonal (yellow arrows) and left circumflex arteries (gray arrow). Middle panel: Computed tomography myocardial perfusion imaging during adenosine stress. Short-axis views of the left ventricle during adenosine stress showing hypo-enhancement corresponding to perfusion defects in the territory of the left anterior descending artery (yellow arrows) and left circumflex artery (gray arrows). Lower panel: Magnetic resonance myocardial perfusion imaging during adenosine stress. Short-axis views at 3 mid-ventricular slices over the left ventricle are presented with perfusion defects that correlate to the computed tomography images. (Adapted from Williams et al, J Cardiovasc Comput Tomogr, 2013).

Table 7-1) Baseline characteristics of study participants (parentheses show %).

Parameter	Data (n=24)
Age (yrs)	63 ± 7
Male	20 (83)
BMI	29 ± 5
Hypertension	13 (54)
Hct	0.43 ± 0.02
Diabetes	
Type 1	0 (0)
Type 2	3 (13)
Angina	23 (96)
NSTEMI	4 (17)
STEMI	3 (13)
PVD	0 (0)
CVD	2 (8)
Smoking	
Current	6 (25)
Previous	15 (63)
PCI	4 (17)
Medication	
Statin	21 (88)
Beta-blocker	20 (83)
Angiographic data (per vessel)	
Group 1	46 (64)
Group 2	26 (36)

Abbreviations for Table 7-1: Body mass index (BMI), Haematocrit (Hct), non-ST segment elevation myocardial infarction (NSTEMI, see subsection 4.2 and Figure 4-5 for QRS complex signal), ST segment elevation myocardial infarction (STEMI), peripheral vascular disease (PVD), cardiovascular disease (CVD), percutaneous coronary intervention (PCI).

Table 7-2) Diagnostic accuracy (i.e. sensitivity, specificity, PPV, NPV) (95% CI) of visual MR estimates is shown. PPV: positive predictive value and NPV: negative predictive value, are presented in per vessel and per patient basis.

Visual estimates from MR	Per vessel	Per patient
Sensitivity	0.73 (0.50 to 0.88)	0.79 (0.49 to 0.94)
Specificity	0.80 (0.64 to 0.89)	0.88 (0.47 to 0.99)
PPV	0.64 (0.43 to 0.81)	0.92 (0.60 to 0.99)
NPV	0.85 (0.70 to 0.94)	0.70 (0.35 to 0.92)

7.3.3 Quantitative MR analysis versus invasive methods

Initially, quantitative myocardial blood flow analysis was performed on a per vessel basis. ROC analysis was implemented to determine threshold values for absolute myocardial blood flow at stress, myocardial perfusion reserve and mean myocardial perfusion reserve of the two lowest scoring segments, with the greatest sensitivity and specificity to detect obstructive coronary artery disease. Threshold values are presented in Table 7-3.

Table 7-3) Threshold values for all haemodynamic parameters calculated with Fermi and distributed parameter (DP) modelling, in per vessel and per patient basis. Thresholds for myocardial blood flow were measured in ml/min/ml. MBF: myocardial blood flow, DP: distributed parameter, MPR: myocardial perfusion reserve, MPR_2: mean myocardial perfusion reserve of the two lowest scoring segments.

Haemodynamic parameter-Model	Per vessel	Per patient
MBF Fermi (ml/min/ml)	2.6	3.0
MBF DP (ml/min/ml)	1.7	2.1
MPR Fermi	2.1	2.5
MPR DP	1.4	1.9
MPR_2 Fermi	1.8	2
MPR_2 DP	1.2	1.4

Mean values for all Fermi- and distributed parameter modelling-derived haemodynamic parameters, for both Groups 1 and 2, are presented in Table 7-4. Significant differences in haemodynamic parameter values between Groups 1 and 2 for both Fermi and distributed parameter modelling are shown in Table 7-4. Mean values and haemodynamic thresholds are illustrated in Figures 7-2 to 7-7.

Diagnostic accuracy (sensitivity, specificity, positive predictive value and negative predictive value) for Fermi- and distributed parameter modelling-derived haemodynamic parameters calculated on ROC analysis, are presented in Table 7-5. Areas under the curve and positive likelihood ratios for Fermi- and distributed parameter modelling-derived haemodynamic parameters are presented in Tables 7-6 and 7-7, respectively. ROC analysis graphs are illustrated in Figures 7-8 to 7-10.

Significant differences were observed in all distributed parameter modelling-derived microvascular characteristics, between Groups 1 and 2 ($P < 0.01$).

Table 7-4) Mean (SD) values for Fermi- and distributed parameter modelling-derived haemodynamic parameters, for Groups 1 and 2 are presented. Also, significant differences between Group 1 and Group 2 in per vessel and per patient based analysis are shown. P values for distributed parameter modelling were consistently higher compared to Fermi modelling in both per vessel and pet patient based analysis. Notations as in Table 7-3.

Haemodynamic parameter- Model	Per vessel		Per patient		Per vessel	Per patient
	Group 1	Group 2	Group 1	Group 2	Group 1 vs Group 2	Group 1 vs Group 2
MBF Fermi (ml/min/ml)	2.54 (0.95)	1.95 (0.64)	3.13 (0.64)	1.93 (0.72)	0.0026	0.000000002
MBF DP (ml/min/ml)	2.03 (0.70)	1.36 (0.39)	2.52 (0.39)	1.42 (0.47)	<0.0001	<0.000000001
MPR Fermi	2.20 (0.83)	1.54 (0.57)	2.72 (0.63)	1.59 (0.59)	0.0002	0.0000000001
MPR DP	1.80 (0.69)	1.12 (0.38)	2.27 (0.59)	1.20 (0.38)	<0.0001	<0.0000000001
MPR_2 Fermi	1.87 (0.78)	1.10 (0.48)	2.31 (0.68)	1.23 (0.53)	0.000001	0.0000000002
MPR_2 DP	1.55 (0.63)	0.86 (0.31)	1.98 (0.54)	0.96 (0.31)	<0.000001	0.0000000001

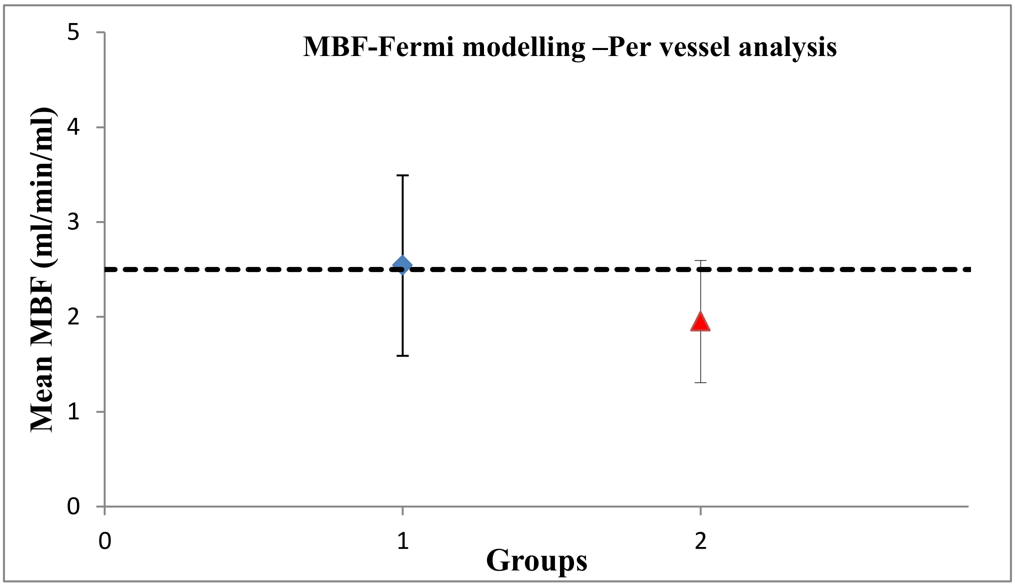

Figure 7-2) Fermi modelling-derived mean myocardial blood flow (MBF) values and haemodynamic threshold calculated on ROC analysis, for identifying obstructive vessels (per vessel analysis).

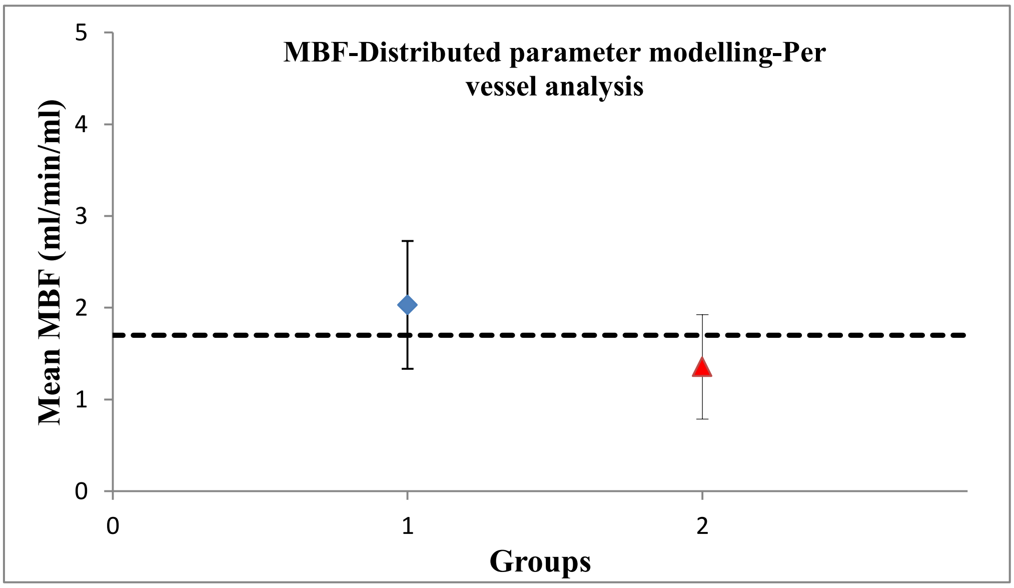

Figure 7-3) Distributed parameter modelling-derived mean myocardial blood flow (MBF) values and haemodynamic threshold calculated on ROC analysis, for identifying obstructive vessels (per vessel analysis).

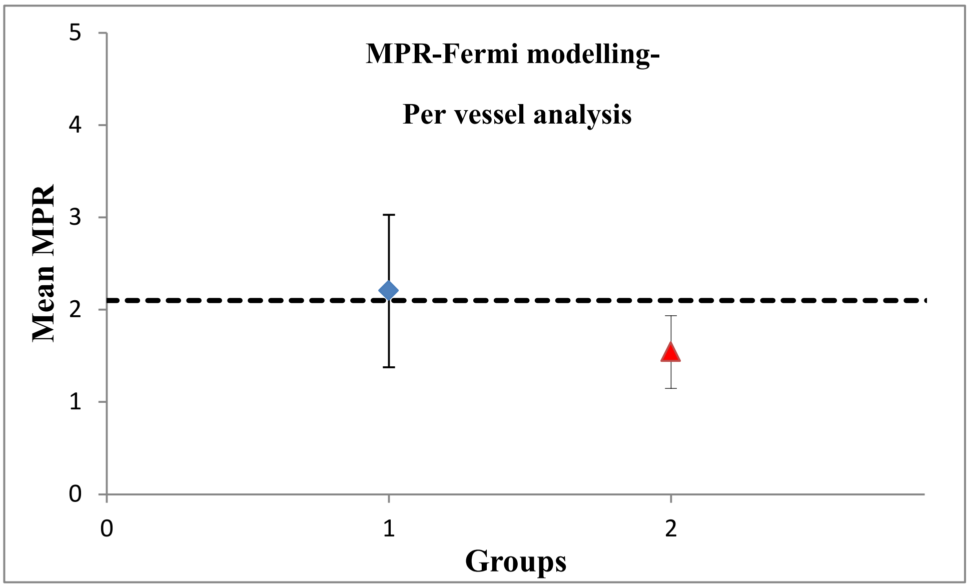

Figure 7-4) Illustrations of Fermi modelling-derived mean myocardial perfusion reserve (MPR) values and haemodynamic threshold, between Groups 1 and 2.

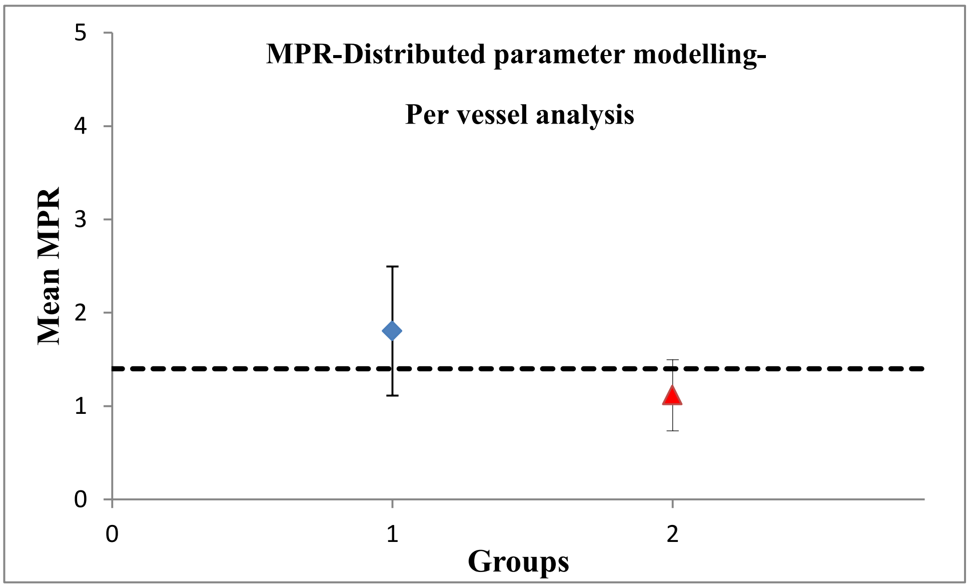

Figure 7-5) Graphic representation of distributed parameter modelling-derived mean myocardial perfusion reserve (MPR) values and haemodynamic threshold, between Groups 1 and 2.

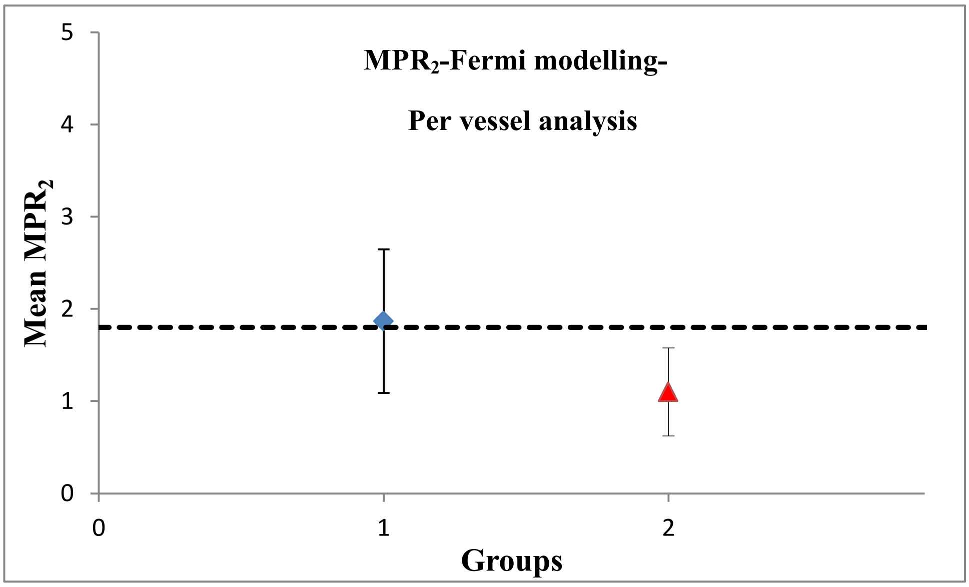

Figure 7-6) Mean myocardial perfusion reserve of the two lowest scoring segments (MPR_2) calculated using Fermi modelling and haemodynamic threshold, between Groups 1 and 2.

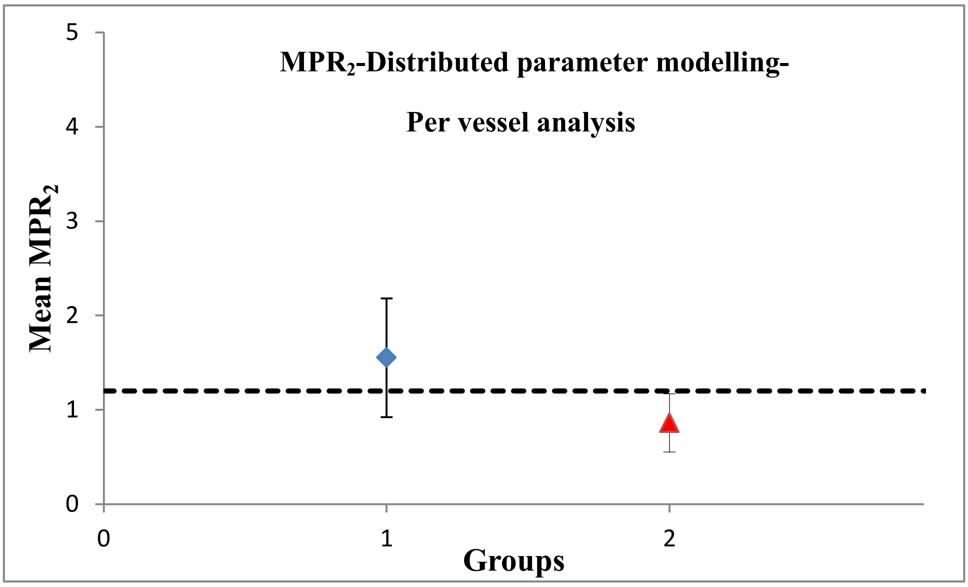

Figure 7-7) Graphic representation of mean myocardial perfusion reserve of the two lowest scoring segments (MPR_2) calculated using distributed parameter modelling and haemodynamic threshold, between Groups 1 and 2.

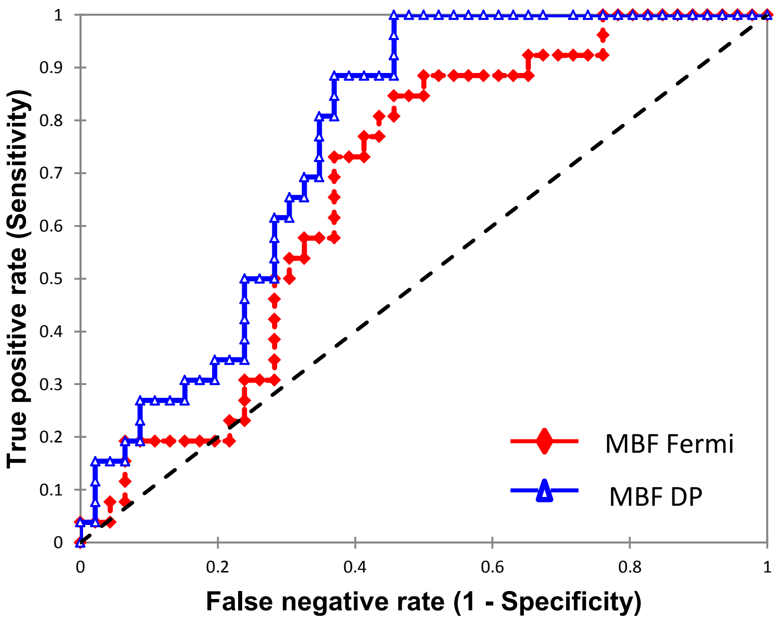

Figure 7-8) ROC graph demonstrating sensitivity and specificity of quantitative MR analysis by absolute myocardial blood flow at stress (MBF, per vessel analysis).

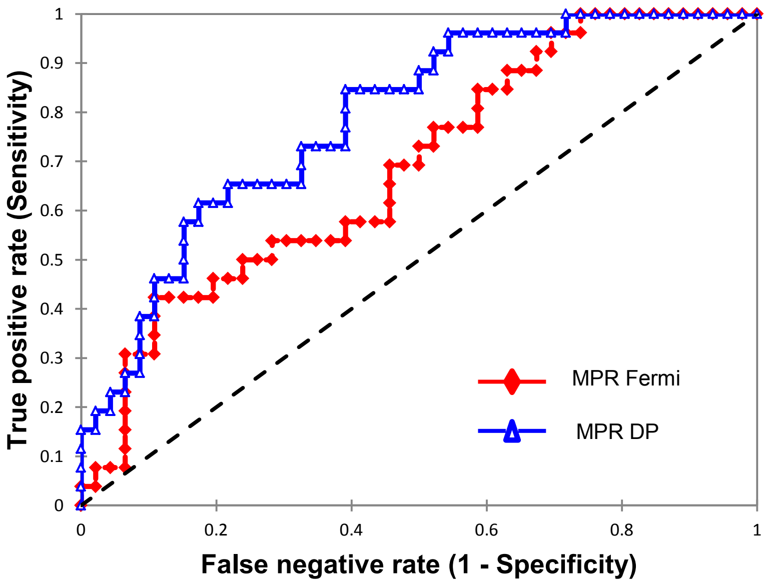

Figure 7-9) ROC graph showing sensitivity and specificity of quantitative MR analysis by myocardial perfusion reserve (MPR, per vessel analysis).

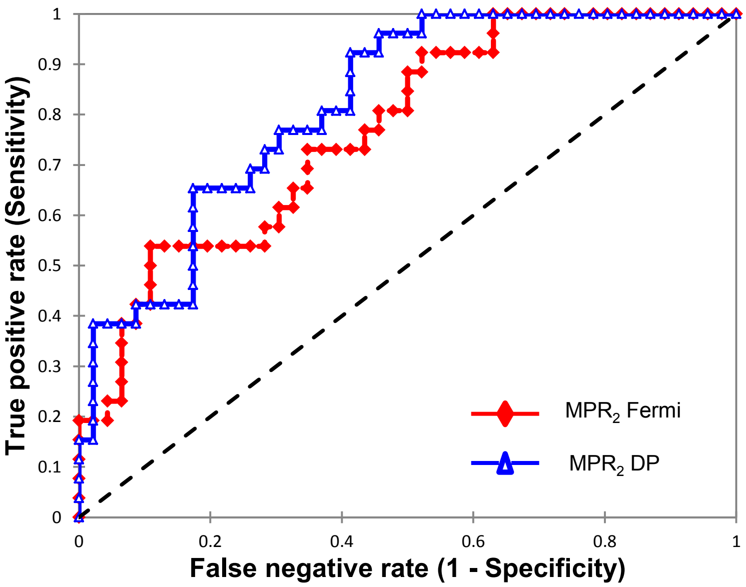

Figure 7-10) ROC graph illustrating sensitivity and specificity of mean myocardial perfusion reserve of the two lowest scoring segments (MPR$_2$, per vessel analysis).

Table 7-5) Diagnostic accuracy (95% CI) of Fermi- and DP modelling-derived haemodynamic parameters, in detecting obstructive coronary artery disease, is shown (per vessel analysis). Notations as in Tables 7-2 and 7-3.

Haemodynamic parameter-Model	Sensitivity	Specificity	PPV	NPV
Fermi-MBF	0.85 (0.76 to 0.94)	0.54 (0.43 to 0.65)	0.51 (0.39 to 0.63)	0.86 (0.74 to 0.98)
DP-MBF	0.89 (0.79 to 0.99)	0.63 (0.52 to 0.74)	0.58 (0.48 to 0.68)	0.91 (0.84 to 0.98)
Fermi-MPR	0.69 (0.50 to 0.88)	0.54 (0.40 to 0.68)	0.46 (0.32 to 0.60)	0.76 (0.62 to 0.90)
DP-MPR	0.85 (0.72 to 0.98)	0.61 (0.48 to 0.74)	0.55 (0.43 to 0.67)	0.88 (0.76 to 1.00)
Fermi-MPR2	0.73 (0.58 to 0.88)	0.65 (0.51 to 0.79)	0.54 (0.40 to 0.68)	0.81 (0.68 to 0.94)
DP-MPR2	0.77 (0.62 to 0.92)	0.70 (0.56 to 0.84)	0.58 (0.46 to 0.70)	0.84 (0.75 to 0.94)

Table 7-6) AUC (95% CI) from ROC analysis in per vessel and per patient basis are shown. AUC: Areas under the curve, rest of notations as in Table 7-3.

AUC	Per vessel	Per patient
MBF Fermi	0.68 (0.55, 0.80)	0.86 (0.77, 0.94)
MBF DP	0.76 (0.65, 0.87)	0.97 (0.92, 1.00)
MPR Fermi	0.69 (0.56, 0.81)	0.85 (0.75, 0.94)
MPR DP	0.79 (0.68, 0.89)	0.94 (0.87, 1.00)
MPR2 Fermi	0.77 (0.66, 0.88)	0.88 (0.80, 0.96)
MPR2 DP	0.82 (0.72, 0.92)	0.96 (0.91, 1.00)

Table 7-7) Positive likelihood ratios in per vessel and per patient analysis are demonstrated.

	Per vessel	Per patient
MBF Fermi	2.65 (1.65 to 4.27)	2.50 (1.01 to 6.17)
MBF DP	3.13 (1.94 to 5.06)	7.50 (1.19 to 40.11)
MPR Fermi	1.86 (1.27 to 2.71)	2.50 (1.01 to 6.17)
MPR DP	3.54 (2.06 to 6.08)	7.50 (1.19 to 41.11)
MPR2 Fermi	2.16 (1.46 to 3.21)	2.33 (0.94 to 5.82)
MPR2 DP	3.00 (1.84 to 4.88)	3.25 (0.96 to 11.04)

Subsequently, quantitative myocardial blood flow analysis was performed in per patient basis. As discussed in subsection 7.3.2, in per patient based analysis, haemodynamic parameters are used to attempt to identify reduced myocardial blood flow in patients with at least one vessel detected with obstructive coronary artery disease (which were here classified in Group 2) against patients with all vessel territories identified with (no, minor or non)-obstructive coronary artery disease (which were classified in Group 1). Threshold values calculated on ROC analysis are presented in Table 7-3.

Distributed parameter modelling-derived myocardial blood flow and myocardial perfusion reserve detected reduced myocardial blood flow in 47 and 46 of the 48 vessel territories of patients with at least one vessel territory classified in Group 2 (3 territories/patient, 16 patients), respectively. Fermi modelling-derived myocardial blood flow and myocardial perfusion reserve both detected reduced myocardial blood flow in 42 of the 48 vessel territories of patients with at least one vessel territory classified in Group 2.

Mean values for all haemodynamic parameter-model combinations, for both Groups 1 and 2, are presented in Table 7-4. Significant differences in haemodynamic parameter values between Group 1 and Group 2, for both Fermi and distributed parameter modelling in per patient based analysis, are presented in Table 7-4. Mean values and haemodynamic thresholds and illustrated in Figures 7-11 to 7-16.

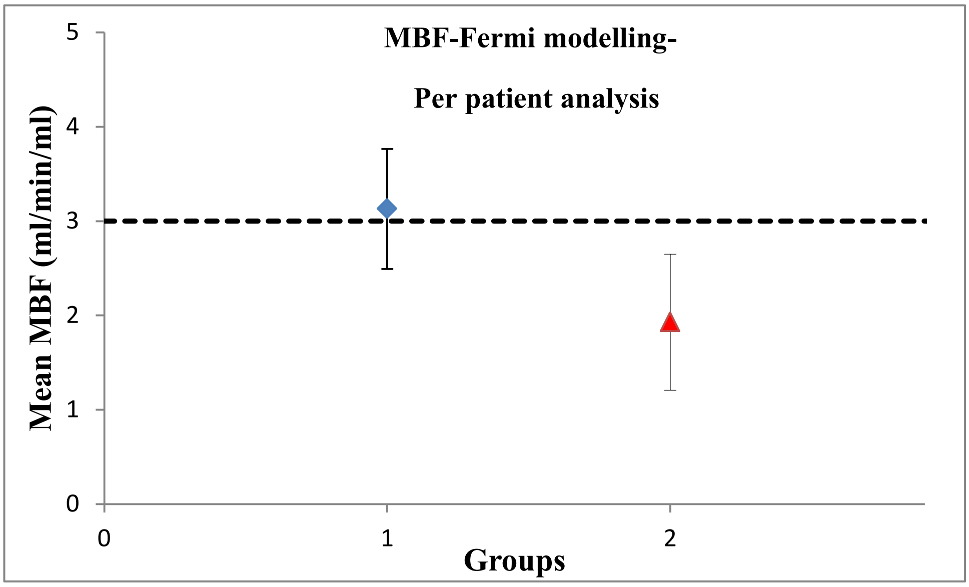

Figure 7-11) Visual representation of Fermi modelling-derived mean myocardial blood flow (MBF) values and haemodynamic threshold, between Groups 1 and 2 (per patient analysis).

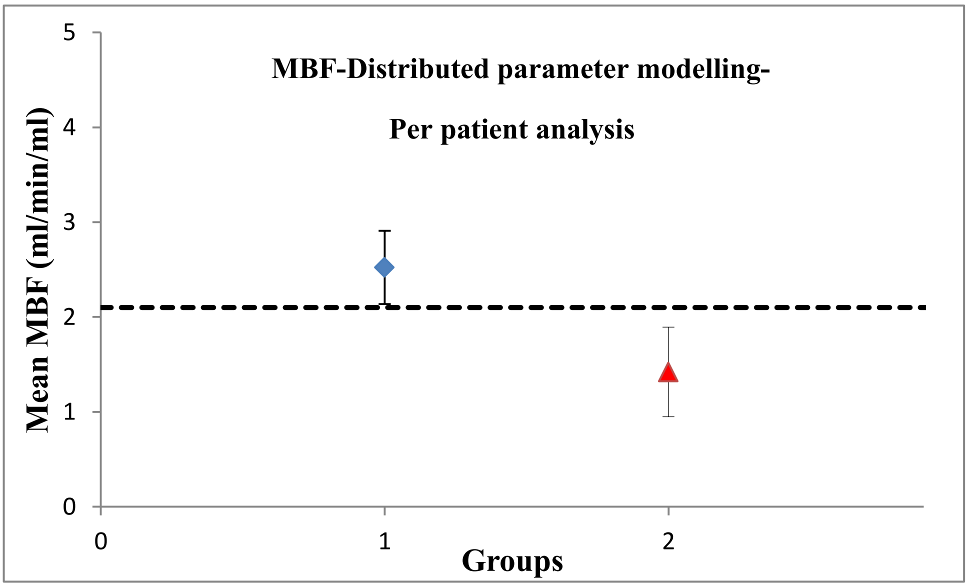

Figure 7-12) Representation of distributed parameter modelling-derived mean myocardial blood flow (MBF) values and haemodynamic threshold, between Groups 1 and 2.

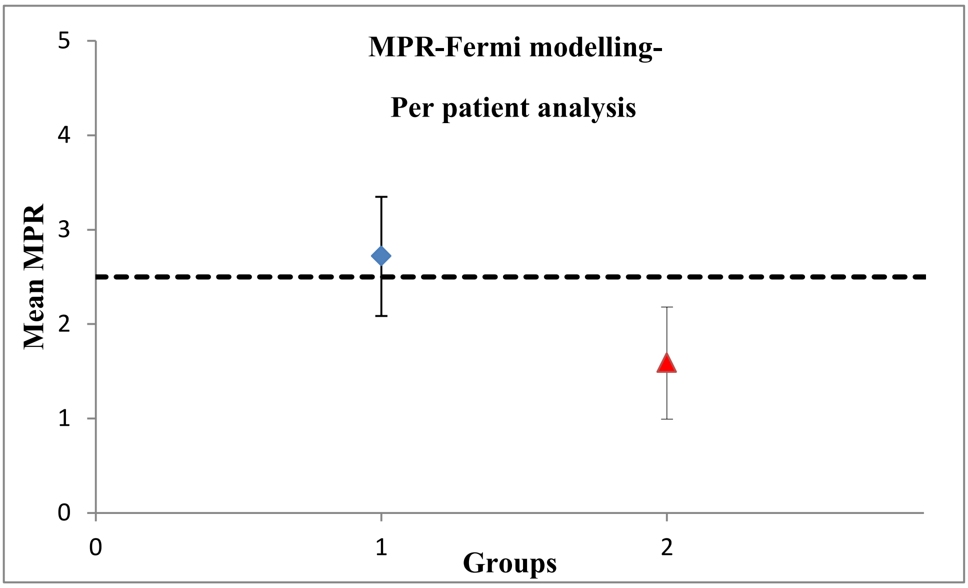

Figure 7-13) Mean myocardial perfusion reserve (MPR) calculated using Fermi modelling and haemodynamic, between Groups 1 and 2.

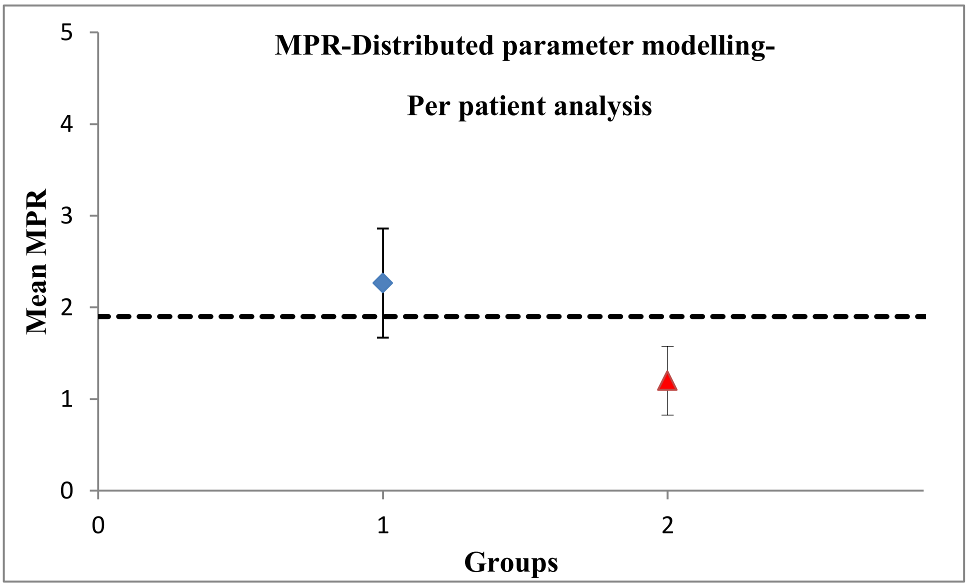

Figure 7-14) Mean myocardial perfusion reserve (MPR) calculated using distributed parameter modelling and haemodynamic threshold on ROC analysis.

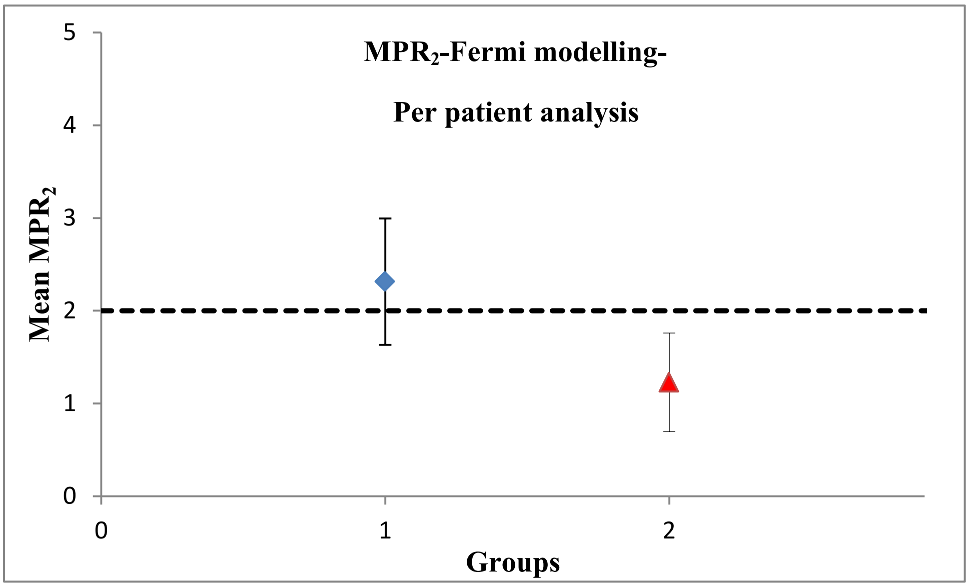

Figure 7-15) Mean myocardial perfusion reserve of the two lowest scoring segments (MPR_2) calculated using Fermi modelling and haemodynamic threshold on ROC analysis.

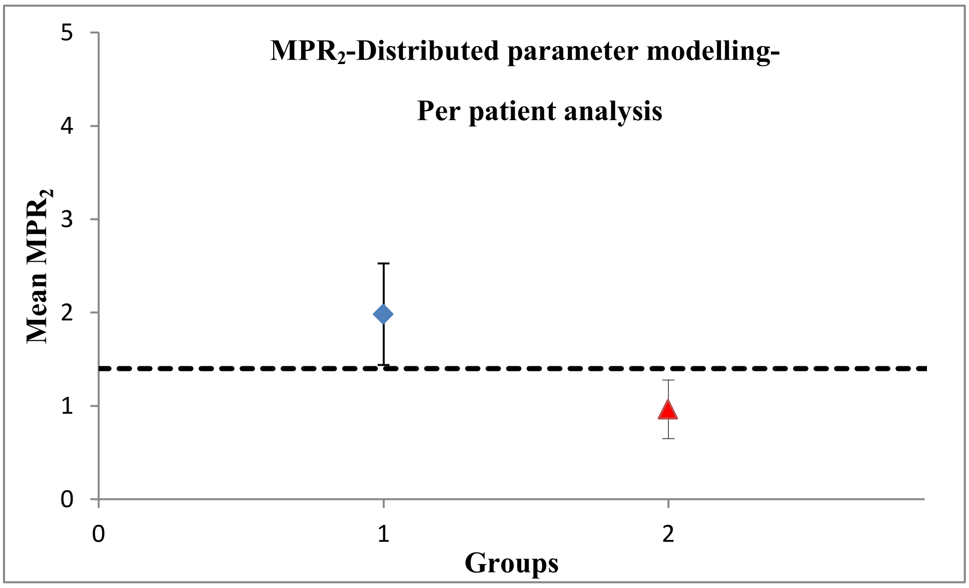

Figure 7-16) Mean myocardial perfusion reserve of the two lowest scoring segments (MPR_2) calculated using distributed parameter modelling and haemodynamic threshold, between Groups 1 and 2.

Diagnostic accuracy for Fermi- and distributed parameter modelling-derived haemodynamic parameters calculated on ROC analysis in per patient basis, are presented in Table 7-8. Areas under the curve and positive likelihood ratios for Fermi- and distributed parameter modelling-derived haemodynamic parameters are presented in tables 7-6 and 7-7, respectively. ROC analysis graphs are presented in Figures 7-17 to 7-19.

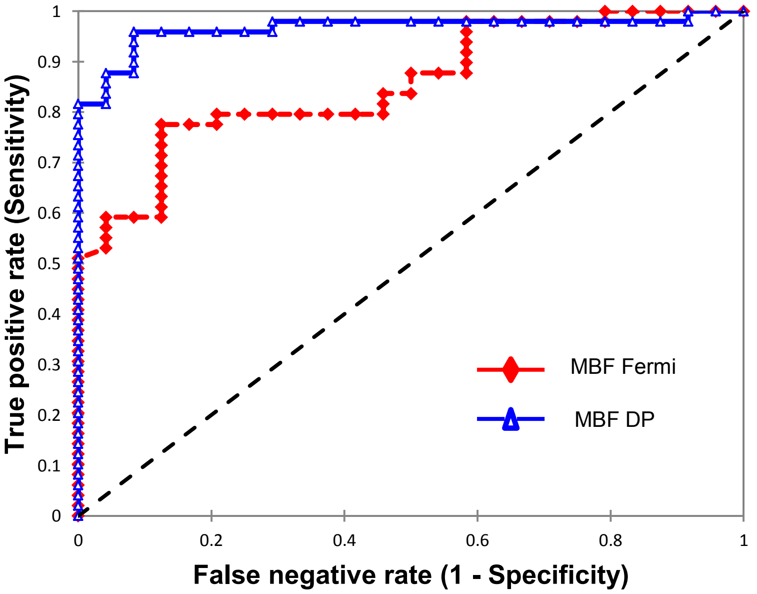

Figure 7-17) ROC graph illustrating sensitivity and specificity of quantitative MR analysis by absolute myocardial blood flow at stress (MBF, per patient analysis).

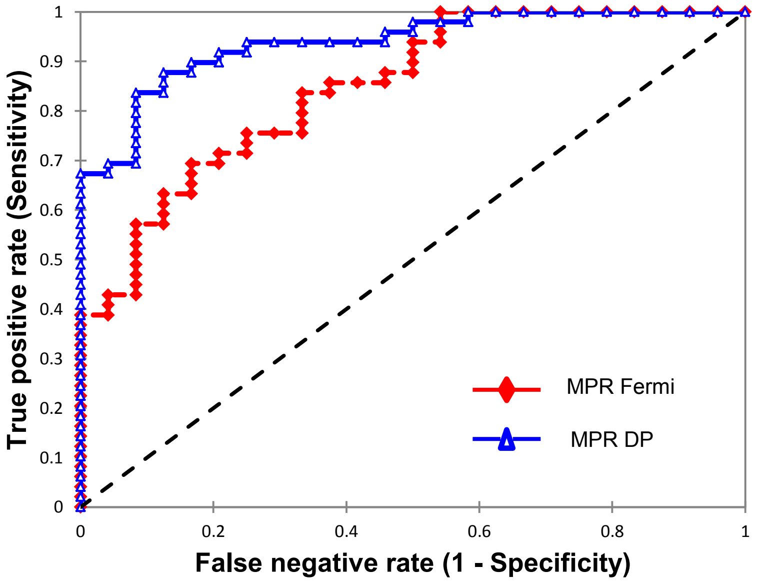

Figure 7-18) ROC analysis demonstrating sensitivity and specificity of quantitative MR analysis by myocardial perfusion reserve (MPR, per patient analysis).

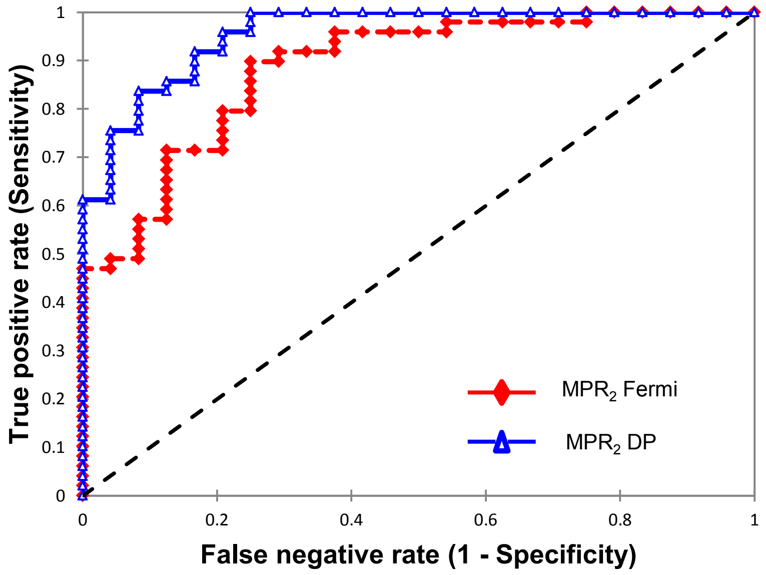

Figure 7-19) ROC analysis showing mean myocardial perfusion reserve of the 2 lowest scoring segments (MPR$_2$, per patient analysis).

Table 7-8) Diagnostic accuracy (95% CI) of Fermi- and DP modelling-derived haemodynamic parameters, in detecting obstructive coronary artery disease, is shown (per patient analysis). Notations as in Tables 7-2 and 7-3.

Haemodynamic parameter-Model	Sensitivity	Specificity	PPV	NPV
Fermi-MBF	0.78 (0.66 to 0.90)	0.88 (0.76 to 1.00)	0.93 (0.86 to 1.00)	0.66 (0.55 to 0.77)
DP-MBF	0.96 (0.91 to 1.00)	0.92 (0.85 to 0.99)	0.96 (0.91 to 1.00)	0.92 (0.84 to 1.00)
Fermi-MPR	0.69 (0.55 to 0.83)	0.83 (0.70 to 0.96)	0.90 (0.80 to 1.00)	0.58 (0.46 to 0.70)
DP-MPR	0.88 (0.76 to 1.00)	0.88 (0.78 to 0.98)	0.94 (0.88 to 1.00)	0.78 (0.66 to 0.90)
Fermi-MPR2	0.80 (0.66 to 0.94)	0.79 (0.62 to 0.94)	0.89 (0.78 to 1.00)	0.66 (0.55 to 0.77)
DP-MPR2	0.92 (0.86 to 0.98)	0.83 (0.74 to 0.92)	0.92 (0.86 to 0.98)	0.83 (0.73 to 0.93)

7.3.4 Visual CT analysis versus invasive methods

The interobserver reliability was kappa=0.80 (95% CI: 0.68 to 0.92) and kappa=0.78 (95% CI: 0.66 to 0.90) for CT angiography and CT perfusion, respectively. The sensitivity, specificity, positive predictive value and negative predictive value of visual estimates from CT angiography, CT perfusion and combined CT angiography/perfusion in detecting a stenosis causing a perfusion deficit are presented in Tables 7-9 and 7-10, for per vessel based and per patient based analysis, respectively.

Table 7-9) Diagnostic accuracy for visual estimates (95% CI) from CT angiography, CT perfusion and CT angiography/perfusion for per vessel territory based analysis.

Visual estimates from CT/ Parameter	CTA	CTP	CTA/CTP
Sensitivity	0.77 (0.56 to 0.90)	0.65 (0.44 to 0.82)	0.85 (0.64 to 0.95)
Specificity	0.87 (0.73 to 0.95)	0.72 (0.56 to 0.84)	0.85 (0.71 to 0.93)
PPV	0.77 (0.56 to 0.90)	0.57 (0.38 to 0.74)	0.76 (0.56 to 0.89)
NPV	0.87 (0.73 to 0.95)	0.79 (0.63 to 0.89)	0.91 (0.77 to 0.97)

Table 7-10) Diagnostic accuracy for visual estimates (95% CI) from CT angiography, CT perfusion and CT angiography/perfusion for per patient based analysis.

Visual estimates from CT/ Parameter	CTA	CTP	CTA/CTP
Sensitivity	0.94 (0.68 to 0.99)	0.81 (0.54 to 0.95)	0.94 (0.68 to 0.99)
Specificity	0.88 (0.47 to 0.99)	0.50 (0.17 to 0.83)	0.88 (0.47 to 0.99)
PPV	0.94 (0.68 to 0.99)	0.76 (0.50 to 0.92)	0.94 (0.68 to 0.99)
NPV	0.88 (0.47 to 0.99)	0.57 (0.20 to 0.88)	0.88 (0.47 to 0.99)

7.4 Discussion

The main findings of this work demonstrated that (1) quantitative MR analysis showed higher diagnostic accuracy (i.e. sensitivity, specificity, positive predictive value and negative predictive value) compared to visual MR analysis. (2) Distributed parameter modelling showed higher diagnostic accuracy than Fermi modelling in detecting obstructive coronary artery disease, both in per vessel and per patient based analysis.

Furthermore, (3) in this data analysis, distributed parameter modelling-derived myocardial blood flow showed higher sensitivity in detecting obstructive coronary artery disease compared to visual estimates from CT analysis, in per vessel based analysis. (4) The highest diagnostic accuracy for the detection of obstructive coronary artery disease was performed by distributed parameter modelling-derived myocardial blood flow at stress, in per patient based analysis.

7.4.1 Visual versus quantitative MR analysis

Data from two patients were considered non-diagnostic for visual assessment, due to low contrast to noise ratio which caused difficulties in detecting relative hypo-enhancement. Thus, these data were excluded from visual analysis. In contrast, model analysis of these data was possible whilst the profiles of dynamic perfusion curves did not differ compared to data from other patients (Figure 7-20).

In per vessel based analysis, visual MR estimates gave higher specificity compared to quantitative MR estimates. However, visual MR estimates showed lower sensitivity, positive predictive value and negative predictive value for the detection of obstructive coronary artery disease than quantitative MR estimates (Tables 7-2 and 7-5). Particularly, quantitative MR analysis showed higher sensitivity using both models and superior positive and negative predictive value using the distributed parameter model, compared to visual MR assessment.

In per patient based analysis, distributed parameter modelling demonstrated superior diagnostic accuracy in detecting obstructive coronary artery disease, compared to visual MR estimates (Tables 7-2 and 7-8). Further interpretation of quantitative MR analysis in per vessel and per patient basis, will be discussed in the following subsections.

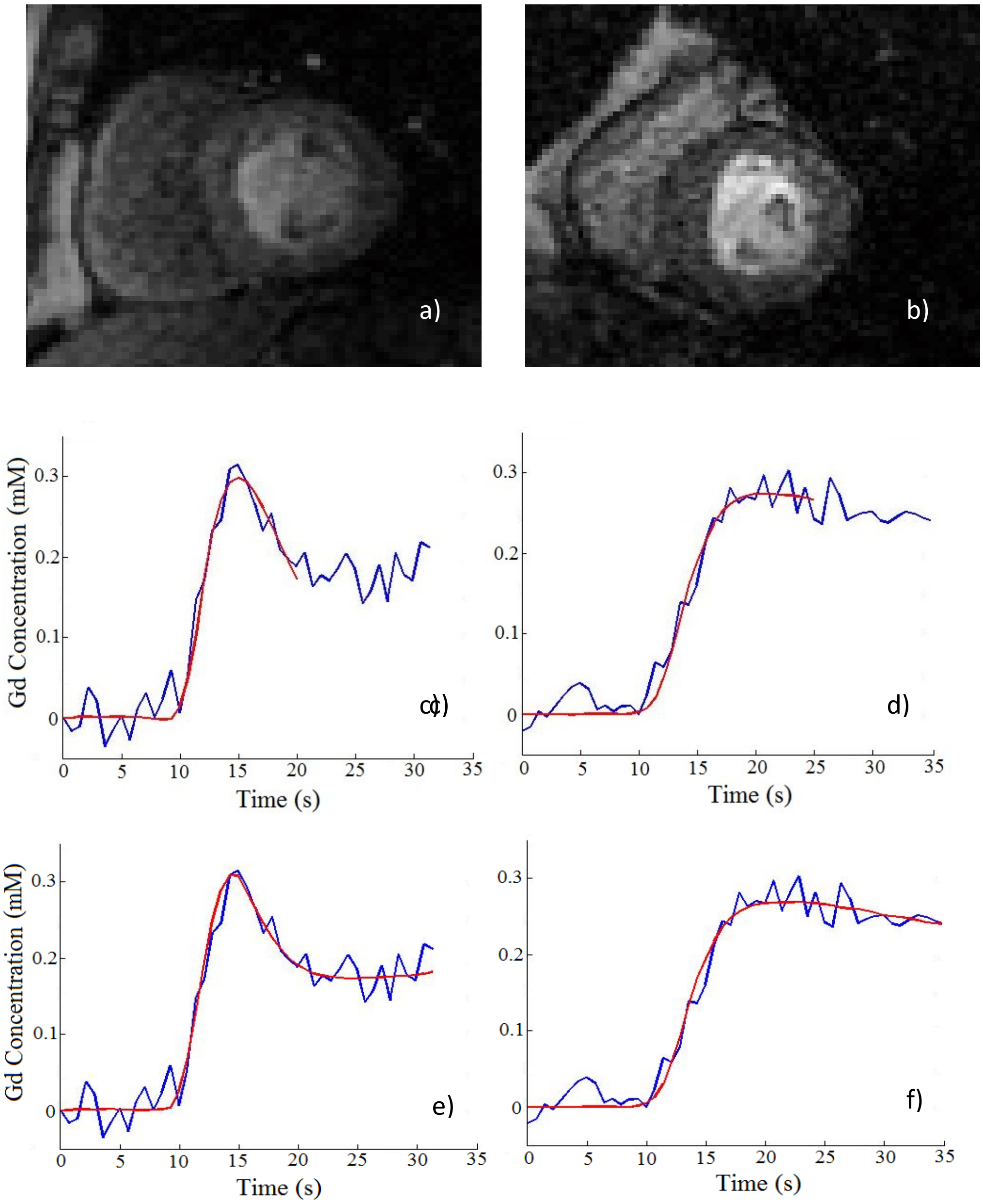

Figure 7-20) Examples of images that were considered non-diagnostic for visual assessment are shown, at the peak of contrast enhancement in the myocardium. Patient 1 (a), identified with no stenotic vessel territories and patient 2 (b), with haemodynamically significant right coronary artery disease. (c) and (d), (e) and (f) are examples of Gadolinium (Gd) concentration-time curves (blue) with Fermi and distributed parameter modelling (red), derived from patients 1 and 2, respectively.

7.4.2 Haemodynamics in quantitative MR analysis

This is the first study implementing 1-barrier 2-region distributed parameter modelling in 24 patients with known or suspected coronary artery disease. Studies using fully quantitative MR perfusion methods are limited either to small numbers of healthy volunteers [29, 36-38, 43] or to the assessment of mean myocardial perfusion reserve of the two lowest scoring segments using Fermi modelling [58, 59].

The optimal thresholds in per vessel (1.7 ml/min/ml) and in per patient (2.1 ml/min/ml) based analysis for hyperaemic myocardial blood flow (Table 7-3), were in agreement with previous positron emission tomography myocardial perfusion studies which aimed to either identify 1, 2 and 3 vessel disease [136] or to localize perfusion defects to significantly stenotic coronary arteries [152, 153] (see Table 7-11). Positron emission tomography is currently the reference standard for absolute quantification of myocardial blood flow [59, 135-137]. At the time of writing this thesis, no other MR perfusion imaging study has accurately identified perfusion abnormalities in the presence of significant coronary artery disease, using absolute myocardial blood flow values at stress.

Table 7-11) Haemodynamic threshold values from previous positron emission tomography (PET) and magnetic resonance imaging (MRI) studies. MBF: myocardial blood flow, MPR: myocardial perfusion reserve, MPR2: mean myocardial perfusion reserve of the two lowest scoring segments.

[Reference] Previous studies (imaging modality, haemodynamic parameter).	Haemodynamic thresholds (angiographic threshold)
[136] Nesterov et al (PET, MBF)	2.50 ml/min/ml (≥ 50%)
[152] Karamitsos et al (PET, MBF)	2.45 ml/min/ml (≥ 50%))
[153] Hajjiri et al (PET, MBF).	1.85 ml/min/ml (≥ 70%)
[153] Hajjiri et al (PET, MPR).	2.00 (≥ 70%)
[137] Kaufmann et al (PET, MPR)	2.50
[58] Lockie et al (MRI, MPR_2)	1.58 (≥ 70%)
[59] Morton et al (MRI, MPR_2)	1.58 (≥ 70%)

The Fermi model demonstrated higher haemodynamic thresholds both in per vessel (2.6 ml/min/ml) and in per patient (3 ml/min/ml) based analysis, compared to distributed parameter modelling (Table 7-3). Threshold values for Fermi modelling were also higher compared to previous PET perfusion studies (Table 7-11) [136, 137, 152-154]. Arterial input function saturation effects that may be present in single bolus data have been previously demonstrated to result in significant overestimation of myocardial blood flow in Fermi modelling [24]. Our group has previously demonstrated that the distributed parameter model appears to be less dependent on arterial input function saturation effects, compared to the Fermi model (chapter 5). Furthermore, it has been previously demonstrated that the Fermi model estimates myocardial blood flow values that were significantly increased compared to distributed parameter modelling estimates using either single [66] or dual bolus imaging, applied to eliminate arterial input function saturation (chapter 5). In a cross-correlation study between magnetic resonance imaging and positron emission tomography, Fermi modelling estimated values of myocardial blood flow both at stress and rest which were considerably higher compared to the Patlak model used for quantification of ^{13}N-ammonia perfusion data [59]. Systematic myocardial blood flow overestimation using Fermi modelling may explain its lower sensitivity in detecting hypoperfusion in obstructive coronary artery disease (susceptible to false negatives) compared to distributed parameter modelling. Fermi modelling showed higher haemodynamic thresholds for myocardial perfusion reserve both in per vessel (2.1) and in per patient (2.5) based analysis, compared to distributed parameter modelling (1.4 and 1.9 respectively, Table 7-3). Higher myocardial perfusion reserve values for Fermi modelling can be explained by higher estimated myocardial blood flow values, compared to those estimated by distributed parameter modelling. Myocardial perfusion reserve ratios generated using both Fermi and distributed parameter modelling (Table 7-3) agree with values by Kaufmann et al, reported for quantitative myocardial perfusion analysis in positron emission tomography (see Table 7-11) [137]. Kaufmann et al, reported that myocardial perfusion reserve values

<2.50 can be interpreted as impaired vasodilator capacity leading to reduced myocardial blood flow. Specifically, it was reported that abnormal myocardial perfusion reserve can be due to narrowing of the epicardial coronary arteries, or (in the absence of angiographically demonstrable findings) can possibly reflect dysfunction of the coronary microcirculation [137]. This study does not specify whether the above haemodynamic threshold is connected with a specific angiographic threshold, for which impaired vasodilator capacity can be interpreted as haemodynamically significant. Haemodynamic thresholds presented in Table 7-11, were lower for studies that aimed to detect reduced blood flow in vessel territories with ≥70% luminal stenosis on invasive coronary angiography (compared to those from studies that used angiographic thresholds of ≥50%). For detection of vessel territories with ≥70% luminal stenosis on invasive coronary angiography, lower myocardial perfusion reserve thresholds can be defined. For example, Hajjiri et al accurately detected impaired myocardial perfusion reserve values in territories with ≥70% luminal stenosis on invasive coronary angiography, using a myocardial perfusion reserve threshold of 2.00 [153]. This can explain the relatively low threshold level demonstrated in this chapter for distributed parameter modelling-derived myocardial perfusion reserve in per vessel analysis. Another reason might be the coincidental effect of microvascular dysfunction in this patient data, as 16 of the 24 patients had at least one vessel identified with obstructive coronary artery disease. Thus, low thresholds maintaining high sensitivity on ROC analysis, minimized the detection of false positives (i.e. detection of reduced blood flow in vessels with no, minor or non-obstructive coronary artery disease), in per vessel analysis. Further

interpretation with respect to physiological considerations in per vessel analysis, is given in subsection 7.4.4.

Similarly, thresholds calculated in this study for mean myocardial perfusion reserve ratios of the two lowest scoring segments are in agreement with values from previous magnetic resonance perfusion imaging studies (Table 7-12) [58, 59]. Low thresholds for distributed parameter modelling-derived myocardial perfusion reserve in per vessel analysis can explain low threshold values for mean myocardial perfusion reserve of the two lowest scoring segments.

It is important that significant differences for myocardial blood flow, myocardial perfusion reserve and two lowest scoring segments of myocardial perfusion reserve) between (no, minor or non)-obstructive and obstructive coronary artery disease were considerably higher for distributed parameter modelling, in comparison with Fermi modelling, in per vessel based analysis (Figures 7-2 to 7-7). This was maintained in per patient based analysis (Figures 7-11 to 7-16). These findings suggest that distributed parameter modelling may have merit in stratification of hypoperfusion in obstructive coronary artery disease, than Fermi modelling.

Significant differences between (no, minor or non)-obstructive and obstructive coronary artery disease were observed for all microvascular characteristic values calculated using distributed parameter modelling. Abnormal decreases of coronary blood flow led to reduced values of permeability surface area product. The intravascular space was significantly reduced as a function of luminal coronary stenosis which may indicate impaired recruitment of coronary arteries [24].

7.4.3 Per vessel based quantitative MR analysis

In per vessel based analysis, the distributed parameter model demonstrated higher diagnostic accuracy against the standard Fermi model in detecting impaired haemodynamics in the presence of obstructive coronary artery disease (Table 7-5). Also, the areas under the curve for distributed parameter modelling were consistently higher for myocardial blood flow, myocardial perfusion reserve and two lowest scoring segments of myocardial perfusion reserve, compared to Fermi modelling (Table 7-5, Figures 7-8 to 7-10).

Distributed parameter modelling-derived myocardial blood flow at stress and myocardial perfusion reserve demonstrated superior diagnostic accuracy in detecting hypoperfusion in obstructive coronary artery disease, compared to all other haemodynamic parameter-model combinations (Table 7-5). Moreover, distributed parameter modelling-derived myocardial blood flow at stress reached higher sensitivity compared to myocardial perfusion reserve and mean myocardial perfusion reserve of the two lowest scoring segments, calculated using the distributed parameter model.

7.4.4 Physiological considerations in per vessel analysis

The specificities and positive predictive values were in a lower range compared to the sensitivities and negative predictive values for both modelling approaches in per vessel based analysis (Table 7-5). This means that quantitative MR analysis has identified hypoperfusion in vessels with (no, minor or non)-obstructive coronary artery disease, which have reduced the specificity and positive predictive value (false positives in per vessel analysis).

72 % of the patients with (no, minor or non)-obstructive disease had at least one vessel with obstructive coronary artery disease. Furthermore, the vast majority of the study participants had been referred for angina (96%), were under treatment for cardiac arrhythmias and hypertension (beta blockers, 83 %), were under medication for hyperlipidemia (statins, 88 %) and were previous smokers (63 %), all high risk factors for microvascular dysfunction [155].

It has been demonstrated that distal pre-arterioles in the myocardial microvascular network are more responsive to changes in the intravascular pressure than other types of myocardial vessels and therefore are responsible for auto-regulation of myocardial blood flow [156]. In addition, arterioles are responsive to changes in the intra-myocardial concentration of metabolites and are mainly responsible for the metabolic regulation of myocardial blood flow [155].

It is important to consider that microvascular dysfunction may have a major impact on global myocardial blood flow [137, 155, 156], which could also affect myocardial perfusion in vessels with (no, minor or non)-obstructive coronary artery disease. This may explain why quantitative MR analysis has detected reduced myocardial blood flow in vessels with (no, minor or non)-obstructive coronary artery disease in our population, which in turn decreased the specificity and positive predictive value of both modelling approaches (false positives in per vessel analysis).

Results from the per vessel based quantitative MR analysis demonstrate that it may not always be possible to discriminate vessel territories classified with (no, minor or non)-obstructive coronary artery in patients with at least one vessel classified with obstructive coronary artery disease using quantitative modelling of MR perfusion data. The coincidental effect of microvascular dysfunction in these patients could possibly explain the homogeneous deficiency in coronary blood flow detected with both quantitative modelling approaches.

7.4.5 Methodological considerations in per vessel analysis

Any possible misregistration between the actual architecture of vessel territories and the standard 16-segment model used for myocardial segmentation [16] is a methodological consideration that should not be excluded in both visual and quantitative MR analysis. Both types of analysis can be subject to overlap of vessel territories which could in turn affect the sensitivity and/or specificity of each method. In addition, misregistration between visual MR analysis and quantitative MR analysis is possible and could influence direct comparisons in diagnostic statistics.

In that context, a previous study demonstrated a combination of left circumflex artery and right coronary artery territories for myocardial blood flow analysis, to overcome any overlaps of the above vessel territories [153]. Despite this, the reference method for quantitative MR analysis of myocardial perfusion still occurs across the three major epicardial arteries. This standard type of analysis was also implemented throughout this study (and throughout this thesis).

7.4.6 Per patient based quantitative MR analysis

The diagnostic accuracy of quantitative MR analysis was further examined in per patient based analysis. All patients with at least one vessel territory classified with obstructive coronary artery disease were stratified in Group 2, whilst patients with all vessels classified with (no, minor or non)-obstructive disease were stratified in Group 1.

The sensitivity and positive predictive value for per patient based analysis were improved for both models compared to per vessel based analysis, with distributed parameter modelling reaching the highest diagnostic accuracy (Table 7-8 versus 7-5). On ROC analysis, distributed parameter modelling-derived myocardial blood flow and perfusion reserve detected 47 and 46 of the 48 territories of patients with at least one vessel territory classified in Group 2, respectively. Fermi modelling-derived myocardial blood flow and perfusion reserve, both detected 42 of the 48 vessel territories. Also, the areas under the curve for distributed parameter modelling were considerably higher for myocardial blood flow, myocardial perfusion reserve and two lowest scoring segments of myocardial perfusion reserve, compared to Fermi modelling (Table 7-5, Figures 7-17 to 7-19).

7.4.7 Physiological interpretations in per patient analysis

The per patient based results indicate that distributed parameter modelling may be able to discriminate haemodynamic states of patients with at least one vessel classified with obstructive disease versus patients with all vessels classified with (no, minor or non)-obstructive disease.

On ROC analysis, the Fermi and distributed parameter models detected reduced myocardial blood flow in the entire myocardium in 10 and 11 of 12 patients with 1- and 2-vessel disease, respectively. This can also indicate that in patients with at least one vessel classified with obstructive disease, the overall myocardial perfusion may be consistently lower compared to patients with all vessels classified with (no, minor or non)-obstructive disease (Figures 7-12, 7-14 and 7-16).

To further establish the haemodynamic thresholds for myocardial blood flow and myocardial perfusion reserve demonstrated at this chapter, a larger study population is needed for a follow-up trial.

7.4.8 Visual CT versus quantitative MR analysis

In per vessel based analysis, combined CT angiography/perfusion showed higher specificity and positive predictive value than CT angiography alone. Although visual estimates from CT perfusion imaging showed low to moderate diagnostic accuracy in detecting obstructive coronary artery disease, it has been shown to be additive to CT angiography in per vessel analysis, which is consistent with previous studies [84, 90, 95, 150].

Even though combined CT angiography/perfusion showed higher specificity and positive predictive value, it performed lower sensitivity in detecting obstructive coronary artery disease, compared to distributed parameter modelling-derived myocardial blood flow.

In per patient based analysis, CT angiography and combined CT angiography/perfusion, reached the highest diagnostic accuracy in detecting obstructive coronary artery disease (note: although marginally lower compared to distributed parameter modelling). Diagnostic accuracy parameters presented in this study for both CT angiography and combined CT angiography/perfusion are in agreement with previous studies and can support the potential of the above methods in the clinical setting, for the detection of obstructive coronary artery disease [84, 150].

7.4.9 Study limitations

The above methods need to be assessed in larger patient cohorts to further assess their diagnostic accuracy.

Invasive coronary angiography outcomes were not quantitatively assessed. However, angiographic outcomes were combined with fractional flow reserve in all patients to discriminate haemodynamically significant coronary atherosclerosis [109, 120, 121].

For magnetic resonance perfusion acquisitions, a single bolus protocol was implemented to eliminate patient discomfort. Thus, it was impossible to assess any myocardial blood flow overestimations at the specific contrast agent dose (0.05 mmol/kg) used in this study, due to arterial input function saturation issues. This assessment was made in a cohort of healthy volunteers in chapter 5 (using dual bolus imaging), in which it was shown that the distributed parameter model was less dependent on saturation effects, although at a lower contrast agent dose (0.03 mmol/kg) [141]. However, it is currently shown here that distributed parameter modelling performed higher sensitivity and specificity in detecting obstructive coronary artery disease in single bolus data, than the Fermi model.

T_1 maps of the myocardium in the absence of contrast enhancement were not acquired in 5 patients. For myocardial blood flow quantification, baseline T_1 values for these patients were estimated from T_1 maps of patients with perfusion defects in the same vessel territories.

Currently, the majority of MR myocardial perfusion studies acquire a limited number (typically 3) of noncontiguous two-dimensional short axis slices. Recently, three-dimensional myocardial perfusion methods have been proposed to overcome any limitations deriving from two-dimensional spatial coverage [157, 158]. Although these methods have not been extensively validated, they may provide a larger cardiac coverage for visual and quantitative MR analysis and could possibly provide a more accurate comparison between MR and CT data through registration of the two 3D datasets.

The validity of visual assessments from CT perfusion images may has been affected by the effects of beta blockers administered in some subjects. Beta blockers may have induced pressure decreases in the vasculature which can possibly influence the coronary haemodynamics. Only visual estimates were used at this study for the analysis of CT data. A more direct comparison between MR and CT data would necessitate performing quantification of stenotic lesions from CT angiographic data and semi-quantification of transmural perfusion ratios from CT perfusion data, using dedicated software [90, 95, 98, 150, 151]. At the time of writing this thesis, none of the quantitative CT data analysis was available. In this chapter, the author aimed to compare the diagnostic accuracy of quantitative MR analysis against the current clinical reference standard (i.e. visual assessment) of MR and CT data analysis.

7.5 Conclusions

Analysis of absolute myocardial blood flow at hyperaemia with distributed parameter modelling showed high sensitivity and negative predictive value in detecting hypoperfusion corresponding to haemodynamically significant stenotic vessel territories, assessed using invasive coronary angiography and fractional flow reserve. In this data analysis, the sensitivity and negative predictive value of distributed parameter modelling was higher in detecting impaired haemodynamics, than in the case of Fermi modelling and visual MR estimates.

Distributed parameter modelling reached superior sensitivity in detecting obstructive coronary artery disease compared to visual estimates from CT imaging. CT perfusion was additive to CT angiography and combined CT angiography/perfusion showed high diagnostic accuracy in detecting obstructive coronary artery disease.

In per patient based analysis, the diagnostic accuracy of all methods was improved. Distributed parameter-derived haemodynamic thresholds on ROC analysis may have potential to be established as important biomarkers, in order to stratify patients with obstructive coronary artery disease.

Comparing quantitative MR analysis against invasive methods and visual estimates from MR and CT, this chapter demonstrates that distributed parameter modelling may have a potential as a non-invasive method, at the setting of detection and prognostication of haemodynamically significant coronary artery disease.

Summary

This chapter detailed assessment of quantitative MR analysis using Fermi and distributed parameter modelling against invasive clinical standard methods, using data from 24 patients with known or suspected coronary artery disease. Quantitative MR analysis was also compared against visual MR and CT analysis.

In per vessel analysis, distributed parameter modelling reached superior sensitivity and negative predictive value in detecting obstructive coronary artery disease, compared to both Fermi modelling and visual MR estimates. Moreover, distributed parameter modelling showed higher sensitivity in detecting obstructive coronary artery disease, compared to visual estimates from CT imaging.

In per patient based analysis, haemodynamic thresholds on ROC analysis for distributed parameter modelling showed the highest sensitivity and negative predictive value in stratifying patients with at least one vessel with obstructive coronary artery disease. Assessing these results in larger patient cohorts can potentially establish the use of quantitative MR analysis for the diagnosis and prognostication of haemodynamically significant coronary artery disease.

8. Conclusions and future work

This thesis describes the development of an MRI cardiac perfusion analysis protocol at 3T. Particularly, it focused on the implementation of Fermi and one-barrier, two-region distributed parameter modelling for measuring myocardial blood flow and additional microvascular characteristics from healthy volunteer, simulated and clinical data.

8.1 Summary of conclusions

The work in chapter 5 detailed a comparison of single versus dual bolus estimates of myocardial blood flow, using Fermi and distributed parameter modelling. Dual bolus imaging was implemented in eight healthy volunteers. For the single bolus analysis, the arterial input function was extracted from the standard (main bolus) contrast agent dose component. For the dual bolus analysis, the pre-bolus arterial input function was scaled and used for deconvolution analysis. Fermi modelling demonstrated significant overestimations in myocardial blood flow in single bolus compared to dual bolus analysis [24, 31, 54, 75]. No significant difference was observed in distributed parameter-derived myocardial blood flow estimates between single and dual bolus analysis, which shows that distributed parameter modelling may be less dependent on arterial input function saturation than Fermi modelling.

Fermi modelling is currently the most popular approach for MR perfusion quantification [31, 54, 58, 59, 75, 76]. However, Fermi modelling systematically introduces considerable myocardial blood flow overestimations in single bolus data corrupted due to arterial input function saturation [31, 54, 75]. Single bolus protocols are still widely used in clinical imaging but are substantially limited to only reliably obtaining qualitative assessments (possibly due to the fact that Fermi modelling is mainly selected for quantitative MR perfusion analysis) [24, 58, 59]. The findings of chapter 5 suggest that distributed parameter modelling may allow quantitative assessments from single bolus imaging that can be less dependent on arterial input function saturation. The distributed parameter model can be implemented in single bolus data provided that a relatively low contrast agent dose is used [141]. It is important to mention that the above model analysis has been assessed using a relatively low contrast agent dose at 3T (0.03 mmol/kg, see future work in subsection 8.3).

Implementation of both models in a pilot cohort of five patients with coronary artery disease (CAD), showed that the distributed parameter model detected reduced myocardial blood flow in all 7 vessels with obstructive lesions and in all 5 vessels with non-obstructive lesions when compared against invasive methods that are currently being used as a clinical gold standard assessment. Fermi modelling detected 6 and 3 vessel territories in these patients, respectively.

In chapter 6, distributed parameter and first-pass distributed parameter modelling were further investigated against ideal values from simulated data. Simulated contrast agent concentration curves were produced through the convolution of the distributed parameter model with the entire contrast agent concentration-time course of an optimum arterial input function (derived from data of a healthy subject) [50, 66, 141]. Distributed parameter modelling can be used to calculate myocardial blood flow as well as additional microvascular characteristics including intravascular space, extravascular-extracellular space, permeability surface area product, extraction fraction and volume of distribution [66]. The fitted parameters T_c, T_e and

T were ranged to simulate a series of normal myocardial blood flow values (1.0-5.0 ml/min/ml of tissue). It was demonstrated that distributed parameter-derived myocardial blood flow values generated using only the first-pass time course of the data were not different versus myocardial blood flow values from simulated data generated using the entire time course. This comparison suggests that estimates of myocardial blood flow generated using distributed parameter modelling were independent on the number of time points of the dataset used for fitting in this simulation (assuming that the time range selected for analysis includes at least the first-pass of contrast).

The extravascular-extracellular space and distribution volume were significantly lower in first-pass distributed parameter modelling as compared to ideal values, due to reductions in the fitted parameter T (mean overall transit time). Thus, it is important to consider that for the precise calculation of the extravascular-extracellular space and distribution volume, distributed parameter modelling may have to be convolved with the entire arterial input function curve [24].

The findings in chapter 6 suggest that the application of distributed parameter modelling can eliminate any uncertainties for the selection of the first-pass range from the entire acquired dataset. The selection of the first-pass range can be challenging either when the concentration minimum is not clearly visible due to noise effects and/ or in dual bolus imaging, in which the bolus dispersion of a scaled pre-bolus arterial input function can be different compared to a standard main bolus arterial input function. Observing no differences in myocardial blood flow estimates between first-pass distributed parameter modelling and simulated data described in this chapter, may in turn contribute to facilitate development and optimisation of more reliable automated software algorithms, for myocardial blood flow quantification. Sensitivity to accurate selection of the first-pass range (mainly when dealing with dual bolus imaging data), currently requires manual input for this process to be reliable. Although mathematical algorithms can potentially be implemented in the future for automatically identifying the first-pass range, interpretation is still needed for dual bolus imaging data whether the first-pass range is selected from the scaled pre-bolus or the standard main arterial input function. A modelling approach such as the distributed parameter model, showing lack of dependence on the number of time points used for fitting, could therefore potentially aid in elimination of these uncertainties and help to facilitate development of automated algorithms.

In chapter 7, data from twenty four patients with known or suspected CAD were analysed. In per vessel analysis, it was shown that the sensitivity and negative predictive value of distributed parameter modelling was higher in detecting reduced myocardial blood flow in obstructive CAD, compared to Fermi modelling and visual MR estimates. Significant differences between vessels classified with obstructive versus non-obstructive CAD were higher for distributed parameter modelling, compared to Fermi modelling. Significant differences were also observed between obstructive and non-obstructive CAD, across all distributed parameter modelling-derived microvascular characteristics. Furthermore, distributed parameter modelling reached superior sensitivity in detecting obstructive CAD, compared to visual estimates from CT imaging.

In per patient based analysis, the diagnostic accuracy of all applied models was further improved. Differences in haemodynamics between obstructive and non-obstructive CAD were considerably increased in per patient compared to per vessel analysis. Haemodynamic thresholds on ROC analysis for distributed parameter modelling showed the highest sensitivity and negative predictive value in stratifying patients with at least one vessel with obstructive CAD.

Both the per vessel and per patient analysis of cardiac MR perfusion data demonstrated that distributed parameter modelling showed higher sensitivity and specificity compared to Fermi modelling (which is currently the most popular approach for myocardial blood flow analysis from MR data). This analysis also showed that distributed parameter modelling may have a potential as a non-invasive tool for the diagnosis and prognostication of haemodynamically significant CAD.

The work presented in chapters 5 and 7 was performed before investigating numerical simulations in chapter 6. This is the reason why first-pass distributed parameter modelling was not investigated in the patient population of chapter 7, for assessing its diagnostic performance in the detection of obstructive coronary artery disease.

8.2 Further discussion

To date, the majority of myocardial perfusion MR studies (including the present work) assume negligible water exchange effects in the myocardial tissue [24, 69]. As described in chapters 2 and 3, the concentration of gadolinium in the myocardium can be indirectly detected through the change in T_1 relaxation rate (in T_1 weighted techniques used for myocardial DCE-MRI). If sufficiently fast, water exchange across the capillary barrier (water exchange between the intravascular and extravascular-extracellular space) and the cellular membrane (between the extravascular-extracellular and intracellular space), may allow proton spins to sample different environments during spin relaxation [24, 159]. The observed T_1 relaxation rate can therefore no longer be determined only by local contrast agent concentrations, but also depends on the rates at which proton spins exchange between spaces and by the relative volumes of these spaces [159].

There are two limiting cases according to which water exchange effects can be negligible: the slow (or no exchange) limit and the fast exchange limit [159]. It is still unknown whether either limit might be closer to myocardial physiology. A previous myocardial perfusion study has shown that the rapid application of radiofrequency pulses (short repetition time) during relaxation recovery can reduce the sensitivity of the observed T_1 relaxation rate to water exchange [28]. Another study has shown that the zero exchange assumption might be reasonable for the interpretation of myocardial contrast enhancement, when a combination of high flip angle (20^0) and short repetition time (2.40 ms) are used in a saturation recovery gradient echo sequence [160]. More recently, Li et al have incorporated a description of water exchange into a tracer kinetic model and suggested that quantification of perfusion from DCE-MRI data is not sensitive to water exchange effects [161]. The investigation of water exchange effects in DCE-MRI is a complex issue and work is still in progress [24, 28, 159-161].

A possible method for assessing whether water exchange effects can affect measurements from DCE-MRI data could be a comparison versus absolute measurements from cardiac positron emission tomography (PET) data [136,137]. Quantification of myocardial blood flow and microvascular characteristics from PET are challenged by other type of technical problems, such as attenuation correction issues or the fact that low spatial resolution PET data often lead to signal spill over from the left ventricle onto the myocardial tissue [154].

PET uses a radioactive tracer such as labelled water and benefits from a more direct relationship between signal intensity and radiotracer concentration [154], compared to DCE-MRI. Moreover, PET has been widely used to assess haemodynamics in healthy volunteers [162, 163], in patients with coronary artery disease [136, 137] and in patients with other cardiac diseases [164]. A thorough comparison between cardiac DCE-MRI and cardiac PET perfusion imaging acquired in the same subjects may provide new insights for the interpretation of absolute measurements obtained through mathematical modelling (see future work, subsection 8.3). This assessment could potentially provide answers with regard to whether the assumption of negligible water exchange effects in cardiac DCE-MRI can overestimate or underestimate myocardial blood flow and volume of distribution [159]. In the data analysis of chapters 5-7, it has been demonstrated that distributed parameter modelling may be less dependent on arterial input function saturation, is independent of the number of time points used for fitting and has better sensitivity and specificity in detecting obstructive CAD than Fermi modelling. Absolute validation of any myocardial blood flow model is challenging and there is no non-invasive imaging methodology that can be considered a true ‘gold standard’ assessment of myocardial blood flow (each has its limitations). Thus, a comparison of DCE-MRI with distributed parameter modelling versus current absolute ‘reference’ measurements derived from PET perfusion imaging acquired in the same subjects, would help to test the results and conclusions of this work.

8.3 Future work

A future aim is to extend the analysis in chapter 5 to examine the behaviour of other model-based [37] or model-independent applications [34, 43], in single versus dual bolus analysis. Moreover, the impact of contrast agent dose in single versus dual bolus analysis can be further assessed for each model application, by recruiting a new healthy volunteer cohort, in which slightly higher (e.g. 0.04, 0.05 mmol/kg) and slightly lower contrast agent doses (e.g. 0.025 mmol/kg) can be investigated. To our knowledge, this has not yet been explored for each model application, possibly because Fermi modelling is currently the preferred method for MR perfusion analysis [31, 54, 58, 59, 75, 76]. Assessing the impact of contrast agent dose using a range of doses may potentially provide more options in the clinical setting for obtaining reproducible quantitative assessments whilst maintaining high contrast-to-noise ratio in the myocardium in patients who have compromised vascular dynamics. Numerical simulations can also be performed to further investigate why distributed parameter modelling is less dependent to arterial input function saturation effects than the Fermi model.

Chapter 6 is currently being prepared as manuscript, for submission to an imaging-based journal. With reference to the work presented in chapter 6, other model-based [66] or model-independent [34, 43] applications can also be investigated as to whether analysis using only the first-pass range can give accurate measurements of myocardial blood flow, compared to ideal values from simulated data. Modelling approaches that prove capable of quantifying blood flow from the first-pass range may be subsequently used for further assessment against simulated first-pass myocardial perfusion data derived from a hardware flow phantom [60]. This process would assess which model application is a better estimate of first-pass phantom data. Also, additional numerical simulations can be performed to assess which is the minimum time frame that can be used to extract reliable information of myocardial blood flow and microvascular characteristics with distributed parameter modelling (it may be less than the first-pass range that was used in this thesis).

The qualitative and quantitative MR analysis versus invasive methods presented in chapter 7 will be submitted as manuscript to a cardiovascular MR- imaging focused journal. Obtaining semi-quantification measurements for transmural perfusion ratios from CT perfusion data [90], would give more direct comparisons against our absolute quantifications from MR imaging. These measurements will be performed in the next few months by a team of experienced clinicians at the Clinical Research Imaging Centre of the University of Edinburgh. Assessing these findings in larger patient cohorts would help to establish haemodynamic thresholds for quantitative MR analysis, at the setting of non-invasive diagnosis of obstructive CAD. Finally, cardiac perfusion PET data have been acquired in a subpopulation (N=8) of this patient cohort. It is our aim to analyse these data and investigate and assess any cross-correlations with absolute measurements from DCE-MRI data.

In addition to the above, the author would like to mention that due to time restrictions it was not possible to examine model application using other nonlinearity correction methods such as the dual sequence [69, 72] or the bookend technique that has been recently investigated for cardiac data [165]. Thus, in the work presented in this thesis, dual bolus imaging was considered to be the gold standard for assessing and interpreting our model comparisons in chapters 5 and 7. The main limitation of the dual bolus imaging might be compatibility issues in contrast agent dispersions between the pre-bolus and the main bolus data (as described in chapter 6). A comparison between different non-linearity methods could potentially demonstrate whether either method can improve myocardial perfusion quantification from DCE-MRI data.

9. References

1. Allender S, Scarborough P, Peto V, Rayner M, Leal J, Luengo-Fernandez R, Alastair, G: European cardiovascular disease statistics. *Department of Public Health, University of Oxford* 2008, 3rd edn, Oxford.
2. Ross R: Atherosclerosis–an inflammatory disease. *N Engl J Med* 1999, 340(2): 115–26.
3. Ross R, Glomset JA: Atherosclerosis and the arterial smooth muscle cell: proliferation of smooth muscle is a key event in the genesis of the lesions of atherosclerosis. *Science* 1973,180 (93): 1332–39.
4. Herrmann J, Lerman A: Coronary Artery Disease. Chapter: Development and Progression: New approaches without traditional revascularization. *Springer* 2012, 1st edn, New York.
5. Jahnke C, Nagel E, Gebker R, Kokocinski T, Kelle, S, Manka, R, Fleck E, Paetsch I: Prognostic value of cardiac magnetic resonance stress tests adenosine stress perfusion and dobutamine stress wall motion imaging. *Circulation* 2007, 115: 1769-1776.
6. Chiribiri A, Bettencourt N, Nagel E: Cardiac Magnetic Resonance Stress Testing: Results and Prognosis. *Curr Cardiol Rep* 2009, 11: 54-60.
7. McRobbie DW, Moore EA, Graves MJ, Prince MR (eds): MRI: From picture to proton. *Cambridge University Press* 2006, 2nd edn, New York.
8. Brown MA, Semelka RC. MRI: Basic pulse principles and applications. *Wiley-Blackwell* 2010, 4th edn, New York.
9. Bernstein MA, King KF, Zhou XJ (eds): Handbook of MRI Pulse Sequences. *Elsevier Academic Press* 2004, 1st edn London.

10. Pintaske J, Martirosian P, Hansjorg G, Requardt M, Gunter E, Lodemann KP, Claussen CD, Schick Fritz: Relaxivity of gadopentetate dimeglumine (Magnevist), Gadobutrol (Gadovist), and Gadobenate Dimeglumine (MultiHance) in human blood plasma at 0.2, 1.5, and 3 Tesla (Erratum). *Invest Radiol* 2006, 41(3): 213-221.
11. Tweedle MF, Wedeking P, Telser J, Sotak CH, Chang CA, Kumar K, Wan X, Eaton SM: Dependence of MR signal intensity on Gd tissue concentration over a broad dose range. *Magn Reson Med* 1991, 22(2): 191–194.
12. Messroghli DR, Radjenovic A, Kozerke S, Higgins DM, Sivananthan MU, Ridgway JP: Modified look-locker inversion recovery (MOLLI) for high-resolution *T*1 mapping of the heart. *Magn Reson Med* 2004, 52: 141–146.
13. Look DC, Locker DR: Time saving in measurement of NMR and EPR relaxation times. *Rev Sci Instrum* 1970, 41: 250-251.
14. Deichmann R, Haase A: Quantification of T1 values by snapshot-FLASH NMR imaging. *J Magn Reson Im* 1992, 96(3): 608-612.
15. Kellman P, Arai AE: Imaging sequences for first-pass perfusion-A review. *J Cardiov Magn Reson* 2007, 9(3): 527-537.
16. Cerqueira MD: Standardized Myocardial Segmentation and Nomenclature for Tomographic Imaging of the Heart: A Statement for Healthcare Professionals From the Cardiac Imaging Committee of the Council on Clinical Cardiology of the American Heart Association. *Circulation* 2002, 105: 539–542.
17. Buzug TM: Computed Tomography: From photon statistics to modern cone-beam. *Springer-Verlag Berlin Heidelberg* 2008, 2nd edn, Berlin.

18. Kalender WA: CT Computed tomography: fundamentals, system technology, image quality, applications. *Publicis Publishing* 2011, 3rd edn, Erlangen.
19. Choi AD, Joly JM, Chen MY, Weigold GW: State of the Art. Physiologic evaluation of ischemia using cardiac CT: Current status of CT myocardial perfusion and CT fractional flow reserve. *J Cardiovasc Comput Tomogr*, 2014, 8: 272-281.
20. Pons-Llado G, Leta-Petracca R (eds): Atlas of non-invasive coronary angiography by multidetector computed tomography. *Springer* 2006, 1st edn, New York.
21. Hoffmann U, Millea R, Enzweiler C, Ferencik M, Gulick S, Titus J, Achenbach S, Kwait D, Sosnovik D, Brady TJ: Acute myocardial infarction: contrast-enhanced multi-detector row CT in a porcine model. *Radiology*, 2004, 231: 697–701.
22. Mahnken, AH, Koos R, Katoh M, Wildberger JE, Spuentrap E, Buecker A, Gunther RW, Kuhl HP: Assessment of myocardial viability in reperfused acute myocardial infarction using 16-slice computed tomography in comparison to magnetic resonance imaging. *J Am Coll Cardiol*, 2005, 45: 2042–7.
23. Rohrer M, Bauer H, Mintorovitch J, Requardt M, Weinmann HJ: Comparison of magnetic properties of MRI contrast media solutions at different magnetic field strengths. *Invest Radiol* 2005, 40(11): 715-24.
24. Jerosch-Herold M: Quantification of myocardial perfusion by cardiovascular magnetic resonance. *J Cardiov Magn Reson* 2010, 12: 57-67.

25. Larsson HBW, Fritz-Hansen T, Rostrup E, Søndergaard L, Ring P, Henriksen O: Myocardial perfusion modelling using MRI. *Magn Reson Med* 1996, 35: 716-726.

26. Fritz-Hansen T, Rostrup E, Larsson HBW, Sondergaard L, Ring P, Henriksen O: Measurement of the arterial concentration of Gd- DTPA using MRI: a step toward quantitative perfusion imaging. *Magn Reson Med* 1996, 36: 225–31.

27. Fritz-Hansen T, Hove JD, Kofoed KF, Kelbaek H, Larsson HBW: Quantification of MRI measured myocardial perfusion reserve in healthy humans: a comparison with positron emission tomography. *J Magn Reson* 2008, 27: 818-24.

28. Jerosch-Herold M, Wilke N, Stillman AE: Magnetic resonance quantification of the myocardial perfusion reserve with a Fermi function model for constrained deconvolution. *Med Phys* 1998, 25: 73–84.

29. Biglands J, Magee D, Boyle R, Larghat A, Plein S, Radjenović A: Evaluation of the effect of myocardial segmentation errors on myocardial blood flow estimates from DCE-MRI. *Phys in Med Biol* 2011, 56(8): 2423–43.

30. Christian TF, Rettmann DW, Aletras AH, Liao SL, Taylor JL, Balaban RS, Arai AE: Absolute myocardial perfusion in canines measured by using dual-bolus first-pass MR imaging. *Radiology* 2004, 232: 677-84.

31. Utz W, Greiser A, Niendorf T, Diet R, Schulz-Menger J: Single- or dual-bolus approach for the assessment of myocardial perfusion reserve in quantitative MR perfusion imaging. *Magn Reson Med* 2008, 59: 1373-77.

32. Zierler KL: Equations for measuring blood flow by external monitoring of radioisotopes. *Circ Res* 1965, 16: 309-321.

33. Zierler KL: Indicator dilution methods for measuring blood flow, volume, and other properties of biological systems: A brief history and memoir. *Ann Biomed Eng* 2000, 28: 836-48.

34. Jerosch-Herold M, Swingen C, Seethamraju RT: Myocardial blood flow quantification with MRI by model-independent deconvolution. *Med Phys* 2002, 29: 886-897.

35. Tikhonov AN, Goncharsky AV, Stepanov VV, Yagola AG: Numerical methods for the solution of ill-posed problems. *Springer Netherlands*, 1995, The Netherlands.

36. Pack NA, DiBella EV, Rust TC, Kadrmas DJ, McGann CJ, Butterfield R, Christian PE, Hoffman JM: Estimating myocardial perfusion from dynamic contrast-enhanced CMR with a model-independent deconvolution method. *J Cardiovasc Magn Reson* 2008, 10: 52-62.

37. Pack NA, DiBella EV: Comparison of myocardial perfusion estimates from dynamic contrast-enhanced magnetic resonance imaging with four quantitative analysis methods. *Magn Reson Med* 2010, 64: 125–137.

38. Jerosch-Herold M, Seethamraju RT, Swingen CM, Wilke NM, Stillman AE: Analysis of myocardial perfusion MRI. *J Magn Reson Imag* 2004, 19: 758–770.

39. Verotta D: Two constrained deconvolution methods using spline functions. *J Pharm Biopharm* 1993, 21(5): 609-636.

40. Keeling SL, Kogler T, Stollberger R: Deconvolution for DCE-MRI using an exponential approximation basis. *Med Image Anal* 2009, 13: 80–90.

41. Neyran B, Janier MF, Casali C, Revel D, Canet Soulas EP: Mapping myocardial perfusion with an intravascular MR contrast agent: robustness of deconvolution methods at various blood flows. *Magn Reson Med* 2002, 48:166–179.

42. Batchelor P, Chiribiri A, Nooralipour NZ, Cvetkovic Z: Arma regularization of cardiac perfusion modelling. *In: International Conference on Acoustics, Speech and Signal Processing, ICASSP*, 2010, 642–645.

43. Zarinabad N, Chiribiri A, Hautvast GLTF, Ishida M, Schuster A, Cvetkovic Z, Batchelor PG, Nagel E: Voxel-wise quantification of myocardial perfusion by cardiac magnetic resonance. Feasibility and methods comparison. *Magn Reson Med* 2012, 68: 1994–2004.

44. Larsson HBW, Stubgaard M, Frederiksen JL, Jensen M, Henriksen O, Paulson OB: Quantitation of blood-brain barrier defect by magnetic resonance imaging and gadolinium-DTPA in patients with multiple sclerosis and brain tumors *Magn Reson Med* 1990, 16: 117–31.

45. Tofts PS, Kermode AG: Measurement of the blood–brain barrier permeability and leakage space using dynamic MR imaging: 1. Fundamental concepts *Magn Reson Med* 1991, 17: 357–67.

46. Brix G, Semmler W, Port R, Schad LR, Layer G, Lorenz WJ: Pharmacokinetic parameters in CNS Gd-DTPA enhanced MR imaging. *J Comput Assist Tomogr* 1991, 15: 621–8.

47. Larsson HBW, Tofts PS: Measurement of blood–brain barrier permeability using dynamic Gd-DTPA scanning-a comparison of methods. *Magn Reson Med* 1992, 24:174–6.

48. Tofts PS, Brix G, Buckley DL, et al: Estimating kinetic parameters from dynamic contrast-enhanced T1-weighted MRI of a diffusible tracer: standardized quantities and symbols. *J Magn Reson Imag* 1999, 10: 223–32.
49. O'Connor JP, Jackson A, Parker GJ, Jayson GC: DCE-MRI biomarkers in the clinical evaluation of antiangiogenic and vascular disrupting agents *Br J Cancer* 2007, 96: 189–95.
50. Sourbron SP, Buckley DL: Tracer kinetic modelling in MRI: estimating perfusion and capillary permeability. *Phys Med Biol* 2012, 57: R1–R33.
51. Kety SS: The theory and application of the exchange of inert gas in lung and tissues. *Pharmacol Rev* 1951, 3: 1-41.
52. Axel L: Tissue mean transit time from dynamic computed tomography by a simple deconvolution technique. *Invest Radiol* 1983, 18: 94-99.
53. Radjenovic A, Biglands JD, Larghat A, Ridgway JP, Ball SG, Greenwood JP, Jerosch-Herold M, Plein S: Estimates of systolic and diastolic myocardial blood flow by dynamic contrast-enhanced MRI. *Magn Reson Med* 2010, 64: 1696-1703.
54. Hsu L-Y, Rhoads KL, Holly JE, Kellman P, Aletras AH, Arai AE: Quantitative myocardial perfusion analysis with a dual-bolus contrast-enhanced first-pass MRI technique in humans. *J Magn Reson Im* 2006, 23: 315-322.
55. Kostler H, Ritter C, Lipp M, Beer M, Hahn D, Sandstede J: Prebolus quantitative MR heart perfusion imaging. *Man Reson Med* 2004, 52: 296-299.
56. Hsu LY, Groves DW, Aletras AH, Kellman P, Arai AE: A quantitative pixel-wise measurement of myocardial blood flow by contrast-enhanced first-pass CMR perfusion imaging. *J Am Coll Cardiol: Cardiov Imaging* 2012, 5: 154–66.

57. Larghat A, Biglands J, Maredia N, Greenwood JP, Ball SG, Jerosch-Herold M, Radjenovic A, Plein S: Endocardial and epicardial myocardial perfusion determined by semi-quantitative and quantitative myocardial perfusion magnetic resonance. *Int J Cardiovasc Imaging* 2012, 28(6): 1499-511.
58. Lockie T, Ishida M, Perera D, et al: High-resolution magnetic resonance myocardial perfusion imaging at 3.0-Tesla to detect hemodynamically significant coronary stenoses as determined by fractional flow reserve. *J Am Coll Cardiol* 2011, 57: 70–75.
59. Morton G, Chiribiri A, Ishida M, et al. Quantification of absolute myocardial perfusion in patients with coronary artery disease: comparison between cardiovascular magnetic resonance and positron emission tomography. J Am Coll Cardiol 2012, 60(16): 1546–55.
60. Chiribiri A, Schuster A, Ishida M, et al: Perfusion Phantom: An efficient and reproducible method to simulate myocardial first-pass perfusion measurements with cardiovascular magnetic resonance. *Magn Reson Med* 2013, 69(3): 698-707.
61. Sangren WC, Sheppard CW: A mathematical derivation of the exchange of a labeled substance between a liquid flowing in a vessel and an external compartment. *Bull Math Biophys* 1953, 15: 387-93.
62. Goresky CA, Ziegler WH, Bach GG: Capillary exchange modelling, barrier-limited and flow-limited distribution. *Circ Res* 1970, 27: 739-764.
63. Goresky CA, Bach GC, Nadcau BE: On the uptake of materials by the intact liver: the transport and net removal of galactose. *J Clin Invest* 1973, 52: 991-1009.

64. Rose CP, Goresky CA: Vasomotor control of capillary transit time heterogeneity in the canine coronary circulation. *Circ Res* 1976, 39: 541-54.

65. Garpebring A, Ostlund N, Karlsson M: A novel estimation method for physiological parameters in dynamic contrast-enhanced MRI: application of a distributed parameter model using Fourier-domain calculations. *IEEE Trans Med Imaging* 2009, 28: 1375-1383.

66. Broadbent DA, Biglands JD, Larghat A, Sourbron SP, Radjenovic A, Greenwood JP, Plein S, Buckley, DL: Myocardial blood flow at rest and stress measured with dynamic contrast-enhanced MRI: Comparison of a distributed parameter model with a fermi function model. *Magn Reson Med* 2013, 70: 1591-1597.

67. Schwitter J: Myocardial perfusion. *J Magn Reson Im* 2006, 24: 953-963.

68. Utz W, Niendorf T, Wassmuth R, Messroghli D, Dietz R, Schulz-Menger J: Contrast-dose relation in first-pass myocardial MR perfusion imaging. *J Magn Reson Im* 2007, 25: 1131-5.

69. Gatehouse PD, Elkington AG, Ablitt NA, Yang GZ, Pennell DJ, Firmin DN: Accurate assessment of the arterial input function during high-dose myocardial perfusion cardiovascular magnetic resonance. *J Magn Reson Im* 2004, 20: 39-45.

70. Kim D, Axel L: Multislice, dual-imaging sequence for increasing the dynamic range of the contrast-enhanced blood signal and CNR of myocardial enhancement at 3T. *J Magn Reson Imaging* 2006, 23: 81-6.

71. Breton E, Kim D, Chung S, Axel L: Quantitative contrast-enhanced first-pass cardiac perfusion MRI at 3 Tesla with accurate arterial input function and myocardial wall enhancement. *J Magn Reson Imaging* 2011, 34(3): 676-84.

72. Cernicanu A, Axel L: Theory-based signal calibration with single-point T1 measurements for first-pass quantitative perfusion MRI studies. *Acad Radiol* 2006, 13: 686-693.

73. Hsu LY, Kellman P, Arai AE: Nonlinear myocardial signal intensity correction improves quantification of contrast-enhanced first-pass MR perfusion in humans. *J Magn Reson Imaging* 2008, 27: 793-801.

74. Vallee JP, Lazeyras F, Kasuboski L, Chatelain P, Howarth N, Righetti A, Didier D: Quantification of myocardial perfusion with FAST sequence and Gd bolus in patients with normal cardiac function. *J Magn Reson Imaging* 1999, 9(2): 197-203.

75. Christian TF, Aletras AH, Arai AE: Estimation of absolute myocardial blood flow during first-pass MR perfusion imaging using a dual-bolus injection technique: comparison to single-bolus injection method. *J Magn Reson Imaging* 2008, 27(6): 1271-1277.

76. Ishida M, Schuster A, Morton G, et al: Development of a universal dual-bolus injection scheme for the quantitative assessment of myocardial perfusion cardiovascular magnetic resonance. *J Cardiov Magn Reson* 2011, 13:28.

77. Brodoefel H, Burgstahler C, Tsiflikas I, Reimann A, Schroeder S, Claussen CD, Heuschmid M, Kopp AF: Dual-source CT: effect of heart rate, heart rate variability, and calcification on image quality and diagnostic accuracy. *Radiology* 2008, 247: 346-355.

78. Meijboom WB, Meijs MF, Schuijf JD, et al: Diagnostic accuracy of 64-slice computed tomography coronary angiography: a prospective, multicenter, multivendor study. *J Am Coll Cardiol* 2008, 52: 2135-2144.

79. Miller JM, Rochitte CE, Dewey M, et al: Diagnostic performance of coronary angiography by 64-row CT. *N Engl J Med* 2008, 359: 2324-2336.
80. Carrigan TP, Nair D, Schoenhagen P, et al: Prognostic utility of 64-slice computed tomography in patients with suspected but no documented coronary artery disease. *Eur Heart J* 2009, 30: 362-371.
81. Gopal A, Nasir K, Ahmadi N, et al: Cardiac computed tomographic angiography in an outpatient setting: an analysis of clinical outcomes over a 40-month period. *J Cardiovasc Comput Tomogr* 2009, 3: 90-95.
82. Hadamitzky M, Freissmuth B, Meyer T, Hein F, Kastrati A, Martinoff S, Schomig A, Hausleiter J: Prognostic value of coronary computed tomographic angiography for prediction of cardiac events in patients with suspected coronary artery disease. *JACC Cardiovasc Imaging* 2009, 2: 404-411.
83. Min JK, Shaw LJ, Devereux RB, et al: Prognostic value of multidetector coronary computed tomographic angiography for prediction of all-cause mortality. *J Am Coll Cardiol* 2007, 50: 1161-1170.
84. Williams MC, Newby DE: CT myocardial perfusion: a step towards quantification. *Heart* 2012, 98: 521-522.
85. Mowatt G, Cook JA, Hillis GS, Walker S, Fraser C, Jia X, Waugh N: 64-Slice computed tomography angiography in the diagnosis and assessment of coronary artery disease: systematic review and meta-analysis. *Heart* 2008, 94: 1386-93.
86. Park MJ, Jung JI, Choi YS, Ann SH, Youn HJ, Jeon, GN, Choi HC: Coronary CT angiography in patients with high calcium score: evaluation of plaque characteristics and diagnostic accuracy. *Int J Cardiovasc Imaging* 2011, 27(1): 43-51.

87. Rispler S, Keidar Z, Ghersin E, et al: Integrated single photon emission computed tomography and computed tomography coronary angiography for the assessment of hemodynamically significant coronary artery lesions. *J Am Coll Cardiol* 2007, 49: 1059-1067.

88. Schuijf JD, Wijns W, Jukema JW, et al: J. Relationship between noninvasive coronary angiography with multi-slice computed tomography and myocardial perfusion imaging. *J Am Coll Cardiol* 2006, 48: 2508-2514.

89. Di Carli MF, Dorbala S, Curillova Z, Kwong RJ, Goldhaber SZ, Rybicki FJ, Hachamovitch R: Relationship between CT coronary angiography and stress perfusion imaging in patients with suspected ischemic heart disease assessed by integrated PET-CT imaging. *J Nucl Cardiol* 2007, 14: 799-809.

90. George RT, Arbab-Zadeh A, Miller JM, et al: Adenosine stress 64- and 256-row detector computed tomography angiography and perfusion imaging: a pilot study evaluating the transmural extent of perfusion abnormalities to predict atherosclerosis causing myocardial ischemia. *Circ Cardiovasc Imaging* 2009, 2: 174-182.

91. Sun Z: Coronary CT angiography with prospective ECG-triggering: an effective alternative to invasive coronary angiography. *Cardiovasc Diagn Ther* 2012, 2(1): 28-37.

92. Hausleiter J, Meyer T, Hermann F, et al: Estimated radiation dose associated with cardiac CT angiography. *JAMA* 2009, 301(5): 500-507.

93. Hausleiter J, Meyer T, Martuscelli E, et al: Image quality and radiation exposure with prospectively ECG-triggered axial scanning for coronary CT angiography:

the multicenter, multivendor, randomized PROTECTION-III study. *JACC Cardiovasc Imaging* 2012, 5(5): 484-493.

94. Hu H, He DH, Foley WD, Fox SH: Four multi-detector-row helical CT: Image quality and volume coverage speed. *Radiology* 2000, 215: 55-62.
95. George RT, Silva C, Cordeiro MA, DiPaula A, Thompson DR, McCarthy WF, Ichihara T, Lima JA, Lardo AC: Multidetector computed tomography myocardial perfusion imaging during adenosine stress. *J Am Coll Cardiol* 2006, 48: 153-160.
96. Zhang LJ, Peng J, Wu S-Y, Yeh BM, Yeh BM, Zhou CS, Lu GM: Dual source dual energy CT of acute myocardial infarction: correlation with histopathological findings in a canine model. *Invest Radiol* 2010, 45: 290-297.
97. Kido T, Kurata A, Higashino H, Inoue Y, Kanza RE, Okayama H, Higaki J, Murase K, Mochizuki T: Quantification of regional myocardial blood flow using first-pass multidetector-row computed tomography and adenosine triphosphate in coronary artery disease. *Circ J* 2008, 72: 1086-1091.
98. George RT, Arbab-Zadeh A, Cerci RJ, et al: Diagnostic performance of combined noninvasive coronary angiography and myocardial perfusion imaging using 320-MDCT: The CT angiography and perfusion methods of the CORE320 multicenter multinational diagnostic study. *AJR Am J Roentgenol* 2011, 197(4): 829-837.
99. Williams MC, Cruden NL, Uren NG, Newby DE: Image in cardiovascular CT: A low-dose comprehensive cardiac CT protocol assessing anatomy, function, perfusion, and viability. *J Cardiovasc Comput Tomogr* 2013, 7: 69-72.

100. Bastarrika G, Ramos-Duran L, Rosenblum MA, Kyoung Kang D, Rowe GD, Schoepf UJ: Adenosine-stress dynamic myocardial CT perfusion imaging. Initial clinical experience. *Invest Radiol* 2010, 45: 306-313.

101. George RT, Jerosch-Herold M, Silva C, Kitagawa K, Bluemke DA, Lima JA, Lardo AC: Quantification of myocardial perfusion using dynamic 64-detector computed tomography. *Invest Radiol* 2007, 42: 815-822.

102. Ruzsics B, Lee H, Zwerner PL, Gabregziabher M, Costello P, Schoepf UJ: Dual-energy CT of the heart for diagnosing coronary artery stenosis and myocardial ischemia-initial experience. *Eur Radiol* 2008, 18: 2414-2424.

103. Ruzsics B, Schwarz F, Schoepf UJ, et al: Comparison of dual-energy computed tomography of the heart with single photon emission computed tomography for assessment of coronary artery stenosis and of the myocardial blood supply. *Am J Cardiol* 2009, 104: 318-326.

104. Graser A, Johnson TRC, Chandarana H, Macari M: Dual energy CT: preliminary observations and potential clinical applications in the abdomen. *Eur Radiol* 2009, 19: 13-23.

105. Ho KT, Chua KC, Klotz E, et al: Stress and rest dynamic myocardial perfusion imaging by evaluation of complete time attenuation curves with dual source CT. *JACC Cardiovasc Imaging* 2010, 3: 811-20.

106. Nakauchi Y, Iwanaga Y, Ikuta S, et al: Quantitative myocardial perfusion analysis using multi-row detector CT in acute myocardial infarction. *Heart* 2012, 98: 566-72.

107. Yeung IWT, Lee T-Y, Del Maestro RF, Kozak R, Bennet JB, Brown T: An absorptiometry method for the determination of arterial blood concentration of injected iodinated contrast agent. *Phys Med Biol* 1992, 37: 1741–58.

108. Cenic A, Nabavi DG, Craen RA, Gelb AW, Lee TY: Dynamic CT measurement of cerebral blood flow: A validation study. *Am J NeuroRadiol* 1999, 20: 63-73.

109. Tonino PAL, De Bruyne B, Pijls NHJ, et al: Fractional flow reserve versus angiography for guiding Percutaneous Coronary Intervention. *N Engl J Med* 2009, 360: 213-224.

110. Beller GA, Zaret BL: Contributions of nuclear cardiology to diagnosis and prognosis of patients with coronary artery disease. *Circulation* 2000, 101: 1465-78.

111. Shaw LJ, Iskandrian AE: Prognostic value of gated myocardial perfusion SPECT. *J Nucl Cardiol* 2004, 11: 171-85.

112. Shaw LJ, Berman DS, Maron DJ, et al: Optimal medical therapy with or without percutaneous coronary intervention to reduce ischemic burden: results from the Clinical Outcomes Utilizing Revascularization and Aggressive Drug Evaluation (COURAGE) trial nuclear substudy. *Circulation* 2008, 117: 1283-91.

113. Davies RF, Goldberg AD, Forman S, et al: Asymptomatic Cardiac Ischemia Pilot (ACIP) study two-year follow-up: outcomes of patients randomized to initial strategies of medical therapy versus revascularization. *Circulation* 1997, 95: 2037-43.

114. Erne P, Schoenenberger AW, Burckhardt D, et al. Effects of percutaneous coronary interventions in silent ischemia after myocardial infarction: the SWISSI II randomized controlled trial. *JAMA* 2007, 297: 1985-91.

115. Boden WE, O'Rourke RA, Teo KK, et al: Optimal medical therapy with or without PCI for stable coronary disease. *N Engl J Med* 2007, 356: 1503-16.

116. Pijls NH, van Schaardenburgh P, Manoharan G, et al: Percutaneous coronary intervention of functionally nonsignificant stenosis: 5-year follow-up of the DEFER Study. *J Am Coll Cardiol* 2007, 49: 2105-11.

117. Tonino PAL, Fearon WF, De Bruyne B, Oldroyd KG, Leesar MA, Ver Lee PN, MacCarthy PA, van't Veer M, Pijls NHJ: Angiographic versus functional severity of coronary artery stenoses in the FAME study. *J Am Coll Cardiol* 2010, 55: 2816–2821.

118. Fischer JJ, Samady H, McPherson JA, et al: Comparison between visual assessment and quantitative angiography versus fractional flow reserve for native coronary narrowings of moderate severity. *Am J Cardiol* 2002, 90: 210-5.

119. Topol EJ, Nissen SE. Our preoccupation with coronary luminology: the dissociation between clinical and angiographic findings in ischemic heart disease. *Circulation* 1995, 92: 2333-42.

120. Pijls NH, De Bruyne B, Peels K, et al: Measurement of fractional flow reserve to assess the functional severity of coronary artery stenoses. *N Engl J Med* 1996, 334: 1703-8.

121. De Bruyne B, Pijls NH, Bartunek J, et al: Fractional flow reserve in patients with prior myocardial infarction. *Circulation* 2001, 104: 157-162.

122. De Bruyne B, Pijls NH, Kalesan B, et al: Fractional flow reserve-guided PCI versus medical therapy in stable coronary artery disease. *N Engl J Med* 2012, 367(11): 991-1001.

123. Cooper MA, Nguyen TD, Spincemaille P, Prince MR, Weinsaft JW, Wang Y: How accurate is MOLLI T1 mapping in vivo? Validation by spin echo methods. *PLoS ONE* 2014, 9(9): 1-6.

124. Carr J, Simonetti O, Bundy J, Li D, Pereles S, Finn JP: Cine MR angiography of the heart with segmented true fast imaging with steady-state precession. *Radiology* 2001, 219: 828–834.

125. Bundy J, Simonetti O, Laub G, Finn JP: Segmented trueFISP cine imaging of the heart. In: *Proc 7th Annual Meeting ISMRM*, Philadelphia 1999, 1282.

126. Blaimer M, Breuer F, Mueller M, Heidemann RM, Griswold A, Jakob PM: SMASH, SENSE, PILS, GRAPPA: How to choose the optimal method. *Top Magn Reson Imaging* 2004, 15: 223-236.

127. Griswold MA, Jakob PM, Heidemann RM: Generalized autocalibrating partially parallel acquisitions (GRAPPA). *Magn Reson Med* 2002, 47: 1202–1210.

128. Deshmane A, Gulani V, Griswold MA, Seiberlich N: Parallel imaging. *J Magn Reson Im* 2012, 36: 55-72.

129. Atkinson D, Hill DLG, Stoyle PNR, Summers PE, Clare S, Bowtell R, Keevil SF: Automatic compensation of motion artifacts in MRI. *Magn Reson Med* 1999, 41: 163-170.

130. Di Bella EVR, Parker DL, Sinusas AJ: On the dark rim artifact in dynamic contrast-enhanced MRI myocardial perfusion studies. *Magn Reson Med* 2005, 54: 1295-1299.

131. Dornier C, Ivancevic MK, Thevanez P, Vallee JP: Improvement in the quantification of myocardial perfusion using an automatic spline-based registration algorithm. *J Magn Reson Im* 2003, 18: 160-168.

132. Von Land CD, Rohini R, Reiber JHC: Development of an improved centerline wall motion model. *Proceed Comput Cardiol* 1990, 687-690.

133. Van der Geest RJ: Automated image analysis techniques for cardiovascular magnetic resonance imaging. PhD thesis, Leiden University 2011, 11-44.

134. Hendel RC, Patel MR, Kramer CM, et al: ACCF/ACR/SCCT/SCMR/ ASNC/NASCI/SCAI/SIR 2006 appropriateness criteria for cardiac computed tomography and cardiac magnetic resonance imaging. *J Am Coll Cardiol* 2006, 48: 1475–97.

135. Jaarsma C, Leiner T, Bekkers SC, Crijns HJ, Wildberger JE, Nagel E, Nelemans PJ, Schalla, S: Diagnostic Performance of Noninvasive Myocardial Perfusion Imaging Using Single-Photon Emission Computed Tomography, Cardiac Magnetic Resonance, and Positron Emission Tomography Imaging for the Detection of Obstructive Coronary Artery Disease. *J Am Coll Cardiol* 2012, 59: 1719-1728.

136. Nesterov SV, Han C, Mäki M, Kajander S, Naum AG, Helenius H, Lisinen I, Ukkonen H, Pietilä M, Joutsiniemi E, Knuuti J: Myocardial perfusion quantitation with 15O-labelled water PET: high reproducibility of the new

cardiac analysis software (Carimas). *Eur J Nucl Med Mol Imaging* 2009, 36: 1594-1602.

137. Kaufmann P. A, Camici PG: Myocardial blood flow measurement by PET: technical aspects and clinical applications. *J Nucl Med* 2005, 46: 75-88.

138. Messroghli DR, Greiser A, Fröhlich M, Dietz R, Schulz-Menger J: Optimization and validation of a fully-integrated pulse sequence for modified look-locker inversion-recovery (MOLLI) T1 mapping of the heart. *J Magn Reson Im* 2007, 26: 1081-1086.

139. Kershaw LE, Hutchinson CE, Buckley DL: Benign prostatic hyperplasia: evaluation of T1, T2, and microvascular characteristics with T1-weighted dynamic contrast-enhanced MRI. *J Magn Reson Im* 2009, 29: 641-648.

140. Byrd RH, Gilbert JC, Nocedal J: A Trust Region Method Based on Interior Point Techniques for Nonlinear Programming. *Math Program* 2000, 89: 149–185.

141. Papanastasiou G, Williams MC, Kershaw LE, et al: Measurement of myocardial blood flow by magnetic resonance perfusion imaging. Comparison of distributed parameter and Fermi models with single and dual bolus. *J Cardiov Magn Reson* 2015, 17: 17.

142. Nandalur KR, Dwamena BA, Choudhri AF, Nandalur MR, Carlos RC: Diagnostic performance of stress cardiac magnetic resonance imaging in the detection of coronary artery disease: a meta-analysis. *J Am Coll Cardiol* 2007, 50: 1343–53.

143. Rieber J, Huber A, Erhard I, et al: Cardiac magnetic resonance perfusion imaging for the functional assessment of coronary artery disease: a comparison

with coronary angiography and fractional flow reserve. *Eur Heart J* 2006, 27: 1465-71.

144. Al-Saadi N, Nagel E, Gross M, et al: Improvement of myocardial perfusion reserve early after coronary intervention: assessment with cardiac magnetic resonance imaging. *J Am Coll Cardiol* 2000, 36: 1557-64.

145. Schroeder S, Achenbach S, Bengel F, et al: Cardiac computed tomography: indications, applications, limitations, and training requirements: report of a Writing Group deployed by the Working Group Nuclear Cardiology and Cardiac CT of the European Society of Cardiology and the European Council of Nuclear Cardiology. *Eur Heart J* 2008, 29: 531-56.

146. Bettencourt N, Rocha J, Ferreira N, et al: Incremental value of an integrated adenosine stress-rest MDCT perfusion protocol for detection of obstructive coronary artery disease. *J Cardiovasc Comput Tomogr* 2011, 5: 392-405.

147. Magalh TA, Cury RC, Pereira AC, et al: Additional value of dipyridamole stress myocardial perfusion by 64-row computed tomography in patients with coronary stents. *J Cardiovasc Comput Tomogr* 2011, 5: 449-58.

148. Papanastasiou G, Kershaw LE, Williams MC, et al: A multi-modality cross validation study of cardiac perfusion using MR and CT. ISMRM 21st Annual Meeting Proceedings, 2013, Salt Lake City, UTAH.

149. Papanastasiou G, Williams MC, Dweck MR, et al: Comparison of distributed parameter and Fermi modelling of cardiac MR perfusion with CT perfusion in coronary artery disease versus invasive coronary angiography. ISMRM-ESMRMB Joint Annual Meeting Proceedings, 2014, Milan, Italy.

150. Williams MC, Reid JH, McKillop G, Weir NW, van Beek EJR, Uren NG, Newby DE: Cardiac and coronary CT comprehensive imaging approach in the assessment of coronary heart disease. *Heart* 2011, 97: 1198-1205.

151. Williams MC, Weir NW, Mirsadraee S , Millar F, Baird A, Minns F, Uren NG, McKillop G, Bull RK, van Beek EJR, Reid JH, Newby DE: Iterative reconstruction and individualized automatic tube current selection reduce radiation dose while maintaining image quality in 320-multidetector computed tomography coronary angiography. *Clinic Radiol* 2013, 68: 570-577.

152. Karamitsos T, Leccisotti L, Arnold J, et al: Relationship between regional myocardial oxygenation and perfusion in patients with coronary artery disease: insights from cardiovascular magnetic resonance and positron emission tomography. *Circ Cardiovasc Imaging* 2010, 3: 32–40.

153. Hajjiri MM, Leavitt MB, Zheng H, Spooner AE, Fischman AJ, Gewirtz H: Comparison of positron emission tomography measurement of adenosine-stimulated absolute myocardial blood flow versus relative myocardial tracer content for physiological assessment of coronary artery stenosis severity and location. *J Am Coll Cardiol Img* 2009, 2: 751–8.

154. Kaufmann PA, Gnecchi-Ruscone T, Yap JT, Rimoldi O, Camici PG: Assessment of the reproducibility of baseline and hyperemic myocardial blood flow measurements with ^{15}O-labeled water and PET. *J Nucl Med* 1999, 40: 1848-1856.

155. Camici PG, Crea F: Coronary microvascular dysfunction. *N Engl J Med* 2007, 356: 830-40.

156. Chilian WM: Coronary microcirculation in health and disease: summary of an NHLBI workshop. *Circulation* 1997, 95: 522-8.

157. Shin T, Hu HH, Pohost GM, Nayak KS: Three dimensional first-pass myocardial perfusion imaging at 3T. Feasiblity study. *J Cardiovasc Magn Reson* 2008, 10: 57.

158. Jogiya R, Kozerke S, Morton G, de Silva K, Redwood S, Perera D, Nagel E, Plein S: Validation of dynamic 3-dimensional whole heart magnetic resonance myocardial perfusion imaging against fractional flow reserve for the detection of significant coronary artery disease. *J Am Coll Cardiol* 2012, 60(8): 756-765.

159. Jerosch-Herold M, Wilke N: Cardiovascular magnetic resonance. Chapter: Myocardial perfusion imaging theory. *Elsevier* 2010, 2nd edn, Philadelphia.

160. Donahue KM, Weisskoff RM, Chesler DA, Kwong KK, Bogdanov AA Jr, Mandeville JB, Rosen BR: Improving MR quantification of regional blood volume with intravascular T1 contrast agents: accuracy, precision, and water exchange. *Magn Reson Med* 1996, 36: 858-67.

161. Li X, Springer CS, Jerosch-Herold M: First-pass DCE-MRI with extravasating CR: Evidence for human myocardial capillary recruitment in adenosine-induced hyperemia. *NMR in Biomedicine* 2009, 22(2): 148-157.

162. Czernin J, Muller P, Chan S, et al: Influence of age and hemodynamics on myocardial blood flow and flow reserve. *Circulation* 1993, 88: 62-69.

163. Uren NG, Camici PG, Melin JA, et al: Effect of aging on myocardial perfusion reserve. *J Nucl Med* 1995, 36: 2032-2036.

164. Cecchi F, Olivotto I, Gistri R, Lorenzoni R, Chiriatti G, Camici PG: Coronary microvascular dysfunction and prognosis in hypertrophic cardiomyopathy. *N Engl J Med* 2003, 349: 1027-1035.

165. Broadbent DA, Biglands JD, Ripley DP, Higgins DM, Greenwood JP, Plein S, Buckley DL: Sensitivity of quantitative myocardial dynamic contrast-enhanced MRI to saturation pulse efficiency, noise and T1 measurement error: comparison of nonlinearity correction methods. *Magn Reson Med* 2015, (in press).

10. Appendix

The author presents here mathematical processes to provide a better understanding to the reader for some of the basic operations that were used throughout this thesis. Particularly, the mathematics leading to equation 2-18 (Appendix 1) and to equation 3-1 (Appendix 2) are provided by combining background information from [12-14, 25-27] and using knowledge from algebra and linear differential equations theory. The author also provides mathematical theory with regard to convolution, impulse response and deconvolution (Appendix 3), important subject areas for blood flow quantification from medical imaging data [17]. In the last subsection (Appendix 4), the basic steps for replicating contours and segmentation in Matlab are presented.

10.1 Appendix 1

The Bloch equations are a set of relationships that were developed by physicist Felix Bloch and calculate the nuclear magnetisation in a three dimensional Cartesian system M_x, M_y, M_z as a function of time:

$$\frac{dM_x}{dt} = \gamma(M_y B_z - M_z B_y) - \frac{M_x}{T_2} \quad (10\text{-}1)$$

$$\frac{dM_y}{dt} = \gamma(M_z B_x - M_x B_z) - \frac{M_y}{T_2} \quad (10\text{-}2)$$

$$\frac{dM_z}{dt} = \gamma(M_x B_y - M_y B_x) - \frac{M_z - M_o}{T_1} \quad (10\text{-}3)$$

where B_x, B_y, B_z are the x, y and z components of the main magnetic field B, γ is the gyromagnetic ratio, T_1 and T_2 are T_1 and T_2 relaxation times and M_o is the fully relaxed longitudinal magnetisation.

Considering that in MRI, the main magnetic field B_o is applied along the z-axis, it can be derived that $B_x=B_y=0$ and $B_z=B_o$. Bloch equations can then be simplified to:

$$\frac{dM_x}{dt} = \gamma M_y B_o - \frac{M_x}{T_2} \tag{10-4}$$

$$\frac{dM_y}{dt} = -\gamma M_x B_o - \frac{M_y}{T_2} \tag{10-5}$$

$$\frac{dM_z}{dt} = -\frac{M_z - M_o}{T_1} \tag{10-6}$$

To mathematically describe changes in longitudinal magnetisation M_z as a function of time, equation 10-6 is used. Equation 10-6 is a first order linear differential equation. Solving equation 10-6 for M_z gives the expression for the exponential recovery of longitudinal magnetization after the application of a preparation pulse (e.g. saturation, inversion pulse). The solution of 10-6 is provided here by the author.

Equation 10-6 can be rewritten:

$$\frac{dM_z}{dt} + \frac{M_z}{T_1} = \frac{M_o}{T_1} \Rightarrow$$

This is in the form:

$$\frac{dy}{dx} + p(x) \cdot y = q(x)$$

The integrating factor is:

$$g(x) = e^{\int p(x)dx}$$

So, here the integrating factor equals:

$$g(t) = e^{\int \frac{1}{T_1}dt} \Rightarrow$$

$$g(t) = e^{\frac{t}{T_1}}$$

Multiplying 10-6 by the integrating factor:

$$\frac{dM_z}{dt} \cdot e^{\frac{t}{T_1}} + \frac{M_z}{T_1} \cdot e^{\frac{t}{T_1}} = \frac{M_o}{T_1} \cdot e^{\frac{t}{T_1}} \Rightarrow$$

By using the product rule:

$$\frac{d}{dt}(M_z \cdot e^{\frac{t}{T_1}}) = \frac{M_o}{T_1} \cdot e^{\frac{t}{T_1}} \Rightarrow$$

Finally solving for M_z:

$$M_z \cdot e^{\frac{t}{T_1}} = \int \frac{M_o}{T_1} \cdot e^{\frac{t}{T_1}} dt \Rightarrow$$

$$M_z(t) \cdot e^{\frac{t}{T_1}} = M_o \cdot e^{\frac{t}{T_1}} + C \Rightarrow$$

$$M_z(t) = M_o + C \cdot e^{-\frac{t}{T_1}} \tag{10-7}$$

The boundary conditions are now investigated.

1. In equation 10-7, at t=0 and for a 180° preparation pulse, $M_z(0) = -M_o$ and:

$$-M_o = M_o + C \Rightarrow$$

$$C = -2M_o$$

and equation 10-7 becomes:

$$M_z(t) = M_o - 2M_o \cdot e^{-\frac{t}{T_1}}$$

$$M_z(t) = M_o \cdot (1 - 2 \cdot e^{-\frac{t}{T_1}}) \qquad (10\text{-}8)$$

2. In equation 10-7, at t=0 and for a 90° preparation pulse, $M_z(0) = 0$ and:

$$0 = M_o + C \Rightarrow$$

$$C = -M_o \Rightarrow$$

and equation 10-7 becomes:

$$M_z = M_o \cdot (1 - e^{-\frac{t}{T_1}}) \qquad (10\text{-}9)$$

Following the application of a non-selective preparation pulse, the magnetisation is allowed to relax for a specific amount of time (inversion time or TI). If $M_z^1(-)$ is the longitudinal magnetisation just before the first slice-selective α-radiofrequency-pulse and $M_z^n(-)$ is the longitudinal magnetisation before the nth successive α-radiofrequency-pulse, then:

For a 180° preparation pulse:

$$M_z{}^1(-) = M_o \cdot (1 - 2 \cdot e^{\frac{-TI}{T_1}}) \qquad \text{(See 10-8)}$$

For a 90° preparation pulse:

$$M_z{}^1(-) = M_o \cdot (1 - e^{-\frac{TI}{T_1}}) \qquad \text{(See 10-9)}$$

Whilst:

$$M_z{}^n(+) = M_z{}^n(-) \cdot \cos a \qquad (10\text{-}10)$$

where M_z^n (+) is the longitudinal magnetisation right after the n^{th} successive α-radiofrequency-pulse. Just before the n^{th} α-radiofrequency-pulse, the general formula for the longitudinal magnetisation is:

$$M_z{}^n(-) = M_z{}^{n-1}(+) \cdot e^{-\frac{TR}{T_1}} + M_O \cdot (1 - e^{-\frac{TR}{T_1}}) \Rightarrow \qquad (10\text{-}11)$$

And by using equation 10-10:

$$M_z{}^n(-) = M_z{}^{n-1}(-) \cdot \cos(a) \cdot e^{-\frac{TR}{T_1}} + M_O \cdot (1 - e^{-\frac{TR}{T_1}}) \qquad (10\text{-}12)$$

If:

$$a = \cos(a) \cdot e^{\frac{-TR}{T_1}}$$

$$b = 1 - e^{\frac{-TR}{T_1}}$$

Then:

$$M_z{}^n(-) = M_z{}^{n-1}(-) \cdot a + M_O \cdot b \qquad (10\text{-}13)$$

As described in [25-27], M_z^n (-) can also be expressed as a function of the first signal in the train, i.e. M_z^1 (-). Thus, equation 10-13 can also be expressed as:

$$M_z{}^n(-) = M_z{}^1(-) \cdot a^{n-1} + M_O \cdot b \sum_{k=0}^{k=n-2} a^k \Rightarrow$$

$$M_z{}^n(-) = M_z{}^1(-) \cdot a^{n-1} + M_O \cdot b \cdot \frac{1 - a^{n-1}}{1 - a} \qquad (10\text{-}14)$$

After many α pulses, magnetisation reaches a constant value $M_z{}^c$ which can be defined by equation 10-15 for n=∞:

$$M_z{}^c = M_o \cdot \frac{1-e^{\frac{-TR}{T_1}}}{1-\cos(a)\cdot e^{\frac{-TR}{T_1}}} \qquad (10\text{-}15)$$

For T_1=1000 ms, the full recovery of M_z in an inversion-recovery experiment will be achieved at a time of about 4 to 5 times T_1. Due to the application of successive a pulses, there is a constant loss of longitudinal magnetisation (after each a pulse) and therefore, one observes an effective relaxation time T_1^* which is smaller than T_1 [14]. The magnetisation signal M_z^n (-) is related to M_z^c through the following treatment:

$$M_z{}^n(-) - M_z{}^c = [M_z{}^1(-)\cdot a^{n-1} + M_o \cdot b \cdot \frac{1-a^{n-1}}{1-a}] - [M_o \cdot \frac{b}{1-a}] \Rightarrow$$

$$M_z{}^n(-) - M_z{}^c = M_z{}^1(-)\cdot a^{n-1} + M_o \cdot \frac{b}{1-a}\cdot(1-a^{n-1}-1) \Rightarrow$$

$$M_z{}^n(-) - M_z{}^c = M_z{}^1(-)\cdot a^{n-1} - M_z{}^c \cdot a^{n-1} \Rightarrow$$

$$M_z{}^n(-) = M_z{}^c + M_z{}^1(-)\cdot a^{n-1} - M_z{}^c \cdot a^{n-1} \Rightarrow$$

$$M_z{}^n(-) = M_z{}^c + (M_z{}^1(-) - M_z{}^c)\cdot a^{n-1}$$

For an inversion recovery experiment at t=0, M_z^1 (0)= -1 and:

$$M_z{}^n(-) = M_z{}^c - (1+M_z{}^c)\cdot a^{n-1} \qquad (10\text{-}16)$$

Equation 10-16 can be written as a monoexponential curve:

$$M_z(t) = M_z{}^c - (1+M_z{}^c)\cdot e^{-\frac{t}{T_1^*}} \qquad (10\text{-}17)$$

With:

$$M_z{}^c = M_o \cdot \frac{1-e^{\frac{-TR}{T_1}}}{1-e^{\frac{-TR}{T_1^*}}}$$

Because TR<<T_1*<T_1, M_z^c can be given in a good approximation by:

$$M_z{}^c = \frac{T_1 *}{T_1}$$

Hence, the time dependence of magnetisation is given by:

$$M_z(t) = M_o{}^* - (M_o + M_o{}^*) \cdot e^{-\frac{t}{T_1^*}} \tag{10-18}$$

With:

$$M_o * = M_o \cdot \frac{T_1 *}{T_1} \tag{10-19}$$

If

$A = M_o * = M_o \cdot T_1 * / T_1$

$B = M_o + M_o * = M_o \cdot (1 + T_1 * / T_1)$

equation 2-18 can be derived from 10-18:

$$M_z(t) = A - B \cdot \exp(-\frac{t}{T_1^*}) \tag{2-18}$$

where A, B and T_1* can be calculated by a three-parameter fit.

Finally T_1 can be calculated from equation 2-19:

$$T_1 = T_1 * (B / A - 1) \tag{2-19}$$

10.2 Appendix 2

As discussed in Appendix 1, the longitudinal magnetisation just before the nth a-radiofrequency pulse is given by equation 10-14:

$$M_z{}^n(-) = M_z{}^1(-) \cdot a^{n-1} + M_o \cdot b \cdot \frac{1-a^{n-1}}{1-a} \qquad (10\text{-}14)$$

Because the MR signal is detected in the x-y plane, the magnetisation in the detection plane after the nth a-radiofrequency pulse is:

$$M_{xy}{}^n(+) = M_z{}^n(-) \cdot \sin a$$

Thus, the MR signal generated after n a radiofrequency pulses in a saturation recovery FLASH sequence is given by [25]:

$$SI = \Omega \cdot M_o \cdot \sin a \left[\left(1 - e^{-PD \cdot R_1}\right) \cdot a^{n-1} + b \frac{1-a^{n-1}}{1-a} \right] \Rightarrow$$

$$SI = \Psi \cdot \left[\left(1 - e^{-PD \cdot R_1}\right) \cdot a^{n-1} + b \frac{1-a^{n-1}}{1-a} \right] \qquad (3\text{-}1)$$

where SI is the MR signal intensity, Ψ is a calibration constant dependent on instrumental conditions, receiver gain, proton density and the flip angle α. PD is the pre-pulse delay which is the time between saturation pulse and the central line of k-space.

10.3 Appendix 3

Convolution is a mathematical technique with multiple applications that can be used to calculate the zero state response of a system to an arbitrary input signal by using the impulse response of the system. The zero state response of a system is the response to an input when the system has zero initial conditions. In mathematical terms, convolution can be seen as a mathematical operation of two functions f and g, producing a third function. The third function can typically be a modified version of one of the original functions f or g [17].

The tissue impulse response is the basic property of a system which defines the way that the system responds to a stimulus or excitation (i.e. input signal). This can be schematically summarized in the following graph:

$$f(t) \longrightarrow \boxed{h(t)} \longrightarrow g(t)$$

where f(t) is the input signal and g(t) is the output.

Let assume a linear and time-invariant system (LTI). If we now consider that the input is an impulse δ(t), then by definition, the output of the signal is the impulse response:

$$\delta(t) \longrightarrow \boxed{\text{LTI}} \longrightarrow h(t)$$

Because of time-invariance, if the impulse is delayed by τ, then the output (i.e. impulse response) is also delayed by the same delay:

$$\delta(t-\tau) \longrightarrow \boxed{\text{LTI}} \longrightarrow h(t-\tau)$$

Due to linearity, if the input is scaled by a factor, then the output is also scaled by the same factor. For example, if the input and output will be scaled by the factor f(τ)dτ:

$$\delta(t-\tau)\cdot f(\tau)d\tau \longrightarrow \boxed{\text{LTI}} \longrightarrow h(t-\tau)\cdot f(\tau)d\tau$$

Furthermore, if we integrate the input from negative to positive infinity, the output is also integrated:

$$\int_{-\infty}^{+\infty} \delta(t-\tau)\cdot f(\tau)d\tau \longrightarrow \boxed{\text{LTI}} \longrightarrow \int_{-\infty}^{+\infty} h(t-\tau)\cdot f(\tau)d\tau$$

From the shifting property of the tissue impulse response, it is known that:

$$\int_{-\infty}^{+\infty} \delta(t-\tau)\cdot f(\tau)d\tau = f(t) \tag{10-20}$$

Hence:

$$f(t) \longrightarrow \boxed{\text{LTI}} \longrightarrow \int_{-\infty}^{+\infty} h(t-\tau)\cdot x(\tau)d\tau$$

By definition and based on the first diagram, if the input is f(t) then the output is g(t):

$$f(t) \longrightarrow \boxed{\text{LTI}} \longrightarrow g(t)$$

Thus, the response of the system to a series of delayed input functions is:

$$g(t) = \sum_{i=0}^{\infty} f(\tau)\cdot h(t-\tau) \tag{10-21}$$

Taking the limit as τ tends to 0, the summation in 10-20 yields the convolution integral:

$$g(t) = \int_{0}^{t} f(\tau)\cdot h(t-\tau)dt \tag{10-22}$$

Equation 10-22 states that the output is equal to the sum of the responses from all individual impulses. Equation 10-22 can also be derived if the outputs of the last two diagrams will be equated. Thus, it can be concluded that if the tissue impulse response is known, it is possible to calculate the output for any given input.

The question that arises is how is it possible to calculate the tissue impulse response, if the input and output functions are known? In other words, how f(t) and g(t) functions are deconvolved, to calculate h(t)?

The author here presents the model for deconvolution. The central idea is to convert our functions into the frequency domain using Fourier transform (FT). In the frequency domain, the output in equation 20-21 can be now calculated by the following multiplication (equation 10-23):

$$g(t) = \int_0^t f(\tau) \cdot h(t-\tau) dt \overset{FT}{\Rightarrow}$$

$$\hat{g} = \hat{f} \cdot \hat{h} \qquad (10\text{-}23)$$

where $\hat{g}$, $\hat{f}$ and $\hat{h}$ is the frequency domain of functions g, f and h respectively.

To complete the deconvolution process, it is possible to get the tissue impulse response through the following division:

$$\hat{h} = \frac{\hat{g}}{\hat{f}} \qquad (10\text{-}24)$$

Finally, by using inverse Fourier transform (IFT), we can get the tissue impulse response in the time domain:

$$\hat{h} \overset{IFT}{\Rightarrow} h(t) \qquad (10\text{-}25)$$

10.4 Appendix 4

Basic steps for replicating contours and segmentation in Matlab are presented.

1) After manual contouring in QMass, the x and y coordinates of all contours from each perfusion data set were saved in a txt file. A Matlab code was created to automatically identify and extract x and y coordinates of all contours from txt files which were then saved in a Matlab matrix. In a separate matrix, x and y coordinates of all starting points (blue crosses in Figure 4-11) across all dynamic perfusion images were also identified and saved. At this stage, it was possible to read and visualize cardiac contours and starting points on MR perfusion images in Matlab environment (Figure 10-1).

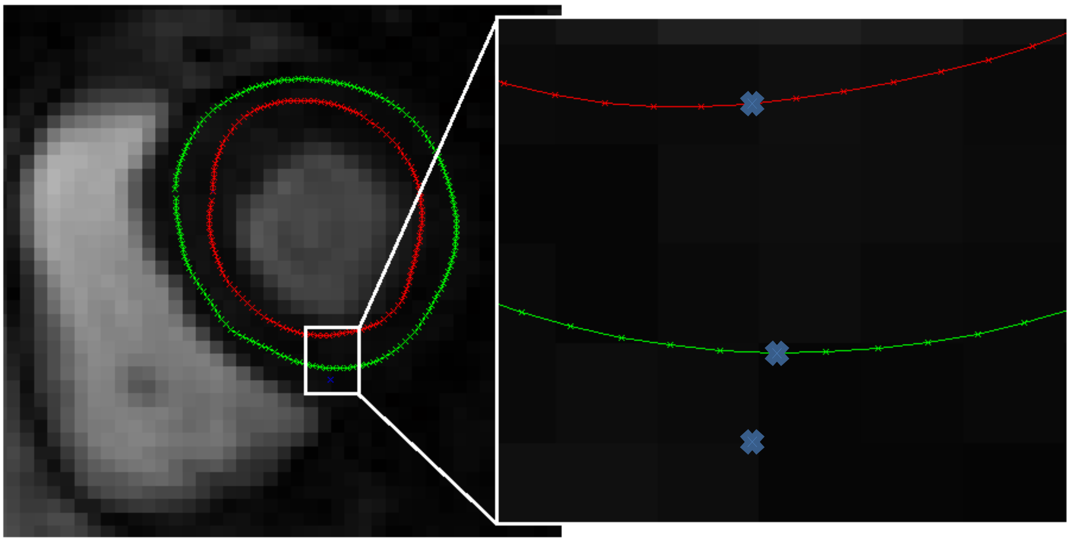

Figure 10-1) a) Example image in Matlab of x and y coordinates of all endocardial (red x) and epicardial (green x) points read on MR perfusion images. b) Starting point and the nearest endocardial and epicardial points are shown with blue x.

2) From this step onwards, all geometrical and linear algebra operations that are automatically performed in QMass were interpreted and replicated in Matlab. In Qmass, the reference point for initiating myocardial segmentation is the starting point (blue cross in QMass and blue x in Matlab, Figures 4-11 and 10-1 respectively). The starting point is set by the user (in one image) at the conjunction of the left and right ventricles and myocardial segmentation is then automatically performed. To initiate myocardial segmentation in Matlab, the nearest (one endocardial and one epicardial) point to the starting point was detected by applying the Pythagorean Theorem (equation 10-26) and Matlab coding. This can be detailed using Cartesian coordinates in Figure 10-2. In Matlab, the upper left corner in the image is (0,0).

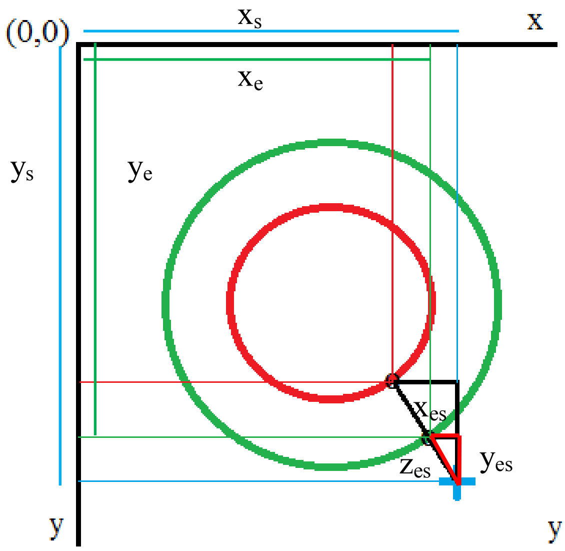

Figure 10-2) Endocardial (red) and epicardial (green) contours in Matlab Cartesian coordinates. The nearest endocardial and epicardial (black circles) point to the starting point was detected. x_s, y_s are the coordinates of the starting point and x_e, y_e are the coordinates of

the epicardial contour point (for simplicity only the epicardial contour point coordinates are presented here and the relative (imaginary) triangle is illustrated with red).

Using equation 10-26 which is derived from the Pythagorean Theorem, it was possible to calculate the distances between the starting point and all the endocardial and epicardial contour points. The minimum distance was then detected and saved to define the nearest endocardial and epicardial contour point to the starting point.

$$z_{es} = \sqrt{({x_{es}}^2 + {y_{es}}^2)} \tag{10-26}$$

where $x_{es}=x_e-x_s$ and $y_{es}=y_e-y_s$. x_e, y_e and x_s, y_s are the x and y coordinates of each contour point (endocardial or epicardial) and of the starting point respectively. z_{es} is the hypotenuse of the (imaginary) triangles formed with the other two sides being x_{es} and y_{es}, as shown in Figure 10-2.

3) Both endocardial and epicardial contours were divided into 100 equally spaced points as first described in the study by von Land et al [132] and detailed in the thesis of van der Geest [133]. Starting from the nearest point to the starting point in both endocardial and epicardial contours, unequally spaced points were interpolated using parametric splines (using a Matlab function). After interpolation, the endocardial and epicardial contours were divided into 100 equally spaced points.

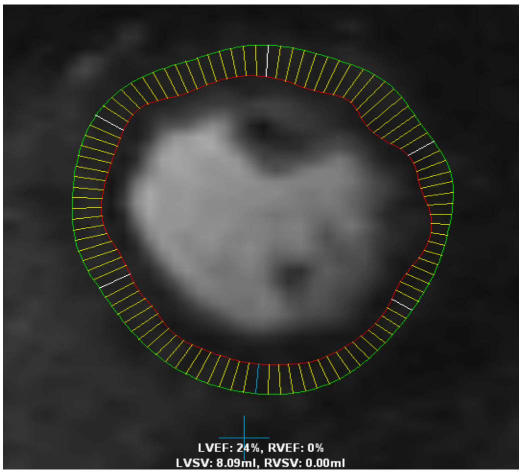

Figure 10-3) Myocardium is divided into 100 equally spaced chords in QMass. The same process (steps 3-7) was replicated in Matlab.

4) A centerline was created by calculating the midpoints between all endocardial and epicardial (equally spaced) points. This can be described by the following set of equations:

$$\Delta x = x_{ep} - x_{en} \qquad (10\text{-}27)$$

Similarly, $\Delta y = y_{ep} - y_{en}$

$$Midpoint(x, y) = \frac{\Delta x}{2} + x_{en}, \frac{\Delta y}{2} + y_{en} \qquad (10\text{-}28)$$

where x_{ep}, y_{ep} and x_{en}, y_{en} are the x and y coordinates of the epicardial and endocardial equally spaced contour points respectively.

5) Starting from the nearest midpoint (m_o) to the starting point, the slope of the tangent line to each midpoint was then calculated using linear algebra (equation 10-29).

$$Tangent_{m_o} = \frac{y_{m_{o-2}} - y_{m_{o+2}}}{x_{m_{o-2}} - x_{m_{o+2}}} \qquad (10\text{-}29)$$

where x_{mo-2}, y_{mo-2} and x_{mo+2}, y_{mo+2} are the x and y coordinates of the second consecutive midpoint before and after m_o (Figure 10-4).

Subsequently, the slope of the perpendicular to the $Tangent_{mo}$ was calculated (equation 10-30). The point at which the perpendicular line intersects with the y axis was calculated using the linear equation (equation 10-31).

$$Perpendicular_{m_o} = \frac{-1}{Tangent_{m_o}} \qquad (10\text{-}30)$$

$$b_p = y_{m_o} - Perpendicular_{m_o} \cdot x_{m_o} \qquad (10\text{-}31)$$

where b_n is the point at which the extension of the $Perpendicular_{mo}$ line intersects with the y axis and x_{mo} and y_{mo} are the coordinates of the midpoint m_o (Figure 10-4).

6) Between consecutive points along the cardiac contours (i.e. both endocardial and epicardial), (straight) line segments can be observed. The slopes of individual line segments could be calculated using equation 10-32.

$$lineseg = \frac{y_{o-1} - y_o}{x_{o-1} - x_o} \qquad (10\text{-}32)$$

where x_{o-1}, y_{o-1} and x_o, y_o are the x and y coordinates of two consecutive points (i.e. ending points of each line segment) along the cardiac contours. Also, the point at which the extension of each line segment intersects with the y axis was calculated using the linear equation (equation 10-33).

$$b_l = y_o - lineseg \cdot x_o \qquad (10\text{-}33)$$

where b_l is the point at which the extension of the line segment intersects with the y axis and x_o and y_o are the coordinates of the cardiac (endocardial or epicardial) contour point. Step 6 was repeated for all endocardial and epicardial line segments.

7) The x and y coordinates of the intersections of the perpendicular line (Perpendicular$_{mo}$) with individual line segments was then calculated (equation 10-34 and 10-35). m_o is the nearest midpoint to the starting point. en_o and ep_o can also be defined, as the nearest endocardial and epicardial points to the starting point respectively. Since cardiac contouring can form curved lines, it was unknown with which line segment Perpendicular$_{mo}$ actually intersects. To account for complex curvatures when it was necessary for cardiac contouring to avoid image artifacts, the intersection points of three line segments before and after each en_o and ep_o were calculated.

$$X = \frac{b_l - b_p}{m_p - m_l} \tag{10-34}$$

$$Y = ml \cdot X + b_l \tag{10-35}$$

where X and Y are the coordinates of the intersection points.

The intersection points of the Perpendicular$_{mo}$ line with 6 line segments were calculated in total (with 6 endocardial line segments and 6 epicardial line segments). To discriminate from these intersection points the correct line segment with which the Perpendicular$_{mo}$ intersects (i.e. the correct X, Y point) and to exclude the possibility that the Perpendicular$_{mo}$ intersects with imaginary extensions of neighboring line segments, three algebraic relationships had to be satisfied:

a) First, the magnitude of the cross product of the line segment (with ending points: x_{o-1}, y_{o-1} and x_o, y_o) and the (straight) line formed between the contour point X, Y and x_o, y_o had to be zero. This proves that the above straight lines are collinear.

$$u \times v = (u_2 v_3 - u_3 v_2)i + (u_3 v_1 - u_1 v_3)j + (u_1 v_2 - u_2 v_1)k \tag{10-36}$$

$$u \times v = ai + bj + ck \tag{10-37}$$

$$A = |u \times v| = \sqrt{(a^2 + b^2 + c^2)} \tag{10-38}$$

Equation 10-36 describes the cross product of vectors u and v. Let u be the line segment and v be the line formed between the contour point X, Y and x_o, y_o. These straight line segments are two-dimensional vectors and thus, the first and second terms in equation 10-36 are neglected. Equation 10-37 represents the numeric solution of equation 10-36 whilst equation 10-38 gives the magnitude of the cross product. In two dimensional vectors, the terms a and b in equations 10-37 and 10-38 are zero.

b) The dot product of the aforementioned straight lines had to be positive.

$$u \cdot v = u_1 v_1 + u_2 v_2 + u_3 v_3 \tag{10-39}$$

Equation 10-39 gives the dot product of vectors u and v. u represents again the line segment and v is the line formed between the contour point X, Y and x_o, y_o. In two dimensional vectors the third term is neglected.

c) The squared distance between the line segment points x_{o-1}, y_{o-1} and x_o, y_o had to be bigger than the above dot product.

$$Squareddis = \sqrt{[(x_o - x_{o-1})^2 + (y_o - y_{o-1})^2]} \qquad (10\text{-}40)$$

b) and c) prove that the line formed between the contour point X, Y and x_o, y_o is aligned with the line segment defined by x_{o-1}, y_{o-1} and x_o, y_o and that the X, Y point can be found within the limits of the specific line segment. The correct X and Y coordinates were then saved.

A graphical representation of the above process is presented in Figure 10-4.

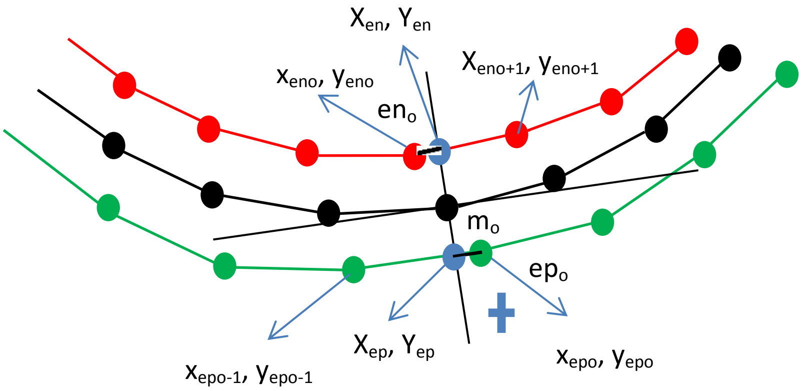

Figure 10-4) Graph showing consecutive endocardial (red), midpoint (black) and epicardial (green) equally spaced points. Tangent and perpendicular to the midpoint lines are illustrated. Line segments between consecutive contour points are shown for each cardiac contour. Small (black) line segments between X, Y and x_o, y_o along the endocardial (en) and epicardial (ep) contours are shown. The first chord perpendicular to the nearest midpoint (m_o) to the starting point is shown. The blue cross represents the starting point.

Step 7 was repeated for all 100 midpoints. X, Y points along both endocardial and epicardial contours were defined and saved. A line (i.e. half chord) was drawn to connect the correct X, Y point (along both endocardial and epicardial contours) with its corresponding midpoint m_o. Note that this line was always perpendicular to the midpoint. At the end of the processing, 100 chords were created which were connecting endocardial and epicardial points as shown in Figure 10-5c.

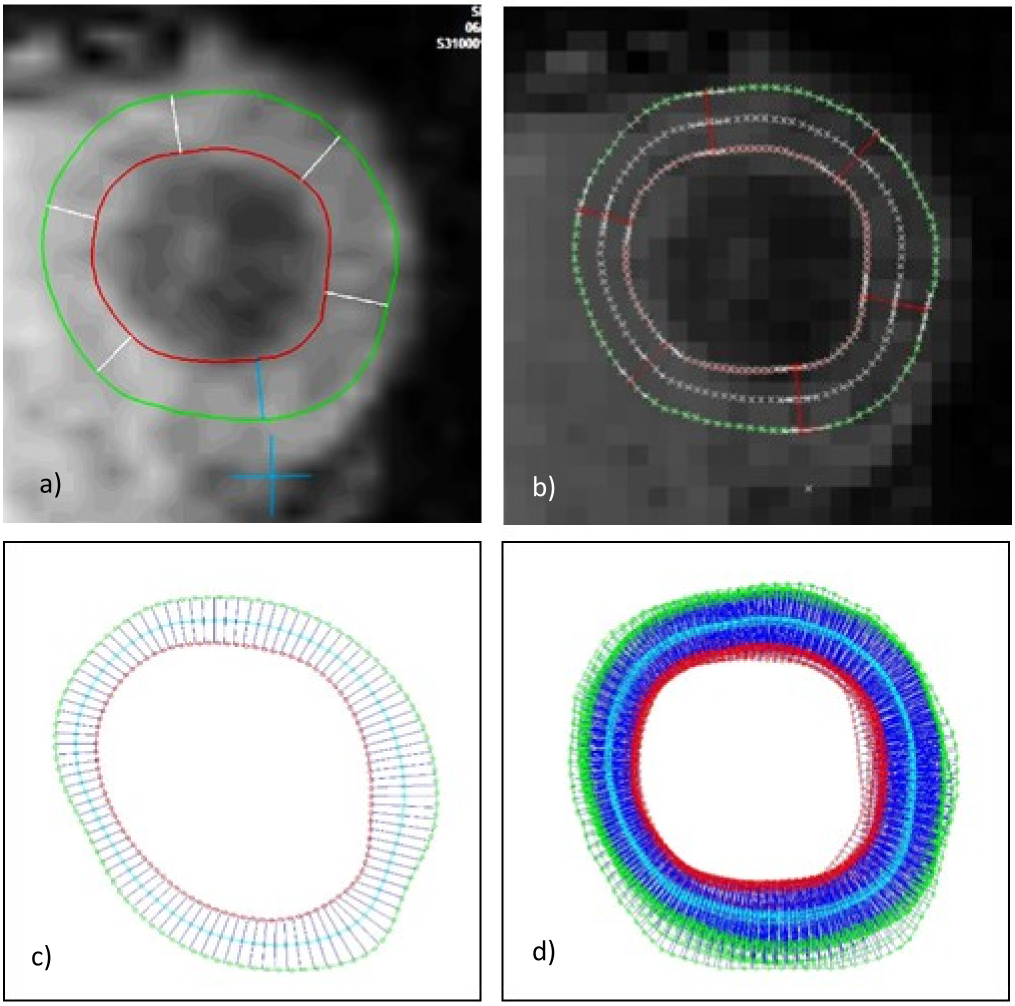

Figure 10-5) a) Myocardial segmentation in Qmass. b) Myocardial segmentation replicated in Matlab. c) Endocardial (red) and epicardial (green) contours with centerline (blue) and all 100 chords. d) All contours and chords for a full perfusion data set replicated in Matlab.

8) Based on the QMass method for myocardial segmentation, basal and mid-ventricular short axis views of the myocardium were divided into 6 myocardial segments. Starting from the first chord (i.e. chord perpendicular to the nearest

midpoint to the starting point) and counting anti-clockwise, myocardial segments 1, 2, 3, 4, 5 and 6 (see Figure 4-11) consisted of 17, 17, 16, 17, 17 and 16 chords respectively. Apical slice was divided into 4 equal myocardial segments each one consisted of 25 chords. These segments were then renumbered according to the AHA model [Figure 4-4, 16]. Using this information, average signal intensity was extracted from each myocardial segment using Matlab.

List of figures

Figure 2-1 (a) The rotation of a positively charged nucleus producing a local magnetic field (magnetic moment) is shown. (b) Randomly orientated magnetic moments of individual protons in the absence of an external magnetic field. Their net magnetisation vector sum is 0……………………………………………………23

Figure 2-2 (a) At equilibrium, M_0 is parallel to B_0. As the 90^o excitation radiofrequency pulse is applied, M_0 is tilted to rotate in a spiral path to end up perpendicular with B_0. (b) M_0 start to precess about B_1 (MRI: From picture to proton, 2006)……………………………………………………………………...25

Figure 2-3 The following can be viewed if the observer is placed in the rotating frame of reference (the frame rotation matches the Larmor frequency). 1. Spin-echo (a) Protons dephasing and rephasing. Net magnetization M_0 (shown as the thick blue arrow) before the application of radiofrequency pulse, aligned along the longitudinal z-direction parallel to B_0. (b) M_0 is tilted along the transverse x-y orientation after the application of a 90^o excitation radiofrequency pulse. (c) Protons lose phase coherence and start to dephase. (d) After the application of a 180^o refocusing pulse and subsequent time, protons rephase and create a spin-echo. 2. Gradient echo (e) Immediately after a 90^o pulse, all spins are in phase. (f) Application of a gradient will increase the precession frequency of some spins whilst reduce it in others. (g) Application of a gradient of different polarity at time T causes the spins to refocus. (h) Spins eventually return back into their initial state and at subsequent time, create a gradient-echo...27

Figure 2-4 The slice selective gradient is presented. The radiofrequency bandwidth is centred about the Larmor frequency. Only protons inside the radiofrequency bandwidth are excited. The thickness of the slice relates to the gradient strength and the radiofrequency bandwidth range (MRI: From Picture to Proton, 2006)...............28

Figure 2-5 (a) Frequency encoding gradient. After excitation, all protons within the excited (slice) volume precess at the same frequency. When G_{RO} is applied, it causes a variation in the frequencies of the protons. The frequency of precession for each proton depends upon its position (according to equation 2-4). (b) Phase encoding gradient. Similarly to the concept of the frequency encoding gradient, before the application of G_{PE}, all protons precess at the same frequency. Following application of G_{PE}, a proton increases or decreases its precessional frequency depending upon its position (equation 2-4). As shown, a proton located in $y_2=0$ experiences no effect from G_{PE}. However, a proton located at y_3 precesses faster during the application of G_{PE}. When G_{PE} is switched off, the proton precesses at its original frequency but is now ahead (phase shift φ_3) of the reference frequency (shown here with the dashed line). A phase shift has been induced in the proton by G_{PE}. In the same way, a proton located at y_1, decreases its frequency during the application of G_{PE}. Thus, after G_{PE} is turned off, it precesses at its original frequency but is now behind (phase shift φ_1) the reference frequency (MRI: Basic pulse principles and applications, 2010)...............31

Figure 2-6 One of the visualised directions in all MR images is the readout direction. The other is the phase encoding direction as shown...32

Figure 2-7 k-space representation. (a) k-space matrix is a raw data matrix having the same number of rows (number of readout or frequency encoding steps defined as

N_{RO}) and columns (number of phase encoding steps defined as N_{PE}) as (b) the final image. (c) k-space filling for different (reverse linear) phase encoding steps. k-space and corresponding images showing: (d) image reconstruction using all spatial frequencies, (e) using only low spatial frequencies from the centre of k-space and (f) using only high spatial frequencies from the edges of k-space................................36

Figure 2-8 Longitudinal (T_1) and transverse (T_2) relaxation time illustrated. Although they occur simultaneously, T_1 is much slower than T_2 (MRI: Basic pulse principles and applications, 2010)…………………………………………………..39

Figure 2-9 A standard spin echo sequence is shown. A single echo is produced at time TE after the excitation pulse and localised by a slice selective gradient (G_{SS}), a readout gradient (G_{RO}) and a single phase encoding gradient (G_{PE})………………..42

Figure 2-10 Following an α pulse, an echo is formed after the application of a phase offset to each successive flip angle (i.e. same flip angle but in a different direction) and/ or a negative (-) and a positive (+) gradient in the readout direction (G_{RO}). The two gradients are of the same magnitude but of different polarity…………………44

Figure 2-11 MOLLI pulse sequence scheme is shown. Each vertical bar represents one image acquisition. Three sets of Look-Locker (LL) experiments are performed successively (LL1 = three images, LL2 = three images, LL3 = five images) with increasing inversion time within one breath-hold’s time. To select end-diastole, images were acquired using a specific trigger delay (TD). For T_1 calculation, images are regrouped for post-processing according to their effective inversion time (Messroghli et al, Magn Reson Med, 2004)...49

Figure 2-12 A multislice saturation recovery FLASH scheme. TI is the inversion time which is the time between the saturation pulse and the centre of the readout (centre of k-space), T_{slice} is the time per slice and T_{image} is the time for image readout (adapted by Kellman et al, J Cardiovasc Magn Reson, 2007)…………………….....51

Figure 2-13 A mathematical approximation of monochromatic x-ray attenuation. An object of thickness $\Delta\eta$ with a constant attenuation coefficient μ is assumed. Equal parts of the same absorbing medium attenuate equal fractions of the x-ray radiation (Computed Tomography: From photon statistics to modern cone-beam, 2008)……53

Figure 2-14 a) The first generation of CT scanners used a pencil beam geometry and a single detector. The above configuration is rotated through different projection angles γ (through 180^0). Each point inside the field of view needs to be irradiated from all different positions. b) The second generation CT scanners used x-ray sources with fan-beam geometry, combined with a short detector array. The configuration in b needs also to be rotated since the fan angle is about 10^0. c) The third generation of CT scanners uses fan angle of about 40^0-60^0 whilst the detection array consists of up to 1000 detector elements. The entire field of view can be measured simultaneously and the acquisition time has been considerably reduced (Computed Tomography: From photon statistics to modern cone-beam, 2008)........55

Figure 2-15 Rotating frame (ξ, η) compared to the fixed frame (x, y) is shown. p_γ (ξ) represents the attenuation profile of the x-ray beam versus the coordinate ξ of the detector array, for the particular projection angle γ (Computed Tomography: From photon statistics to modern cone-beam, 2008)…………………………………...56

Figure 3-1 Left panel: Two compartment exchange model which assumes that the extravascular-extracellular space (v_e) and the intravascular plasma space (v_p) are both compartments. In each of these compartments, the contrast agent concentration is assumed to be homogeneous. Right panel: The distributed parameter model can be considered as a sequence of infinitesimal two compartment exchange models. The contrast agent concentrations in each of these compartments depend on the position x along the capillary direction..71

Figure 4-1 Example image of all 9 phantoms, visualised using MATLAB. From phantoms 1 to 9, the gadolinium concentration was gradually increased (see Table 4-1). A region of interested is shown in phantom 1, from which the signal intensity was extracted..84

Figure 4-2 Linear regression analysis of T_1 relaxation times calculated using spin echo inversion recovery (SEIR) and MOLLI techniques…………………………...87

Figure 4-3 Spin echo inversion recovery experiment. Red curve: experimental curve for phantom 5 showing signal intensities versus inversion times. Blue curve: Model (equation 2-17) fit from which M_0 and T_1 relaxation time were calculated…...........88

Figure 4-4 MOLLI experiment. Red curve: experimental curve for phantom 5 showing signal intensities versus inversion times. Blue curve: Model (equation 2-18) fit from which A, B, T_1^* and T_1 relaxation time were calculated…………………...88

Figure 4-5 a) A typical ECG signal showing a P wave, a QRS complex and a T wave. b) MRI-compatible ECG electrodes used for MRI-gating…………………..91

Figure 4-6 Configuration of the 3T MR system and the 32-channel (phased array) cardiac coil placed over the chest…..…………….……………..……………….92

Figure 4-7 a) HASTE images (on the axial plane). Along the long axis of the heart, it was possible to select the exact position for two-chamber view imaging, with the use of the MR system software. b) Two-chamber cardiac views were acquired (TrueFISP technique). The exact position for the acquisition of four-chamber views could be again selected through the MR system software. c) Four-chamber views were acquired (TrueFISP). It was then possible to choose the exact height at which the short axis views would be acquired. d) Short axis view scan, the images had optimum spatial resolution and the anatomy of the heart could be clearly visualised (e.g. papillary muscles inside the left ventricle which is located at the right part of the image-red arrow)……………………………………………………………….94

Figure 4-8 ECG-gating for dynamic perfusion acquisition. a) Using a specific time delay after the R peak (illustrated with the red box), b) three short axis views (from basis to the apex of the left ventricle) and one long axis view could be acquired at diastole. Dynamic acquisition was possible during a breath-hold (to minimize respiratory motion artifacts) for 50 time points (i.e. sequential RR intervals), to track the delivery of the contrast agent through the cardiac chambers (adapted from Cerqueira et al, 2002)……………………………………………………………..96

Figure 4-9 Four short axis view perfusion images are shown in different phases of contrast enhancement. a) Baseline (also known as pre-contrast) images before contrast arrive into the right atrium and ventricle. b) Contrast bolus arrival in the right ventricle. c) Contrast bolus passes into the lungs (through the pulmonary circulation) and then contrast enhancement in the left ventricle can be observed. d) Contrast bolus is passing from the left ventricle into the myocardium through the coronary arteries. Contrast enhancement in the myocardium is shown……….……97

Figure 4-10 Short axis view T1 map generated using MOLLI. Signal intensity in each pixel corresponds to a tissue T_1 relaxation time……………………………100

Figure 4-11 Endocardial (red) and epicardial (green) contours are presented in a perfusion image of a healthy volunteer during peak contrast enhancement. The blue cross indicates the starting point from which myocardial segmentation can be adjusted. Basal and mid-ventricular slices of the myocardium were automatically divided into 6 equal segments (apical slice was divided in 4 equal segments). a) Generous contouring: myocardial areas are exposed to contamination from blood pool signal (red arrows), dark rim artifacts (blue arrow) and contamination from the surrounding tissues (green arrows). b) Conservsative contouring was performed to avoid contamination of myocardial areas from the left ventricle blood pool signal (red arrows), dark rim artifacts (blue arrow) and contamination from the surrounding tissues (green arrows). Contrast in the images has been adjusted to highlight artifacts which are not always distinctive but can affect quantification [131]……….……102

Figure 4-12 Dynamic signal intensity curves across all 50 time points for the same myocardial segment. Signal intensity values extracted using Matlab (magenta line) and signal intensity values extracted using QMass (blue line) are illustrated. A paired t-test showed no difference between myocardial segments for all 4 healthy volunteers……………………………………………………………………..104

Figure 4-13 FLASH saturation recovery prepared single-shot gradient echo pulse sequence. Consecutive α pulses, PD and $\alpha_{k=0}$ are shown. This scheme is repeated within each RR interval at each dynamic perfusion image acquisition. During an RR interval, all lines of k-space are acquired for each (dynamic) perfusion image…...106

Figure 4-14 Centric k-space ordering………………………………………………..107

Figure 4-15 Signal intensities (SI) derived using Matlab (experimental mean values with standard deviations, blue curve) and calculated values estimated using equation 4-1 (red)…………………..……………………….108

Figure 4-16 Linear regression analysis of signal intensity (SI) values are shown. Experimental SI on the y axis and measured SI on the x axis calculated using equation 4-1……………………………………………………………………..109

Figure 4-17 a) Left ventricle with selected area is shown from which b) a 9x9 pixel grid is extracted. Black frame surrounds all pixels from which signal intensity curves are extracted and converted into gadolinium concentration curves which are averaged and used for myocardial blood flow analysis……………………………………...111

Figure 4-18 Signal intensity values (a.u.) (with standard deviations) versus actual Gd concentration (mM). Non-linearity is induced in phantoms 5-11, whilst a plateau is observed at higher concentrations (phantoms 7-11). Gd: gadolinium.……………..115

Figure 4-19 T1 relaxation times (ms) and standard deviations versus actual Gd concentrations (mM). Exponential decay of T1 relaxation time as gadolinium concentration is increasing is shown. Gd: gadolinium. …………………….........116

Figure 4-20 Calculated (standard deviations) versus actual Gd concentration (mM). Gd: gadolinium……………………………………………………………………117

Figure 4-21 Dual bolus injection scheme………………………………………119

Figure 4-22 Patient being placed supine in Aquilion ONE CT scanner…………..121

Figure 5-1 Mid-ventricular dynamic cardiac perfusion images are shown from a healthy volunteer. Dynamic perfusion image (a) before contrast enhancement, (b) contrast enhancement in the right ventricle, (c) peak contrast enhancement in myocardial tissue and (d) post (wash out) contrast enhancement in myocardial tissue………………………………………………………………………………133

Figure 5-2 Mid-ventricular dynamic cardiac perfusion images are illustrated from a patient with a perfusion abnormality in the infero-septal and inferior myocardial regions (white arrows). Dynamic perfusion image (a) before contrast enhancement, (b) contrast enhancement in the right ventricle, (c) peak contrast enhancement in myocardial tissue and (d) post (wash out) contrast enhancement in myocardial tissue………………………………………………………………………………134

Figure 5-3 Examples of Fermi and distributed parameter model fits at rest (a, b) and at stress (c, d) from the same volunteer (dual bolus analysis). Fermi (e) and distributed parameter (f) model fits during hyperemia of a pathological myocardial segment (single bolus analysis). DP: distributed parameter model, Gd: gadolinium……………………………………………………………………………136

Figure 5-4 Scaled pre-bolus arterial input function versus standard arterial input function from the same examination. In volunteer 1 (a) and volunteer 2 (b) scaled pre-bolus (blue) arterial input function and main bolus arterial input function (red) are shown. Gd: gadolinium…………………………………………………………...137

Figure 5-5 Bland Altman plots of a) dual bolus (DB)-distributed parameter (DP) versus single bolus (SB)-DP myocardial blood flow (MBF) values and b) DB-Fermi versus SB-Fermi MBF values…………………………………………………...140

Figure 5-6 Mean Fermi-MBF (a), distributed parameter-MBF (b), Fermi-MPR (c), distributed parameter MPR (d) versus ICA/FFR classification. MBF: myocardial blood flow, MPR: myocardial perfusion reserve, ICA: invasive coronary angiography, FFR: fractional flow reserve…………………………………...142

Figure 6-1 Arterial input function used to generate simulated data. First-pass and entire course of the contrast agent bolus in the blood pool is shown (AIF). Solid line: AIF (arterial input function), solid line with circles: simulated tissue curve……....154

Figure 6-2 Scaled pre-bolus arterial input function (blue) and standard main bolus arterial input function (red). A difference in contrast agent bolus dispersion is apparent. This can influence the reproducibility of myocardial blood flow analysis as the selection of the end point of the first-pass range becomes subjective. Does the end point in the scaled pre-bolus or in the standard main bolus arterial input function define the first-pass range? Also, note that the end point of the first-pass is not obvious in the case of the scaled arterial input function due to substantial noise effects……………………………………………………………………………155

Figure 6-3 (a) Arterial input function without noise (blue line), with noise level 1 (red dashed line) and noise level 2 (green dashed-dot line). (b) Simulated curves without noise (blue line), with noise level 1 (red dashed line) and noise level 2 (green dashed-dot line). A time delay has been used between curves for clarity...........158

Figure 6-4 Visual representation of linear regression analysis showing ideal values versus first-pass distributed parameter modelling-derived values for myocardial blood flow (MBF, blue diamond), permeability surface area product (PS, green diamond), extravascular-extracellular space (v_e, blue circles) and volume of distribution (v_d, green circles). Black dashed line shows perfect relationship between y and x axis data (i.e. ideal values=measured values). First-pass distributed parameter modelling-derived values for v_e and v_d are consistently underestimated as compared to ideal values...164

Figure 6-5 Example images of DP and first-pass DP modelling in simulated curves with first-pass to recirculation peak ratio of 1.5. Dashed black and blue lines indicate the height of the first-pass peak and of the recirculation peak, respectively. Simulated curves with no noise (a, b), with noise level 1 (c, d) and noise level 2 (e, f)............165

Figure 6-6 Example images of DP and first-pass DP modelling in simulated curves with first-pass to recirculation peak ratio of 1.4. Dashed black lines show the height of the first-pass peak whilst the dashed blue lines indicate the height of the recirculation peak. Simulated curves with no noise (a, b), with noise level 1 (c, d) and noise level 2 (e, f)...166

Figure 7-1 Images from the same patient. Upper panel: Computed tomography coronary angiography (**A** and **B**) and invasive coronary angiography (**C**) images showing stenoses in the left anterior descending, first diagonal (yellow arrows) and left circumflex arteries (gray arrow). Middle panel: Computed tomography myocardial perfusion imaging during adenosine stress. Short-axis views of the left ventricle during adenosine stress showing hypo-enhancement corresponding to perfusion defects in the territory of the left anterior descending artery (yellow arrows) and left circumflex artery (gray arrows). Lower panel: Magnetic resonance myocardial perfusion imaging during adenosine stress. Short-axis views at 3 mid-ventricular slices over the left ventricle are presented with perfusion defects that correlate to the computed tomography images. (Adapted from Williams et al, J Cardiovasc Comput Tomogr, 2013)……………………………………………….186

Figure 7-2 Fermi modelling-derived mean myocardial blood flow (MBF) values and haemodynamic threshold calculated on ROC analysis, for identifying obstructive vessels (per vessel analysis)..………………...…………………………………..192

Figure 7-3 Distributed parameter modelling-derived mean myocardial blood flow (MBF) values and haemodynamic threshold calculated on ROC analysis, for identifying obstructive vessels (per vessel analysis)………………………………192

Figure 7-4 Illustrations of Fermi modelling-derived mean myocardial perfusion reserve (MPR) values and haemodynamic threshold, between Groups 1 and 2…...193

Figure 7-5 Graphic representation of distributed parameter modelling-derived mean myocardial perfusion reserve (MPR) values and haemodynamic threshold, between Groups 1 and 2……………………………………………………………..193

Figure 7-6 Mean myocardial perfusion reserve of the two lowest scoring segments (MPR_2) calculated using Fermi modelling and haemodynamic threshold, between Groups 1 and 2……………………....…………………………………….....194

Figure 7-7 Graphic representation of mean myocardial perfusion reserve of the two lowest scoring segments (MPR_2) calculated using distributed parameter modelling and haemodynamic threshold, between Groups 1 and 2…………………………...194

Figure 7-8 ROC graph demonstrating sensitivity and specificity of quantitative MR analysis by absolute myocardial blood flow at stress (MBF, per vessel analysis)……………………………………………………...………………195

Figure 7-9 ROC graph showing sensitivity and specificity of quantitative MR analysis by myocardial perfusion reserve (MPR, per vessel analysis)…………….195

Figure 7-10 ROC graph illustrating sensitivity and specificity of mean myocardial perfusion reserve of the two lowest scoring segments (MPR_2, per vessel analysis)..196

Figure 7-11 Visual representation of Fermi modelling-derived mean myocardial blood flow (MBF) values and haemodynamic threshold, between Groups 1 and 2 (per patient analysis). ……………………………………….…………………..201

Figure 7-12 Representation of distributed parameter modelling-derived mean myocardial blood flow (MBF) values and haemodynamic threshold, between Groups 1 and 2……………………………………………………………………...201

Figure 7-13 Mean myocardial perfusion reserve (MPR) calculated using Fermi modelling and haemodynamic, between Groups 1 and 2…………………………202

Figure 7-14 Mean myocardial perfusion reserve (MPR) calculated using distributed parameter modelling and haemodynamic threshold on ROC analysis…………….202

Figure 7-15 Mean myocardial perfusion reserve of the two lowest scoring segments (MPR$_2$) calculated using Fermi modelling and haemodynamic threshold on ROC analysis…………………………………………………………………..203

Figure 7-16 Mean myocardial perfusion reserve of the two lowest scoring segments (MPR$_2$) calculated using distributed parameter modelling and haemodynamic threshold, between Groups 1 and 2……………………..………………………203

Figure 7-17 ROC graph illustrating sensitivity and specificity of quantitative MR analysis by absolute myocardial blood flow at stress (MBF, per patient analysis)……………………………………………………………………204

Figure 7-18 ROC analysis demonstrating sensitivity and specificity of quantitative MR analysis by myocardial perfusion reserve (MPR, per patient analysis)……………………………………………………………………205

Figure 7-19 ROC analysis showing mean myocardial perfusion reserve of the 2 lowest scoring segments (MPR$_2$, per patient analysis)……………………………205

Figure 7-20 Examples of images that were considered non-diagnostic for visual assessment are shown, at the peak of contrast enhancement in the myocardium. Patient 1 (a), identified with no stenotic vessel territories and patient 2 (b), with haemodynamically significant right coronary artery disease. (c) and (d), (e) and (f) are examples of Gadolinium (Gd) concentration-time curves (blue) with Fermi and distributed parameter modelling (red), derived from patients 1 and 2, respectively..210

Figure 10-1 a) Example image in Matlab of x and y coordinates of all endocardial (red x) and epicardial (green x) points read on MR perfusion images. b) Starting point and the nearest endocardial and epicardial points are shown with blue x…...271

Figure 10-2 Endocardial (red) and epicardial (green) contours in Matlab Cartesian coordinates. The nearest endocardial and epicardial (black circles) point to the starting point was detected. x_s, y_s are the coordinates of the starting point and x_e, y_e are the coordinates of the epicardial contour point (for simplicity only the epicardial contour point coordinates are presented here and the relative (imaginary) triangle is illustrated with red)……………………………………………………………...272

Figure 10-3 Myocardium is divided into 100 equally spaced chords in QMass. The same process (steps 3-7) was replicated in Matlab………………………………...274

Figure 10-4 Graph showing consecutive endocardial (red), midpoint (black) and epicardial (green) equally spaced points. Tangent and perpendicular to the midpoint lines are illustrated. Line segments between consecutive contour points are shown for each cardiac contour. Small (black) line segments between X, Y and x_o, y_o along the endocardial (en) and epicardial (ep) contours are shown. The first chord perpendicular to the nearest midpoint (m_o) to the starting point is shown. The blue cross represents the starting point…………………………………………………..…278

Figure 10-5 a) Myocardial segmentation in Qmass. b) Myocardial segmentation replicated in Matlab. c) Endocardial (red) and epicardial (green) contours with centerline (blue) and all 100 chords. d) All contours and chords for a full perfusion data set replicated in Matlab……………………………………………………….279

List of Tables

Table 4-1 Table with T_1 relaxation times for all 9 phantoms, calculated using spin echo inversion recovery (SEIR) and MOLLI experiments. Gd: Gadolinium............86

Table 4-2 Peak arterial input function concentrations for 4 healthy volunteers. AIF: Arterial input function. 1 mM=10^{-6} mol/ml……………………………………..112

Table 4-3 Range of peak arterial input function concentration simulations and corresponding volumes of Gadovist solution in ml/ 50 ml is presented………..….114

Table 5-1 Model equations. Fitted parameters for distributed parameter: myocardial blood flow, T is mean overall transit time, T_c is mean capillary transit time, T_e is mean interstitial (i.e. extravascular-extracellular) transit time. Where $s = i \cdot 2 \cdot \pi \cdot f$ and f is the frequency variable in the Fourier transformed data. Fitted parameters for Fermi: myocardial blood flow, τ_0 characterized the width of the shoulder of the Fermi function and k determined the decay rate of R(t) due to contrast agent wash-out. t is the time variable. DP: distributed parameter model, MBF: myocardial blood flow………………………………………………………………………...125

Table 5-2 Microvascular characteristics were calculated by incorporating the fitted parameters of the distributed parameter model into the following relationships (see reference [50]). Myocardial plasma flow (MPF) was used to calculate extravascular-extracellular space (v_e), distribution volume (v_d), permeability surface area product (PS) and extraction fraction (E) and myocardial blood flow (MBF) to calculate intravascular space (v_b). Hematocrit: hct…………………………………….….130

Table 5-3 Healthy volunteer mean (SD) myocardial blood flow values calculated using dual and single bolus analysis. Statistical differences between single and dual bolus analysis are indicated with *. DP: distributed parameter model……..……..138

Table 5-4 Mean microvascular characteristics (SD) estimates for healthy volunteers and for all 3 invasive coronary angiography/fractional flow reserve Groups. Notations as in Tables 5-1 and 5-2…………………………………………………...139

Table 5-5 ICA/FFR classification and mean MBF (SD) at stress measured in ml/min/ml per vessel territories of the three main coronary arteries. LAD, LCX and RCA: left anterior descending, left circumflex and right coronary artery respectively. Vessels with reduced myocardial blood flow are indicated with *. Notations as in Table 5-1 and Figure 5-6…………………………………………………………...143

Table 6-1 Ideal values for set of tissue concentration-time curves with first-pass to recirculation peak ratio of 1.5. F: blood flow, PS: permeability surface area product, E: extraction fraction, v_b=intravascular space, v_e=extravascular-extracellular space, v_d=volume distribution...159

Table 6-2 Ideal values for set of curves with first-pass to recirculation peak ratio of 1.4. Notations as in Table 6-1..160

Table 6-3 P values from paired *t*-test comparisons between DP- and first pass DP-derived results versus actual values. Comparisons are shown in curves with first pass to recirculation peak ratio of 1.5. Mod: Modelling, F: flow (ml/min/ml), PS: permeability surface area product (ml/min/ml), E: extraction fraction (%), v_b: intravascular space (%), v_e: extravascular extracellular space (%), v_d: distribution volume (%), N_0: without noise, N_1: noise level 1, N_2: noise level 2, FPDP: first pass distributed parameter modelling. Statistically significant differences are indicated with *……………………………………………………………………162

Table 6-4 P values from paired *t*-test comparisons between DP- and first pass DP-derived results versus actual values. Comparisons are shown in curves with first pass to recirculation peak ratio of 1.4. Notations as in Table 6-3……………………….163

Table 7-1 Baseline characteristics of study participants (parentheses show %)…..187

Table 7-2 Diagnostic accuracy (i.e. sensitivity, specificity, PPV, NPV) (95% CI) of visual MR estimates is shown. PPV: positive predictive value and NPV: negative predictive value, are presented in per vessel and per patient basis………………...188

Table 7-3 Threshold values for all haemodynamic parameters calculated with Fermi and distributed parameter (DP) modelling, in per vessel and per patient basis. Thresholds for myocardial blood flow were measured in ml/min/ml. MBF: myocardial blood flow, DP: distributed parameter, MPR: myocardial perfusion reserve, MPR_2: mean myocardial perfusion reserve of the two lowest scoring segments……………………………………………………………………189

Table 7-4 Mean (SD) values for Fermi- and distributed parameter modelling-derived haemodynamic parameters, for Groups 1 and 2 are presented. Also, significant differences between Group 1 and Group 2 in per vessel and per patient based analysis are shown. P values for distributed parameter modelling were consistently higher compared to Fermi modelling in both per vessel and pet patient based analysis. Notations as in Table 7-3……………………………………………...191

Table 7-5 Diagnostic accuracy (95% CI) of Fermi- and DP modelling-derived haemodynamic parameters, in detecting obstructive coronary artery disease, is shown (per vessel analysis). Notations as in Tables 7-2 and 7-3…………………….……197

Table 7-6 AUC (95% CI) from ROC analysis in per vessel and per patient basis are shown. AUC: Areas under the curve, rest of notations as in Table 7-3……..……198

Table 7-7 Positive likelihood ratios in per vessel and per patient analysis are demonstrated……………………………………………………………………199

Table 7-8 Diagnostic accuracy (95% CI) of Fermi- and DP modelling-derived haemodynamic parameters, in detecting obstructive coronary artery disease, is shown (per patient analysis). Notations as in Tables 7-2 and 7-3…………………...……206

Table 7-9 Diagnostic accuracy for visual estimates (95% CI) from CT angiography, CT perfusion and CT angiography/perfusion for per vessel territory based analysis……………………………………………………………………..207

Table 7-10 Diagnostic accuracy for visual estimates (95% CI) from CT angiography, CT perfusion and CT angiography/perfusion for per patient based analysis…..….207

Table 7-11 Haemodynamic threshold values from previous positron emission tomography (PET) and magnetic resonance imaging (MRI) studies. MBF: myocardial blood flow, MPR: myocardial perfusion reserve, MPR2: mean myocardial perfusion reserve of the two lowest scoring segments……….…….212

Acknowledgements

To my mother, Vassiliki. It may not be enough to say thank you for all the emotional support through the years and for teaching me that life is not important without a youthful heart and integrity.

To my father, Andreas. For the endless discussions, scientific and personal, as well as for teaching me that life is more meaningful and interesting with freedom of thought. My admiration and love for both is beyond words.

To my partner in life, Marianna. Words will fade if I will attempt to describe my feelings and how special and supportive you are. I will take a moment to say that with you around, my dreams become stronger and happier.

Thank you to my beloved sister, Christina for always being available for a discussion about everything. I wish you luck and may your greater dreams come true.

Thank you to my supervisor, Scott. I can only feel grateful and lucky for being introduced to the world of medical imaging by an academic like Scott Semple. Thank you for transmitting scientific knowledge and training, the guidance and support. I really enjoyed all the times we discussed about MR physics and medical imaging, about work but also about life.

To my good friends, especially to Dias and Kostis. It is impossible not to feel lucky when I share with them fun and philosophical discussions, childhood memories and adulthood experiences.

Finally, great acknowledgments to my advisors and colleagues for their contribution to this work and for the very educational moments they offered. Particularly, special thanks to David Newby, Lucy Kershaw, Michelle Williams, Tom MacGillivray, Calum Gray, Martin Connell, Shirjel Alam and to the radiographers of our centre Annette Cooper and David Brian.

Publications

Journal papers:

Papanastasiou G, Williams MC, Dweck MR, Alam S, Cooper A, Mirsadraee S, Newby DE, Semple SIK: Quantitative assessment of myocardial blood flow in coronary artery disease by cardiovascular magnetic resonance: comparison of Fermi and distributed parameter modeling against invasive methods. *J Cardiov Magn Reson* 2016, 18: 57.

Papanastasiou G, Williams MC, Kershaw LE, Dweck MR, Alam S, Mirsadraee S, Connell M, Gray C, MacGillivray T, Newby DE, Semple SIK: Measurement of myocardial blood flow by magnetic resonance perfusion imaging. Comparison of distributed parameter and Fermi models with single and dual bolus. *J Cardiov Magn Reson* 2015, 17: 17.

Conference abstracts:

Papanastasiou G, Kershaw LE, Williams MC, Dweck MR, Alam S, Mirsadraee S, Gray C, MacGillivray T, Newby DE, Semple SIK: A multimodality cross-validation study of cardiac perfusion using MR and CT. ISMRM 21st Annual Meeting Proceedings, 2013, Salt Lake City, UTAH.

Papanastasiou G, Williams MC, Alam S, Dweck MR, Mirsadraee S, Gray C, Connell M, MacGillivray T, Newby DE, Semple SIK: Assessing the reliability of DP and Fermi estimates in single and dual bolus cardiac MR perfusion imaging. *J Cardiov Magn Reson* 2014, ***16*** *(Suppl 1):*P347, New Orleans.

Papanastasiou G, Williams MC, Dweck MR, Mirsadraee S, Weir N, Alam S, Stirrat C, Newby DE, Semple SIK: Comparison of distributed parameter and Fermi modelling of cardiac MR perfusion with CT perfusion in coronary artery disease versus invasive coronary angiography. ISMRM-ESMRMB Joint Annual Meeting Proceedings, 2014, Milan, Italy (also oral presentation at the 20th Annual Scientific ISMRM Meeting of the British Chapter, 2014, Edinburgh, United Kingdom).

..The enemy of man is not germs, but man himself, his pride, his prejudices, his stupidity, his arrogance. It was not enough to overthrow governments or masters, total revolution of thought was needed…

..Peace is not the opposite of war, any more than death is the opposite of life. Every war is a defeat to the human spirit…

..Until the man has become fully human, until he learns to conduct himself as a member of the earth, he will continue to create gods who will destroy him…

..He spoke frequently of the past, it is true, not as something dead and forgotten however, but rather as something which we carry with us, something which fructifies the present and makes the future inviting. He spoke of little things and of great with equal reverence; he was never too busy to pause and dwell on the things which moved him; he had endless time on his hands, which in itself is the mark of a great soul. How can I ever forget that last impression he made upon me when we said farewell at the bus station in the heart of Athens? There are men who are so full, so rich, who give themselves so completely that each time you take leave of them, you feel it is absolutely of no consequence whether the parting is for a day or forever. They come to you brimming over and they fill you to overflowing. They ask nothing of you except that you participate in their superabundant joy of living. They never inquire which side of the fence you are on because the world they inhabit has no fences. They make themselves invulnerable by habitually exposing themselves to every danger. They grow more heroic in the measure that they reveal their weaknesses…

From the book ‘The Colossus of Maroussi’, 1939, Greece.

Henry Miller